FEDERAL UNIVERSITY OF SANTA MARIA
CENTER OF TECHNOLOGY
ELECTRICAL ENGINEERING GRADUATE PROGRAM

William Guidolin da Rosa

ANALYSIS, MODELING AND CONTROL OF SELF-OSCILLATING RESONANT CONVERTERS

Santa Maria, RS
2023

ANALYSIS, MODELING AND CONTROL OF SELF-OSCILLATING RESONANT CONVERTERS

by

William Guidolin da Rosa

Doctoral dissertation presented to the Doctoral Course of the Electrical Engineering Graduate Program, in the Energy Processing area, of the Federal University of Santa Maria (UFSM-RS), in partial fulfillment of the requirements for the degree of **Doctor in Electrical Engineering.**

Advisor: Dr. Eng. Álysson Raniere Seidel
Co-Advisor: Dr. Eng. Fábio Ecke Bisogno

Santa Maria, RS, Brasil
2023

To my mother, who has always been there for me, through the good times and the bad, with her unconditional love, support and encouragement. You are my inspiration and my strength. Thank you for everything.

To God, who is the source of all love and friendship, who has blessed me with the gift of true friends, who have supported me, guided me, and comforted me throughout this journey. You are the ultimate friend, who never leaves me nor forsakes me. Thank you for your grace and mercy.

ACKNOWLEDGEMENTS

To professors Dr. Eng. Álysson R. Seidel, Dr. Eng. Fábio E. Bisogno, Dr. Eng. Maikel F. Menke, and Rodrigo V. Tambara for their invaluable friendship, guidance, and transmission of knowledge. To my colleagues at GEDRE and GSEC for their friendships, contributions, and constant dialogues over the years, which definitely helped in building part of the knowledge shown in this doctoral dissertation. To the Federal University of Santa Maria (UFSM-RS) and the Industrial Technical College of Santa Maria (CTISM) for providing the structure and support for the development of activities related to study and research during my undergraduate, master's, and doctoral studies. To the Postgraduate Program in Electrical Engineering (PPGEE) for their support and technical assistance in activities related to teaching and research.

To the *Aperfeiçoamento de Pessoal de Nível Superior* (CAPES)[1] for the financial support.

To the *Conselho Nacional de Desenvolvimento Científico e Tecnológico* (CNPq) and the *Fundação de Amparo à Pesquisa do Estado do Rio Grande do Sul* (FAPERGS)[2] for the financial support through programs PROEX, PRPGP/UFSM, INCT-GD.

To the members of the examining board for their past, present, and future contributions on a research field that is often overlooked but holds a dear space in my heart.

[1] O presente trabalho foi realizado com apoio da Coordenação de Aperfeiçoamento de Pessoal de Nível Superior - Brasil (CAPES/PROEX) - Código de Financiamento 001, proc. 23038.000776/2017-54.

[2] O autor gostaria de agradecer o CNPq, CAPES e FAPERGS. Este trabalho foi financiado pelo governo brasileiro através do programa PROEX, PRPGP/UFSM, INCT-GD. CNPq proc 465640/2014-1, 311911/2015-3, 409632/2016-3, 313338/2018-3, CAPES proc 23038.000776/2017-54, FAPERGS proc 17/2551-0000517-1.

RESUMO

ANÁLISE, MODELAGEM E CONTROLE DE CONVERSORES RESSONANTES AUTO-OSCILANTES

AUTOR: WILLIAM GUIDOLIN DA ROSA
ORIENTADOR: ÁLYSSON RANIERE SEIDEL, DR. ENG.
COORIENTADOR: FÁBIO ECKE BISOGNO, DR. ENG.

Nesta tese é discutida a análise, modelagem e controle do Conversor Ressonante Auto-Oscilante. Conhecido por suas notáveis características de custo-benefício, eficiência e simplicidade, este foi amplamente utilizado em aplicações relacionadas à iluminação artificial, como reatores eletrônicos para lâmpadas de descarga. Todavia, dada a complexidade dé análise e projeto de sua estrutura de realimentação positiva, observada pela necessidade de utilização de técnicas simplificadas de controle não-linear para o projeto em malha aberta, a operação em malha fechada foi pouco explorada na literatura. O fato é que pouco se sabe sobre as potencialidades de operação deste conversor como seguidor de referência, visto que a presença de uma realimentação positiva intrínseca pode sugerir a inviabilidade de tal prática. Desde a busca por um atuador compatível com as características do conversor, passando pela modelagem e efetivamente à operação como seguidor de referência, esta tese busca expandir o breve conhecimento disponível sobre este conversor, colocando-o no patamar de conversores que tradicionalmente permitem a operação em malha fechada, elencando, a partir de uma análise minuciosa, suas peculiaridades e características frente as demais topologias. Busca-se, em uma primeira etapa desta tese, explorar a análise e o projeto do CRAO por meio da revisão bibliográfica das diversas metodologias até então propostas, solidificando o entendimento sobre a operação auto-oscilatória do conversor em malha aberta. A partir disto, discutem-se formas de expandir a operação do CRAO, desvencilhando-o da operação tradicional em malha aberta com realimentação intrínseca positiva, ao introduzir atuadores que permitam a operação do conversor como *Pulse-Frequency Modulator* (PFM) ou *Pulse-Width Modulator* (PWM). Posteriormente, propõe-se uma revisão bibliográfica minuciosa das técnicas de modelagem utilizadas para conversores ressonantes, cujo resultado auxiliou na definição de uma metodologia capaz de gerar as novas funções de transferência necessárias ao projeto dos controladores para operação em malha fechada do CRAO.

Palavras Chave: Conversor Ressonante Auto-Oscilante; Modelagem; Controle; Atuadores; Operação em Malha Fechada; Seguidor de referência.

ABSTRACT

Doctoral Dissertation
Post-Graduation Program in Electrical Engineering
Federal University of Santa Maria, RS, Brazil

ANALYSIS, MODELING, AND CONTROL OF SELF-OSCILLATING RESONANT CONVERTERS

AUTHOR: WILLIAM GUIDOLIN DA ROSA
ADVISOR: ÁLYSSON RANIERE SEIDEL, DR. ENG.
CO-ADVISOR: FÁBIO ECKE BISOGNO, DR. ENG.

In this doctoral dissertation, the analysis, modeling, and control of the Self-Oscillating Resonant Converter are discussed. Known for its remarkable cost-benefit, efficiency, and simplicity, it has been widely used in applications related to artificial lighting, such as electronic ballasts for discharge lamps. However, given the complexity of analyzing and designing its positive feedback structure, observed by the need to use simplified non-linear control techniques for open-loop design, closed-loop operation has been little explored in the literature. The fact is that little is known about the potential of operating this converter as a reference follower, since the presence of intrinsic positive feedback may suggest the impracticality of such practice. From the search for an actuator compatible with the converter's characteristics, through modeling and effectively operating as a reference follower, this doctoral dissertation seeks to expand the brief knowledge available on this converter, placing it on par with converters that traditionally allow closed-loop operation, listing, from a thorough analysis, its peculiarities and characteristics compared to other topologies. In a first stage of this doctoral dissertation, we seek to explore the analysis and design of the CRAO through a bibliographic review of the various methodologies proposed so far, solidifying the understanding of the converter's self-oscillatory operation in open-loop. From this, ways to expand the operation of the CRAO are discussed, disengaging it from traditional open-loop operation with intrinsic positive feedback by introducing actuators that allow the converter to operate as a Pulse-Frequency Modulator (PFM) or Pulse-Width Modulator (PWM). Subsequently, a thorough bibliographic review of modeling techniques used for resonant converters is proposed, whose result helped define a methodology capable of generating new transfer functions necessary for designing controllers for closed-loop operation of the CRAO.

Keywords: Self-Oscillating Resonant Converter; Modeling; Control; Actuation Mechanisms; Closed-loop operation; Reference following.

LIST OF FIGURES

LIST OF TABLES

SYMBOLOGY

SORC	Self-Oscillating Resonant Converter
SOCC	Self-Oscillating Command Circuit
CT	Current Transformer
E	SORC's bus voltage
v_{ab}	Filter's input voltage
i_f	Filter's current
i_s	SOCC's secondary currents
i_m	SOCC's magnetizing current
i_z	SOCC's Zener current
i_g	MOSFET's gate current
Z_f	Filter's total impedance
Y_f	Filter's total admitance
C_r	Filter's series capacitor
C_p	Filter's parallel capacitor
L_r	Filter's series inductor
L_p	Filter's parallel inductor
R_o	Filter's load
L_p, L_{s1}, L_{s2}	SOCC's self inductances
L_m	SOCC's magnetizing inductance
Q	Filter's quality factor
ω_o	Filter's angular resonant frequency
f_o	Filter's resonant frequency
ω_s	Filter's angular switching frequency
f_s	Filter's switching frequency
T_s	Switching period
C_1	Startup circuit capacitor
R_1	Startup circuit resistor
R_2	C_1 discharge resistor
D_1	C_1 discharge diode
$d_{z1\text{-}z4}$	CCAO's Zener diodes
V_z	Zener diode breakdown voltage
V_f	Zener diode voltage drop
S_1	*High-side MOSFET*
S_2	*Low-side MOSFET*

K	Proportionallity factor
α_i	CT's primary to secondary ratio
G_f	Filter's elements block
G_m	Magnetizing inductance block
G_{Cgs}	Gate-to-source capacitance block
G	Block of the linear part of the system
N	Describing function block
$r(t)$	Generic control system's input
$c(t)$	Generic control system's output
$u(t)$	Generic control system's non-linear output
C_{gs}	MOSFET's gate-to-source capacitance
C_{gd}	MOSFET's gate-to-drain capacitance
C_{ds}	MOSFET's drain-to-source capacitance
C_{eq}	MOSFET's gate equivalent capacitance
v_s, v_{in}	Voltage applied to the filter
t_{fn}	Tsypkin's equation
ε	Amplitude of the oscillating condition i_p
I_{LED}	LED current
V_{LED}	LED voltage
r_D	LED dynamic resistance
V_{TH}	LED thresold voltage
P_o	LED string power
R_{LED_ac}	LED resistance at the filter output
Q	MOSFET Gate charge
I_{DC}	VCT auxiliary current
t_r	Rising time of C_{eq}
ϕ	Angle caused by C_{eq}
u	Input array of the LSM
y	Output array of the LSM

TABLE OF CONTENTS

1

INTRODUCTION

In this chapter, the basic knowledge regarding the subject of this doctoral dissertation is explored. A brief discussion about lighting systems is required to understand the circumstances that enabled the birth of the Self-Oscillating Resonant Converter. Initially employed as a simple topology for cost-effective electronic ballasts, its usage has been consistently neglected primarily due to the rise of solid-state lighting technology as a more attractive artificial lighting source. The challenges behind its analysis and design are delineated, with a brief review of the progression of its currently available open-loop design methodologies and the aspects that led to its oversight as a closed-loop alternative to power control stages.

1.1 INTRODUCTION

One of the most significant challenges of contemporary research in the electrical engineering field is to preserve an equilibrium status between energy generation and consumption. This equilibrium constantly changes as societies develop and can be achieved from changes in both processes, either by increasing the energy generation to keep up with ever-increasing consumption at the expense of resources or by improving the consumption process itself.

An existing example of a shift in this equilibrium is the Brazilian crisis in the energy sector, expected to repeat in the following years, just as it happened from June 2001 to March 2022[3]. The Brazilian energetic matrix, composed mainly of the hydroelectric sector, suffers from low reservoir levels, partly from the Amazon rainforest deforestation. Summing up the increased residential demand for energy during the COVID-19 pandemic, specialists foresee consistent increases in energy pricing in the following years. A considerable portion of those increases relates to the urgent necessity of employing non-renewable sources to compensate for the current energy deficit, thermoelectric energy being the main one.

On the other hand, on a more formal approach, the energy deficit could be damped given the optimal consumption of the generated energy. An example of this subject is optimizing the various electronic systems used in residences, such as ballasts for discharge lamps and drivers for LED, electronic heaters, air conditioners, and other potentially improvable electronic devices. Replacing electromagnetic ballasts for electronic ones, choosing LEDs with higher efficiency and better-optimized drivers, preferring heaters and air conditioners with inverter topologies are all choices that favor the optimization end of energy consumption. Also, alternative decentralized renewable energy sources could be used to complement such practices, such as photovoltaic panels, with the same potential for optimization, given the usage of devices such as solar inverters.

The replacement of electromagnetic ballasts for electronic ones has already taken place in mass over the last couple of decades, as their features were too good to pass by. The electronic device undoubtedly surpassed the electromagnetic counterpart with a higher frequency of

[3] More information about the 2001 brazilian energy crysis can be found at: https://www.nytimes.com/2001/06/06/world/energy-crisis-in-brazil-is-bringing-dimmer-lights-and-altered-lives.html

operation, efficiency, and smaller size and volume, considerably increasing the lamp's lifespan while reducing adverse effects associated with the low-frequency operation, such as the stroboscopic effect[4][5]. As a result of this replacement process, company researchers were motivated to develop new, smaller, and more efficient lamps that were also more environmentally friendly[6]. Simultaneously, academic researchers focused on improving the electronic system attached to the lamp bulbs by proposing circuit topologies with reduced power losses and higher lifespan with extra functionalities. Among those are circuits with universal input capability and systems that allow for the operation of different types of lamps[7], including the possibility of varying its output power, i.e., its luminosity, to match the current ambiance requirement.

In the advances following its creation around the 1940s, the discharge lamps quickly overthrew the incandescent lamps designed by Thomas Edison in the 1880s. In the 1960s, however, a lighting emitting type diode initially intended to work as a simple luminous indicator in the colors red and green walked its first steps. In the following decades, LED lighting suffered constant upgrades due to the research and development of more suitable and adequate materials, efficiently emitting infrared, red, and green lights. However, it was not until 1994 that the secrets behind blue-light emission were cracked at the Nichia Corporation, using *Indium Gallium Nitride* as a substrate for LEDs. Concurrently, researchers Isamu Akasaki and Hiroshi Amano at Nagoya University developed a *Gallium Nitride* substrate for LEDs. They won the 2014 Nobel Prize in Physics[8], finding the missing puzzle piece required to enable LEDs to emit white light. Nowadays, Solid-State Lighting (SSL), the type of lighting created by LEDs, is in

[4] The stroboscopic effect is a phenomenon where a certain equipment appears to be stationary to the viewer's perception, even though it is actually in movement.

[5] In the case of discharge lamps operating at 50 or 60 Hz, there is a flickering caused by the zero crossing of the supply current at double those frequencies, which are not noticed by the human eye. The danger lies on the objects illuminated by the flickering discharge lamps however, which may be rotatory machines that under the stroboscopic effect may appear to be stationary or running slower than it actually is, potentially increasing the likelihood of accidents.

[6] Since their introduction in 1998, T5 lamps have consistently replaced their T8 counterparts and can be considered the state-of-the-art devices of the fluorescent niche today. According to Yancey (1998) and GE Lighting (2002), despite the equivalent luminous efficacy of T5 and T8 lamps, the reduced surface of the T5 model allows for manufacturers to use 60 % less glass and phospor materials when compared to T12 models, and 38 % when compared to T8 ones. According to Van Vleef (1996), the T5 models contain 3 mg of Mercury, and the introduction of an improved coating technology also helped to prevent mercury to be absorbed by the phospor layer and the bulb glass.

[7] In order to compromise with the NBR 14418, Lopes (2018) proposes a system that feeds any of three models of T5 lamps (24, 39 and 49 W), by using a SEPIC PFC stage connected to an assymetric half-bridge resonant converter.

[8] For more information regarding the 2014 Nobel Prize in physics, refer to: https://www.nobelprize.org/prizes/physics/2014/press-release/

a very venerable position regarding technological advancements. Rated amongst the most efficient ways of producing artificial lighting due to its excellent luminous efficiency (lumens per watt), the LED also has a lifespan that greatly surpasses former technologies such as discharge and incandescent lamps.

Like the discharge lamps, the LEDs require an intermediate circuit that connects them to the power source. A common characteristic among the various circuit topologies proposed and developed is guaranteeing that the LED operates safely within its recommended electric requirements, such as electrical current and voltage. Furthermore, as these circuits are known, the LED drivers must have efficiency levels compatible with the SSL technology to avoid underutilization below its designed lifespan. Not only that, but ideally, the driver's lifespan must, at the very least, be equal to that of the LED lamp itself. Every aspect of efficient power consumption, especially for artificial lighting, involves using efficient, robust, and durable electronic systems compatible with the technologies they are driving. As it happened for the discharge lamps era, replacing electromagnetic for electronic ballasts was a requirement; for SSL systems, highly efficient and durable electronic devices compatible with the LED lifespan are necessary.

An attractive low-cost alternative that the industry has extensively used as a solution for electronic ballasts since the early 1990s is the Self-Oscillating Resonant Converter (SORC). In essence, it is a DC to AC inverter but with a straightforward switching network that does not require Integrated Circuits (IC) and its additional circuitry to function. The switching network that substitutes the IC in the SORC, known as the Self-Oscillating Command Circuit (SOCC), was an idea from the early 1940s, used in telecommunication systems, telemetry, frequency modulation/demodulation, and to a lesser extent, power conversion. However, his usage considerably grew with the 1950s development of new semi-conductors like the Bipolar Junction Transistor (BJT), which allowed it to be further associated with increased power density in power conversion applications[9]. The 1959 discovery of Metal-Oxide-Semiconductor Field-Effect Transistors (MOSFET) and their 1960s production growth were the factors that set the Self-Oscillating Command Circuit to become one of the most popular topologies for cost-effectiveness and robustness in lighting systems for the next decades.

[9] V. B. Hulme (1959) demonstrated many potential applications for the circuit known today as SOCC that originated from the popularized BJT. Among those are the magnetic multivibrators, frequency-modulated oscillators, magnetically biased oscillators, magnetic flip-flops, and applications in telemetry that include frequency modulation, chopper amplification, demultiplexing and its synchronization, as well as phase-lock variations.

A commonly employed circuit to operate LEDs and, especially, discharge lamps is the series Resonant Converter. This topology operates under imposed frequency defined by an IC, as shown in Figure 1(a), or with a frequency determined by the SOCC, as shown in Figure 1(b). This variant of the circuit operates with a Three-Winding Current Transformer (TWCT) and four Zener diodes, being able to drive LEDs, as shown in Figure 1(c), and discharge lamps, as shown in Figure 1(d). The subtle difference in the type of network that imposed the resonant converter's frequency was a defining factor for popularizing electronic ballasts in the early 2000s. The reduced production cost and potential volume reduction that the SOCC offered compared to the IC switched resonant converters certainly encouraged the acquisition of electronic ballasts and the subsequent substitution of their electromagnetic counterparts. Even in these last years, with the ongoing popularization of SSL technology, which still translated into higher LED bulb prices, a considerably popular and budget alternative for residential lighting that uses the SOCC is the Compact Fluorescent Lamp (CFL).

Figure 1 - Resonant Converters (a): Traditionally IC switching (b) Self-Oscillating Command switching (c) LED load (d) Fluorescent lamp load.

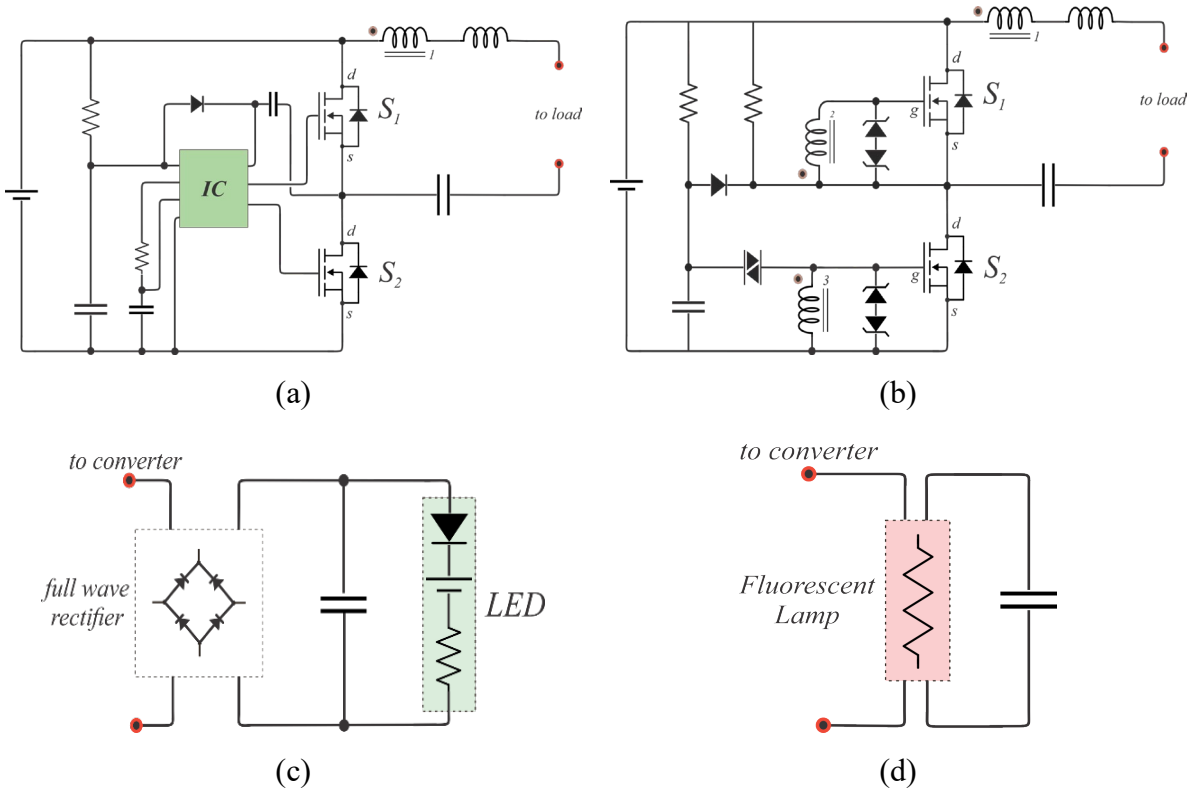

Source: Author

Despite being an uncomplicated solution for higher frequency switching of resonant converters and having the aforementioned characteristics, the SOCC has constantly been the

discussion target regarding its design and analysis. This fact holds due to the difficulty of analyzing a positive-type feedback network that, in the case of the SORC, for example, feeds the output filter current positively as gate-charge for the bridge MOSFETs. The usage of simple circuit analysis tools for linear systems does not hold in the case of the SOCC due to the non-linear characteristic of the square-wave voltage generated by the Zener diodes, which is also reflected in the switches. Moreover, as examined further into this doctoral dissertation, the SOCC may impose an instability condition[10] on the converter, thus requiring both a methodology to design the SOCC and reliable stability analysis.

Unlike traditionally switched converters, the dependence this converter has on its gate-drive network makes the pursuit of a widely accepted and suitable design technique still an ongoing process up to today. To understand how it worked and how it could be designed, the first efforts made by researchers started in the 1900s by acknowledging the SORC as a relay system, managing its design from a control point of view with null reference. This realization, shown in (ATHERTON, 1987) and called Standard Relay Control System (SRCS), is the fundamental basis of almost every design technique proposed for the SORC so far. The main idea of this analysis is to predict the effect the relay element, i.e., the non-linear part of the system has on the linear part $G(s)$. The reference of the system $r(s)$ is null because the output $y(s)$ is directly connected to the input of the relay element, whose output is again applied to the linear part, closing the self-oscillation loop. The analysis of non-linear systems through this structure has been used on pretty different applications in varied areas[11]. In the SORC's case, the relay system represents the polarity change of the Zener voltage applied to the gate of the MOSFETs, which originated from the output filter current $y(s)$ through the TWCT.

Another very interesting characteristic regarding SORCs as compared to IC switched converters is the dead time, which is a critical parameter in the operation of resonant converters, especially LLC converters. It is the time delay implemented in the control algorithm to prevent both switches in a half-bridge or full-bridge configuration from being on at the same time, which could lead to a damaging condition known as shoot-through. Dead time ensures that one

[10] The Nyquist Criterion (NC) is widely used to design and investigate the stability of linear time-invariant (LTI) systems, where techniques such as Lyapunov are preferred when analyzing non-linear ones. Although the SORC contains a hard non-linearity imposed by the SOCC, the usage of a linearization technique called Describing Function allows the SORC stability to be assessed by the NC.

[11] The 1974 Tsypkin's book on relay control systems showed the SRCS applicability on automatic temperature regulation systems with different types of delays, vibrational voltage controller for generators, automatic frequency control for communication and location radio devices, automatic speed control for motors, and many others. More information can be found in Tsypkin's book from pages 7 to 17.

switch is turned off before the other is turned on. In LLC converters, dead time can be programmed externally using two external components (INSTRUMENTS, 2006), (INFINEON, 2021). SORCs, on the other hand, have an inherent ability to operate under neglected preoccupation for the dead time. This is due to their intrinsic self-oscillating nature. In SORCs, the switching frequency is determined by all of the circuit elements related to the oscillation frequency, such as the resonant tank, load, driving circuit, and switching devices. A good example of this principle can be observed in (STMICROELECTRONICS, 2011), where the two switches are not intentionally turned on at the same time because of their opposing base-emitter junction thresholds. To prevent the generation of a bridge shoot-through current, it is recommended to add a so-called "interlock delay time" or the more popular "dead time" into the control scheme. With this additional time, one of the two switches is always turned off first, and the other one will be turned on after the dead time has expired, thus preventing a bridge shoot-through caused by the asymmetrical turn-on and turn-off times of the switches. Therefore, while dead time is a critical consideration in the design and operation of LLC converters, SORCs have an inherent ability to manage this parameter due to their self-oscillating nature. This makes SORCs particularly robust and versatile for a wide range of applications (ZAUPA *et al.*, 2023), (NIWA *et al.*, 2018).

Figure 2 - Standard Relay Control System.

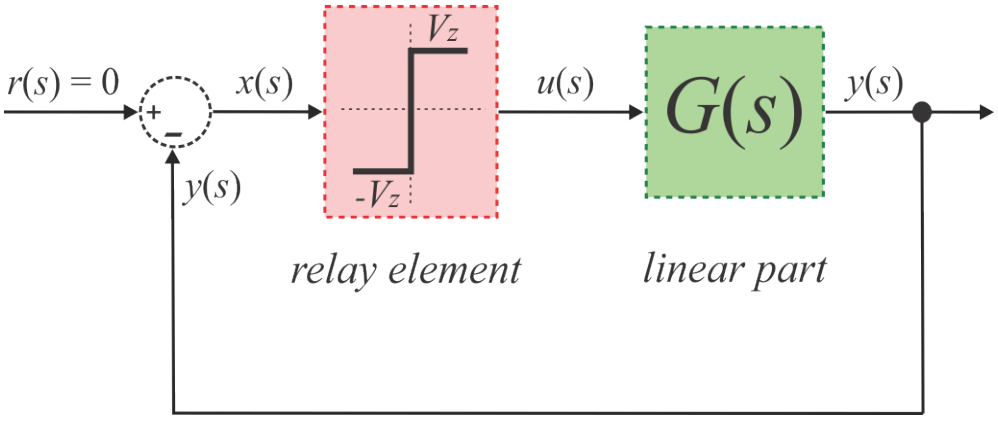

Source: Author

Among the proposed design methodologies, the three main ones utilize the SRCS to predict the relay element's effect in the linear part of the system. The main goal of every method is to find the relay's parameters that guarantee the self-oscillation of the design on the desired frequency. The first one is called the Tsypkin's Hodograph Method (THM) and is the most thorough method, providing a graphically intuitive way of predicting the evolution of the

system's amplitude as a function of the frequency. The THM uses the Fourier series and the superposition principle to calculate the effect that a noninfinite amount of harmonics from the relay element has in the linear part of the system. This method establishes the necessary conditions for self-oscillation and is thoroughly depicted in (CHANG; CHANG; BRUNING, 1999) to design a SORC.

The second method is called the Hamel Locus Method (HLM). It is, in essence, considerably similar to the THM because it also uses the superposition principle and is interested in the harmonics from the output of the relay element and their effects in the linear part. However, as opposed to the THM that analyses the frequency domain, the HLM operates in the time domain with variables resulting from the differential equations of the linear portion of the system. This similarity between the THM and the HLM is curious and was analyzed in previous works (JUDD, 1975). As stated by the author:

> " (…) the Hamel necessary conditions for the existence of a simple limit cycle in a SRCS can be obtained from the corresponding Tsypkin conditions by a simple transformation using the Poisson sum formula. Moreover, this relationship is an aid in the understanding of approximate analysis methods, which are based on the exact conditions of Tsypkin and Hamel. A comparison of these different approximations was made by using the notation and techniques of Judd and Chirlian (1974). It was found that the Tsypkin approximation (including the describing function) tends to be most accurate for high-frequency designs, whereas the Hamel-type approximations tend to be most accurate for low-frequency designs. The two approximate methods appear to complement each other well."

As briefly mentioned by the author, the last-mentioned linearization method employed to design the SORC is a simplified version of the HLM and, more particularly, the THM. Known as the Describing Function Method (DFM), this simplified technique was first published shortly after the findings of Hamel and Tsypkin as being a particular case of the frequency domain where there was no interest in a noninfinite number of harmonics. Instead, only the effect of the fundamental harmonic of the relay's output is considered in the analysis. This simplification is usually accurate and provides good results when the linear system to which the relay is connected can be characterized as a low-pass system[12].

The required stability analysis for systems that operate under a stable limit cycle, such as the SORC, can generally be graphically analyzed, as is the case for the HLM and the THM, by observing the evolution of their functions positions on the complex plane. As for the DFM,

[12] This commonly occurs in resonant converters with output LC, LCC and LLC filters operating close to their resonant frequencies. Realistically, for ZVS operation with MOSFET driven converters, the system ideally operates slightly above the resonant frequency, hence presenting an inductive characteristic. This particular operation allows for the usage of the simplified technique of the DF.

the Extended Nyquist Criteria (ENC) can attest to the system's stability due to the linearization process. The stability analysis and the search for stable limit cycles become ever more critical with further discussions of this doctoral dissertation, particularly as we begin to consider extra feedback loops with infinite possible limit cycles within a specific closed-loop operating range.

One of the most challenging design characteristics of the Self-Oscillating Command Circuit (SOCC) is the non-linearity represented by the polarity change of the MOSFET gate-to-source voltage v_{gs}. To elucidate the proper design of converters operated with this kind of intrinsic positive-type feedback circuit, many authors presented different points of view regarding the non-linear analysis. The THM, the Z transform (MCVEY; NURRE, 1964), the time-domain analysis of the HLM, and the classic DFM technique with the ENC have a common focal point: the proper insertion of the non-linearity in the topology design, which results in an appropriate prediction of the sustained self-oscillation.

The SORC is usually designed around a single operating frequency point for most applications, using one of the mentioned design methodologies to support the analysis of stable limit cycles around that single point. A reasonably common usage is to feed fluorescent lamps or LED strings around a unique operating point with well-defined electrical characteristics, such as working current, voltage, power, and equivalent resistance, as well as a single input voltage. The filter topology falls into three categories, the LC series, LCC (paralleled capacitor), and LLC (paralleled inductor) chosen based on primary characteristics such as the load type, and secondary necessities, like isolated output. The SORC will likely have its self-oscillating frequency varied due to load or bus voltage changes[13].

Considering its extensive usage for lighting systems, along with this single operating point characteristic, it was only natural that various luminous intensity variation research and applications, i.e., dimming, emerged through the SORC. Most of those, like (TAO *et al.*, 2001) and (MICHEL *et al.*, 2002), proposed the variation of self-oscillating frequency by actively altering the magnetizing current of the TWCT through additional active elements such as microcontrollers and BJTs, changing the bulb's power. Other alternatives, such as (SEIDEL, Á. R. *et al.*, 2003), suggested adding impedances near the magnetizing current path to alter the current relationship in the TWCT's secondary, such as RC and LC branches, passively affecting the frequency for the same effect. Some proposals go a step further regarding frequency variation and explore extra functionalities of the SORC, as shown by (KOHLER *et al.*, 2019).

[13] This statement may not hold true in the case of the LLC resonant converter operating with IC driven MOSFETs. However, in the case of the LLC SORC, further assessment of the frequency variation is required.

A closed-loop system that feeds LEDs containing a SEPIC converter connected to an LC SORC compensates for bus voltage variations applied to the latter stage.

Although most reported applications generally have open-loop operation characteristics, a small number of works ventured into detecting input and load variations. In (PAPPIS; MACHADO; PRADO, 2004) and (PERDIGAO *et al.*, 2016), the authors propose an electronic ballast capable of distinguishing between two input voltage levels, 127 and 220 V, changing the output filter switching frequency to compensate for the voltage increase. The author in (DE *et al.*, 2012) proposes a SEPIC converter as Power Factor Correction (PFC) stage connected to a SORC Power Control (PC) stage, designed to detect a family of T5 fluorescent lamps automatically. The method is based on three possible identification scenarios: the self-oscillating frequency, discharge lamp current, and phase angle between the input of the resonant filter and the lamp current. Interestingly, the SORC is used as the PC stage and generates the self-oscillating switching for both itself and the PFC stage. However, the compensation that detects the lamp type occurs at the PFC stage level through a duty cycle selection logic, not the SORC, where the magnetizing inductance remains unchanged. Furthermore, the pre-heating of the FL electrodes occurs through a separate flyback converter switched with a 555 timer IC. Some interesting future works suggested by the author are worth mentioning, such as:

> ‘(...) employing the Self-Oscillating Command Circuit in the pre-heating of the lamps electrodes. However, this task presents great complexity, given the precision in pre-heating time and voltage, presented by the IC 555;
>
> (...) adding protections to the SEPIC Self-Oscillating Half-Bridge, to detect the absence of lamp and/or damage to it, given that in this case the system operates around the resonant frequency, risking damage;
>
> (...) adding lamps to the detection strategy;
>
> (...) implementing the detection methods with the Self-Oscillating Command Circuit;
>
> (...) allow for the system to operate under universal input voltage and dimming.’

From an up-to-date perspective of the author’s reflections on the future works regarding the proposed system, it is agreed that the SOCC was not a viable option to implement the pre-heating and detection strategy. The self-oscillating frequency of both the PFC and PC stage depends on the SOCC magnetizing inductance and several other parameters, such as PC stage load and PFC stage output voltage. Suppose the magnetizing inductance can not be varied. In that case, the more straightforward solution is precisely employing analog-to-digital converters to create a detection strategy based on the load that modifies the PFC output voltage. As for the pre-heating, using a viable cost-effect timer such as the 555 was probably the best strategy given the SOCC limitations. Experimental results were provided related to both the pre-heating and

steady-state operation with each lamp model. Given that there was no input voltage variation or dimming, the absence of a small signal model for the system was not required.

Through the investigation of most methodologies that proposed techniques of frequency variation for the SORC, a certainly recurring one seems to be the modulation of the TWCT's magnetizing current. This modulation occurs actively through devices such as microcontrollers and BJT or passively through the addition of RLC networks and variable resistors. A handful of exceptions took advantage of the converter's frequency dependence on its input voltage and load characteristics by manipulating the PFC stage connected to it. An even more uncommon alternative to the SORC's frequency variation worth noticing was suggested in (PERDIGAO *et al.*, 2016), where the filter's series inductance was replaced by a Variable Inductor (VI). This principle affects the frequency in a similar way to that of the input voltage or load variation. However, in terms of design and stability analysis, this proposal requires an exceptionally accurate investigation of the impacts of the quality factor in predicting stable limit cycles and calculating the TWCT magnetizing inductance.

Furthermore, most of those methodologies utilized frequency domain design and stability analysis through the simplified DFM, with a few exceptions employing time-domain techniques, which lack the former method’s simplicity regarding stability inspection. Also, given that most observed goals were to investigate open-loop schemes to vary the output power, either through frequency variation or PFC stage management, there was no discussion regarding low signal modeling analysis for resonant converters operating with the SOCC. In reality, only a couple of techniques would likely be able to work under a closed-loop state, such as the one that places the VI in series with the output filter, given that this device could act as an actuator through the DC injection in its auxiliary windings. For this reason, there was no inherent need for a small signal modeling discussion for this type of converter.

1.2 OBJECTIVES OF THIS DOCTORAL DISSERTATION

This doctoral dissertation seeks to initially review and explore the uniqueness of the Self-Oscillating Resonant Converter in as many aspects as deemed satisfactory to provide meaningful information regarding its closed-loop operation.

For that endeavor, a review of the primary design methodologies employed for design and stability[14] analysis is required to assess if these techniques sum up to the closed-loop study in terms of precision on fixed operating points and the stability of such limit cycles, both in time and frequency domains.

The stability of limit cycles is strongly related to the filter topology of resonant converters. Hence, a comprehensive analysis of various resonant filters applicable to the modulated SORC and an assessment of aspects such as quality factor, impedance, and resonant frequency can show relevant information regarding the closed-loop operation. This filter analysis will help to clarify many potential applications for the SORC.

Regarding actuation mechanisms that allow for the SORC operation as a reference follower, a concrete goal of this doctoral dissertation is to discuss frequency variation methods and propose new techniques not previously presented in the literature. These techniques must maintain the attractive characteristics that classically portray the SORC while molding it into a potential resonant topology for closed-loop applications.

The small-signal modeling of the SORC is also one of the primary purposes of this doctoral dissertation. The previous discussions may award satisfactory developments regarding the precision and feasibility of closed-loop operation with different filter topologies, load types, and optimized actuators. However, given the intrinsic nature of the positive feedback network that switches the SORC, the difficulty of presenting small-signal modeling has discouraged its accomplishment so far.

[14] Those methodologies are the THM and the DFM, both analysing from a frequency point-of-view.

2

COMPLETE ANALYSIS OF AN OPEN-LOOP SELF-OSCILLATING RESONANT CONVERTER

In this chapter, the complete open-loop analysis of the Self-Oscillating Resonant Converter is carried out. Initially, its structure is presented along with its operating principle. The mainstream model for the Sel-Oscillating Command Circuit is presented as it highlights any modifications proposed in the literature to produce any form of modulation for the converter. A thorough analysis of the most employed output resonant filters is proposed to assess the converter's general stability and potential applications. The open-loop design methodologies are reviewed, and its usage for the closed-loop design is assessed. A novel actuation concept that allows Pulse Frequency Modulation of the converter is proposed and analyzed. A complete open-loop LCC parallel SORC is implemented and analyzed.

2.1 INTRODUCTION

The advantages of soft-switched Resonant Converters (RC) are well known in the literature. Given certain operating conditions, these converters function in the Zero Voltage Switching (ZVS) region, which offers a considerable reduction in the semiconductor's switching losses. With these losses maintained within acceptable levels, the switching frequency f_s can be further increased beyond the traditional dozens of kHz, decreasing the size of the resonant converter's reactive components, reducing costs, and increasing the power density of the system.

Nowadays, given the continuous research and development of semiconductor switches capable of operating under ever-increasing high-stress conditions, the maximum f_s restrictions of a cost-effective resonant converter turn the gate-driver into a crucial subject of analysis. The state-of-the-art commercially available Integrated Circuit (IC) gate-drivers can operate up to several MHz[15]. However, there are cases where these devices lack robustness; having either maximum bus voltage restrictions or requiring additional circuitry and extra voltage sources builds up cost for the system. The Self-Oscillating Command Circuit (SOCC) poses a significant alternative to the earlier cases, an uncomplicated, low-priced, and robust gate-driver solution (BONACHE-SAMANIEGO *et al.*, 2020).

The SOCC has a Three-Winding Current Transformer (TWCT) that acts as intrinsic feedback between the converter's resonant tank and the switching device, allowing the filter current i_p to be used as gate-charge for the switching devices' capacitances. The SOCC does not require any additional circuitry besides a TWCT, and four Zener diodes, along with a start-up circuit composed of a diac, a diode, a film capacitor, and a resistor (SEIDEL; BISOGNO; DO PRADO, 2007). Besides, no external timers or voltage sources are needed while being absent of any bus voltage restrictions and presenting noticeable cost-effectiveness due to the reduced number of components.

---

[15] A good example is the LM5113, a high-frequency, high and low side gte driver for enhancement mode GaN FETs. Due to the application related to it, the bus voltage is restricted at around 100 V. At the current price check, this IC costs U$ 1.781 per item on a 1k units order.

Another interesting and more general example is the LMG1210, which is a half-bridge driver for both Si and GaN FETs with adjustable dead timer for applications up to 50 MHz. However, there are also bus voltage restrictions at around 200 V. At the current price check, this IC costs U$ 2.216 per item on a 1k units order.

Integrated Circuits with higher bus voltage limits, such as the UCC27714 at 600 V voltage limit, despite costing half the price of an ultra fast gate-driver (this IC costs around U$ 1.22 per item on a 1k units order), this device hardly reaches the MHz range without considerable rise times and supply currents.

Resonant converter topologies that operate with the SOCC as gate-drivers are referred to, in the literature, as Self-Oscillating Resonant Converters (SORC). Being able to operate with different types of loads, both AC and DC, their application has been firmly established in the artificial lighting niche, especially as Electronic Ballasts (EB) for Fluorescent Lamps (FL) and Compact Fluorescent Lamps (CFL) (SEIDEL, Á. R. *et al.*, 2003).

Figure 3 shows both the classic and the proposed closed-loop structures of a SORC discussed further in this chapter. An inverter stage, usually with an asymmetric half-bridge configuration, is connected to a resonant tank whose configuration depends on the type of load. The tank current is then fed back to the switching semiconductors of the inverter through the SOCC.

Figure 3 - Structure of the Conventional and the Proposed Closed-Loop SORC.

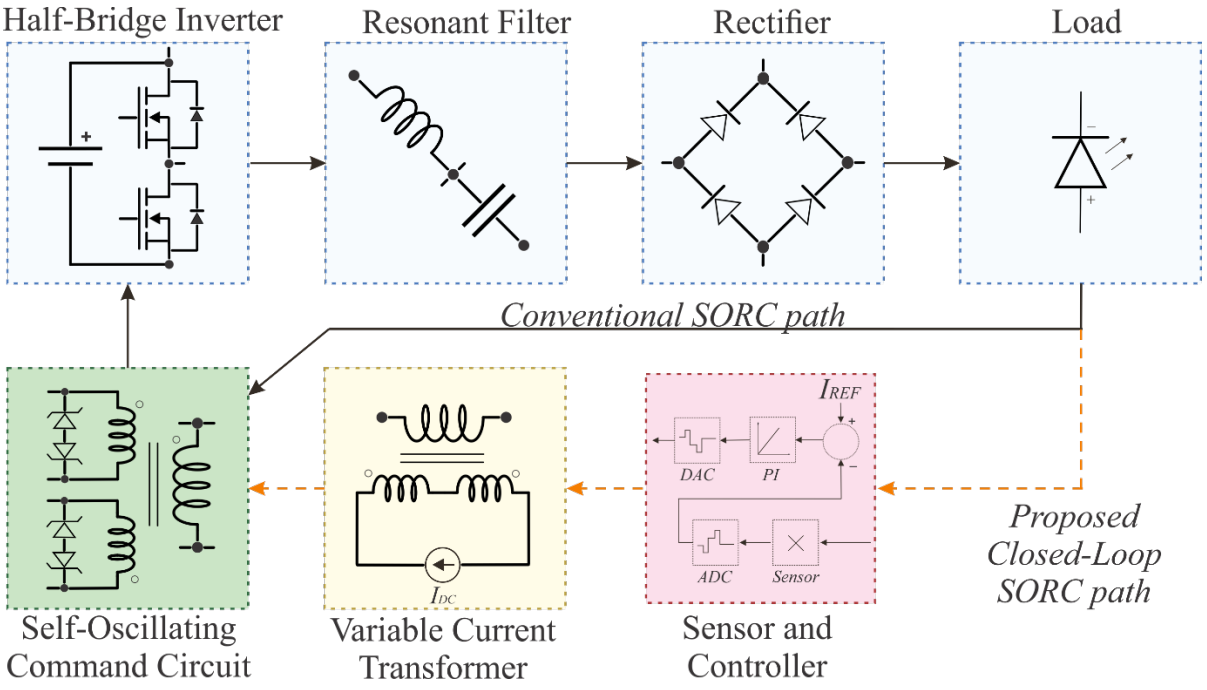

Source: Author

Despite the numerous advantages of both RC and the SOCC individually, the SORC is mainly known for being employed in open-loop applications with no extra layers of control due to the presence of an inherent positive-type analogic feedback network, i.e., the SOCC. This atypical characteristic resulted in a modest amount of researches regarding this subject. Primarily concentrated in the fluorescent lighting niche, where the majority of papers aimed towards the open-loop operation of EB with variable output, i.e., dimming, disregarding any reference values or external feedback circuits (SEIDEL, Á. R. *et al.*, 2003),(TAO *et al.*,

2001),(SEIDEL, A. R. *et al.*, 2003),(MICHEL *et al.*, 2002),(J. S. GLASER, 2002). Furthermore, some papers focused on the universal input operation of EB through the addition of extra circuitry for input voltage detection (PAPPIS; MACHADO; PRADO, 2004). For all the cases mentioned above, the solution presented was to limit the amplitude of the magnetizing current i_m of the SOCC through the introduction of external impedances, varying the self-oscillating frequency f_s.

Alternatively, a replacement of the SORC resonant tank's series inductor by a Variable Inductor (VI) was proposed in (PERDIGAO *et al.*, 2016). The paper proposed to control the amount of energy transferred to the load by injecting a DC current into the VI, varying the filter's series inductance. Unlike the previous methods, the VI does not function as a traditional Pulse-to-Frequency Modulator (PFM) technique because it modifies the output filter characteristics[16] of the SORC instead of acting on the switching device.

The limited capability to accomplish wide ranges of frequency variation, coupled with the challenge to follow a reference signal and potentially establish a closed-loop while eventually presenting gate-signal deterioration, end up discouraging the application of methods (SEIDEL, Á. R. *et al.*, 2003)-(PAPPIS; MACHADO; PRADO, 2004) as feasible actuation mechanisms for the closed-loop SORC. For the VI technique in (PERDIGAO *et al.*, 2016), due to the influence of the series inductance in critical characteristics like the output filter quality factor and resonant frequency f_0, in order to deal with the parameter dependence naturally imposed by the SORC, an overly complex system of equations would need to be solved.

A new concept of actuator mechanism for the SORC will be proposed and discussed in this doctoral dissertation to overcome these limitations. The basic notion is to modify the magnetizing inductance L_m of the SOCC's TWCT, directly related to changes in f_s, through a device called Variable Current Transformer (VCT), whose equivalent magnetizing inductance L_m can be varied through the injection of a small DC current (MENDES *et al.*, 2019). As opposed to the previously discussed methods, it will be shown that this one offers a minor effect on both the systems' efficiency and the gate-driver signal deterioration while having the convenience of not modifying the output filter characteristics and acting as a traditional PFM.

This chapter will introduce and develop the necessary aspects behind the operation of the SORC paired with the proposed VCT mechanism, leading to the proposed closed-loop SORC. The second part of this chapter enlightens the basic operating principle of the traditional

[16] When the filter series inductor is changed, both the quality factor and the resonant frequency also change. This changes both the filters magnitude and phase characteristics.

SORC through a brief review of its structure and main characteristics. The third section presents a brief review of the resonant filters that are most frequently used with the SORC. The fourth part of this chapter delves into the self-oscillating network, i.e., the SOCC, explaining the attributes that make this an attractive gate-driver alternative for classical lighting applications and novel honorable mentions that are interestingly synergy with the SORC. The fifth section shows modulation techniques that were previously employed to modulate the SORC's output. The sixth section of this chapter focuses on the VI and its introduction as a device that could be an actuation mechanism for the closed-loop SORC. The seventh section introduces the new Variable Current Transformer (VCT) actuation device. Section eight delves into the SORC design methodologies that serve as a tool to design the SOCC in high-frequency in an open-loop and give a graphical overview of the closed-loop operation.

2.2 SORC OPERATING MODES

The SORC requires a Startup circuit composed of R_1, C_1, and the diac d_c from Figure 4. When the bus voltage E is applied to R_1 and C_1, the voltage across C_1 rises until it is equal, in value, to the breakdown voltage of d_c. At this point, the diac is shortly turned on, applying a positive gate-to-source voltage v_{gs} on S_2. The Startup presents a set of particularities that, if not avoided, can prevent the circuit from ide operating. This problem may happen during steady-state, when d_c applies a pulse to the gate of S_2 while S_1 is active, shorting both switches. To avoid this, the insertion of the diode D_1 causes the discharge of C_1 in every conduction period of S_1. Also, given that the time constant of R_1C_1 is higher than the conduction time of both S_1 and S_2, the capacitor will be discharged before it reaches the breakdown voltage of d_c. A re-activation of the startup circuit is avoided this way, preventing reactivation of the Startup circuit within the steady-state regime.

In addition to these considerations, it's important to note that the performance of the SORC is highly dependent on the precise timing and sequencing of the switching actions. Any deviation from the ideal timing can lead to inefficiencies or even damage to the circuit components. Therefore, careful design and testing are crucial to ensure the reliable operation of the SORC. Furthermore, the use of high-quality components can significantly enhance the longevity and efficiency of the circuit, making it a more viable option for various applications.

Figure 4 shows the SORC circuit during the first step of operation: The conduction of S_2. The band-pass filter's series capacitor C_r and series inductor L_r are the active filter reactive

elements; the TWCT inductances L_p and L_{s2} comprise the currently active switching network along with d_{z3} and d_{z4}; the output rectifier[17] and the load[18] are active.

Figure 4 - The Self-Oscillating Resonant Converter on its first Step of Operation.

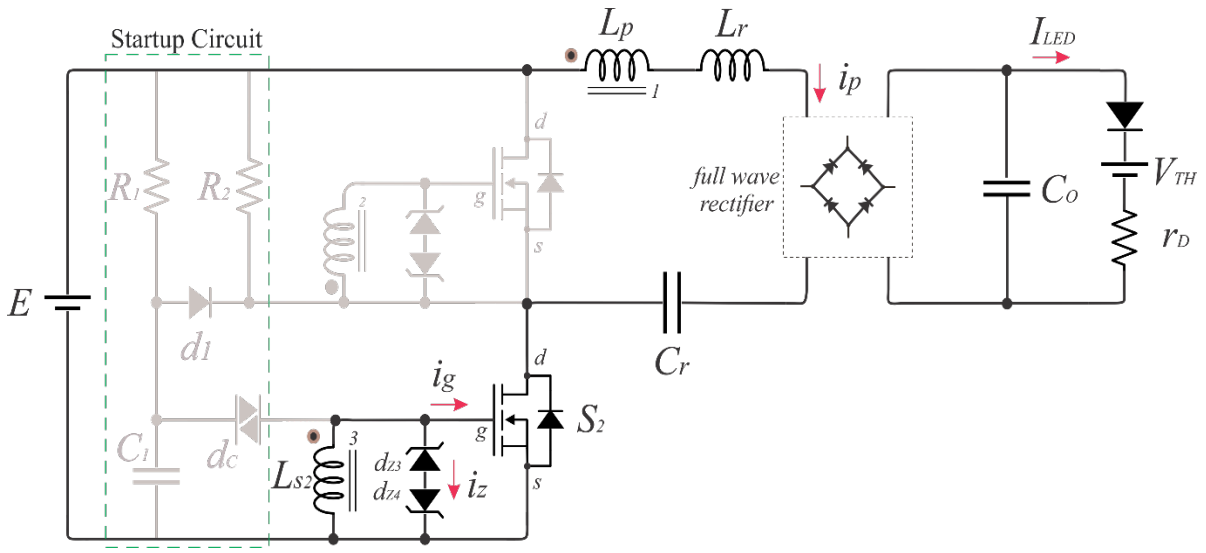

Source: Author

This mode always begins with a positive semi-cycle of v_{gs} applied to S_2. Two distinct situations may lead to this state; the first assumption is that v_{gs} may be applied to S_2 through the start-up circuit; and the second assumption is, if the converter is already in its steady-state operation, the voltage v_{gs} is then applied through the low-side inductance L_{s2} and the Zener diodes $d_{Z3,\ Z4}$ through the reflection of the primary current i_p circulating in the filter. Both conditions result in S_2 conducting, thus connecting the bus voltage E to the filter, making a current path for i_p through the resonant filter and the load. At this point, the SOCC begins its operation, i_p forces a redundancy on the positive v_{gs} of S_2 due to the coupling of the TWCT. Simultaneously, due to the opposing polarity of L_{s1}, the v_{gs} of S_1 has a negative value, causing the high-side MOSFET to remain in the OFF state.

[17] The real operation of the rectifying stage will be neglected in this chapter. Due to the usual inductive characteristic of the resonant filter given by the switching frequency being slightly higher to the resonant one, all the diodes may be active during half a period. This characteristic can be noted further into the chapter when the waveforms are presented. Hence, the rectifier stage is considered as an ideal rectifying block element for sake of simplification.

[18] This doctoral dissertation does not necessarily focuses on a single type of application. Even though the SORC is depicted as an LED driver, many applications may take advantage of the SORC's simplicity.

Figure 5 shows the SORC circuit during the second step of operation: The conduction of S_1. Here, all the filter and load elements remain active, similarly to the first step. However, the polarity of v_{gs} is now inverted due to the evolution of the filter current i_p from the last stage.

Figure 5 - The Self-Oscillating Resonant Converter on its first Step of Operation.

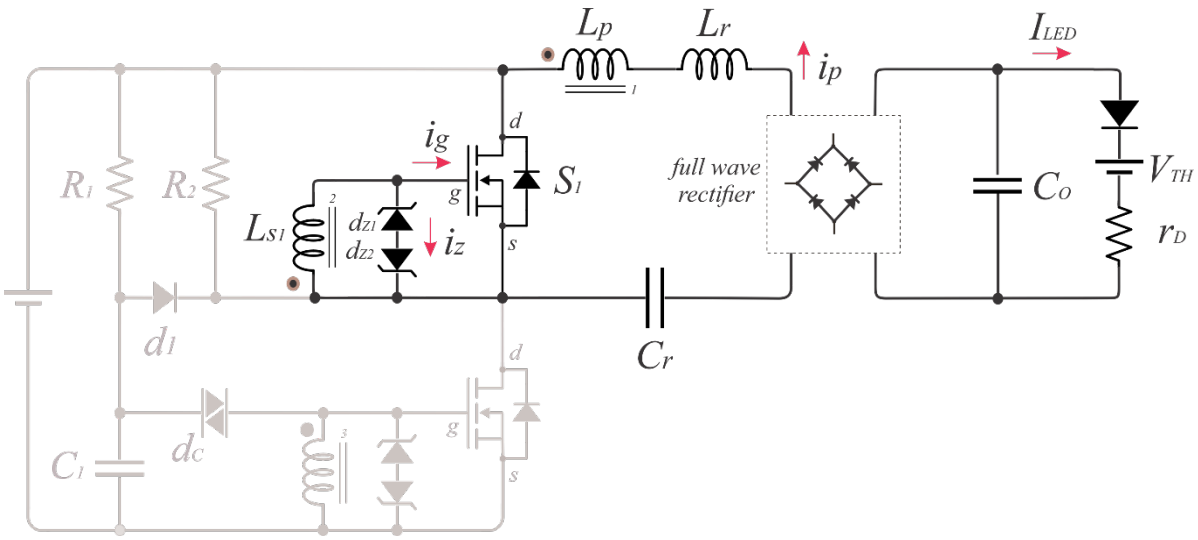

Source: Author

The second mode begins with a positive v_{gs} applied to the gate of S_1, while a negative v_{gs} is applied to the gate of S_2. If the converter is designed to work within the ZVS region, the orientation of the drain-to-source current i_{ds} causes the drain-to-source capacitance C_{ds} to be discharged at the instant that precedes the conduction of S_1, forcing the device to be turned ON with zero voltage, significantly reducing commutation losses. Furthermore, the conduction of S_1 forces E away from the system, resulting in the resonance between the filter elements and the load. Hence, i_p decreases and evolves into its negative semi-cycle, lasting until the end of this step, forcing L_p to, once again, apply a positive v_{gs}[19] on the gate of S_2, restarting to the first step of the operation. Traditionally, SORC topologies use Zener diodes with breakdown voltages around the maximum gate voltage, usually 12 to 16 V, even though it also works with smaller voltages in the range of the switches threshold voltage[20].

[19] The same notation is used to represent the gate variables of both the high and low side of the MOSFETs, given that the gate and Zener currents and the gate voltages are exactly the same, but with opposed polarities caused by the CT. This facilitates the subsequent analytical analysis as consider that the device is reflected to its secondary.

[20] This might be explained by the reduction in the magnetizing inductance of the TWCT when higher gate voltages are used. It is interesting to note that higher gate voltages translate into higher gate-charges

It is interesting to note that the duration of both steps, i.e., the self-oscillating period, depends on many parameters, such as the filter component values, the load characteristics, and most importantly, the L_m of the TWCT. The dependence above is an intrinsic characteristic of self-oscillating type converters and does not occur on traditional IC switched converters[21].

Figure 6 shows the key waveforms that further illustrate the operation of the SORC in steady-state, divided into the two steps mentioned earlier, where some key points can be observed. The current i_p flows through the primary inductance L_p of the CT, while a portion of the secondary current flows through the secondary inductances L_{s1} and L_{s2}. The current i_s splits between two currents, each with an essential role in the switching process, being i_g responsible for providing gate-charge to S_1 and S_2, changing the polarity of the voltage applied and thus the state of the MOSFETs, while i_z keeps v_{gs} clamped during their ON and OFF states.

Figure 6 - The Self-Oscillating Resonant Converter Main Waveforms.[22]

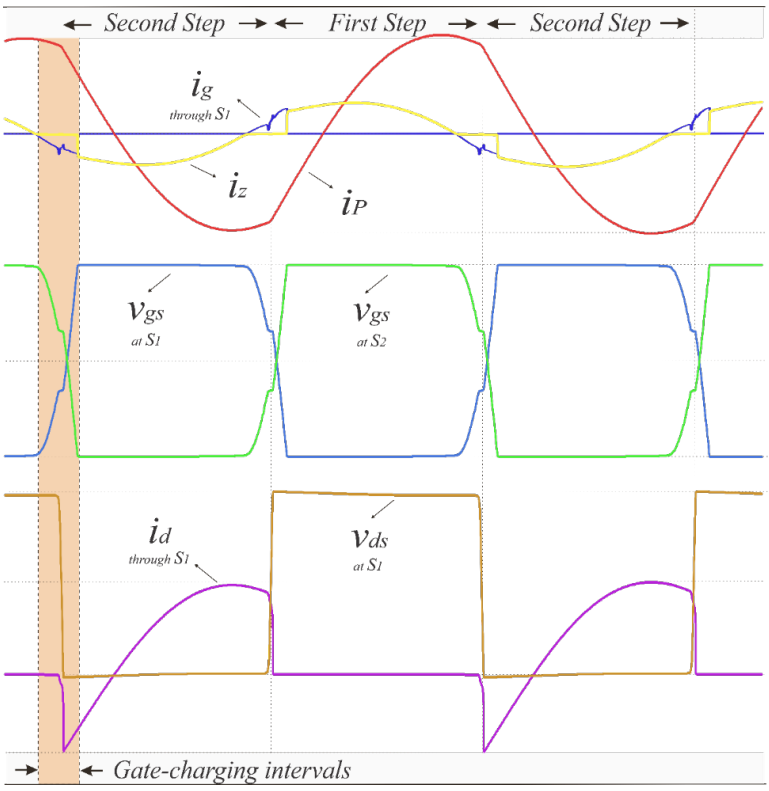

Source: Author

(INTERNATIONAL RECTIFIER, [*s. d.*]). Minimum gate charge is the electric charge, usually given in nano-Coulombs (nC), that is required to turn on the switching device.

[21] Due to the positive-type feedback network that controls the switching of the converter, any parameters that might change the output filter current characteristics will also affect the switching frequency. On IC switched converters, such as 2111 or 2153, the frequency is imposed and independent of the output.

[22] At the switching point from one step to the other, the current ip can be observed to have a phase angle. This occurs due to the ZVS operation of the S1 and S2 for switching frequencies higher than the resonant frequency (fs > f0). This is one of the most attractive characteristics attained by the SORC.

2.3 RESONANT FILTER ANALYSIS

The resonant filter is considered the output stage of the SORC. Connected right after the inverter stage, it attenuates voltage or current harmonics with order higher than the fundamental one. For the SORC, the voltage applied to the filter is a square-type asymmetric voltage, while the filter is usually of the LC series or LCC parallel type for lighting applications. Despite the absence of mentions of the LLC parallel filter, given the possibility of isolated output, it is also a fascinating and viable filter for lighting and Wireless Power Transfer (WPT) applications. Among the most common methodologies used to analyze resonant filters is the First Harmonic Approximation (FHA) (STEIGERWALD, 2015)(PAVÃO *et al.*, 2001).

A common objective shared by every filter that grants the SORC one of its most attractive characteristics is to help with soft switching. Usually, when the switching frequency of the inverter is higher than the resonant frequency of the output filter, in the switching instant when the MOSFET starts changing its state to ON and its current is oriented from source to drain, the C_{ds} capacitance discharges before the device start conducting, achieving what is called a Zero Voltage Switching. However, every filter has its characteristic of soft switching on frequencies above and below the resonant one. Furthermore, for parallel filters, whose presence of an extra parallel reactive element causes the filter to have an extra resonant frequency, presenting a new set of particularities.

As far as filter comparison goes in the literature, not much can be found in regards to lighting and modeling as main topics, due to the main factor when chosing one filter over the other being to respect the electrical characteristics of the load, such as current and voltage required, or necessity of isolation. However, a very interesting and one of the most complete analysis regarding resonant filter comparison is seen in (CYR *et al.*, 1995), where the authors present a comparative study of different resonant converter topologies operating above the resonant frequency of the oscillating circuit. The authors compare two basic structures, namely the series resonant converter (CRS) and the parallel resonant converter (CRP), as well as a modified structure called the series-parallel resonant converter with a capacitive filter (CRSPFC). The main objective of the study is to analyze the performance of these structures and identify their advantages and disadvantages. The paper starts with an introduction that explains the use of resonance in static converters to enable high-frequency operation and reduce the weight and volume of reactive components. It introduces the CRS and CRP as the two basic resonant converter structures. The CRS operates above the resonant frequency and offers high efficiency, rational use of semiconductor components, and short-circuit operation. However, it

cannot operate without a load due to the switching conditions. On the other hand, the CRP allows operation without a load by placing a reactive element (capacitor) in parallel with the load, but it has lower efficiency and operates under more challenging conditions. To overcome the drawbacks of both structures, the authors propose the CRSPFC, which offers a compromise between the CRS and CRP. The paper then discusses simplifying assumptions made in the modeling of resonant converters to facilitate analysis and calculations.

Next, the paper describes the detailed circuit configuration and state equations for each operating sequence of the CRS and CRP structures. The state equations are formulated and presented for comparison purposes. The paper also introduces a normalized representation of the equations to facilitate the comparison between the different topologies.

Furthermore, the CRSPFC structure is presented, which is a modified version of the series resonant converter with a capacitive filter at the secondary side of the transformer. The paper describes the operation of the CRSPFC and provides the corresponding state equations for each operating sequence.

In the experimental section, the authors present simulation algorithms and experimental setups to validate the theoretical analysis. They compare the performance of the three converter structures based on theoretical and experimental results. The paper concludes by outlining a 1-kW module for each structure, highlighting the potential applications and advantages of each topology.

Overall, a comprehensive review of different resonant converter topologies is provided, including the series resonant converter, parallel resonant converter, and series-parallel resonant converter with a capacitive filter. The main arguments of the authors revolve around the performance characteristics, advantages, and disadvantages of each topology. The results include theoretical formulations, state equations, and experimental comparisons, allowing readers to understand and evaluate the different converter structures. The paper contributes to the field of power electronics by providing insights into the design and operation of resonant converters for high-frequency applications.

On (OUTEIRO; BUJA, 2015), the authors investigate RPCs with resonant tank networks (RTNs) composed of two, three, and four elements using the FHA. RPCs are advantageous due to their ability to operate at high switching frequencies, resulting in increased power density and reduced magnetic part sizes. The FHA analysis simplifies the analysis by assuming that only the fundamental harmonic affects the RPC operation, thanks to the filtering action of the RTN. The paper begins by introducing the background and advantages of RPCs compared to conventional converters. It highlights the complexity of RPC analysis due to

multiple operation modes and the duration of resonant oscillations, especially as the number of elements in the RTN increases. To facilitate analysis, the frequency domain and FHA method are commonly adopted. The main objective of the paper is to investigate the characteristics of RPCs with two, three, and four elements in the RTN using the FHA method. The authors analyze the input impedance, voltage gain, and efficiency for different topologies. They also address the merits and limitations of each topology. The paper provides the equivalent circuits of a DC-DC RPC topology, including the control switch network (CSN), RTN, diode rectifier (DR), low-pass filter (LPF), and resistive load. It explains the approximation of CSN as a sinusoidal generator and the approximation of DR-LPF set based on the type of LPF used.

For two-element RPC topologies, the paper focuses on series resonant circuits (SRC) and parallel resonant circuits (PRC). It presents the AC equivalent circuits and analyzes their characteristics such as input impedance and voltage gain as functions of the fundamental frequency and resonant frequency. The SRC exhibits load-dependent input impedance and unity voltage gain at resonance, while the PRC shows nearly independent input impedance and variable voltage gain. For three-element RPC topologies, the paper introduces the LLC and LCC topologies obtained by adding an inductor or a capacitor to the two-element configurations. It presents the AC equivalent circuits and discusses the voltage gain characteristics for different values of the quality factor. The LLC topology shows peak voltage variations depending on the load and allows voltage regulation with small changes in the CSN switching frequency. The LCC topology exhibits similar behavior to the SRC or PRC, depending on the load conditions. The paper also includes efficiency analysis for the PRC topology, showing the relationship between efficiency, quality factor, and frequency ratio.

A very interesting conclusion found by the authors is that, despite not highlighting the least efficient filter, they found that the most efficient filter among the investigated RPC topologies is the PRC. The PRC topology is characterized by connecting the effective load resistor in parallel to the resonant capacitor. When the resistance is significantly higher than the reactance of the capacitor, the current through the RTN and the switches is almost independent of the load. This results in improved efficiency. Additionally, the voltage across C_p increases with R_e, allowing for significant output voltage adjustment by adjusting the switching frequency of the control switch network.

On a more high-voltage application, on grid connected VSCs (Voltage Source Converters), the authors in (YAGNIK; SOLANKI, 2018) compare the performance of LCL, LC, and L filters for grid-connected VSCs. L and LC filters were popular until now, but with increased power quality stresses, the value of L increases which becomes less economic. The

LCL filter provides an attractive alternative for the L and LC configuration. It is interesting to note that even on applications in the range of dozens of kV, the filtering stage is also a challenging topic to discuss.

2.3.1 The LC Series Filter

The LC series filter is commonly used on resonant inverters for LED applications . When operated above its resonant frequency, an inductive characteristic dictates the status of the converter's output, granting Zero Voltage Switching of the MOSFETs. However, operation on frequencies much higher than that of the resonant one may incur reduced efficiencies due to the reactive flow on the filter (ALMEIDA *et al.*, 2015). Figure 7 and Figure 8 show the output magnitude of the LC series filter and the output phase as a function of frequency for different quality factors Q, respectively. As it can be seen, the filter's maximum gain is 1, i.e., the fundamental value of the output voltage of the LC series filter is equal to the fundamental value of the input. This gain occurs precisely when the switching frequency is equal to the resonant frequency. Furthermore, for lower quality factors, the output value has a lower sensitivity to frequency variation when compared to the higher quality factor.

In addition to the points mentioned, it's important to note that the LC series filter's performance is also influenced by the load impedance. The load impedance can affect the resonant frequency and the quality factor Q of the filter, which in turn can impact the filter's output voltage and phase characteristics. Moreover, the LC series filter's performance can be significantly affected by component tolerances and aging. For instance, the inductance and capacitance values can change over time due to factors such as temperature variations and component aging. These changes can shift the resonant frequency and alter the filter's performance. Therefore, when designing an LC series filter for a SORC, it's crucial to consider these factors and possibly incorporate compensation mechanisms to maintain optimal performance over the converter's lifetime. Future works could explore these aspects in more detail, providing a more comprehensive understanding of the LC series filter's behavior in SORC applications.

Figure 7 – Output Voltage Magnitude versus Frequency characteristic of the LC series filter.

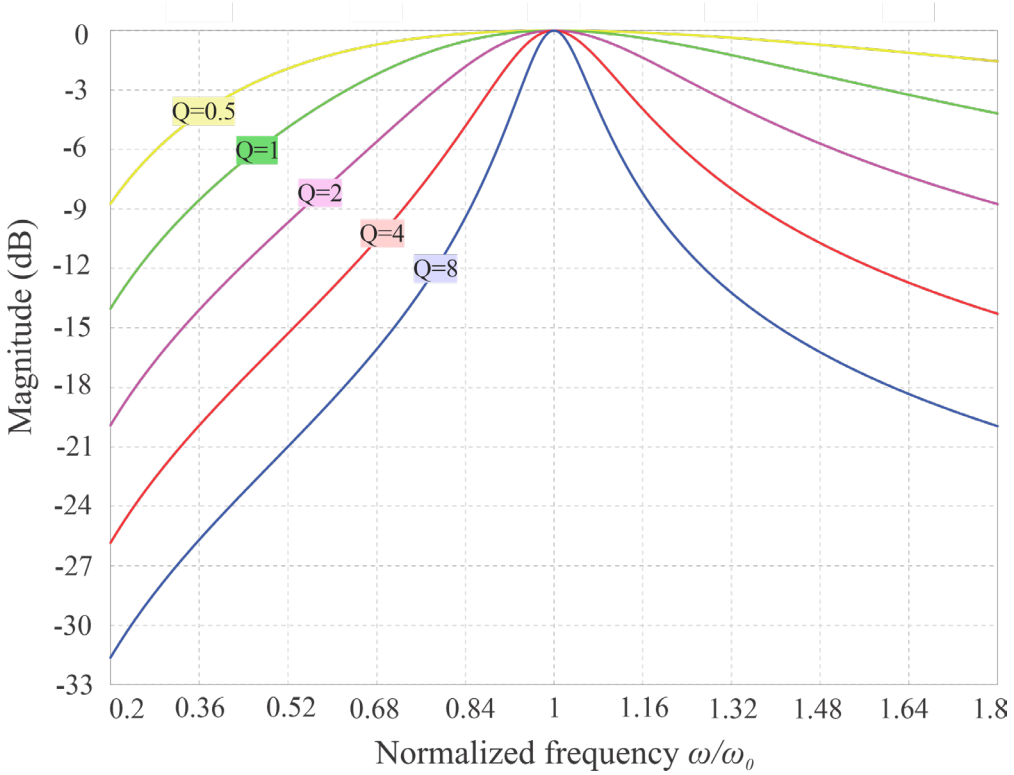

Source: Author

Figure 8 – Output Voltage Phase versus Frequency characteristic of the LC series filter.

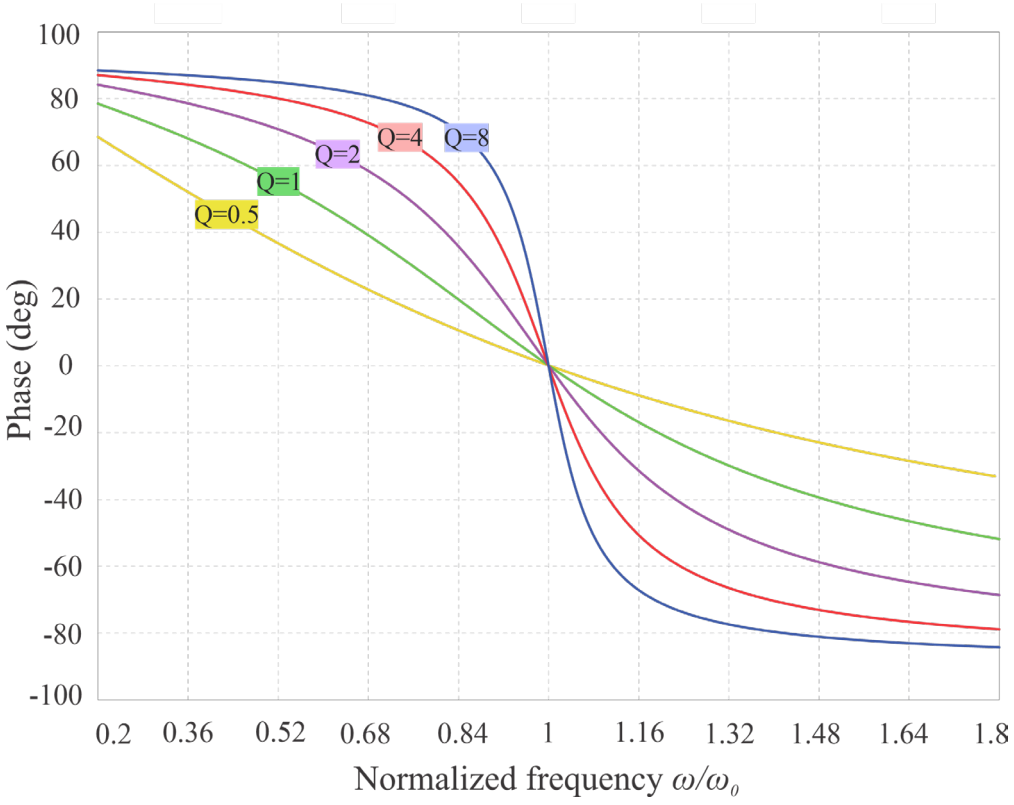

Source: Author

In (ALMARDY; BHAT, 2019) an LC-L type dc–dc series-resonant converter with a capacitive output filter is explored using fixed-frequency control. The converter operations for different modes during different intervals have been presented using the operating waveforms. The converter is analyzed using the classic approximate analysis approach, and the design procedure is illustrated with a design example. PSIM simulation results for the designed converter are given for load and input voltage variations. It is shown that the converter operates in zero-voltage switching (ZVS) at the minimum input voltage and for different load conditions. On the other hand, at the maximum input voltage from full load to light load, leading switches operate with ZVS, whereas lagging switches operate with zero-current switching (ZCS).

A very interesting work using the series LC-parallel LC (LCLC) resonant converter with a capacitive output filter is shown in (MATHEW, 2021), which is an emerging favorite for high-frequency, high-voltage applications. The use of the capacitive output filter ensures reduced peak voltage stress of the rectifier diodes, which is equal to the clamped output voltage. Although the topology exhibits various modes of operation, it predominantly operates in one mode with a lagging power factor. Existing literature utilizes conventional fundamental harmonic approximation (FHA) due to its simplicity. However, FHA has accuracy limitations when applied to analyze low quality factor ($Q<2$) tuned resonant circuit since higher-order harmonics are neglected. To resolve this issue, this doctoral dissertation presents an improved frequency domain-based analysis of the LCLC resonant converter with a capacitive output filter, considering the harmonics of both the input and load side of the converter .

In (MIN; HUI, 2019), the author discusses the characteristic analysis of an LC series resonant bidirectional DC-DC converter. Traditional bidirectional DC-DC converters have many problems, such as high return power, limited soft-switching range, and switching off at peak current. The LC series resonant DC-DC converter with an inductive-capacitive resonance network has become a research hotstop for dealing with some of these nuisances. In this paper, the equivalent circuit and mathematical model of an LC series resonant DAB converter are established by fundamental wave analysis method. On the basis of explaining the working principle of phase-shifting control mode in detail, the working mode of an LC series resonant DC-DC converter is analyzed, the switching-off conditions of the converter are deduced, and the power transmission characteristics and soft-switching characteristics of the converter under different switching-off conditions are analyzed. This paper shows that even more basic topologies of resonant filters are capable of solving more complex problems.

2.3.2 The LCC Filter

Known by its extensive usage in lighting applications, more specifically in electronic ballasts for fluorescent lamps, the LCC parallel filter, as a contrast to the LC series, offers a higher than unity gain for the output voltage, which was especially important during the lamp start, where the equivalent resistance of the bulb was higher than the steady-state resistance. The gain and phase characteristic for this filter can be observed in Figure 9 and Figure 10. Resonant converters employing the LCC parallel filter are considered standard in the literature (BISOGNO *et al.*, 2002; CHANG, 2001; CHANG; CHANG; BRUNING, 1999; FLORES-GARCÍA *et al.*, 2010, 2011; GAO *et al.*, 2000; LIN; CHEN; CHEN, 2012; LIN; WANG, 2006; SEIDEL; BISOGNO; DO PRADO, 2007). An interesting fact is that the LCC parallel filter is also capable of driving LEDs. However, extra attention should be paid to the parallel capacitor, which introduces the possibility of gains higher than 1.

Figure 9 – Output Voltage Magnitude versus Frequency characteristic of the LCC parallel filter.

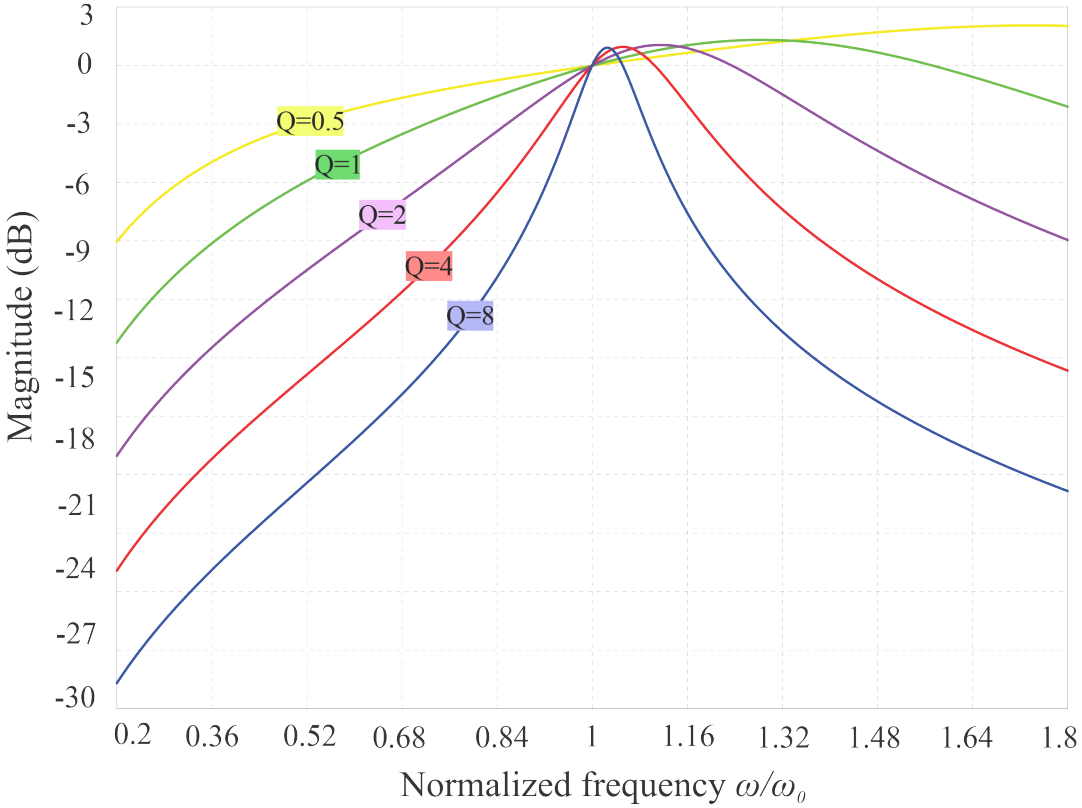

Source: Author

Figure 10 – Output Voltage Phase versus Frequency characteristic of the LCC parallel filter.

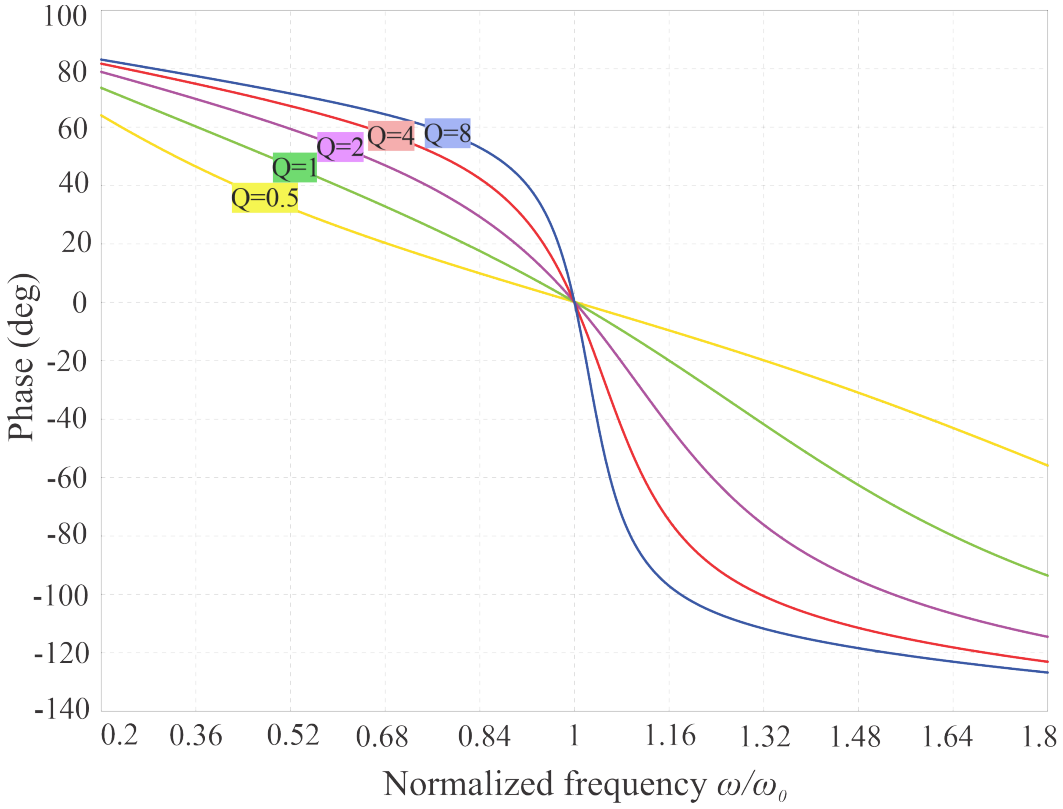

Source: Author

The author in (JAIN; MASSIMIANI, 2021) discusses the analysis of a Half-Bridge LCC resonant DC-DC converter and its voltage gain computation using the Fundamental Harmonic Approximation (FHA) approach. It discusses how it gained popularity in various applications due to their high efficiency, low electromagnetic interference (EMI) emissions, and the ability to operate at high frequencies. The article starts by highlighting the increasing demand for higher switching frequencies in power electronics due to the trend of miniaturization. It provides a generalized block diagram of an AC-DC converter power supply and explains the role of resonant converters in achieving high power density and efficiency. Regarding the converter, the article describes the configuration and components of the Half-Bridge LCC resonant converter, including the PFC stage, resonant tank circuit, and the use of soft switching techniques to reduce switching losses. It explains how the converter operates under zero-voltage switching (ZVS) and zero-current switching (ZCS) conditions. Then, The FHA method is introduced as an analysis technique for resonant converters. It relies on the assumption that the energy transfer to the load is highly associated with the fundamental harmonic of the current and voltage waveforms. By treating the resonant tank waveforms as a sinusoid operating at the fundamental frequency, accurate gain equations can be derived using FHA. Also, Through

mathematical transformations and calculations, the transfer function of the resonant tank is obtained, representing the relationship between the output voltage and the input voltage.

From the author's perspective, the FHA approach provides a reliable and accurate method for analyzing the voltage gain of the Half-Bridge LCC resonant DC-DC converter. The use of FHA allows for simplified modeling and calculations while considering the fundamental harmonic components of the waveforms. Although the results of the analysis are not explicitly mentioned in the provided excerpt, based on the description, the FHA approach likely provides a precise and accurate representation of the voltage gain of the Half-Bridge LCC resonant converter. The derived gain equations can be utilized for design optimization and performance evaluation of the converter.

In terms of comparison, the authors in (ZHENG; LU; LI, 2020) discusses the adoption of a variable frequency control strategy for resonant converters with LLC and LCC resonant structures. The converters operate in ZVS region. The paper presents theoretical research results obtained through FHA and verifies them using Saber simulations in current continuous mode. The main findings of the paper include the suitability of LLC resonant structure for low-voltage and high-current patterns, while LCC resonant structure is suitable for high-voltage and low-current patterns. The paper provides a summary of the advantages and disadvantages of the two resonance control structures. By adjusting the values of resonant inductance and distributed capacitance, the resonant power supply can be tuned to work in the required area.

The paper emphasizes the importance of designing the resonant cavity of both structures for achieving ZVS and high switching efficiency. The theoretical analysis section establishes the gain formulas for LLC and LCC using the FHA approach. The gain formulas are used to draw gain curves in MATLAB for different values of inductance coefficients and capacitance coefficients. The results show that the optimal ratio of distributed capacitance to resonant capacitance is five for LCC resonant structure, while the optimal ratio of excitation inductance to resonant inductance is also five for LLC resonant structure. The paper presents graphs illustrating the changes in gain with frequency for different inductance and quality factor values. Overall, the paper provides insights into the variable frequency control strategy for resonant converters with LLC and LCC resonant structures. It discusses the design considerations, advantages, and disadvantages of the two structures, and presents theoretical and simulation results to support the findings.

A very unfrequently discussed topic in the literature is the synergy between the LCC filter and LEDs. This filter has clearly been thoroughly explored for articial lightning applications using fluorescent lamps. In (WONG *et al.*, 2018), the author addresses the problem

of current imbalance in multistring LED lighting systems. Previous research has focused on active and passive approaches to solve this problem. However, independent control of different LED strings is becoming more important for achieving desirable brightness and color spectrums in lighting applications. The existing approaches have limitations in achieving current balancing and independent control simultaneously, posing a challenge for LED driver design. The authors propose a fully switched-capacitor-controlled LCC resonant converter to address this challenge. They replace all fixed capacitors in the resonant tank of the LCC converter with switch-controlled capacitors (SCCs). By varying the effective capacitances of the SCCs under constant switching frequency, the proposed system enables regulation of the common AC bus voltage, current balancing, and individual current control of LED strings using a single LED driver. This approach reduces circuit complexity and improves circuit performance.

The prototype was built using specific components and had a maximum power of approximately 60 W. The experimental results showed that ZVS was achieved by the half-bridge switches. The waveforms of the common bus voltage and the current in a blue LED string indicated that the current leads the voltage by 90 degrees, confirming that the branch impedances are dominated by series capacitive impedances. The waveforms of the sensed current and the current in a red LED string further supported the capacitive nature of the branch impedances. The prototype successfully demonstrated that the synchronized sawtooth signal generated by the capacitive branch impedance could be used for independent control and current balancing without the need for additional current-sensing transformers. The waveforms of the voltages and currents in different LED strings showed that the currents could be well-balanced by applying the same control angle to the capacitors, even with significant deviations in the ac equivalent resistances of the LED strings. The current sharing deviation under the same capacitive control angle was approximately 1.4%. Furthermore, the prototype exhibited the capability for independent control and current balancing under different operating conditions. Dimming of the red LED string while maintaining the blue LED string at a constant current level was successfully demonstrated. Additionally, blue LED string dimming using a burst length pulse width modulation (BL-PWM) technique was achieved, where the current of the blue LED string pulsed between two levels. The experimental efficiency of the prototype, considering the losses mainly due to conduction and core losses, was measured to be 85.5% when operating all strings at the maximum current level.

In conclusion, the proposed fully switched-capacitor-controlled LCC resonant network showed promising results for independent control and current balancing of multicolor-multistring LED lighting systems. The experimental verification validated the effectiveness of the proposed idea

and suggested potential improvements in efficiency through optimization of operating points and magnetic design. The technique can be extended to other resonant network variants for various dimmable large-area LED applications. The paramount point here is that the LCC filter can also become a hotstop for research to use in conjunction with LEDs, as opposed to whats commonly thought about this topology of filter, at least on the lightning niche, not being adequate to the LED electrical characteristics.

2.3.3 The LLC Filter

The parallel LLC resonant converters are commonly used in high efficiency and high power density applications that require easy implementation of magnetic integration, such as converters with multiple isolated outputs (JIN; RUAN, 2005; LAI; SHYU, 2007; SHRIVASTAVA; SINGH, 2012; YOU *et al.*, 2016), (VENTURINI *et al.*, 2013). Furthermore, the resonant filter characteristic of soft switching turns the converter into a generally low EMI device (LUO *et al.*, 2018). An exciting characteristic regarding the output magnitude and the phase characteristics regarding frequency, as shown in Figure 11 and Figure 12, is that the LLC can vary its output voltage with considerably minor switching frequency variations.

For the LLC parallel filter, there a two resonant frequencies, a higher one, defined by the effect of both series capacitor and inductor, and a lower frequency, which aggregates the effect of the parallel inductor. Usually, the higher resonant frequency defines the point at which the fundamental value of the output voltage is equal to the fundamental of the input through the FHA, i.e., unity gain and the operation is generally desired to occur at frequencies slightly higher than this one, due to ZVS. For frequencies between the lower and the higher resonant frequencies, the impedance angle of the filter is lower than zero, having the capacitive characteristic.

Figure 11 – Output Voltage Magnitude versus Frequency characteristic of the LLC parallel filter.

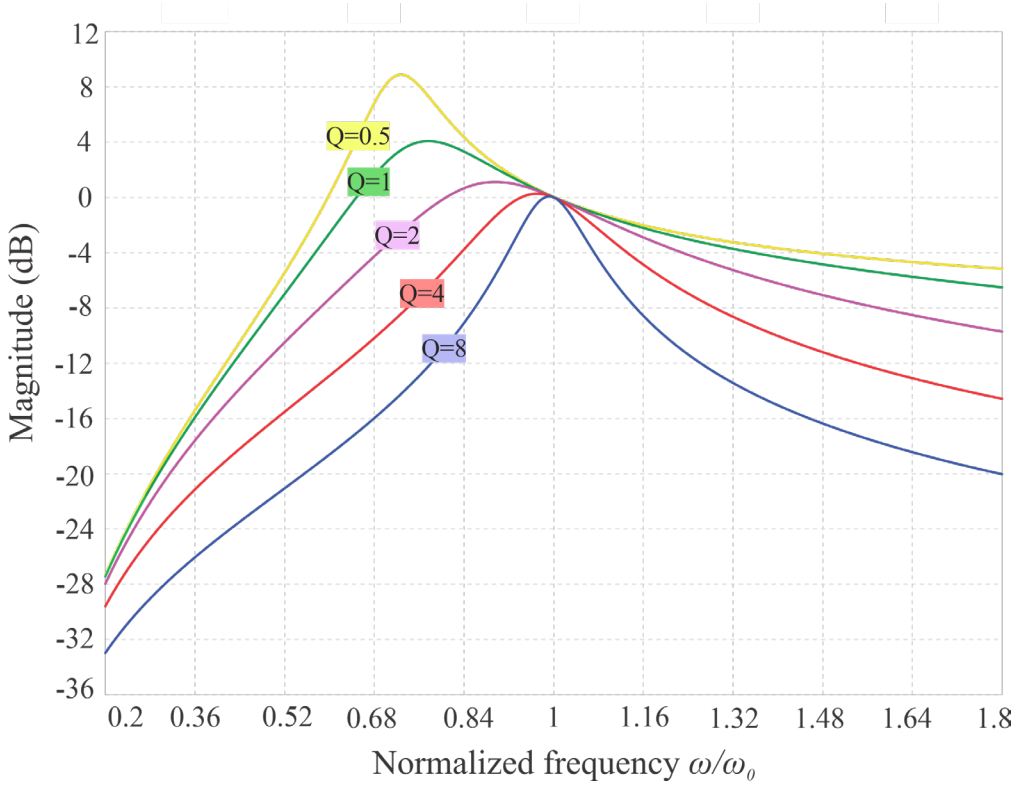

Source: Author

Figure 12 – Output Voltage Phase versus Frequency characteristic of the LLC parallel filter.

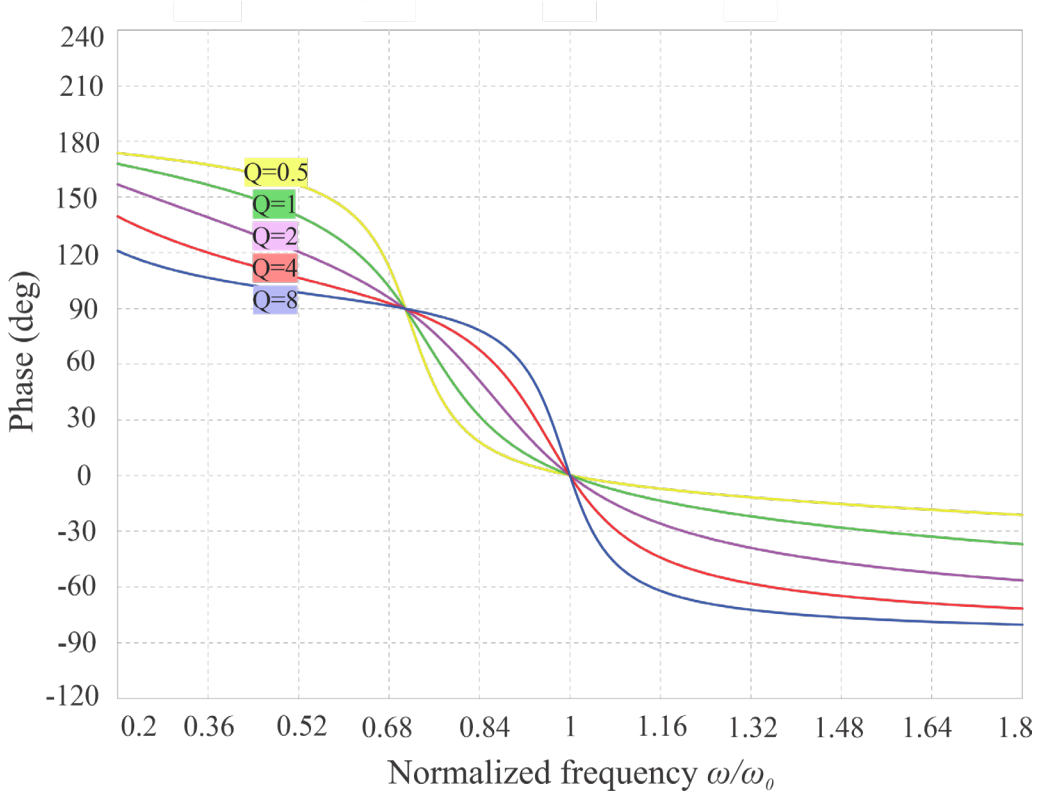

Source: Author

An interesting paper discussing the LCC limitations in achieving wide dimming ranges with LED as load is shown in (MA; XIE; JIANG, 2017), where a method to extend the load range and voltage range of LLC resonant converters for dimmable LED lighting applications is proposed. The conventional LLC resonant converter is analyzed, and its limitations in achieving wide dimming range are identified. The paper introduces the concept of a variable resonant inductor (VRI) as a key component in the proposed LLC converter. The VRI is a current-controlled device that adjusts the inductance based on the LED current. By using the VRI, the output load range and voltage range of the LLC converter can be significantly extended without changing the circuit structure or control scheme.

The analysis of the conventional LLC converter reveals that the presence of parasitic capacitors limits the dimming capability of the converter. The paper takes into account the effects of these capacitors and presents the DC voltage gain curves of the conventional LLC converter with parasitic capacitors considered. In contrast, the proposed LLC converter with VRI overcomes the limitations of the conventional converter. The VRI allows for wider dimming range by adjusting the inductance according to the LED current. The paper provides experimental results based on laboratory prototypes of the conventional and proposed LLC converters, demonstrating the effectiveness of the proposed approach. Overall, the proposed LLC resonant converter with VRI offers a simple and efficient solution for achieving wide dimming range in high-power LED lighting applications. By optimizing the gain curve through the use of the VRI, the converter can maintain stability and high efficiency across a wide range of loads.

2.3.4 Feasibility of modulation of self-oscillating filter topologies

In accordance to the primary objective of this doctoral dissertation, which is to accurately model and control a complete SORC, in this section, the feasibility of modulation of self-oscillating filter topologies LC, LLC and LCC will be discussed for different load and quality factor conditions. This discussion should help in the choice of either one of the commonly used topologies and their characteristics and objectively define goals for the modulated SORC resonant filter design. The schematic diagrams of the tested filters is shown in Figure 13. The simulation setup is based on changing the SOCC equivalent magnetizing inductance L_m by varying each individual winding L_p, L_{s1} and L_{s2}. On each simulation, three changes of 30 % of the maximum normalized inductance are performed.

Figure 13 – Schematic diagrams of the analyzed filter topologies operating as self-oscillating resonant converters; (a) LC (b) LLC e (c) LCC.

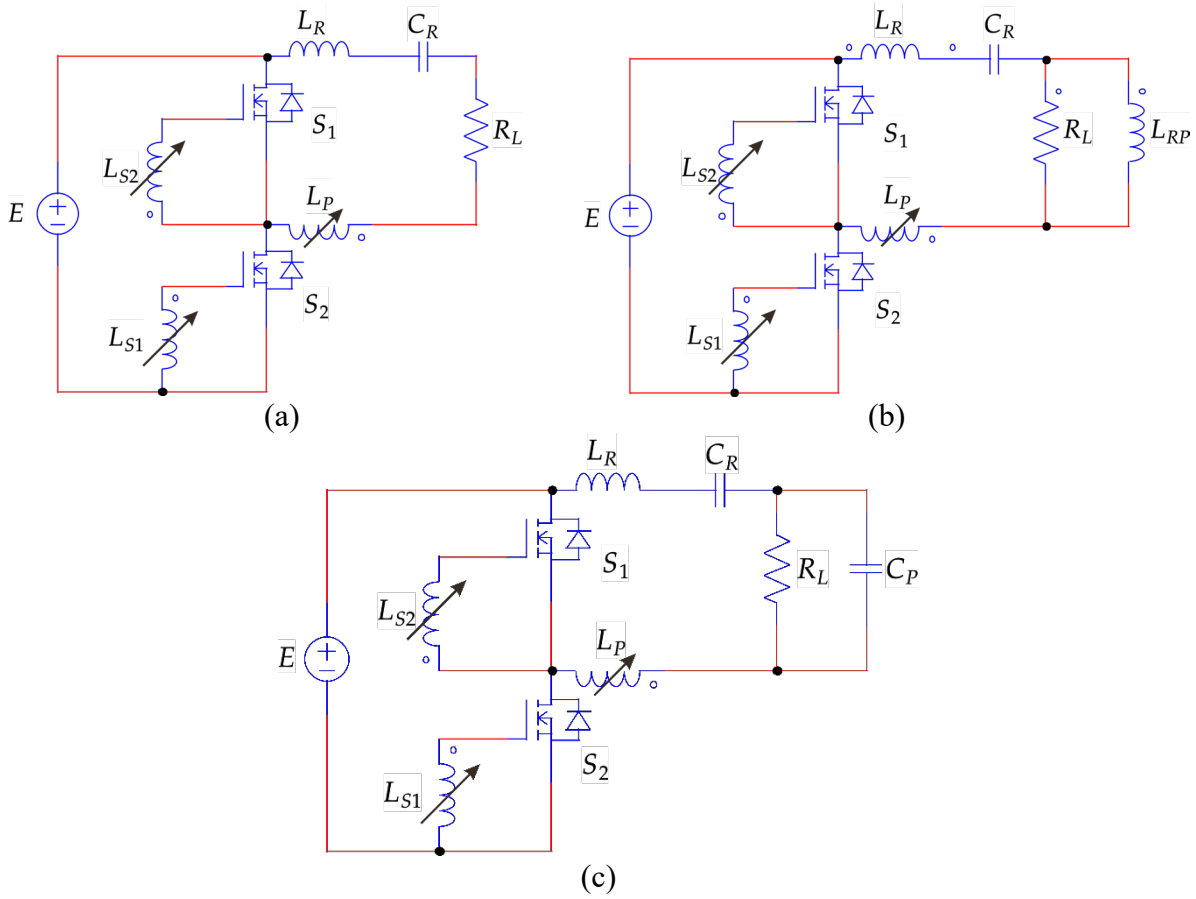

Source: Author

Figure 14 shows the simulation of the LC filter topology. It can be seen that for higher values of R_L, the topology is feasible as a resonant filter stage for a modulated SORC as shown by the changes. It can also be seen that for higher Q values, the resonant current is more susceptible to changes on L_m. This can be explained through the aforementioned graphics, such as the one from Figure 7, where the output magnitude of the filter varies more abruptly when changes in frequency occur for higher Q values.

For low values of R_L, however, for both values of Q analyzed, the LC filter ceases to be a feasible option as resonant filter topology for modulated SORCs. This fact is due to the inability of the filter, at such R_L values, to perform modulation under certain switching frequencies between the resonant and a stable minimum frequency. This can be observed by the dashed blue line indicating the non-self-oscillating margin.

The non-self-oscillating margin indicates that the nominal current of 0.75 A cannot be obtainable as an operating point for the converter due to the inability of the LC SORC to operate at that respective frequency. If the current indicated in the graphics are higher than 0.75 A and

an non-self-oscillating margin is indicated, it means that any decrease in frequency that would reduce the current closer to the nominal value actually reaches an unstable limit cycle that leads the resonant current to 0, this is known as Zero Magnitude Non-Self-Oscillating Point (ZMNSOP). The ZMNSOP occurs for LC filter with Q=1 and R=100.

The non-self-oscillating margin on results that show the non-transient current below the dashed line, i.e., for currents lower than 0.75 A, mean that the system is operating at a higher frequency than the required to operate at the nominal current. Furthermore, decreasing the frequency leads to another unstable limit cycle, as the current never rests at the nominal value. This decrease in frequency causes the SORC to shift its operation to the Maximum Magnitude Non-Self-Oscillating Point (MMNSOP). At this point, the SORC operates close to the resonant frequency, and the higher the value of L_m, the closer f_s gets to f_0. The ZMNSOP occurs for LC filter with Q=5 and R=10.

Figure 14 - Simulation resuls of the feasibility of the LC filter topology operating as modulated SORC. Resonant filter current i_P *vs* time, under three changes on L_m.

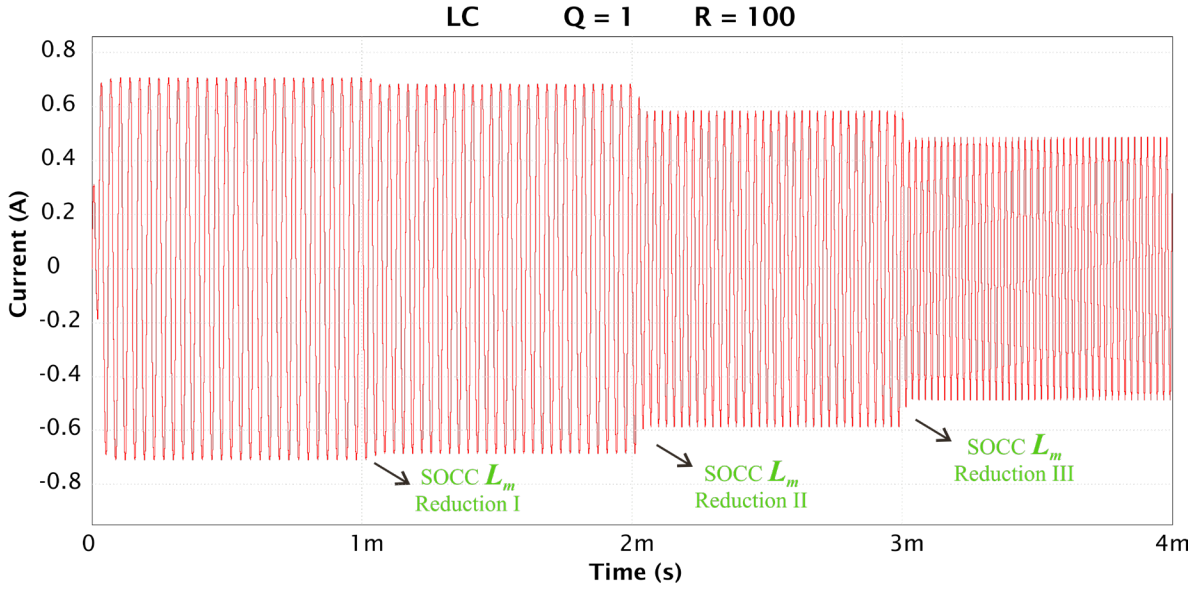

(a)

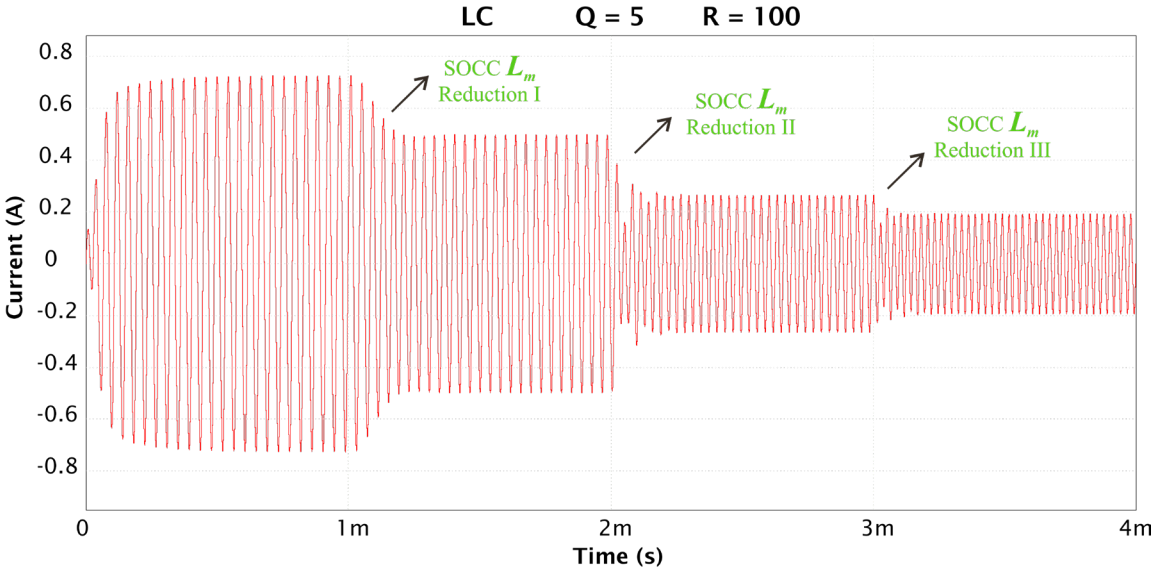

(b)

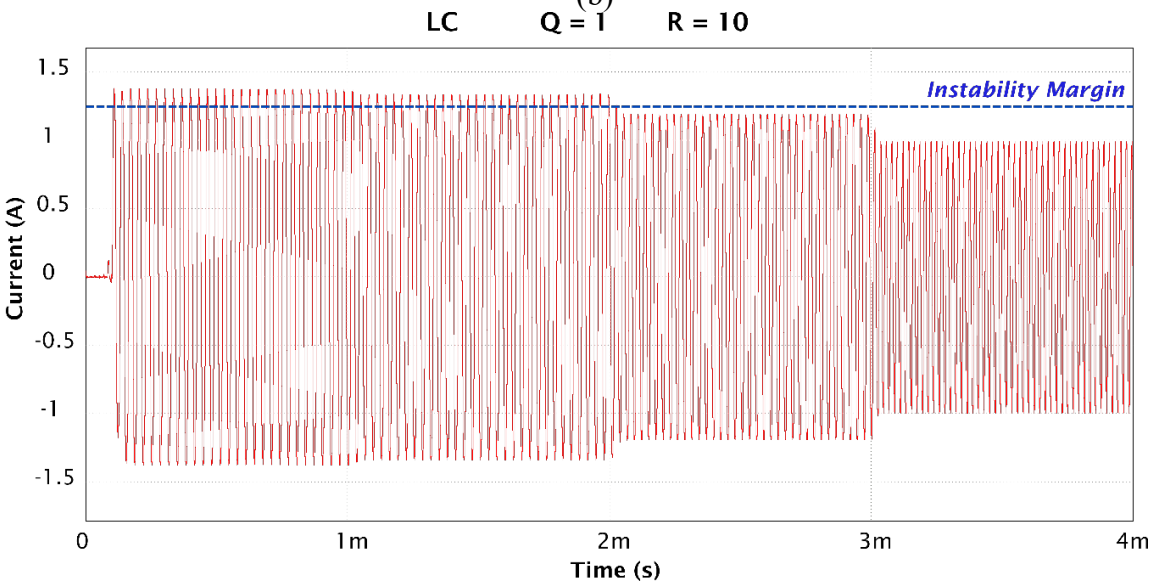

(c)

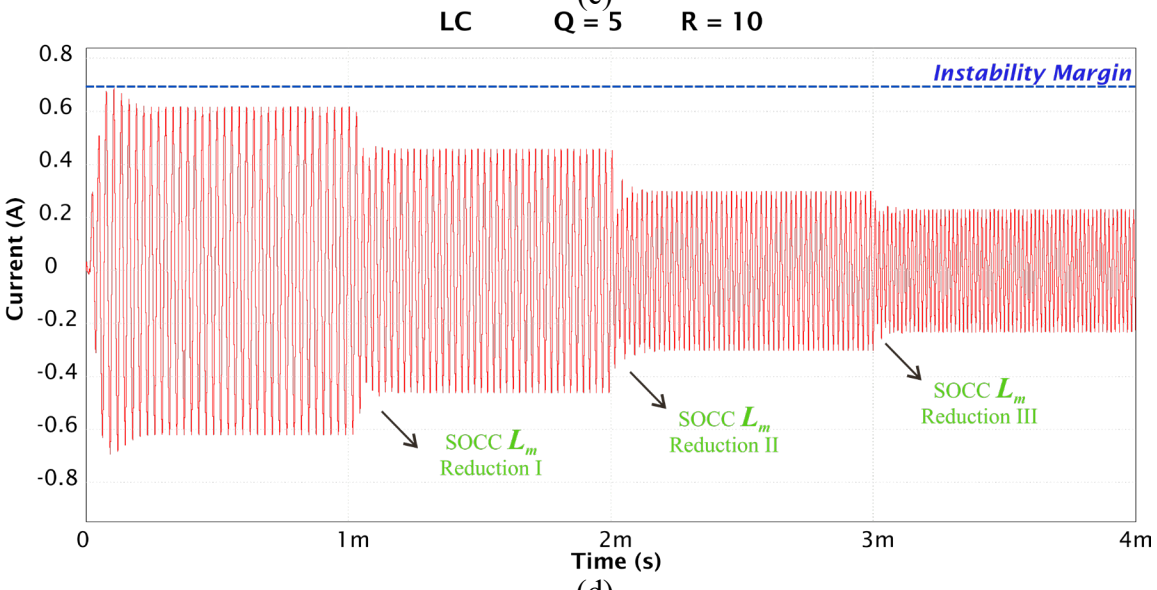

(d)

Source: Author

For the LCC filter, simulations were also performed for different values of $C_p = C_s$, $C_p = 2C_s$ and $C_p = 0.5\ C_s$ and the results are shown in Figure 15. For higher values of C_p, even the higher R_L wasnt able to produce a wide range of sustained self-oscillated modulation. Only ZMNSOP type instabilities were detected under the tested ranged for the LCC filter topology. Furthermore, higher values of Q seem likely to be unfeasible for LCC SORC modulated systems due to the frequently present MMNSOP.

Figure 15 - Simulation results of the feasibility of the LCC filter topology operating as modulated SORC. Resonant filter current i_P *vs* time, under three changes on L_m.

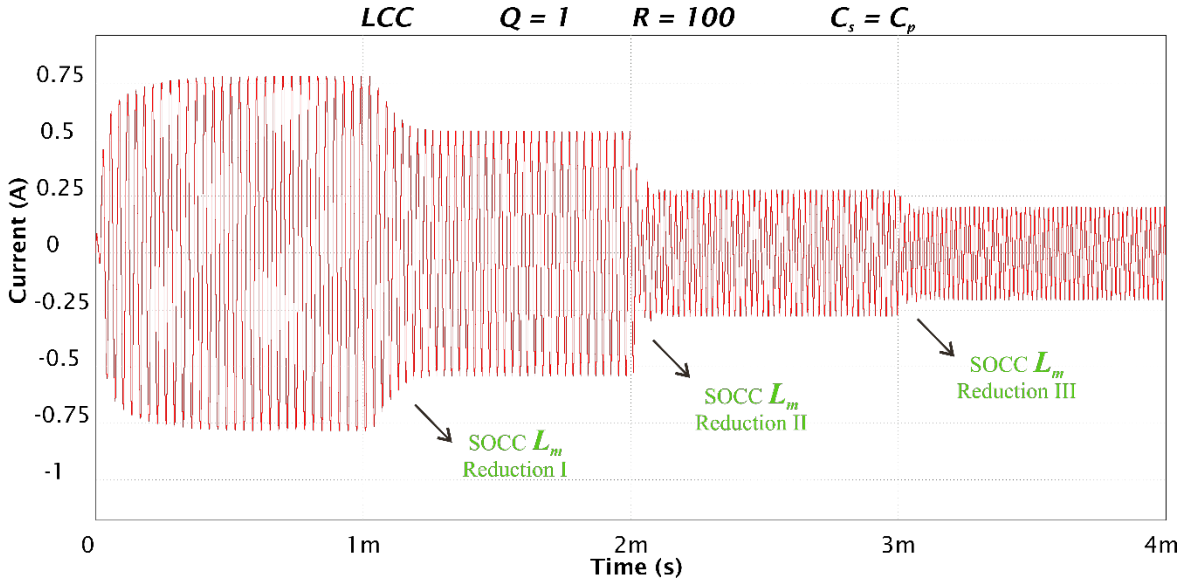

(a)

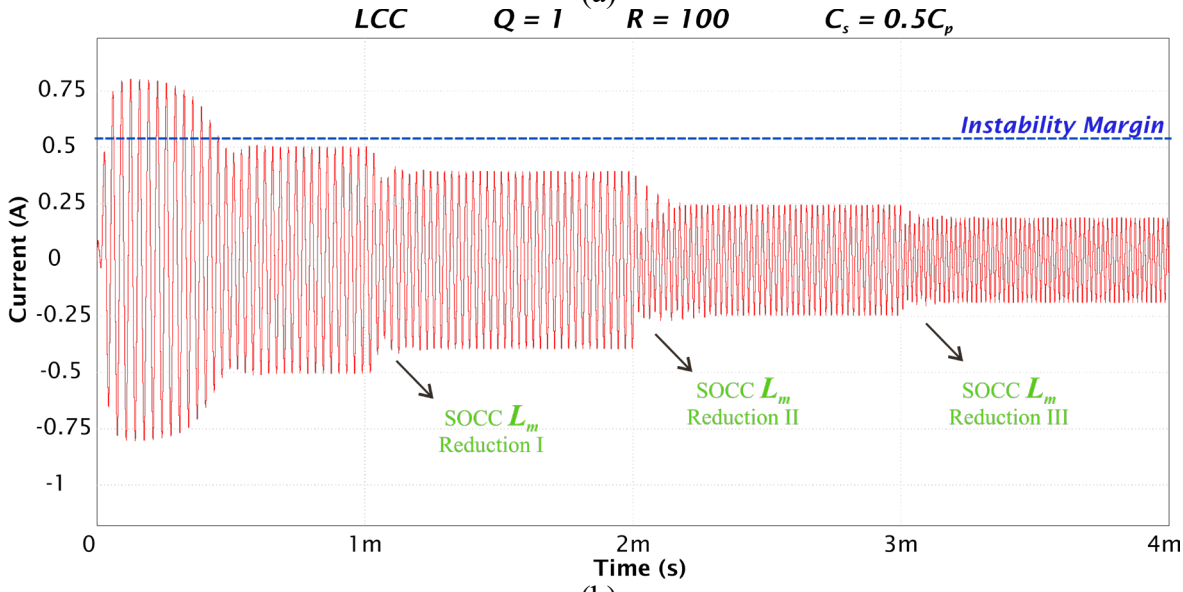

(b)

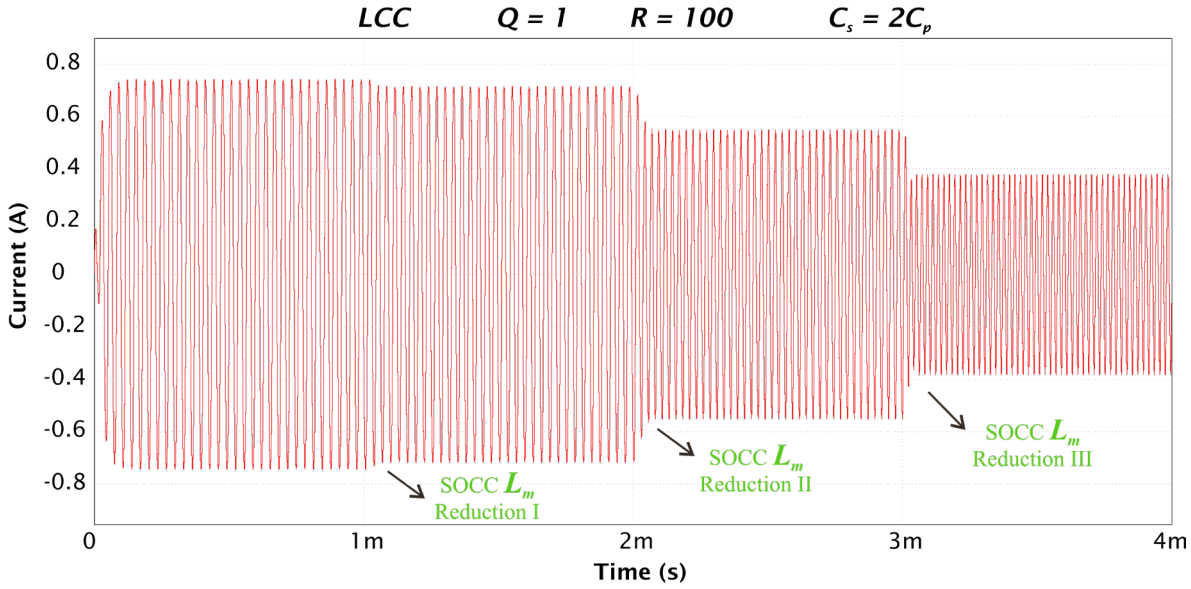
LCC Q = 1 R = 100 $C_s = 2C_p$
Current (A)
0.8
0.6
0.4
0.2
0
-0.2
-0.4
-0.6
-0.8
0
1m
2m
3m
4m
Time (s)
SOCC L_m Reduction I
SOCC L_m Reduction II
SOCC L_m Reduction III

(c)

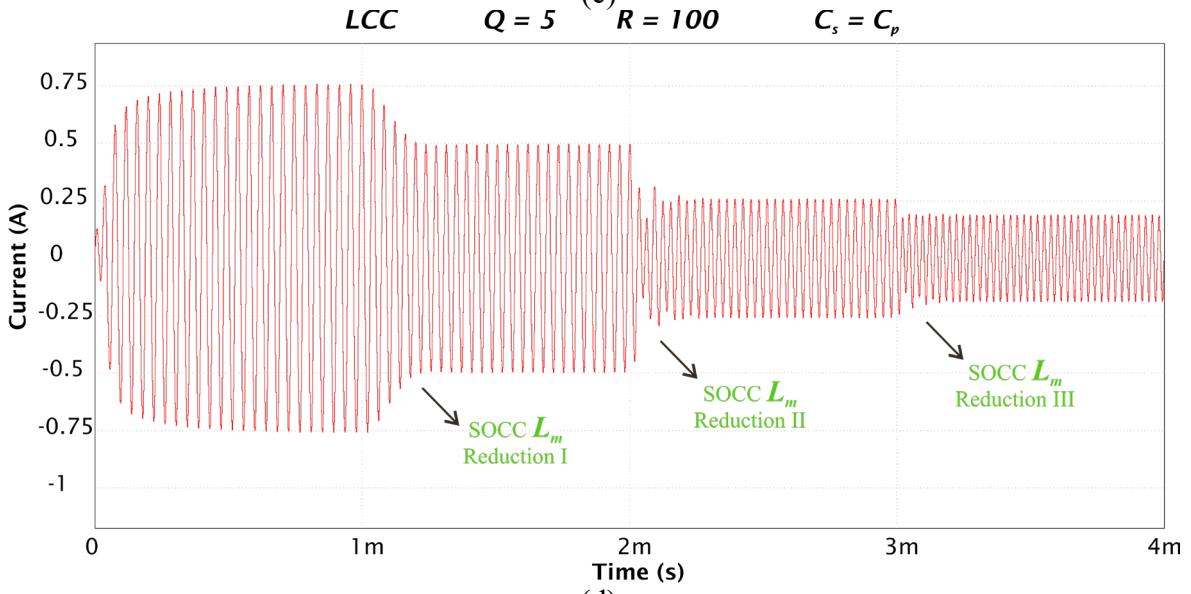
LCC Q = 5 R = 100 $C_s = C_p$
Current (A)
0.75
0.5
0.25
0
-0.25
-0.5
-0.75
-1
0
1m
2m
3m
4m
Time (s)
SOCC L_m Reduction I
SOCC L_m Reduction II
SOCC L_m Reduction III

(d)

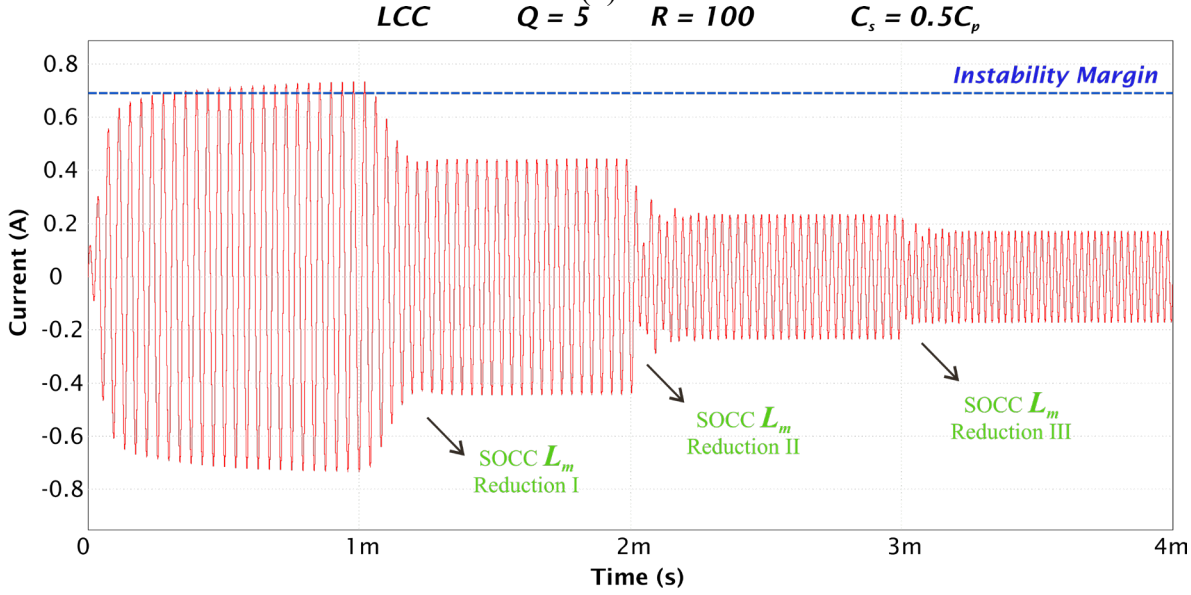
LCC Q = 5 R = 100 $C_s = 0.5C_p$
Instability Margin
Current (A)
0.8
0.6
0.4
0.2
0
-0.2
-0.4
-0.6
-0.8
0
1m
2m
3m
4m
Time (s)
SOCC L_m Reduction I
SOCC L_m Reduction II
SOCC L_m Reduction III

(e)

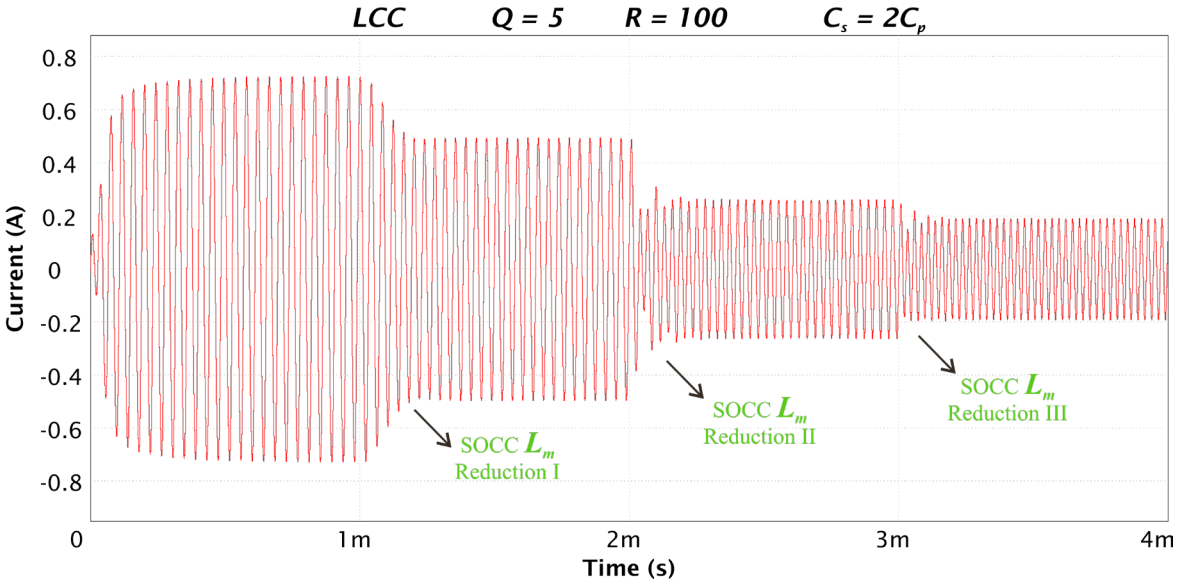
LCC Q = 5 R = 100 $C_s = 2C_p$
Current (A)
0.8
0.6
0.4
0.2
0
-0.2
-0.4
-0.6
-0.8
0
1m
2m
3m
4m
Time (s)
SOCC L_m Reduction I
SOCC L_m Reduction II
SOCC L_m Reduction III

(f)

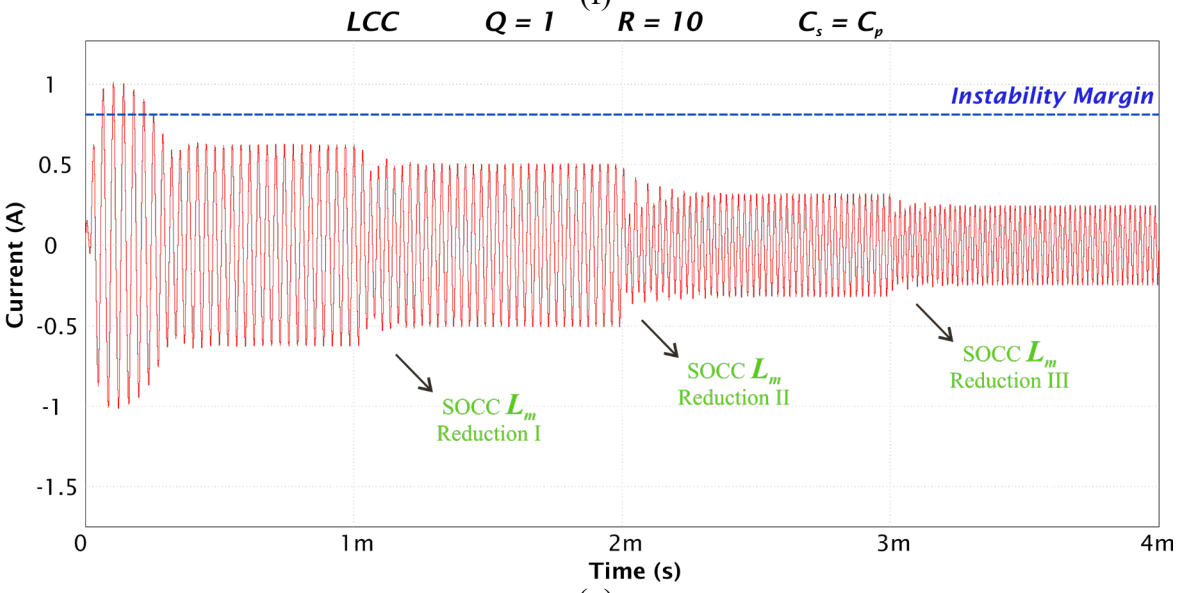
LCC Q = 1 R = 10 $C_s = C_p$
Instability Margin
Current (A)
1
0.5
0
-0.5
-1
-1.5
0
1m
2m
3m
4m
Time (s)
SOCC L_m Reduction I
SOCC L_m Reduction II
SOCC L_m Reduction III

(g)

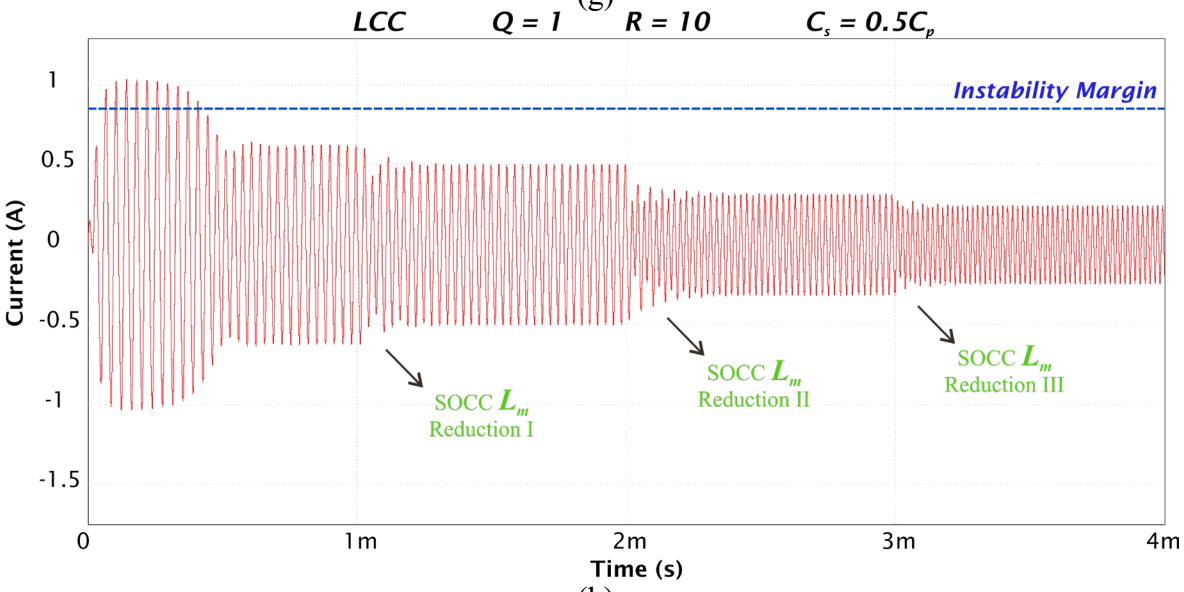
LCC Q = 1 R = 10 $C_s = 0.5C_p$
Instability Margin
Current (A)
1
0.5
0
-0.5
-1
-1.5
0
1m
2m
3m
4m
Time (s)
SOCC L_m Reduction I
SOCC L_m Reduction II
SOCC L_m Reduction III

(h)

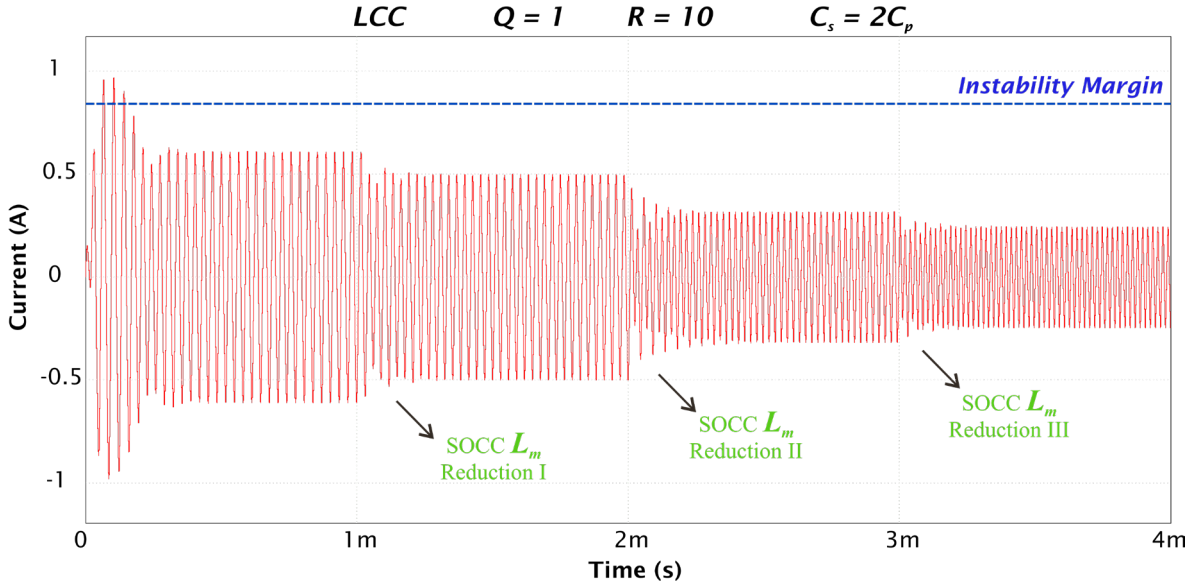

(i)

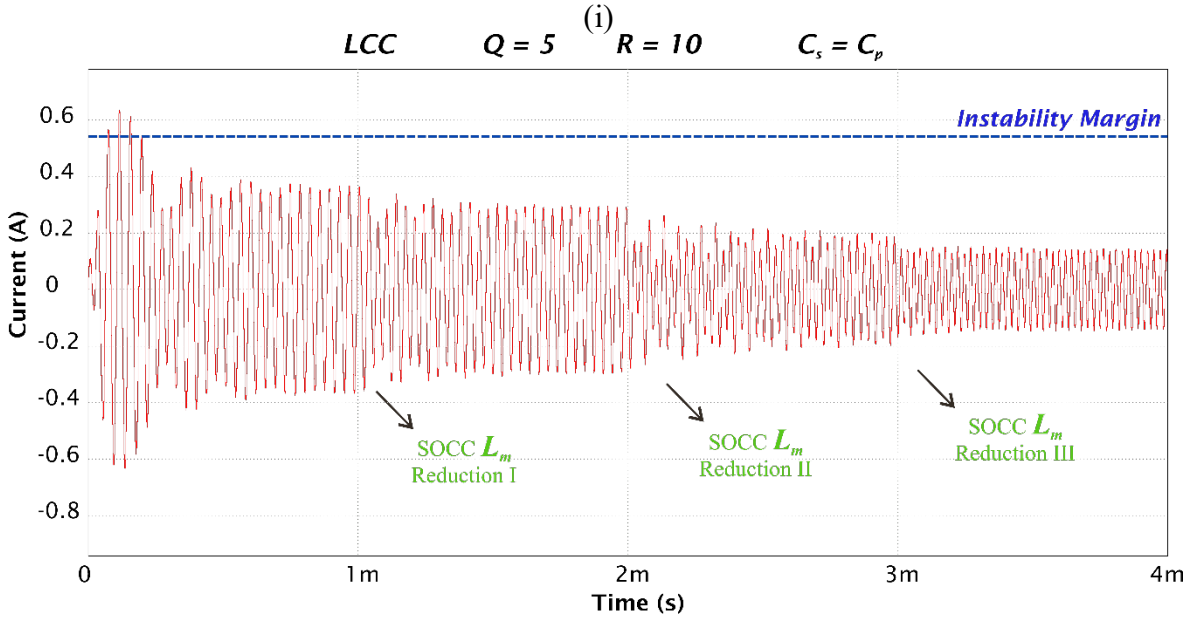

(j)

For the LLC filter, simulations were also performed for different values of $L_p = L_s$, $L_p = 2L_s$ and $L_p = 0.5\ L_s$ and are shown in Figure 16. The LLC modulated SORC with high R_L values has a great feasibility with presence of NSO margin over a wide range of Q values. However, for low R_L values, the LLC filter presents the same ZMNSOP type of instability as the LCC filter for a range of Q values equal to, and higher than 1.

Figure 16 - Simulation results of the feasibility of the LLC filter topology operating as modulated SORC. Resonant filter current i_P vs time, under three changes on L_m.

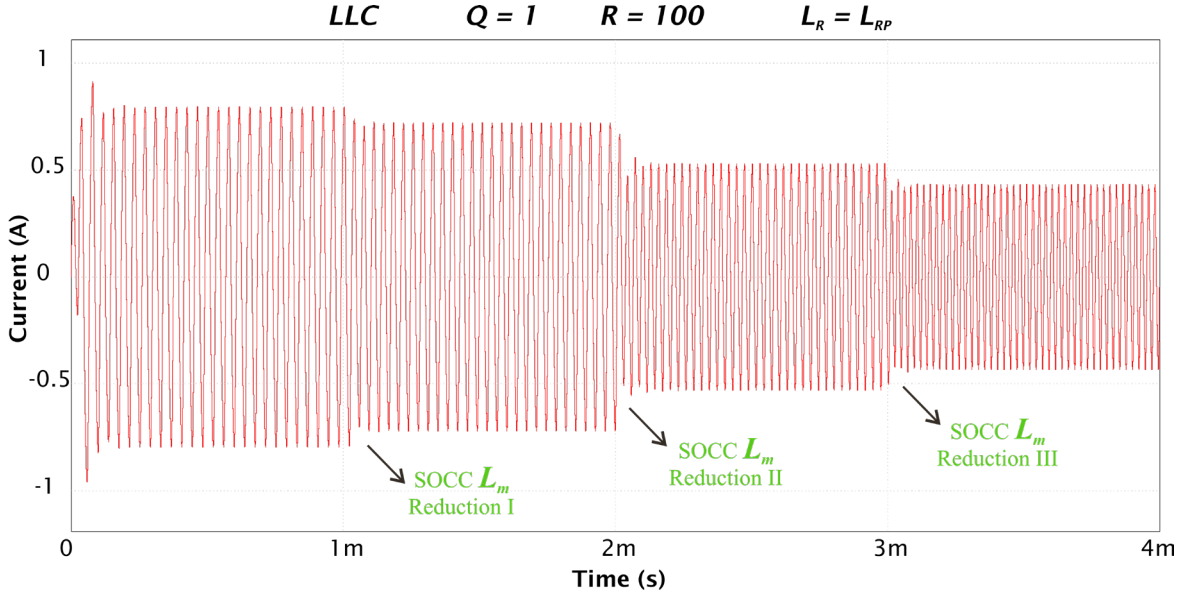

(a)

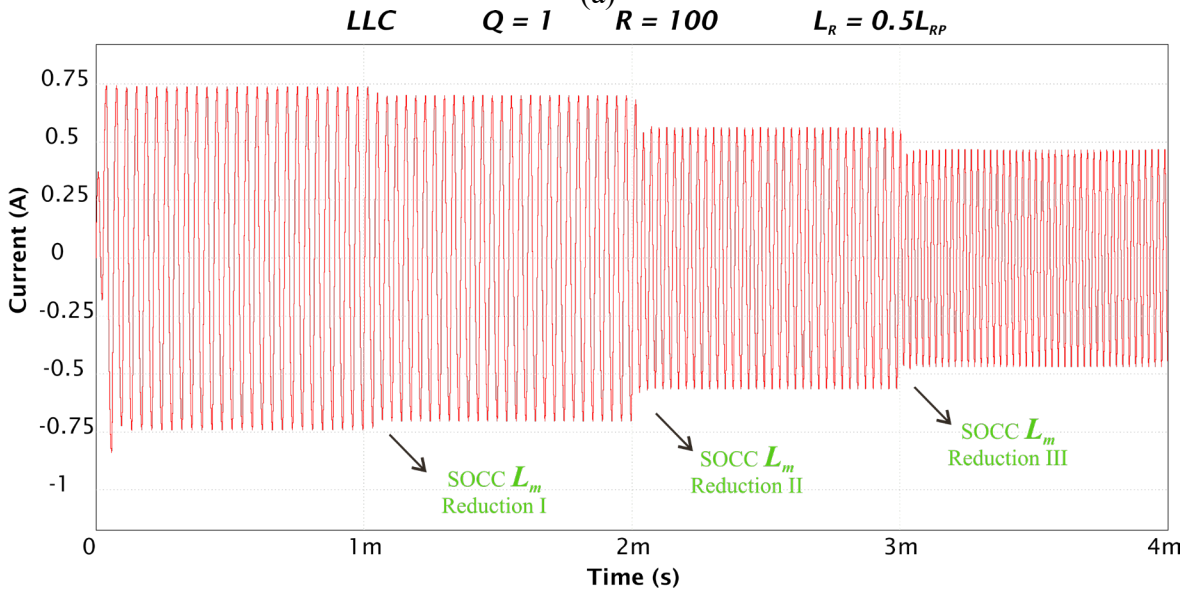

(b)

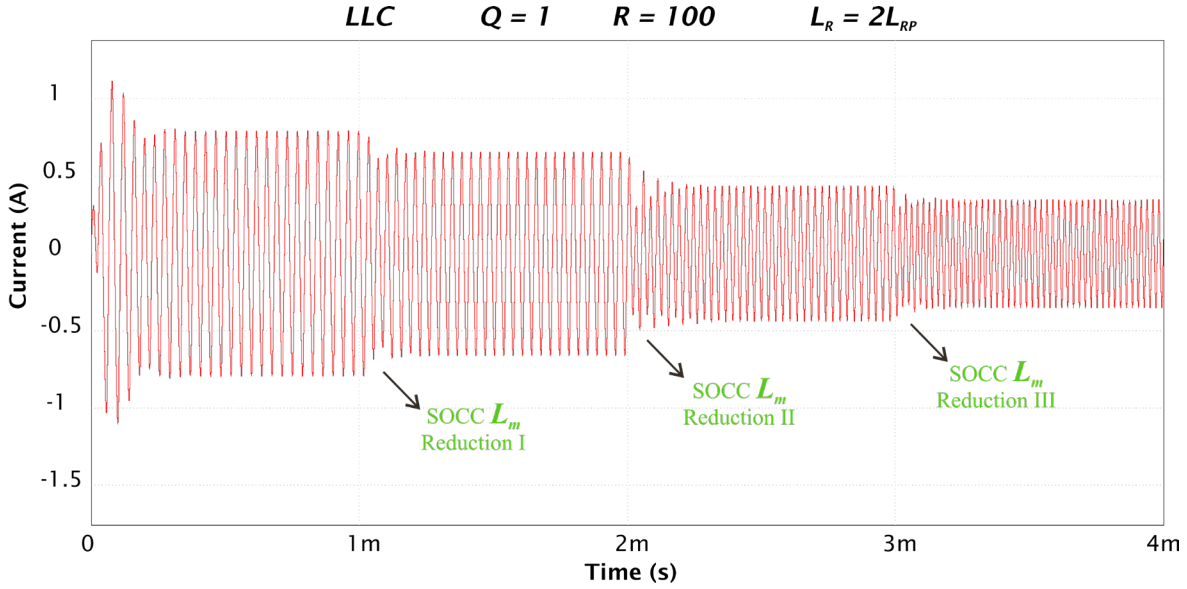
LLC Q = 1 R = 100 $L_R = 2L_{RP}$
Current (A)
1
0.5
0
-0.5
-1
-1.5
0
1m
2m
3m
4m
Time (s)
SOCC L_m Reduction I
SOCC L_m Reduction II
SOCC L_m Reduction III

(c)

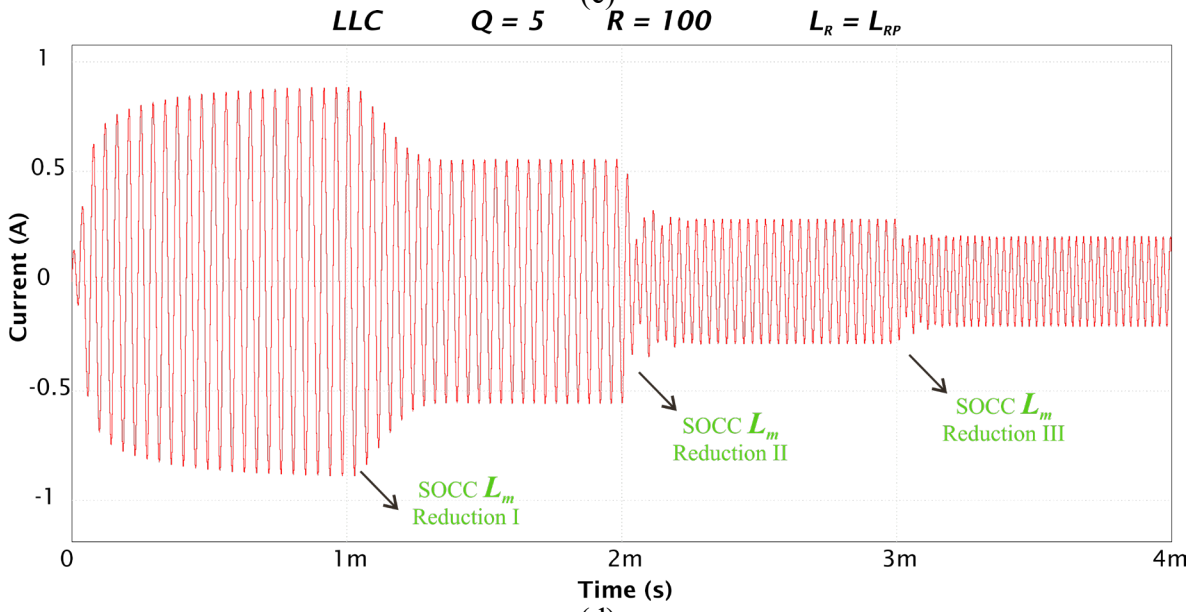
LLC Q = 5 R = 100 $L_R = L_{RP}$
Current (A)
1
0.5
0
-0.5
-1
0
1m
2m
3m
4m
Time (s)
SOCC L_m Reduction I
SOCC L_m Reduction II
SOCC L_m Reduction III

(d)

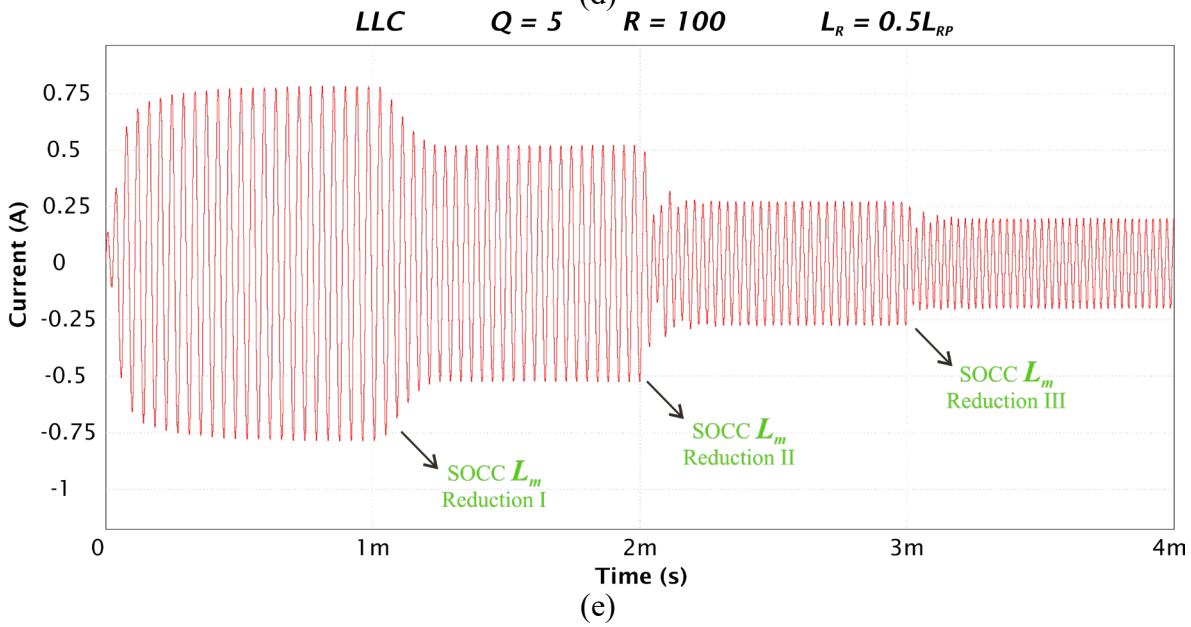
LLC Q = 5 R = 100 $L_R = 0.5L_{RP}$
Current (A)
0.75
0.5
0.25
0
-0.25
-0.5
-0.75
-1
0
1m
2m
3m
4m
Time (s)
SOCC L_m Reduction I
SOCC L_m Reduction II
SOCC L_m Reduction III

(e)

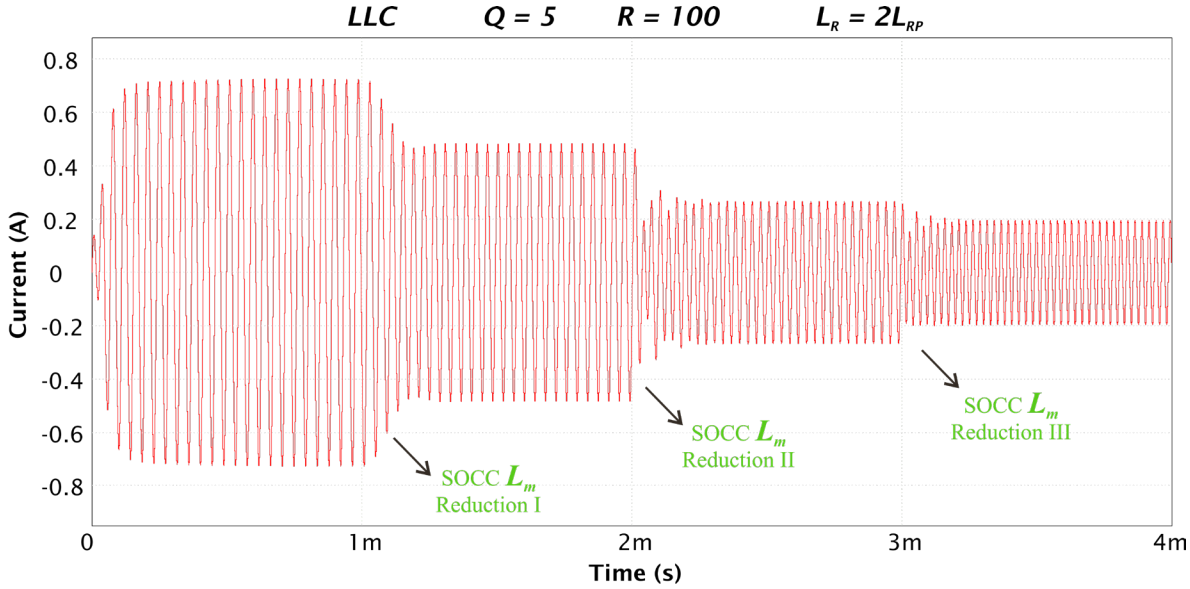

(f)

Source: Author

Table 1 summarizes the simulation results of the modulated SORC filter topologies in terms of the Modulated Stability (M.S.), Q and R_L. The LC, LCC and LLC filters all work considerably well with R_L values that are sufficiently high, with both low and high Q values. For higher Q values, due to how fast the magnitude of the output of the filter varies with frequency, smaller values of L_m produce a more sizeable modulation when compared to lower Q values. However, for the LCC filter, even for higher values of R_L and low Q values, higher values of C_P seem to introduce an NSO margin into the modulated system. The LLC filter has a great feasibility, properly modulating the system over a wide range of frequencies above the resonance given proper values of R_L. Both LLC and LCC filters present the same type of ZMNSOP instability. The LC filter has both ZMNSOP and MMNSOP types depending on the values of Q and R_L.

Table 1 - Summary of the simulation results from the modulated SORC filter topologies.

	LC				**LCC** $C_R = C_P$				**LLC** $L_R = L_{RP}$			
R_L	10		100		10		100		10		100	
Q	1	5	1	5	1	5	1	5	1	5	1	5
M. S.	*U*	*U*	*S*	*S*	*U*	*U*	*S*	*S*	*U*	*U*	*S*	*S*

	LCC $C_R = 2C_P$				**LCC** $C_R = 0.5C_P$				**LLC** $L_R = 2L_{RP}$				**LLC** $L_R = 0.5L_{RP}$			
R_L	10		100		10		100		10		100		10		100	
Q	1	5	1	5	1	5	1	5	1	5	1	5	1	5	1	5
M. S.	*U*	*U*	*S*	*S*	*U*	*U*	*U*	*U*	*U*	*U*	*S*	*S*	*U*	*U*	*S*	*S*

Source: Author

2.4 SOCC EQUIVALENT MODEL

A well-known equivalent circuit of the SOCC reflected to its secondary side is shown in Figure 17(a) (GANZ, 1962). The TWCT is commonly implemented through the toroidal core geometry shown in Figure 17(b). This model emulates the switching process of the SORC and has been used, with acceptable precision, as an essential tool to design this converter.

Figure 17 - The (a) Self-Oscillating Command Circuit Equivalent Model and (b) TWCT.

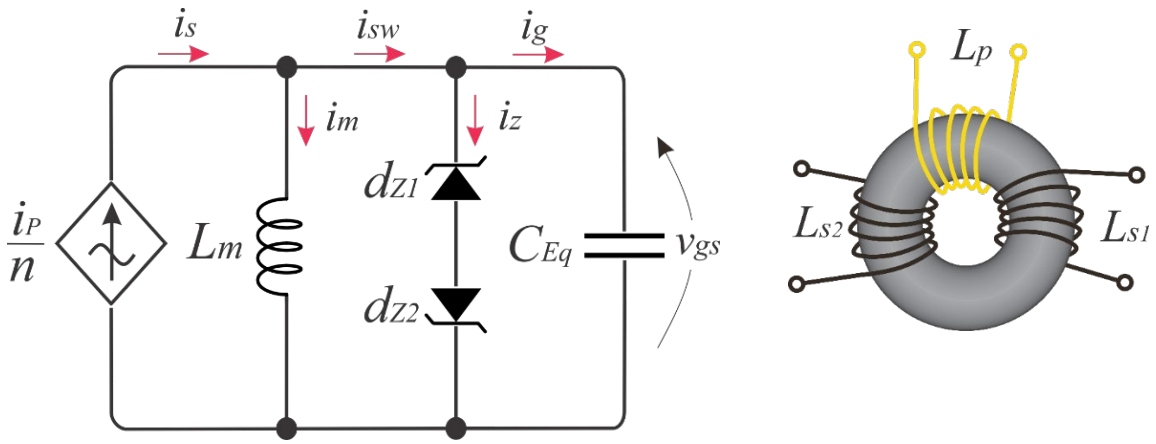

Source: Author

The AC current dependent current source i_P/n represents the portion of i_p that flows through the SOCC secondary windings. The L_m of the CT, along with the applied voltage v_{gs} and the value of C_{Eq}, dictate the portion of i_s that flows through S_1 and S_2 in the form of gate-charge or through the Zener arm, d_{Z1}-d_{Z4}, to maintain the v_{gs} voltage clamped. It is usual to represent the sum of the currents i_g and i_z as the switching current i_{sw}, simplifying the quantitative analysis of the i_m of the CT. The ratio between currents is given by (1).

$$\frac{i_p}{n} = i_m + i_z + i_g \tag{1}$$

From the waveforms of the SOCC from Figure 18, this relationship is a crucial point for the analysis of both standard and closed-loop SORC, given that most methodologies aiming for frequency variation tend to manipulate the ratio between these currents in order to vary i_m. As illustrated on the waveforms, the peaks of i_m define the precise moments of state change of the MOSFETs, which translates to the value of f_s. An easy way to modify it would be to change the CT's L_m value, as given by (2).

$$i_m(t) = \frac{1}{L_m}\int_0^t v_{gs}(t)\,dt + i_m(0) \tag{2}$$

Figure 18 - The Self-Oscillating Command Circuit Main Waveforms.

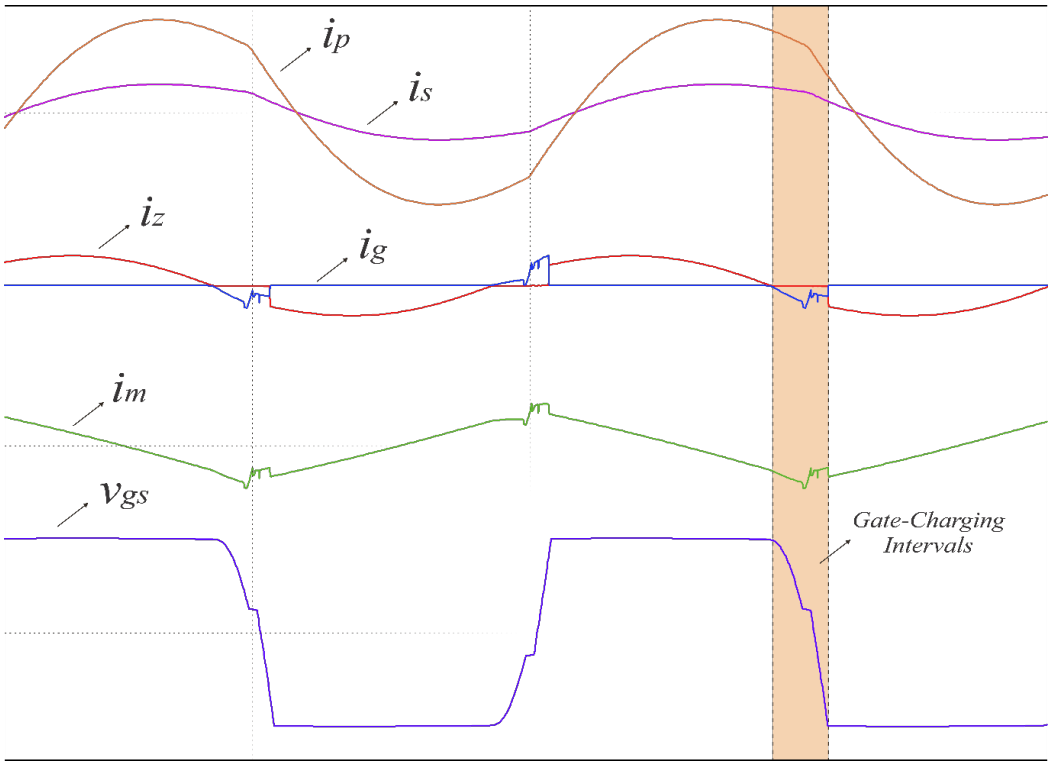

Source: Author

2.4.1 SOCC Closed-Loop limitations

The usage of the SORC as the standalone converter depicted so far was consistent with the early development of electronic systems for artificial lighting in the past, with most topologies of Electronic Ballasts for FL presenting some self-oscillating command. However, its usage has been considerably insubstantial as a solution for more complex low-cost and high-power density applications, especially when extra control layers are required.

One of the most significant reasons for this is that no traditional external gate-driver is responsible for switching or controlling S_1 and S_2, as the SOCC performs this whole function. Working similarly to other nonlinear oscillators, such as the *Colpitts* and the *Royer*, the SOCC operates as an intrinsic positive-type feedback loop between the output (i_p) and the input (i_g). Furthermore, the passive characteristic of the SOCC elements restricts the feasibility of extra layers of control loop with reference, as there is no obvious actuation mechanism. The inductances L_p, L_{s1}, and L_{s2} of the TWCT that f_s cannot be modified through trivial methods, nor can the voltage applied, *i.e.,* the Zener voltage, be easily varied.

2.5 SORC FREQUENCY VARIATION TECHNIQUES

The self-oscillating frequency analysis and manipulation of the SORC have been the subject of analysis in some works in the literature. This section focuses on displaying these works. The frequency variation can occur via direct modulation of the magnetizing current by including the addition of parallel branches in the SOCC or by employing a variable filter series inductor.

2.5.1 Frequency variation through parallel branches

Figure 19 shows a common principle to modify the value of f_s, which is to change the amplitude of i_m through the addition of parallel branches, causing a deviation of the current that would otherwise flow through L_m, to instead flow through R_a and C_a. This method has been consistently employed in the literature, providing exciting results for such a simple solution.

Figure 19 - Paralleled branched equivalent model employed for frequency variation

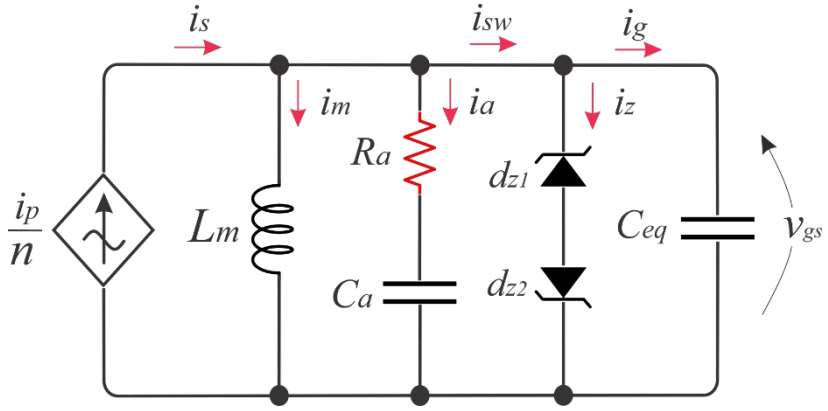

Source: Author

Although this is a simple solution, as it allows the usage of straightforward impedance branches as *LR* and *CR* for easily achievable frequency tuning, additional paths placed on a current-based circuit like the SOCC can have an undesirable effect on the system efficiency. Moreover, even though this is a viable alternative in terms of open-loop frequency variation, as done in (J. S. GLASER, 2002; SEIDEL, Á. R. *et al.*, 2003; TAO *et al.*, 2001), (SEIDEL, A. R. *et al.*, 2003), it still lacks the feasibility of implementing extra control layers due to the absence of a precise actuation mechanism that allows reference tracking.

Figure 20 depicts the procedure of impedance insertion in the SOCC. A significant issue with this method is the increased power loss on the auxiliary resistor that occurs on the lowest

frequencies of the SORC's operating range as f_s reduces towards f_0, the circulating current in the resonant tank increases in value, along with the SOCC current, to the point where frequency variation may become unfeasible due to excessive power losses on R_a. Furthermore, gate voltage may present further undesired distortions caused by the addition of *LR* and *CR* branches.

Figure 20 - Gate waveforms for the paralleled branched SOCC.

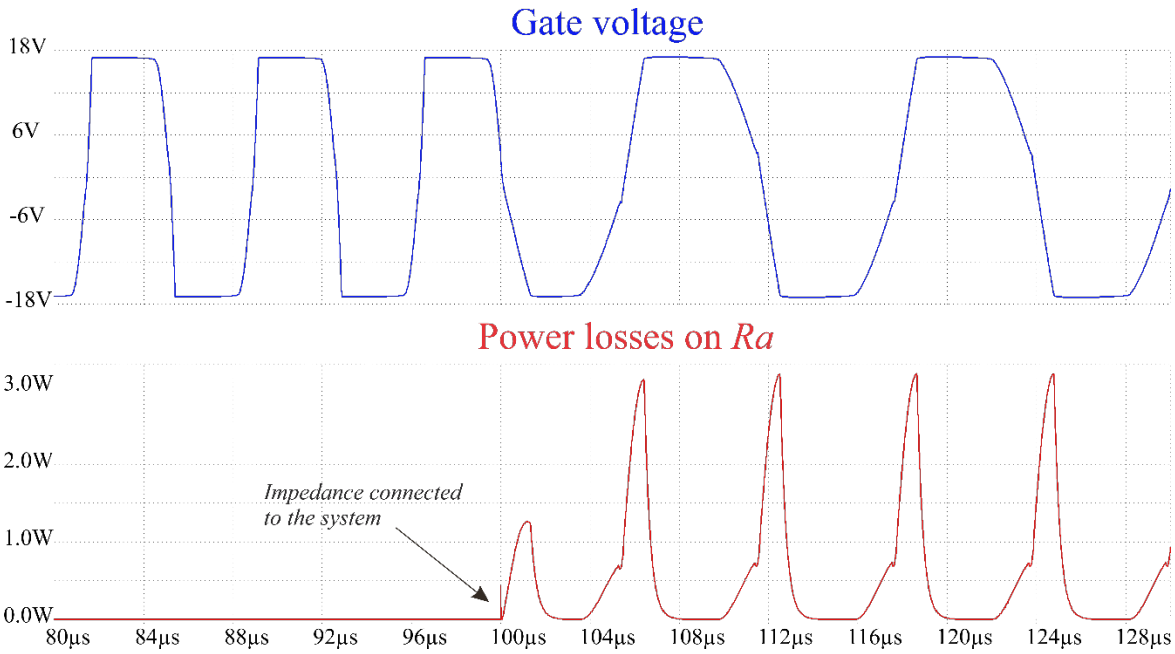

Source: Author

2.5.2 Frequency variation through variable inductor L_R

Another alternative, as seen in (PERDIGAO *et al.*, 2016), replaces the series inductor L_r of the resonant filter of the SORC with a VI. This method constitutes a more feasible alternative, given that the VI can be considered an actuation mechanism that works through the insertion of a DC current.

The circuit, shown in Figure 21, is an equivalent version of the one shown in Figure 4 and Figure 5. However, it suppresses the switching elements of the SOCC and instead considers only the square wave voltage applied to the filter, V_s. This simplified circuit has been extensively employed in SORC design methodologies (SEIDEL, Á. R. *et al.*, 2003)-(J. S. GLASER, 2002) and is essential to design the filter elements through the First Harmonic Approximation (FHA) prior to the SOCC design.

Figure 21 - SORC frequency variation through filter Variable Inductor.

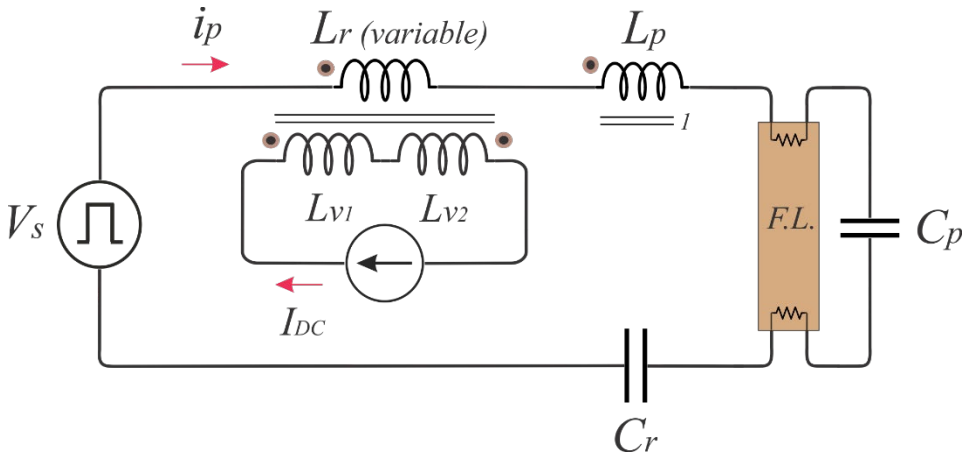

Source: Author

Despite being an extra step ahead of the previous method regarding the feasibility of control layers, the VI placed in the filter has some constraints. First, due to the SORC intrinsic feedback characteristic, varying the filter inductor results not only in a variation of f_s but simultaneously changes the filter's output power and the quality factor Q and f_0 of the filter. Second, as per usual, the necessity of employing complex non-linear design techniques, such as the Describing Function Method (DFM) (SEIDEL; BISOGNO; DO PRADO, 2007) and the Tsypkin (DO PRADO *et al.*, 2000) methods, discourages the usage of a VI in the filter, as dealing with several varying parameters may become unfeasible.

The third restraint is related to the efficiency of the SORC. While a VI positioned in the filter may be more desirable than associating impedances with L_m, the core volume and losses can escalate noticeably when this device is connected in series with the converter's primary current path, which is especially noticeable for high load currents. However, in these cases, the SORC presents some degree of freedom for the designer to increase the bus voltage, reducing the flowing current through the filter while maintaining the output power.

2.6 THE VARIABLE INDUCTOR

Figure 22(a) and Figure 22(b) show both the VI device and model, which is essentially a magnetic device susceptible to inductance changes on its primary winding N_p when a DC is injected into its auxiliary windings N_{a1} and N_{a2}. It can be modeled using either the Finite Elements Analysis (FEA) or the SPICE behavioral method. The authors in (MARCOS ALONSO *et al.*, 2016c), (ALONSO *et al.*, 2016a, 2017; MARCOS ALONSO *et al.*, 2016a)

model a VI using the SPICE method, employing essential elements such as resistors, voltage, and current sources to model the air gap, linear reluctance R_L, nonlinear reluctances R_{NL}, and magneto-motive forces NI.

Figure 22 –The (a) Variable Inductor and (b) its simplified model.

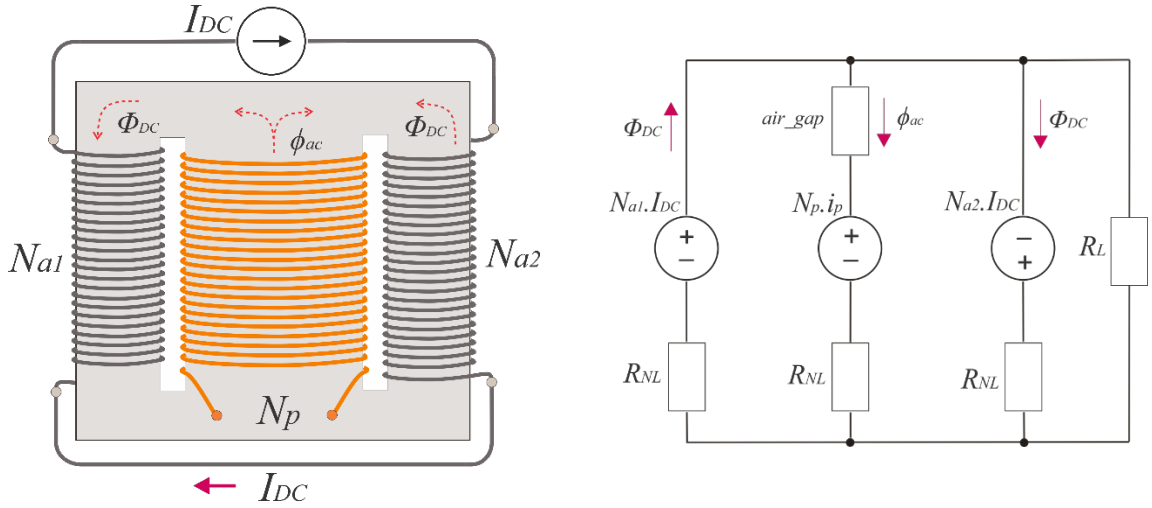

(a) (b)

Source: Author

Using the Brauer model of the *B-H* curve, a relationship between the magnetic field intensity H and the magnetic flux density B can be established, by expressing one as a function of the other, as seen in (3), where k_1, k_2, and k_3 are the specific model constants that vary from each type of core material (MARCOS ALONSO *et al.*, 2016b). Usually, it is interesting to differentiate (3) in (4) for further usage on modeling the devices' reluctance.

$$H(B) = (k_1 e^{k_2 B^2} + k_3) B \tag{3}$$

$$\mu_d(B) = \frac{dB}{dH} = [k_1(1 + 2k_2 B^2) e^{k_2 B^2} + k_3]^{-1} \tag{4}$$

With the help of LTSpice as a simulation tool, it is possible to create behavioral voltage and current sources that emulate the magnetic characteristics of the VI through $H(B)$. This concept allows the analogous electrical simulation of the permeability, reluctance, flux, and inductance values. It can be applied to a wide range of magnetic devices, including multiple winding transformers like the SOCC's CT, requiring for that only the values of k_1, k_2, and k_3, and the core dimensions.

The SORC CT has typically been manufactured using toroidal cores, which possess characteristics such as smaller and concentrated stray fields and distributed air gaps, allowing for lower saturation levels and reduced core volume, all desirable features for the SOCC operation. The air gap in this type of core is inserted during the fabrication process, where a material different from that of the core itself is inserted to act as a distributed gap, such as air, for instance. Having distributed air gaps can be such an advantage regarding the adverse effects that would otherwise be caused by the fringing flux that, nowadays, even E-type cores are being manufactured with distributed air gaps for use in specific applications.

However, in some cases, toroidal core types may be regarded as unfeasible options if mass production is required for the design, as those can turn the manufacturing into an overly time-consuming process. If required, a more feasible option in terms of ease of production that works just as well with the SORC is the E-type core, whose practical results have been attested in this paper and shown below in comparison to the toroidal alternative.

Furthermore, a trending alternative that can easily replace the geometries mentioned above is the planar core type. The replacement of conventional magnetic structures with planar cores allows for further automation of the fabrication process, mainly due to integrating the windings into the Printed Circuit Board (PCB).

2.6.1 Theoretical design of the Variable Inductor

A VI model is characterized by equations that establish a relationship between the magnetic and electrical parts, i.e., the reluctances, gaps, and windings. In order to design a variable inductor, the first step is to select a magnetic core and a maximum inductance value for the design. Magnetic cores manufacturers usually provide a large number of information regarding their devices, which are required for the design and simulation model.

Information such as effective length (l_e), effective area (A_e), effective volume (V_e), average turn length (l_n), winding area (A_w), the permeability of free space (u_0), initial permeability (u_i), and flux density (B) are all required in order to build a model.

The first behavior modeled is the linear reluctance, which has a constant value along the B-H curve, shown in (5). The reluctance of the respective length l_0 and the fringing factor v_0 are used to calculate this reluctance, along with the relative permeability u_r.

$$R_{lin} = \frac{l_0}{\mu_0 \mu_r A_0 v_0} \tag{5}$$

The second behavior modeled is the non-linear reluctance, aggregating the B – H curve effect into the device, shown in (6). For its design, the length l_m and area A_m of each leg of the core are required, and the absolute differential permeability of the material $\mu_d(B)$. The parameters k_1, k_2, and k_3, are required for this design, and they can be derived from the graphical information given by the core manufacturer on the device datasheet through curve-fitting software (ALONSO *et al.*, 2016b).

$$R_{nlin} = \frac{l_m}{\mu_d(B) A_m} \tag{6}$$

The third behavior modeled is the effect of the air gap shown in (7). This type of device is usually constructed with a single air gap on the central leg, whose flux is coupled by the main windings and helps define the inductance value. The external legs of the VI are usually stripped of any air gaps to facilitate the establishment of the dc flux. The air gap can be calculated as a relationship between its length l_g, area A_g and the fringing factor v_g.

$$R_{gap} = \frac{l_g}{A_g v_g} \tag{7}$$

The last behavior is the winding model, which helps establish an interaction between the magnetic and electrical parts of the device. The only impactful parameter worth mentioning is the number of turns of the main winding, N_w, which defines the fundamental relationship between magnetomotive force (MMF) and the winding current i_w shown in (8).

$$fmm(t) = N_w i_w(t) \tag{8}$$

Beyond these basic equations, and for a more comprehensive understanding of variable inductors and their modeling, (MARCOS ALONSO *et al.*, 2017) presents an analytical procedure for further modeling variable inductors. It discusses how a DC magnetic flux is injected into the structure to provide a bias level that allows for magnetic permeability modulation. The AC magnetic flux is superposed to this DC level, making it possible for a variable inductance to be seen from the AC windings. The authors in (PERDIGAO *et al.*, 2016) complete the previously mentioned research very consistently in the sense that it provides a comprehensive overview of variable inductors and variable transformers, including their applications to lighting drivers.

2.7 THE VARIABLE CURRENT TRANSFORMER

To bypass the magnetic path limitation of the toroidal core, in addition to the single toroid, another core has to be introduced, as seen in Figure 23(a), resulting in the Variable Current Transformer device. This modification creates two additional magnetic paths, allowing an extra pair of auxiliary windings to be connected. When circulated with a DC current, these windings can vary the inductance of the three main windings of the SOCC, N_p, N_{s1}, and N_{s2}, which varies L_m, thus changing the f_s of the SORC. Figure 23(b) shows the model of the proposed VCT.

Figure 23 – The (a) Variable Current Transformer device and (b) equivalent model.

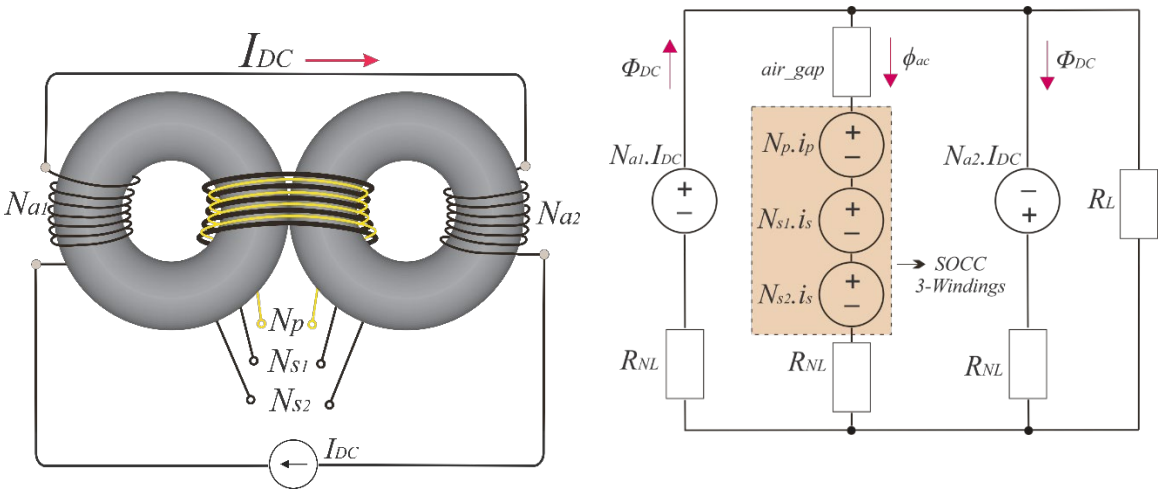

Source: Author

Its analogous magnetic SPICE model, illustrated in Figure 24**,** is similar to the VI presented in (MARCOS ALONSO *et al.*, 2016c). However, the central AC flux now links all three windings of the CT. Furthermore, given the intrinsic distributed air gap characteristic from toroidal cores, two air gap elements were added into each respective section of the core. Even though there is an increased number of air gaps, in comparison to the E-type core VI, the absolute value of its reluctance is much lower.

Figure 24 - LTspice model of the VCT.

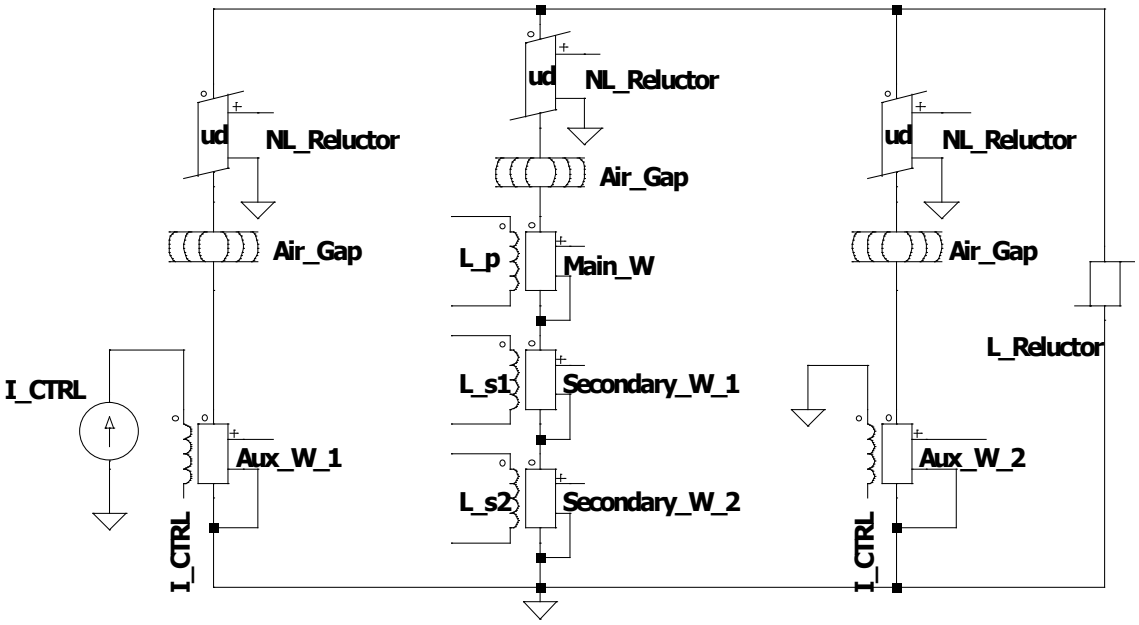

Source: Author

Figure 25 – Equivalent circuit for the behavior of each parameter of the VI.

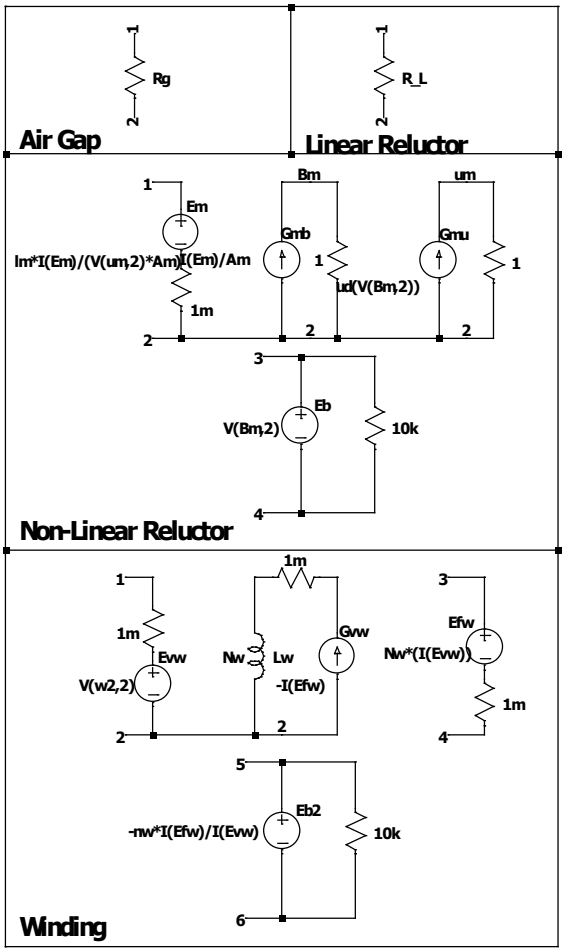

Source: Author

In Figure 25, the equivalent circuit of each element of the VI is shown. A simple resistor should suffice to represent their linear behaviors for simple linear elements such as the air gap and linear reluctance. For the non-linear reluctance, however, voltage and current dependent sources are required to capture the $B(H)$ behavior and the addition of resistors for the current sources and voltage-loop avoidance.

Apart from having voltage and current dependent sources with their respective resistors, the winding element contains an inductor that represents the number of turns of the primary windings. Another exciting aspect of this model is that the winding element contains six terminals, 2 of which are responsible for modeling the magnetic effects, 2 of which represent the electrical nuances, and two extra points to measure the inductance of that winding given in the form of an instantaneous voltage value (uV). The non-linear reluctance also has two extra terminals for measuring the magnetic flux density on that leg, also given in an instantaneous voltage (uV).

Figure 26 shows the behavior of the inductances of the main windings as a function of the applied DC current. In practical terms, the toroidal cores saturate with a smaller DC level than *E*-type cores, making the VCT capable of varying its inductance with a considerably smaller current value.

Figure 26 – "Dc" operating point simulation of the inductance in the main windings as a function of the DC current injected in the auxiliary windings for two different cores.[23]

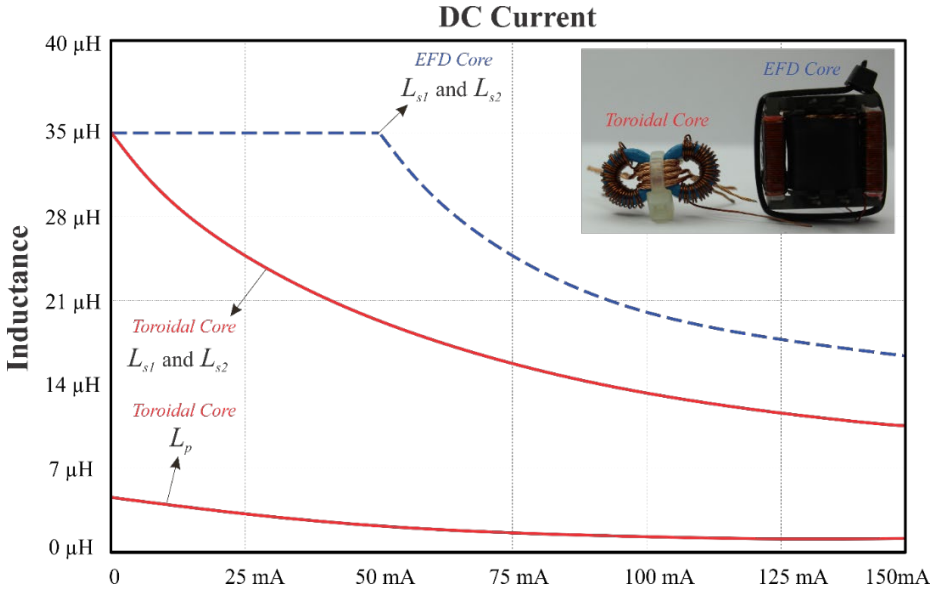

Source:Author

[23] The initial inductance variation of toroidal built VCTs is considerably better than for the EFD core types. Also, it is noticeable that the amount of auxiliary dc current required to completely vary the inductance is also considerably lower for the toroidal core as compared to the EFD.

A couple of minor drawbacks would be the potentially small maximum values of the TWCT inductances, given that the VCT presents a smaller window size and the availability of high-frequency toroidal cores with reduced inductance factor values (A_l). However, in the range of frequencies that SORC is generally employed, the values of these inductances are not usually a problem, as they hardly go over a few dozens of uH. However, if toroidal cores become unfeasible due to fabrication time requirements, an EFD core is can be used as a VCT instead, and its inductance variation is shown as a comparison to its toroidal counterpart. The application of a 150 mA IDC current results in nearly 100 % inductance reduction. The EFD cores generally require a higher DC current level on the auxiliary windings to perform the same amount of inductance change.

This definition of a model for the VCT occurs from the modelling of four magnetic elements: the air gap, the linear reluctance, the non-linear reluctance, and the winding itself. Both the air gap and the linear reluctance are modeled as analog resistances calculated through the length and area of the gap and core legs and the relative and air permeability. The non-linear reluctor and the windings are constructed as electrical circuits with voltage and current dependent sources that emulate the inductance, the number of turns, geometry, and Brauer's coefficients of the core. Further details are shown in [15].

2.7.1 The VCT SOCC Model

After introducing the VCT, the new model for the SOCC can be presented, as shown in Figure 27. This model is based on the classic model (GANZ, 1962), thus emulating the traditional switching process of the SORC while also presenting the characteristics mentioned above that allow the feasibility of a closed-loop self-oscillating system. As the variable L_m is incorporated into the model and is controllable by the current I_{DC}, it is now possible for the SORC to follow a reference value. It is interesting to note the $B(H)$ relationship expressed in the L_m variation as a function of the I_{DC} current, affecting both i_m and the self-oscillating frequency.

With the SORC design methodologies of the next section, it will be shown that this $B(H)$ behavior is reflected through the whole process of frequency detection of the SORC and can be represented in a Nyquist plot just as precisely as the traditionally designed open-loop converters.

Figure 27 - New variable L_m SOCC equivalent model for the proposed Variable Current Transformer.

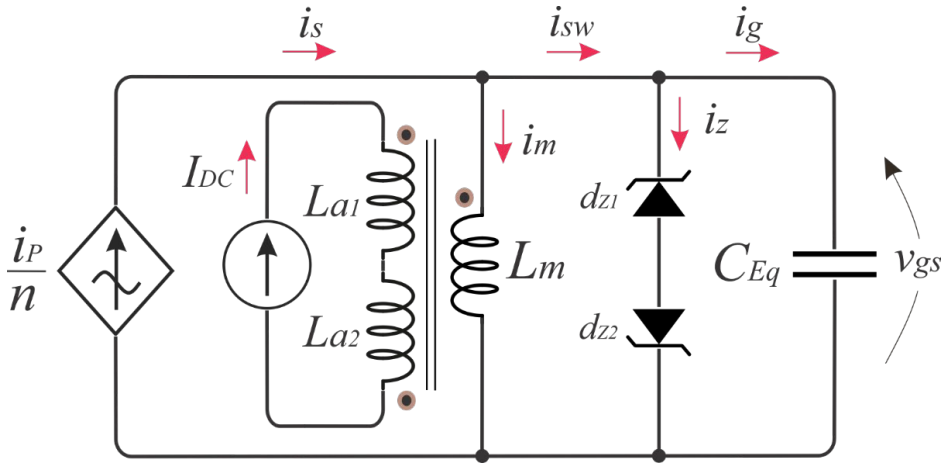

Source: Author

2.8 THE SORC DESIGN METHODOLOGIES

The nonlinear positive-type feedback characteristics of the SORC discussed in the last sections encouraged only a small number of design methodologies. A common point between these methodologies resides on the converter analysis from a standard control system point-of-view, usually employing the block diagram structure from Figure 2, where the linear and nonlinear parts of the system are separated to be subsequently dealt with.

The nonlinearity is represented by the purple hard limit block, which models the polarity change of the Zener voltage. The linear part related to the resonant filter is represented by the blue blocks, K and $G_F(s)$, which corresponds to the constant proportionality between the applied voltage on L_m to the filter, and the block of the filter elements, respectively. The green blocks, α_i, show the linear part related to the SOCC, and $G_M(s)$, which are the turns ratio of the VCT primary windings, and the block of L_m, respectively. The yellow block shows the proposed additional control layer through the previously discussed VCT, capable of reading the i_p current to modify L_m through subtle changes in I_{DC}.

The design methodologies that utilize the block diagram of Figure 28 to perform the SORC design [3],[16],[17] usually realize a simplification of the system by representing it into two blocks, the respective nonlinear and linear system's blocks N and $G(s)$ as shown in Figure 29**.** These methodologies differ on how the nonlinear part affects the linear part and which system parameters are used in the analysis.

Figure 28 - The SORC (a) complete block diagram from a control point-of-view.

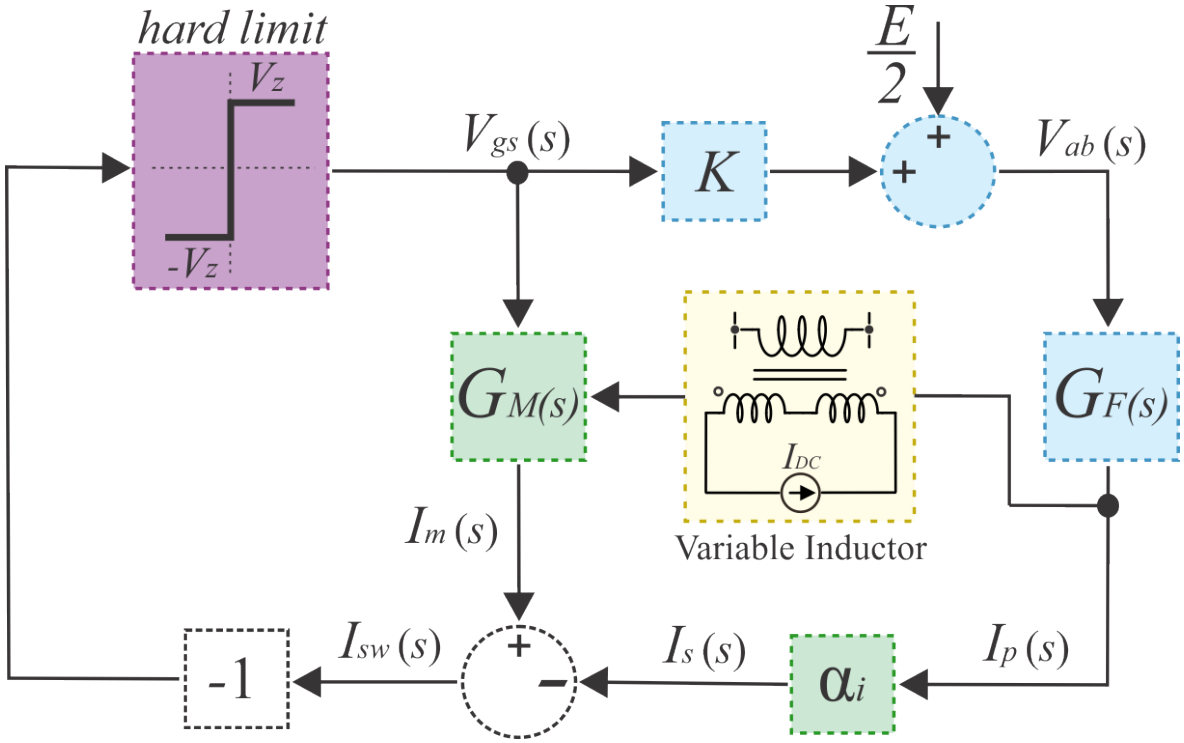

Source: Author

Figure 29 - The SORC simplified block diagram.

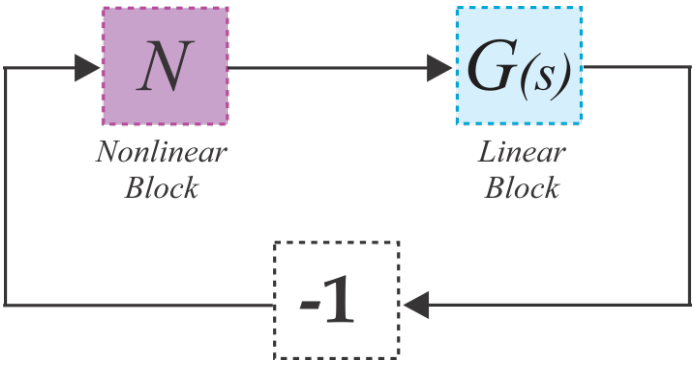

Source: Author

The individual blocks of the entire system and the simplified block can be expressed as (9) and (10).

$$G_M(s) = \frac{1}{L_m s} \qquad G_F(s) = \frac{1}{Z_F} \qquad K = \frac{E}{2V_z} \qquad \alpha_i = \frac{n_p}{n_s} \tag{9}$$

$$G(s) = G_M(s) - K\alpha_i G_F(s) \tag{10}$$

2.8.1 The standard relay control system analysis

Figure 30 represents a classic SRCS with invalid input, a linear and a nonlinear block. This system is constructed in this fashion due to the absence of a reference value $r(t)$ and the realization that the output of the linear part of the system is used as the input of the nonlinear part.

Figure 30 - Null input Standard Relay Control System

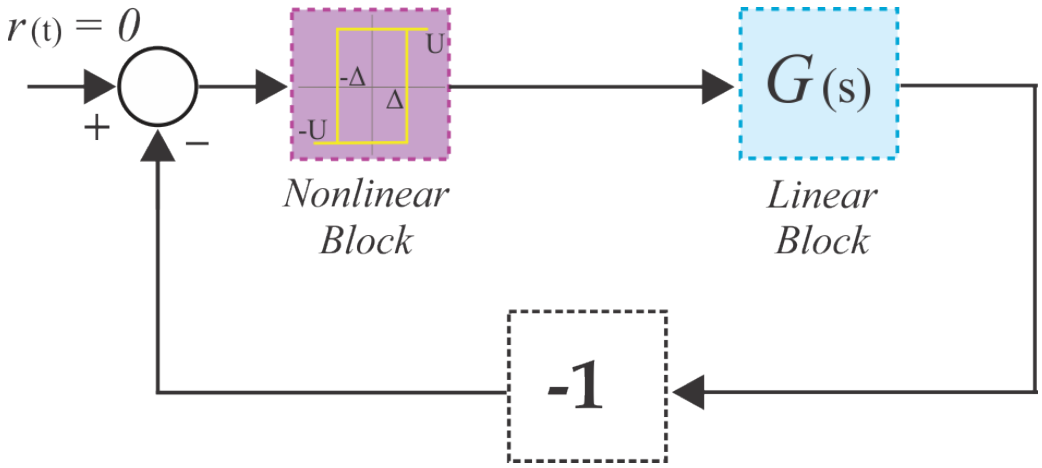

Source: Author

The starting point of analysis for self-oscillations is the same for every methodology and begins by assuming the existence of a limit cycle in the SRCS, and the output of the non-linear part of the system is of the type of that of $u(t)$ shown in Figure 31.

Figure 31 - Output "U" of the non-linear block of the system.

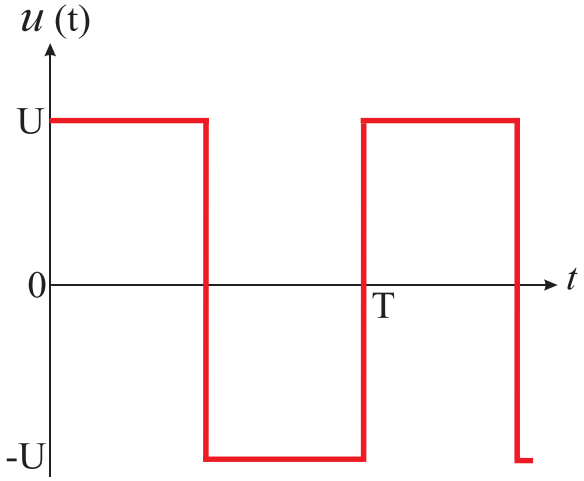

Source: Author

The waveform $u(t)$ is composed of the amplitude and period parameters, T and U of the ideal relay represented by the non-linear block, and can be represented by a Fourier series of (11) for an asymmetrical 0 to E type filter.

$$u(t) = \frac{2U}{\pi} \sum_{n=odd}^{\infty} \frac{1}{n} sen\left(n\omega t\right) \tag{11}$$

The period parameter is defined from the initial supposition of a limit cycle in the angular switching frequency ω equals $2\pi/T$, while the amplitude parameters depend on the relay's qualitative and quantitative characteristics. The analysis of the periodicity of $u(t)$ results in a set of equations known as switching conditions, which are the necessary conditions that grant the self-oscillation in the given frequency of analysis, given by (12) and (13). If we take the current filter i_p into account as an example, these equations dictate that every half period, the current assumes a value $-\Delta$, and its derivative is negative, i.e., it decreases to its negative semi-cycle.

$$e\left(\frac{\pi^{-}}{\omega}\right) = -\Delta \tag{12}$$

$$\dot{e}\left(\frac{\pi^{-}}{\omega}\right) < 0 \tag{13}$$

According to (JUDD; CHIRLIAN, 1974), taking the discontinuities of its waveform into account, the superposition principle can be used to multiply every iteration of $u(t)$ by the linear correspondent portion of the system on that frequency.

$$e\left(\frac{\pi^{-}}{\omega}\right) = \frac{2U}{\pi} \sum_{n=odd}^{\infty} \frac{1}{n} \mathrm{Im}\left[G\left(jn\omega\right)\right] \tag{14}$$

$$\dot{e}\left(\frac{\pi^{-}}{\omega}\right) = \frac{2U}{\pi} \omega \sum_{n=odd}^{\infty} \frac{1}{n} \mathrm{Re}\left[G\left(jn\omega\right)\right] - U \lim_{j\omega \to \infty} \left[j\omega G\left(j\omega\right)\right] \tag{15}$$

By replacing the switching conditions (12) and (13), equations (14) and (15) can be rewritten into (16) and (17).

$$-\frac{\pi\Delta}{2U} = \sum_{n=odd}^{\infty} \frac{1}{n} \mathrm{Im}\left[G(jn\omega)\right] \tag{16}$$

$$\frac{\pi}{2\omega} \lim_{j\omega\to\infty} \left[j\omega G(j\omega)\right] > \sum_{n=odd}^{\infty} \frac{1}{n} \mathrm{Re}\left[G(jn\omega)\right] \tag{17}$$

These equations represent the effect that the nonlinear part of the system has on the linear part while considering the switching conditions. They were extracted from the SRCS analysis with invalid input, which represents the operation of the self-oscillating command circuit. From this point, two distinct paths can be taken in regards to SORC design. It can either be considered that both the input and output of the linear part of the system have a sinusoidal low-pass characteristic, which considerably simplifies the design and leads us to the very well known analysis through the Describing Function Method; otherwise, given that there is no interest in the output of the linear part of the system, or the linear part does not have a low-pass characteristic, the unrestricted Tsypkin analysis can be used.

2.8.2 The Describing Function Method

The DFM (SEIDEL; BISOGNO; DO PRADO, 2007) is a linearization tool that simplifies the nonlinear block N into a linear static gain and equates it to $G(s)$ to find a solution for L_m. This linearization is performed through the relationship between the amplitude of the output U of N (V_z, in the case of the SORC) and the fundamental value of its input (i_{sw}), shown in Figure 32.

Figure 32 - Representation of the Input and Output of the Nonlinear Block for the Describing Function Method

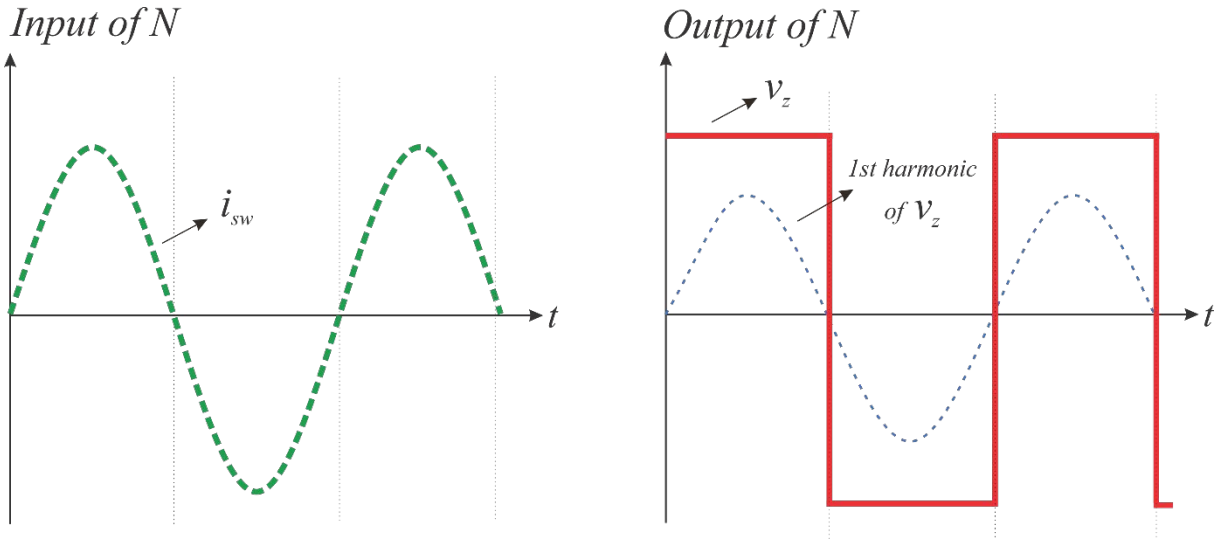

Source: Author

The precision of the DFM tends to be considerably reduced when i_p does not have a sinusoidal characteristic[24]. The DF technique can be used when the system may present a limit cycle, which is the case of the SORC. Furthermore, the DF can only be applied to periodic systems where the input of the linear part is assumed to have a low-pass filter characteristic. Thus, equation (17) is wholly disregarded in this aspect, while equation (16) holds the answer for the nonlinear block *N,* which can be linearized as **(**18).

$$-\frac{\pi\Delta}{2U}=\sum_{n=1}^{\infty}\frac{1}{n}\mathrm{Im}\left[G\left(jn\omega\right)\right] \quad \longrightarrow \quad N=\frac{2V_z}{\pi I_{sw}} \tag{18}$$

As a result of the DFM, the equality between the inverse negative of *N* must be equal to *G*(s). Hence G_M(s) can be isolated in the equation, resulting in the necessary value of L_m that self-oscillates in the required design frequency, expressed as (19).

$$G_M\left(s\right)=-\frac{\pi\cdot I_{sw}}{2\cdot V_z}+K\cdot\alpha_i\cdot G_F\left(s\right) \tag{19}$$

However, the DFM requires a low-pass filter behavior in the output to provide acceptable precision in the design. This is usually true when the SORC is designed around a single operating frequency on standard open-loop applications. Given that the main principle of the closed-loop SORC is to increase f_s to maintain the desired reference value, the filter tends to have increased reactance on a portion of the operating range, and the current tends to become less sinusoidal for higher frequencies. All this analysis leads us to the final intersection of the inverse negative of the DF and the linear part of the system given by the Extended Nyquist Criteria of (20), shown in Figure 33. From the intersection, the block of the magnetizing inductance in the linear part of the system can be isolated and solved to find the final value of L_m from the SOCC that grants the self-oscillation in the designed frequency.

$$1+K_iNG\left(j\omega\right)=0 \tag{20}$$

[24] This usually occurs when the designer choses an operating frequency considerably higher than filter`s resonant frequency, which imposes an inductive characteristic on the output. The filter current then ceases to be sinusoidal and the DFM tends to have its precision lowered.

Figure 33 – Final intersection between the linearized DF and the linear part of the system G(s).

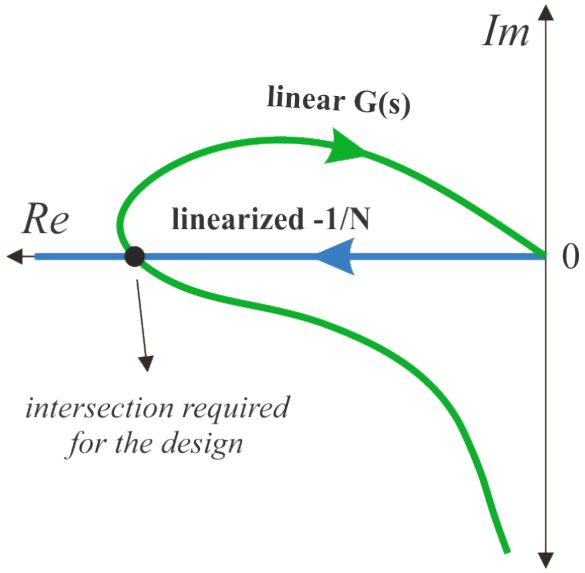

Source: Author

2.8.3 The Tsypkin Method

The Tsypkin method (CHANG; CHANG; BRUNING, 1999; DO PRADO *et al.*, 2000; JUDD; CHIRLIAN, 1974) differs from the DFM in the sense that there is no linearization of *N*. Instead, it focuses on illustrating, from a graphical point of view, the individual effects that every value assumed by the output of the nonlinear blocks has in the linear part of the system, *G*(s), not only the fundamental harmonic. In order to estimate this effect, this method uses the superposition principle, where the response of *G*(s) to the natural action of *N* equals the sum of the responses to every elementary action. A typical form of representing the output of *N* as a sum of harmonic components can be expressed as the square wave voltage applied to the resonant filter (21).

$$v_s(t) = \frac{2E}{\pi} \sum_{n=1,3}^{\infty} \frac{1}{n} \sin(n\omega t) \tag{21}$$

The method works conveniently on periodic systems, presenting a set of equations that characterize a sinusoidal signal, requiring only their values and its derivatives at specific critical points in frequency to be known to perform appropriately. These conditions, as stated by the author, are the necessary conditions for self-oscillation. There is no frequency restriction as a warranty of precision, as compared to the DFM. The classical Tsypkin equation is given by τ_{fn}

(22). This equation represents the periodicity of the SORC filter current by representing its value and its derivate on a given instant (in this case, in the half period π/ω).

$$\tau_{fn}(\omega) = -\frac{1}{\omega}\dot{i}_p\left(\frac{\pi}{\omega_S}\right) - ji_p\left(\frac{\pi}{\omega_S}\right) \tag{22}$$

From the SORC waveforms discussed in the previous sections, shown in Figure 6, i_p has a fixed value at $t = 0$, where its derivative is negative. The same occurs for t = $T/2$, with a positive derivative. These conditions must occur indefinitely for the self-oscillation of the SORC to be maintained. This fact delineates the analysis through Tsypkin's Locus, where ε is the output value of the linear part of the system at those given condition instants. Again, in the same way that was performed with SRCS analysis, the conditions of self-oscillation for the closed-loop SORC can be expressed as (23).

$$i_p(0) = -\varepsilon \quad \left.\frac{di_p(t)}{dt}\right|_{t=0} > 0 \quad i_p(T_s/2) = \varepsilon \quad \left.\frac{di_p(T_s/2)}{dt}\right|_{t=0} < 0 \tag{23}$$

Given the symmetry of i_p, the self-oscillating conditions can be simplified to (24).

$$i_p\left(\frac{\pi}{\omega_s}\right) = \varepsilon \qquad \left.\frac{di_p(t)}{dt}\right|_{t=\frac{\pi}{\omega_s}} < 0 \tag{24}$$

The graphically intuitive Tsypkin's analysis characterizes f_s by analyzing the periodicity of i_p on specific conditional instants, utilizing for that the harmonic representation for the voltage applied to the filter. The relationship between v_s and i_p is the input impedance (or its inverse, the admittance Y_{in}) of the SORC filter. The infinite Tsypkin Locus function τ_{fn} for the SORC can then be constructed as (25). This equation results in a series of points in what is known as the Tsypkin Locus in Figure 34, where the path the system takes regarding frequency can be observed.

$$\tau_{fn}(\omega) = \frac{2E}{\pi}\sum_{n=1,3}^{\infty}\mathrm{Re}\left\{Y\left[\left(j\omega(2n-1)\right)\right]\right\} + j\frac{2E}{\pi}\sum_{n=1,3}^{\infty}\mathrm{Im}\left\{\frac{Y\left[\left(j\omega(2n-1)\right)\right]}{2n-1}\right\} \tag{25}$$

Figure 34 – Various points of Frequency in the Tsypkin Locus and the Tsypkin Hodograph.

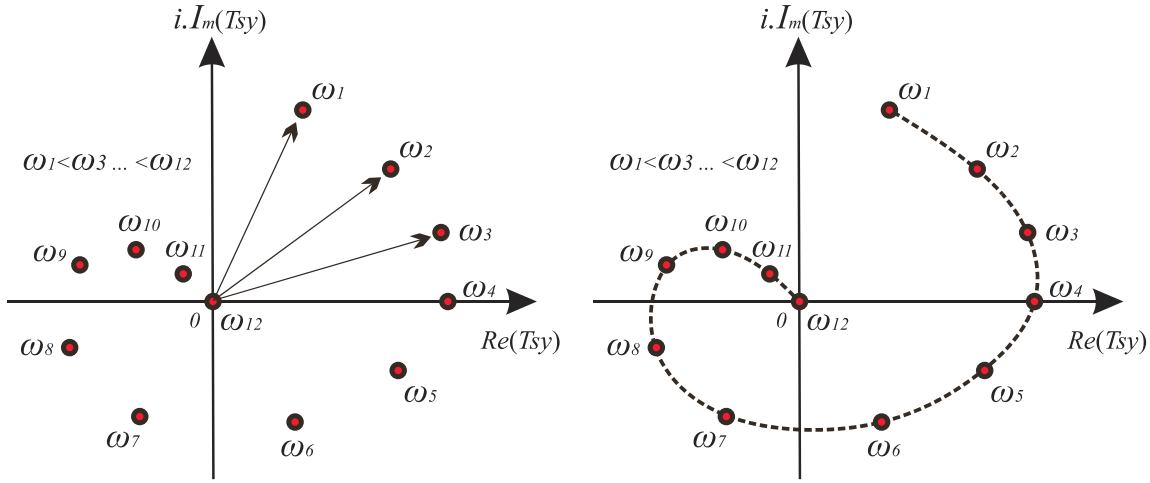

Source: Author

Similar to the DFM, the goal behind τ_{fn} applied to the SORC design is to find the value of L_m that self-oscillates the converter in the chosen f_s, providing as many input parameters as possible be known beforehand (such as input voltage, load, and filter parameters). From the SOCC waveforms, the parameter ε is related to the secondary current i_s through the turns ratio of the VCT, α_i, the Zener breakdown voltage, V_z, and L_m. The magnetizing inductance can then be expressed as (26).

$$L_m = \frac{\pi}{2}\frac{\alpha_i V_Z}{\omega|\varepsilon|} \tag{26}$$

The Tsypkin Locus allows the designer to establish a relationship between the filter input voltage, the self-oscillating frequency, the filter impedance, and the magnetizing inductance of the SORC over a wide range of frequencies. Most importantly, it provides a simple tool to estimate the value of L_m needed for the converter to self-oscillate on a given frequency. This tool is essential in the analysis of an actuator mechanism like the VCT, as the whole idea behind this device is to vary L_m, and hence the frequency, making this the preferred method for the analysis of the VCT closed-loop SORC, instead of the traditional DFM usually employed on the open-loop version.

The graphic from Figure 35 shows the Tsypkin Locus, where the X and Y-axis represent the real and imaginary parts of τ_{fn}, respectively, with ten harmonics of the square wave voltage being considered. Every marked angular frequency ω corresponds to a point in the complex plane related to. The parameter ε is the value of i_p when v_s changes state (self-oscillation),

proportional to the imaginary part of τ_{fn}, where the frequencies lower than f_0 (ω_4 in the graphic) cause the SORC to operate under capacitive characteristic with the absence of soft-switching. The SORC f_s is equal to f_0 when ε is equal to zero, at which point i_p would be consistently in phase with v_s for an ideal case. The operating region of the SORC is generally aimed towards values of ε slightly smaller than zero, where the filter has an inductive characteristic (such as ω_5 and ω_6).

Figure 35 - Tsypkin Locus for the SORC.[25]

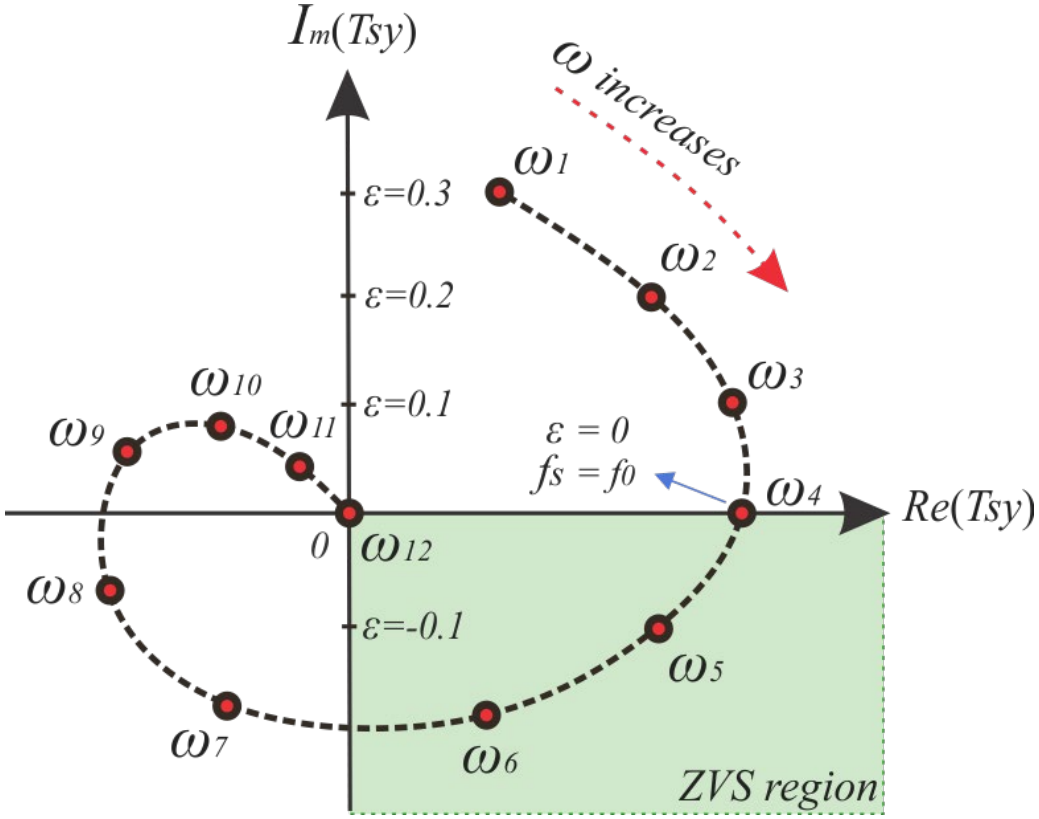

Source: Author

From the Tsypkin Locus, the values of L_m can be observed for each frequency value involved by the green ZVS region. With the SPICE model of the VCT from Figure 24, those values can finally be translated as values of I_{DC} that have to flow through the auxiliary windings of the VCT design. Furthermore, the detection of self-sustained frequencies is more trivial when the Tsypkin's hodographs are used. This fact becomes even more visible when resonant filters are analyzed. According to the author, self-sustained frequencies for non-linear self-oscillating

[25] The graphical analysis through this method also allows for an easy detection of the ZVS region of the converter, which in this case occurs for fs>f0.

systems will occur for Re(Tsy) > 0, which means that the path taken by the hodrograph may contain an infinite number of self-sustained frequencies for the SORC. In Figure 35, for example, there are many stable frequencies between the resonant frequency ω_4 and the frequency ω_6[26].

Another technique employed to investigate the existence of limit cycles in relay systems is the Hamel Locus. By the same time that Tsypkin proposed the limit cycle analysis through his technique, Hamel proposed a similar time domain. Both techniques have a remarkable similarity, where the same conditions for the existence of limit cycles are used, and the output of the nonlinear part of the system is represented in the time domain, while Tsypkin proposed the representation through the Fourier Series in the frequency domain. In fact, according to (JUDD, 1975), the existence of limit cycles from Tsypkin can be obtained from the Hamel Locus through a transformation using the Poisson Formula. Furthermore, even though there is a considerable similarity, the Tsypkin Method seems more precise in higher frequencies. This can be observed from the Poisson Formula, which shifts the weight in the infinite sum of the nonlinear part u(t) output from low frequency to high-frequency terms. In terms of precision, it can be said that all the methods complement each other well. As for the DFM stands in between both techniques, having acceptable precision for all frequencies, as long as the linear part of the system maintains its low-pass characteristic.

[26] After frequency ω_6 occurs, just as the hodograph starts leaving the positive part of the real axis to become negative, interestingly the Z transphorm method shown in (DO PRADO *et al.*, 2000) can attest to the system loss in stability, as the roots of the equation that grants stability to the system are no longer contained within the unit circle.

3

SMALL-SIGNAL MODELING OF AN LC SERIES SELF-OSCILLATING RESONANT CONVERTER

This chapter present the small-signal analysis (SSA) of the LC series Self-Ocillating Resonant Converter (LC-SORC) utilized for powering a string of LEDs, however, the equations for a system operating with generic resistive loads are also provided. The modeling process of the LC-SORC consists on identifying and analyzing the several individual stages and processes involved in the addition of an external control loop to a converter with an intrinsic positive-type feedback, which includes the application of the Extended Describing Function (EDF) method, proposed as a systematic SSA approach to nonlinear switching circuits, being is precisely the case of the LC-SORC. A comparison between the simulation and proposed model indicates that the model exhibits high accuracy in capturing the dynamic behavior of the LC-SORC, making it a suitable and reliable tool for modeling this specific converter. A further comparison with the LSM method used on Chapter II is also performed.

3.1 INTRODUCTION

A SSA is a simplified representation of a nonlinear circuit or system that allows for the analysis of its linear behavior around an operating point. Commonly used in electrical engineering to analyze the response of electronic devices and circuits to evaluate small perturbations or signals superimposed on a steady-state operating condition, it linearizes the circuit equations around the operating point. The small-signal model provides a linear approximation that simplifies the analysis of the system's behavior and facilitates the design and optimization of various electronic systems. This allows designers to understand how the circuit or system responds to small variations, enabling them to evaluate stability, frequency response, and other important performance characteristics in order to design the controller for the external current control loop.

In the context of the research presented in this doctoral dissertation, the focus lies on the investigation of an LC-SORC for the purpose of supplying and regulating current to a string of LEDs. Unlike traditional Integrated Circuit Driven (ICD) voltage-controlled converters, the DC/DC LC-SORC is a current-controlled system with a non-traditional command circuit that uses an intrinsic feedback from the resonant filter, where the precise control and management of current flow assume paramount significance. Consequently, the load model assumes a critical role in accurately capturing the dynamic behavior and characteristics of the converter when inferring about the SSA.

The load model represents the electrical behavior of the LEDs connected to the DC/DC LC-SORC and is crucial for the small-signal analysis process. Since the converter's primary function is to regulate the current supplied to the LED string, an accurate representation of the load is essential to assess the converter's performance in terms of stability, frequency response, and other key parameters. The model takes into consideration factors such as the electrical characteristics of the LEDs, i.e., their voltage-current relationship and any nonlinear behavior exhibited. To achieve a comprehensive understanding of the system's small-signal behavior, it becomes imperative to incorporate an appropriate load model that accurately represents the LED string's electrical behavior under small perturbations.

By integrating an accurate load model into the small-signal analysis of the DC/DC LC-SORC, the identification of potential stability issues becomes feasible, as well as to optimize control strategies, and ultimately enhance the overall efficiency and reliability of the LED lighting system. Therefore, the selection and utilization of an appropriate load model play a crucial role in facilitating a comprehensive and insightful small-signal analysis of the DC/DC

LC-SORC in this study. However, as the focus of this research is on the modeling and control of a self-oscillating resonant converter, the accuracy of the individual modeling of the inverter plus load, *per se* is not the primary concern, albeit being an already discussed topic in the literature with paramount importance. Instead, equations that model the system using the behavior of both LED PWL models and generic resistance loads will be provided in the analysis, allowing for a more comprehensive understanding of the system as a whole.

One one of the major contributions proposed on this chapter is the identification of the individual parts that compose the DC/DC LC-SORC and their respective analysis and modeling. The modeling of the the inverter corresponds to one out of four subjects that generate a required TF. The other parts are the VCT, with two resulting TFs, and the relationship between the SOCC magnetizing inductance and the self-oscillating frequency, that generate the last TF. When put together, these four pieces form the general TF that relate small variations in the output current to small variations in the control signal.

3.2 CHOICE BETWEEN LC, LCC AND LLC TOPOLOGY

The choice between an LC, LCC and LLC resonant converter can depend on several factors. According to the stability analysis on Chapter II, the LCC topology presents frequent stability issues when used on a modulated SORC for lower resistance values and higher values of Q, so the LCC filter is the first neglected topology. One advantage of the LLC topology over the LC topology besides isolated outputs is that the two physical inductors can often be integrated into one physical component, including both the series resonant inductance, L_r, and the transformer's magnetizing inductance, L_m (HUANG, 2010).

The paper in (NI; CHUNG; CHAN, 2013) analyses the difference between LC parallel and series resonant topology in wireless power transfer. The authors find that on the transmitter side, the voltage source in parallel resonant mode is interchangeable with the current source in series resonant mode, under a certain transfer equation, in such a way to have the same output status. And on the receiver end, the topology selection is proven to be related to the load. For heavy load, the parallel topology has more advantages, while for light load; the series topology is the preferable one, but no extra remarks were made in regards to advantages of one over the other. The findings summarized by the author, however, are in accordance to the findings originated from the filter stability analysis, where higher resistive values for the load are more advantageous for the series topology.

On applications involving LED as loads, one advantage of using an LC series resonant converter over an LLC is the simplicity it adds to the modeling of a converter with self-oscillating command. An LC series resonant converter has a simpler circuit topology compared to an LLC resonant converter, which can make it easier to model and analyze, given that the performance of the topology is considerably straightforward when as it usually operates slightly above the resonant frequency. This simplicity can be particularly beneficial to the focus of this doctoral dissertation, which is to accurately model the full DC/DC LC-SORC, due to the designing of the self-oscillating command, as it can simplify the design process and reduce the complexity of the control system. On the cons side, using an LC series resonant converter infers the inability to provide an output voltage that is higher than the input voltage, which makes it not desirable in high voltage applications. Additionally, in case of light load or no-load condition, it can be difficult to control the output voltage (SALEM *et al.*, 2018). Another disadvantage is that LC series resonant converters may not be as efficient as other topologies such as LLC resonant converters, which can result in higher power losses and reduced performance.

In summary, depending on the load type and its electrical characteristics, a DC/DC SORC can be implemented with either one of the LC, LCC or LLC filters. However, in doctoral dissertation, the use of an LC filter on the self-oscillating resonant converter in the SSA will be maintained as it can provide a more accurate SSA not only for performance optimization, but to more easily understand the role that the SOCC has in the modeling feasibility and accuracy. By using a more linear filter, it is possible to provide a better accurate analysis of the impact of every individual part that compose the whole system.Furthermore, it provides the adequate electrical characteristics to the load without needing an extra reactive element. However, should the need arise for a DC/DC LLC or LCC SORC SSA, further discussions on this chapter should provide the required tools for such endeavor, primarily through the application of the EDF on the LLC-SORC as seen in (MENKE *et al.*, 2020), or other discussed tools such as the Average State-Space analysis or the Least-Squares Method of linearization.

3.3 AN OVERVIEW OF THE COMPLETE SYSTEM

The complete LC-SORC is depicted in Figure 36. The common startup circuit used on SORCs is required but its representation can be neglected for the ongoing analysis as it doesnt effect the system at all. The primary objective of the analysis is to derive the control-to-output

transfer function that relates small variations on i_{LED} to the control signal u_c (if a BJT is used) or the control current I_{Ctrl} using the SSA. Although SSA has been previously applied and proposed in the literature for traditional resonant of both LC and LLC configurations as seen in (MENKE *et al.*, 2020; TIAN *et al.*, 2015; YANG; LEE; JOVANOVIC, 1992), for both generic resistive loads and PWL linear model LEDs, this study presents a comprehensive modeling of a self-oscillating type resonant converter that employs the VCT as an actuation mechanism for reference following.

Figure 36 – Schematic representing an overview of the complete analyzed LC-SORC.

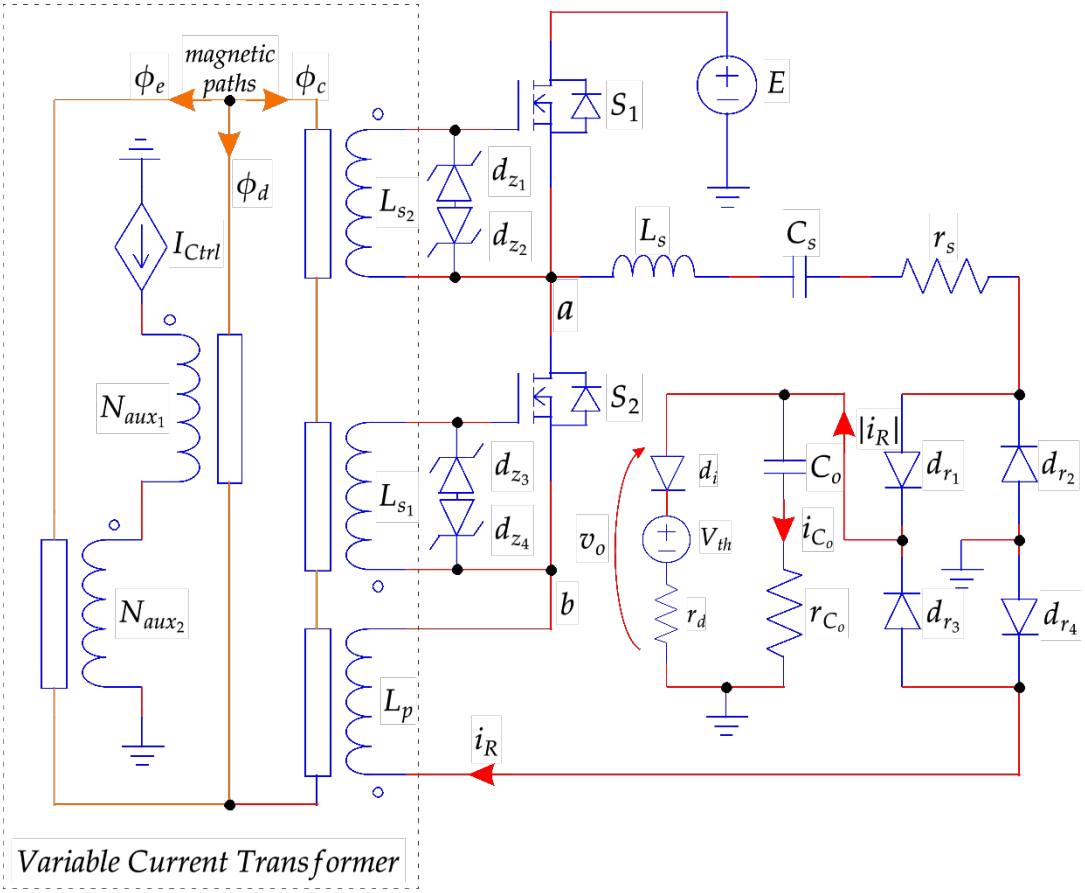

Source: Author.

To achieve this goal, several parts that compose the system as a whole need to be investigated. In essence, the current flowing through the LED string, denoted as I_{LED}, must be regulated to follow a predefined reference value. This control is achieved by injecting a control current, I_{Ctrl}, through the auxiliary windings of the VCT, which alters the equivalent inductance of the SOCC. This variation in inductance directly modulates the self-oscillating frequency of the system, thereby changing I_{LED}. Therefore, it is necessary to first comprehend how small variations in I_{Ctrl} influence the magnetizing inductance L_m. Secondly, how minor changes in L_m

affect the self-oscillating frequency and finally, to examine how I_{LED} responds to changes in the self-oscillating frequency.

With the addition a BJT to implement the control signal u_c, Figure 37 shows a scope of what the final TF resulting from the modeling looks like. The first TF I_{Ctrl}/u_c is related to the BJT dynamic and how the control current behaves on small variations of a controlling signal. The second TF L_m/I_{Ctrl} dictates the dynamic of the proposed VCT by analysing how the equivalent magnetizing inductance varies in accordance to the control current from the previous TF. The third TF f/L_m is a purely based on how the self-oscillating frequency behaves upon small changes on the aforementioned magnetizing inductance. And the last FT I_{LED}/f illustrates the dynamic behind the relationship between the output current and the self-oscillating frequency.

Figure 37 – Final Transfer Function composed from other four individual Transfer Functions

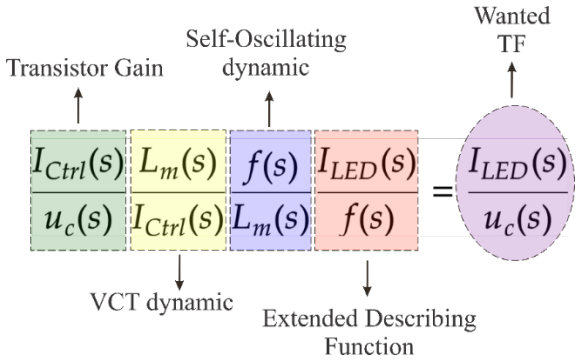

Source: Author

Figure 38 – The Variable Current Transformer with a bias circuit controlled by a BJT through u_C.

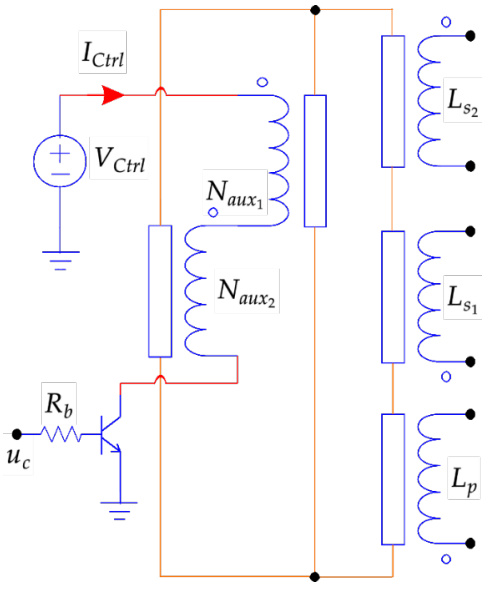

Source: Author

For the SSA analysis of the BJT portion, (WILSON, [*s. d.*]) briefly discusses the small signal model for the common emitter transistor. It explains how the diode is replaced with a linear element (a resistor, called r_π) and the changes in notation. In (HU, 2010), a full chapter presents the theory of the bipolar transistor I-V characteristics, including current gain and output conductance analysis. High-level injection and heavy doping induced band narrowing are introduced. Several bipolar transistor models are introduced, including the *Ebers–Moll* model, charge control model, and especially the small-signal model. An important parameter related to this analysis is the trans-conductance g_m, defined as the change in the collector current divided by change of the base-emitter voltage. When using a signal u_c at the base of a BJT to control the current flowing through its output, (MARCOS ALONSO *et al.*, 2016a) summarizes the exact requirements that are adequate to the system, where its imperative that the level of voltage V_{Ctrl} is kept low enough to ensure minimal losses. It should, however, also be high enough to enable the bipolar transistor to regulate the bias current i_b based on the control voltage u_c applied to the transistor's base circuit. Thus, the transfer function that relates I_{Ctrl} to u_c is given by (27). This equation represents a static gain based on the illustrated parameters, which is valid for the current case given that the dynamic of the remaining TFs is considerably slower. The input impedance and forward current gain of the bipolar transistor are represented by h_{ie} and h_{fe} respectively. The resistance in series with the base of the device is R_b.

$$\frac{i_{Ctrl}(s)}{u_c(s)} = \frac{h_{fe}}{R_b + h_{ie}} \tag{27}$$

Figure 39 shows results of I_{LED} for different values of a DC u_c signal with the system operating in open-loop for testing purposes of the effect of the VCT actuation mechanism on I_{LED}. The first interesting point illustrated is the voltage jump between 0 and 0.9 V on u_c required by the bias voltage to start performing variations on the output. After the bias point, considerably small variations on u_c cause sizeable decreases on I_{LED}, which depend on the input impedance, forward current gain of the transistor, and R_b. The next interesting point illustrated is the relationship between, u_c and I_{LED} and both its value and ripple. As u_c increases, I_{Ctrl} increases and, as the following sections will show, the equivalent magnetizing inductance of the SORC L_m decreases, increasing f_s. The increases in f_s naturally translate into smaller ripple values for V_{LED} and I_{LED}.

Figure 39 – The LED string current I_{LED} for different values of the control signal u_c.

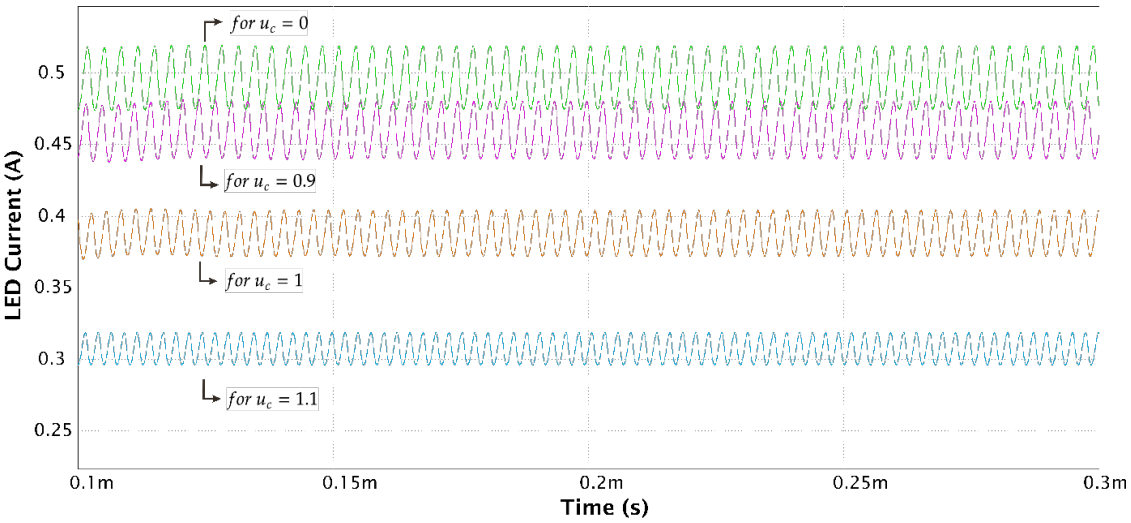

Source: Author

3.4 VARIABLE CURRENT TRANSFORMER SMALL SIGNAL ANALYSIS

After defining $i_{Ctrl}(s)/u_c(s)$, the next step is to delve further into the dynamic characteristics of the chosen magnetic actuator, the VCT. Considering that the first auxiliary winding N_{aux1} has a resistance of R_{aux1}, and N_{aux2} has a resistance of R_{aux2}, the sum of both resistances, namely R_{auxT}, along with the total equivalent inductance of both windings, L_{auxT} has a major impact in the dynamic response of the VCT device due to their time constant.

In a VCT, there are three possible magnetic paths for the flux. The main path, braced by all three SOCC windings, and two secondary paths, each braced by one auxiliary winding and electrically connected in series (PERDIGAO *et al.*, 2016). The flowing of I_{Ctrl} through these auxiliary windings generate a DC flux density in each of the auxiliary magnetic paths with a magnitude B_b that effectively produces a change in the inductance of the main AC magnetic windings of the SOCC. This change on inductance due to B_b, however, is vastly faster than the dynamic pre-imposed on the auxiliary windings by I_{Ctrl} flowing through L_{auxT} and R_{auxT}. Therefore, the VCT analysis is greatly simplified by neglecting the dynamic of the material itself by neglecting the B_b dynamic (MARCOS ALONSO *et al.*, 2016a). Thus, the transfer function becomes (28) and with k_{lb} in (29).

$$\frac{L_m(s)}{I_{Ctrl}(s)} \approx k_l \frac{B_b}{I_{Ctrl}(s)} = \frac{k_l k_{lb}}{1 + s\frac{L_{auxT}}{h_{oe}^{-1} + R_{auxT}}} \tag{28}$$

$$k_{lb} = \frac{h_{oe}^{-1}}{h_{oe}^{-1} + R_{auxT}} \frac{L_{auxT}}{N_b A_b} \tag{29}$$

Where A_b is the effective area of the DC bias magnetic path and k_l is slope of the characteristic VI inductance versus DC magnetic flux at the given steady state operating point.

3.5 INVERTER STAGE SMALL-SIGNAL ANALYSIS

A paper recently published in (LONG; CHEN, 2023) discusses the small signal modeling of an LLC converter with an LED load and a quasi-resonant controller based active ripple rejection. The paper analyzes the defects of the traditional extended description function (EDF) based LLC small signal modeling method when driving an LED load and preents an accuracy improvement method. Detailed small signal model modeling methods have been deduced, and the accuracy of different modeling methods has been compared thoroughly. Although the SORC analyzed in this doctoral dissertation is attached to the LC series topology, this paper presents an interesting discussion point on future analysis involving SORC with LLC.

A paper published in (LIN; CHEN, 2009) presents equivalent circuit models for the LEDs, including the piece-wise linear model (PWL), DC model and small-signal model. In order to characterize the equivalent circuit model of the LEDs, a PWL model is built by adopting the superposition concept of the multi-branch equivalent circuit model. Furthermore, in order to perform the DC and small-signal analysis of the LEDs, the equivalent DC and small-signal resistance are derived from the piece-wise linear model.

In (MENKE *et. al.*, 2019) the authors discuss that for a reliable small-signal model of the LLC LED driver, the equivalent PWL circuit of the LED has to be considered under some conditions throughout the model development.

The author in (MENKE *et al.*, 2020) shows as 20 dB difference, in terms of dynamic behavior, between the control-to-output TF frequency response of an LLC resonant LED driver when the PWL is used, and when a simple equivalent resistance R_{eq} is used, highlighting the need to take into account the LED electrical behavior when modeling the LLC resonant converter. Thus, the author proceeds to model the proposed converted using a methodology presented in (CHANG *et al.*, 2012), however instead of using the equivalent LED resistance R_{eq}, the dynamic model for the LLC resonant LED driver now uses the LED PWL model.

In terms of dynamic behavior, it is imperative to understand beforehand the effects that the LED PWL model has on the control-to-output TF (u to I_{LED}) in order to properly perform the SSA.

In terms of steady-state analysis, it is important to note that the steady-state operating point of the converter also plays an important role on the determination of the small-signal response (VORPERIAN; CUK, 1983). In this analysis, equations will ultimately be derived both for loads that are pure equivalent resistive loads R_L, as well as for the PWL LED. However, it should be noted that when considering that the LED's threshold voltage V_{TH} is equal to zero, the LED dynamic resistance r_D should be equal to R_L, thus the usage for both is straightforward. In the following sections, the difference between using one or the other type of load will be briefly highlighted presenting the tools for ultimately designing an LC-SORC with either one. Figure 40 shows the schematic diagram of the LC series resonant converter where the bus voltage as well as MOSFETs have been omitted, represented instead through an asymmetric square wave voltage.

Figure 40 – Simplified schematic diagram of the the LC series resonant converter supplying an R_L or LED load.

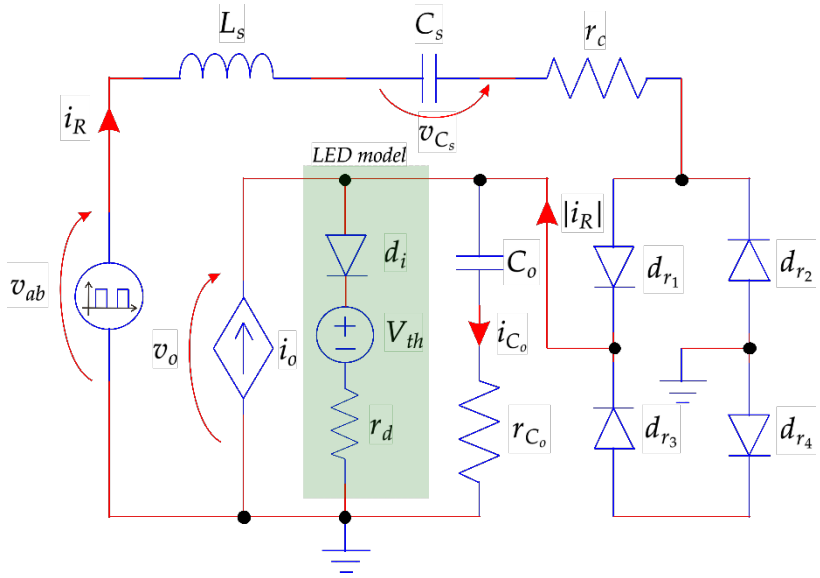

Source: Author

3.5.1 Nonlinear State-Space Equations

Applying the KVL for the portion that extends from the resonant to the rectifying stage, results in the expressions given by.

$$v_{ab}(t) = v_{Cs}(t) + L_s\frac{di_R(t)}{dt} + sgn(i_R(t))v_o(t) \tag{30}$$

The current flowing through the capacitor C_s is given by (31).

$$i_R(t) = C_s\frac{dv_{Cs}(t)}{dt} \tag{31}$$

The current flowing through the output filter capacitor C_o in (33) is given by the sum of the output current and the current flowing out of the rectifier in (32).

$$i_o(t) + |i_R| = C_o\frac{dv_{Co}(t)}{dt} + \frac{v_o(t)}{R_L} \tag{32}$$

$$i_{Co}(t) = |i_R| + i_o(t) - \frac{v_o(t)}{R_L} \tag{33}$$

Applying KVL to the output portion of the rectifier results in the output voltage represented in (34).

$$v_o(t) = i_{Co}(t)r_{Co} + v_{co}(t) \tag{34}$$

By using (33) and substituting in (34), $v_o(t)$ is (35) with r_o being (36).

$$v_o(t) = (|i_R| + i_o(t))r_o + v_{Co}(t)\frac{r_o}{r_{Co}} \tag{35}$$

$$r_o = \frac{r_{Co}R_L}{r_{Co} + R_L} \tag{36}$$

3.5.2 Harmonic Approximation

Three state variables can be identified from the aforementioned equations, namely i_R, v_{Cs} and v_{Co}. These quantities are associated with the resonant inductance, resonant capacitance and the output filter capacitance. Under steady-state operation, i_R and v_{Cs} and are assumed to be nearly sinusoidal. This enables us to approximate their magnitudes by their fundamental terms using Fourier series expansion principle. The Fourier series is commonly used to decompose these periodic signals into a sum of sines and cosines.

Usually, any quantity varying in time, namely $h(t)$, can be represented as (37).

$$h(t) = a_0 + \sum_{k=1}^{\infty}[a_k cos(k\omega_s t) + b_k sin(k\omega_s t)] \tag{37}$$

If only the first harmonic (k=1) is considered while neglecting both the fundamental and superior order harmonics, the resulting equation represents the varying quantity (38).

$$h(t) = a_1 cos(\omega_s t) + b_1 sin(\omega_s t) \tag{38}$$

This representation can be applied to the state variables i_R, v_{Cs}, becoming the sum of sines and cosines given by (39) and (40), where ω_s is the angular switching frequency of the LC-SORC and $v_c(t)$, $v_s(t)$, $i_c(t)$ and $i_s(t)$ are the components' amplitudes, which are considered to be slowly varying in time. This assumption allows for the derivation of the dynamic equivalent model.

$$v_{c_s}(t) = v_c(t) cos(\omega_s t) + v_s(t) sin(\omega_s t) \tag{39}$$

$$i_R(t) = i_c(t) cos(\omega_s t) + i_s(t) sin(\omega_s t) \tag{40}$$

Differentiating (39) and (40) with respect to time yields (41) and (42).

$$\frac{dv_{c_s}(t)}{dt} = \frac{dv_c(t)}{dt} cos(\omega_s t) - v_c(t)\omega_s sin(\omega_s t) + \frac{dv_s(t)}{dt} sin(\omega_s t) + v_s(t)\omega_s cos(\omega_s t) \tag{41}$$

$$\frac{di_R(t)}{dt} = \frac{di_c(t)}{dt} cos(\omega_s t) - i_c(t)\omega_s sin(\omega_s t) + \frac{di_s(t)}{dt} sin(\omega_s t) + i_s(t)\omega_s cos(\omega_s t) \tag{42}$$

3.5.3 Derivation of the Extended Describing Functions

By considering small-signal variations in input voltage E, switching frequency f_s, and duty cycle D, the EDF method provides a comprehensive understanding of the converter's behavior. To effectively capture the nonlinearity present in the system's state-space equations, an essential step in the modeling process involves representing the nonlinear terms through approximated slowly varying terms. This is achieved by employing the EDF concept, which approximates the nonlinear terms $v_{Cs}(t)$, $i_R(t)$ and $v_{Cf}(t)$ using their fundamental sine and cosine components or DC terms. What sets the EDF apart from its predecessor, the Describing Function, is its ability to consider multiple inputs and outputs, as opposed to just a single input. These approximations, known as EDFs, are derived by calculating Fourier expansions for the nonlinear terms. Let $v_{ab}(t)$ be a function of d and E represented in (43).

$$v_{ab}(t) = f_1(d, E) sin(\omega_s t) \tag{43}$$

Also, let sgn($i_R(t)$)v_{LED} be a sum of functions that depend on the sinusoidal and co-sinusoidal counterparts as in (44).

$$sgn(i_R(t))v_{LED} = f_2(i_s, i_c, v_{Co})sin(\omega_s t) + f_3(i_s, i_c, v_{Co})cos(\omega_s t) \tag{44}$$

These functions, denoted as f_1, f_2 and f_3, are called EDF of the nonlinearities. By providing a proportionality between the variables, it is possible to predict the operating point of the converter and have an insight of the behavior of the harmonics of the state variables v_{Cs} and i_R.

For function that contains the behavior of the square wave applied to the resonant filter, only the first harmonic is of interest given the band-pass characteristic of the LC filter. Thus, f_1 can be expressed as (45).

$$f_1(d, E) = \frac{2}{\pi} sin\left(\frac{\pi}{2} d\right) E \tag{45}$$

The functions f_2 in (46) and f_3 in (47) rely on the current flowing from the resonant filter through the rectifier and the voltage effectively observed across the output. These functions can be expressed as the root mean square (rms) values of the voltage across the rectifier's output terminals. To account for the influence of the rectified current, they are formulated in terms of i_s, i_c, and i_p, considering that 4/π factor accounts to the amplitude of the fundamental component of the v_{ab} voltage across the rectifier input terminals. The current i_p is shown in (48).

$$f_2(i_s, i_c, v_{Co}) = \frac{4}{\pi} \frac{i_s}{i_p} v_{Co} \tag{46}$$

$$f_3(i_s, i_c, v_{Co}) = \frac{4}{\pi} \frac{i_c}{i_p} v_{Co} \tag{47}$$

$$i_p = \sqrt{i_s^2 + i_c^2} \tag{48}$$

3.5.4 Harmonic Balance

The harmonic balance method is a technique employed in the frequency domain to determine the steady-state response of nonlinear differential equations (SHAIK; KANKANALA, 2012). By considering that the small-signaldulation frequency is lower than

the switching frequency, the converter's behavior during steady-state operation can be analyzed. The harmonic balance approach involves substituting the equations obtained from harmonic approximation (41) and (42), together with the EDF parameters in (43) to (48) into the nonlinear steady state equations (30) to (36) followed by equating the coefficients of sine, cosine, and DC terms. This process yields the harmonic balance solution, also known as the nonlinear large-signal model of the LC-RC, defined by equations (49) through (53) .

$$L_s\left(\frac{di_c}{dt}+\omega_s i_s\right)+i_c r_s+v_c+\frac{4}{\pi}\frac{v_{Co}i_c}{i_p}v_{Co}=0 \tag{49}$$

$$L_s\left(\frac{di_s}{dt}-\omega_s i_s\right)+i_s r_s+v_s+\frac{4}{\pi}\frac{v_{Co}i_s}{i_p}v_{Co}=\frac{2}{\pi}sin\left(\frac{\pi}{2}d\right)E \tag{50}$$

$$C_s\left(\frac{dv_s}{dt}-\omega_s v_c\right)=i_s \tag{51}$$

$$C_s\left(\frac{dv_c}{dt}+\omega_s v_s\right)=i_c \tag{52}$$

$$C_o\frac{dv_{C_o}}{dt}=\frac{2}{\pi}i_p+i_o-\frac{v_o}{R_L} \tag{53}$$

3.5.5 Steady-state analysis

The next crucial step in the analysis process is to examine the system in its steady-state before proceeding to the small-signal analysis. This is because the small-signal analysis can only be conducted once the steady-state solution of the system has been determined under a specific operating point for $\{E, f_s, d, i_o\}$. As a result of analyzing the system under the steady-state assumption, the DC analysis is obtained. In this state, a new set of state variables is introduced, including i_C, i_S, v_C, v_S, and v_{Co}. Rewritting equations (49) to (53) as in (54) through (58).

$$L_s\left(\frac{dI_c}{dt}\right)=-L_s I_s\omega_s-r_s I_c-V_c-\frac{4}{\pi}\frac{v_{Co}I_c}{I_p} \tag{54}$$

$$L_s\left(\frac{dI_s}{dt}\right)=\frac{2}{\pi}sin\left(\frac{\pi}{2}d\right)E+L_s I_c\omega_s-r_s I_s-V_s-\frac{4}{\pi}\frac{v_{Co}I_s}{I_p} \tag{55}$$

$$C_s\left(\frac{dV_c}{dt}\right) = I_c - C_s\omega_s V_s \tag{56}$$

$$C_s\left(\frac{dV_s}{dt}\right) = I_s + C_s\omega_s V_c \tag{57}$$

$$C_o\left(\frac{dV_{C_o}}{dt}\right) = \frac{2}{\pi}I_p - \frac{v_o}{R_L} \tag{58}$$

Additionally, it is important to note that the output DC bias current i_o is equal to zero, as are the derivatives of the new set of state variables. Hence, considering di_C/dt, di_S/dt, dv_C/dt, dv_S/dt and dv_{Co}/dt equal to zero, and substituting in equations (54) to (58) now considering that v_{Co}(t) is approximately equal to v_0(t), the new set of equations is presented in (59) through (63) considering that the load is a generic resistance R_L.

$$-L_s I_s \omega_s - r_s I_c - V_c - \frac{4}{\pi}\frac{V_{Co} I_c}{I_p} = 0 \tag{59}$$

$$\frac{2}{\pi}sin\left(\frac{\pi}{2}d\right)E + L_s I_c \omega_s - r_s I_s - V_s - \frac{4}{\pi}\frac{V_{Co} I_s}{I_p} = 0 \tag{60}$$

$$I_c - C_s\omega_s V_s = 0 \tag{61}$$

$$I_s + C_s\omega_s V_c = 0 \tag{62}$$

$$\frac{2}{\pi}I_p - \frac{v_0}{R_L} = 0 \tag{63}$$

Now, considering that the load is assumed to be a string of LEDs instead of an equivalent resistance R_L, the PWL equation of the LED at the given operating point is dictated by (64).

$$V_{LED} = r_d I_{LED} + V_{TH} \tag{64}$$

The following set of equations (65) through (73) is then obtained, called Harmonic Balance Equations (HBE) which when solved, gives the steady state point of operation of the converter. Equations (65) through (67) are generally applied independently of the load type. Equations (68) through (70) are interchangeable with (71) through (73) depending on the load type, where the first set is used for the LED PWL model, and the latter is used for an R_L. An interesting fact is the similarity between equations (68) and (71). A resistance R_L as load is basically the dynamic resistance r_D of an LED PWL model with V_{TH} equal to zero. Thus, if $V_{TH} = 0$, then $R_L = r_D$ and both equations are one and the same.

$$I_C = C_s \omega_S V_S \tag{65}$$

$$I_S = -C_s \omega_S V_S \tag{66}$$

$$I_P = \sqrt{I_C^2 + I_S^2} \tag{67}$$

$$V_{LED} = \frac{2 I_P r_d}{\pi} + V_{TH} \tag{68}$$

$$L_s \omega_S I_C + V_S + I_S r_s + \frac{8 r_d I_S}{\pi^2} + \frac{4 I_S V_{TH}}{\pi I_P} = \frac{2E}{\pi} \tag{69}$$

$$-L_s \omega_S I_S + V_C + I_C r_s + \frac{8 r_d I_C}{\pi^2} + \frac{4 I_C V_{TH}}{\pi I_P} = 0 \tag{70}$$

$$V_O = \frac{2 I_P R_L}{\pi} = V_{C_f} \tag{71}$$

$$L_s \omega_S I_C + V_S + I_S r_s + \frac{8 R_L I_S}{\pi^2} = \frac{2E}{\pi} \tag{72}$$

$$-L_s \omega_S I_S + V_C + I_C r_s + \frac{8 R_L I_C}{\pi^2} = 0 \tag{73}$$

3.5.6 Small-signal model formulation: Perturbation and Linearization of the Harmonic Balance Equations

The small-signal formulation analyzes the behavior of the system when it undergoes small changes in its operating conditions. This is achieved by linearizing the system's components and expressing them as a linear model. By perturbing the system's state equations around their operating point presented through the HBE and applying the small-signal variation assumption, it is possible to understand how the system responds to small variations in its input and output signals. This approach is particularly useful for designing a control scheme that can maintain constant output parameters in the presence of variations in the input voltage or load. Such parameter maintenance, in the case of the LC-SORC, is performed through frequency modulation by injecting a DC current through the auxiliary windings of the VCT. In this section, in order to differentiate the small-signal analysis from the steady-state and previous developments, the input signals are e_I (input voltage), d_T (duty cycle), ω_S (switching frequency), and i_O (output current). State variables are denoted as i_C, i_S, v_C and v_S. Equation (74) represents the small-signal perturbations around the steady-state parameters.

$$\begin{aligned} e_I &= E + \hat{e} \\ d_T &= D + \hat{d} \\ \omega_S &= \omega_s + \widehat{\omega_s} \\ i_O &= I_o + \widehat{i_o} \\ v_O &= V_O + \widehat{v_o} \\ i_C &= I_c + \widehat{i_c} \\ i_S &= I_s + \widehat{i_s} \\ v_C &= V_c + \widehat{v_c} \\ v_S &= V_s + \widehat{v_s} \end{aligned} \tag{74}$$

Taking into account the formulation from (65) through (73) on their large-signal non-linear form and performing the linearization around the operating point under the assumption that only the first harmonic term is relevant, it is possible to obtain, under the small-signal assumptions, the relevant differential equations, given by (75) through (80).

$$\frac{d\widehat{i_c}}{dt} = \frac{1}{L_s}\left[L_s\left(I_S\widehat{\omega_s} + \widehat{i_s}\omega_S\right) - r_s\widehat{i_c} - \widehat{v_c} - \frac{4}{\pi}\frac{\widehat{v_{C_o}}I_C}{I_P}\right] \tag{75}$$

$$\frac{d\widehat{i_s}}{dt} = \frac{1}{L_s}\left[\frac{2}{\pi}sin\left(\frac{\pi}{2}d\right)\hat{e} + 2Ecos\left(\frac{\pi}{2}d\right)\hat{d} + L_s\left(I_C\widehat{\omega_s} + \widehat{i_c}\omega_S\right) - r_s\widehat{i_s} - \widehat{v_s} - \frac{4}{\pi}\frac{\widehat{v_{C_o}}I_S}{I_P}\right] \quad (76)$$

$$\frac{d\widehat{v_c}}{dt} = \frac{1}{C_s}\left[\widehat{i_c} - C_s\left(V_S\widehat{\omega_s} + \widehat{v_s}\omega_S\right)\right] \quad (77)$$

$$\frac{d\widehat{v_s}}{dt} = \frac{1}{C_s}\left[\widehat{i_s} + C_s\left(V_C\widehat{\omega_s} + \widehat{v_c}\omega_S\right)\right] \quad (78)$$

$$\frac{d\widehat{v_{C_o}}}{dt} = \frac{1}{C_o}\left[\frac{\widehat{i_s}I_P}{\pi I_S} + \frac{\widehat{i_c}I_P}{\pi I_C} - \frac{\widehat{v_{C_o}}}{R_L} + \widehat{i_o}\right] \quad (79)$$

$$\widehat{v_o} = \frac{\widehat{i_s}I_P}{\pi I_S} + \frac{\widehat{i_c}I_P}{\pi I_C} + \frac{\widehat{v_{C_o}}r_o}{r_{C_o}} + \widehat{i_o}r_o \quad (80)$$

The next step involves expressing the above differential equations in matrix format. In their general format, the form of a transfer matrix is (81).

$$\begin{aligned}\frac{d\hat{x}}{dt} &= A\hat{x} + B\hat{u}\\ \hat{y} &= C\hat{x} + D\hat{u}\end{aligned} \quad (81)$$

Where the state vectors and output vectors for R_L and LEDs are, respectively, x, u_R and u_{LED} (82).

$$\vec{x} = \begin{bmatrix}\widehat{i_c}\\ \widehat{i_s}\\ \widehat{v_c}\\ \widehat{v_s}\\ \widehat{v_o}\end{bmatrix} \quad \overrightarrow{u_R} = \begin{bmatrix}\hat{e}\\ \hat{d}\\ \widehat{\omega_s}\\ \widehat{i_o}\end{bmatrix} \quad \overrightarrow{u_{LED}} = \begin{bmatrix}\hat{e}\\ \hat{d}\\ \widehat{\omega_s}\\ \widehat{v_{th}}\end{bmatrix} \quad (82)$$

Then, for a generic load R_L, the complete system is represented by (83) and (84). Compressed parameters for clarity of representation are highlighted on (85) through (94).

$$\begin{bmatrix} \frac{d\hat{i}_c}{dt} \\ \frac{d\hat{i}_s}{dt} \\ \frac{d\hat{v}_c}{dt} \\ \frac{d\hat{v}_s}{dt} \\ \frac{d\hat{v}_o}{dt} \end{bmatrix} = \begin{bmatrix} \frac{-r_s}{L_s} & -\omega_s & \frac{-1}{L_s} & 0 & \frac{-G_{vco}}{L_s} \\ \omega_s & \frac{-r_s}{L_s} & 0 & \frac{-1}{L_s} & \frac{-H_{vco}}{L_s} \\ \frac{1}{C_s} & 0 & 0 & -\omega_s & 0 \\ 0 & \frac{1}{C_s} & \omega_s & 0 & 0 \\ K_{ic} & K_{is} & 0 & 0 & \frac{-1}{R_L C_o} \end{bmatrix} \begin{bmatrix} \hat{i}_c \\ \hat{i}_s \\ \hat{v}_c \\ \hat{v}_s \\ \hat{v}_o \end{bmatrix} + \begin{bmatrix} 0 & 0 & -I_S & 0 \\ K_1 & 2K_2 & I_C & 0 \\ 0 & 0 & -V_S & 0 \\ 0 & 0 & -V_C & 0 \\ 0 & 0 & 0 & \frac{1}{C_o} \end{bmatrix} \begin{bmatrix} \hat{e} \\ \hat{d} \\ \hat{\omega}_s \\ \hat{i}_o \end{bmatrix} \tag{83}$$

$$\begin{bmatrix} \hat{v}_o \end{bmatrix} = \begin{bmatrix} \frac{I_P r_o}{\pi I_C} & \frac{I_P r_o}{\pi I_S} & 0 & 0 & r_o \end{bmatrix} \begin{bmatrix} \hat{i}_c \\ \hat{i}_s \\ \hat{v}_c \\ \hat{v}_s \\ \hat{v}_o \end{bmatrix} + \begin{bmatrix} 0 & 0 & 0 & \frac{r_o}{r_{C_o}} \end{bmatrix} \begin{bmatrix} \hat{e} \\ \hat{d} \\ \hat{\omega}_s \\ \hat{i}_o \end{bmatrix} \tag{84}$$

$$H_{is} = \frac{4V_{LED}}{\pi} \frac{I_C^2}{I_P^3} \tag{85}$$

$$H_{ic} = \frac{-4V_{LED}}{\pi} \frac{I_C I_S}{I_P^3} \tag{86}$$

$$H_{vco} = \frac{4}{\pi} \frac{I_S}{I_P} \tag{87}$$

$$G_{is} = \frac{-4V_{LED}}{\pi} \frac{I_C I_S}{I_P^3} \tag{88}$$

$$G_{ic} = \frac{4V_{LED}}{\pi} \frac{I_S^2}{I_P^3} \tag{89}$$

$$G_{vco} = \frac{4}{\pi} \frac{I_C}{I_P} \tag{90}$$

$$K_{is} = \frac{2}{\pi}\frac{I_S}{I_P} \tag{91}$$

$$K_{ic} = \frac{2}{\pi}\frac{I_C}{I_P} \tag{92}$$

$$K_1 = \frac{2}{\pi} sin\left(\frac{\pi}{2}d\right) \tag{93}$$

$$K_2 = Ecos\left(\frac{\pi}{2}d\right) \tag{94}$$

Finally, the complete representation for an LC-RC employing LEDs as load is given by (95) and (96).

$$\begin{bmatrix} \frac{d\hat{i}_c}{dt} \\ \frac{d\hat{i}_s}{dt} \\ \frac{d\hat{v}_c}{dt} \\ \frac{d\hat{v}_s}{dt} \\ \frac{d\hat{v}_o}{dt} \end{bmatrix} = \begin{bmatrix} \frac{-(r_s + H_{is})}{L_s} & \frac{-(L_s\omega_s + H_{ic})}{L_s} & \frac{-1}{L_s} & 0 & \frac{-H_{vco}}{L_s} \\ \frac{L_s\omega_s - G_{is}}{L_s} & \frac{-(G_{ic} + r_s)}{L_s} & 0 & \frac{-1}{L_s} & \frac{-G_{vco}}{L_s} \\ \frac{1}{C_s} & 0 & 0 & -\omega_s & 0 \\ 0 & \frac{1}{C_s} & \omega_s & 0 & 0 \\ \frac{K_{is}r_d}{C_o(r_d + r_o)} & \frac{K_{ic}r_d}{C_o(r_d + r_o)} & 0 & 0 & \frac{-1}{C_o(r_d + r_o)} \end{bmatrix} \begin{bmatrix} \hat{i}_c \\ \hat{i}_s \\ \hat{v}_c \\ \hat{v}_s \\ \hat{v}_o \end{bmatrix} + \begin{bmatrix} \frac{K_1}{L_s} & \frac{K_2}{L_s} & -I_C\omega_0 & 0 \\ 0 & 0 & \omega_0 I_S & 0 \\ 0 & 0 & -\omega_0 V_C & 0 \\ 0 & 0 & \omega_0 V_S & 0 \\ 0 & 0 & 0 & \frac{1}{C_o(r_d + r_o)} \end{bmatrix} \begin{bmatrix} \hat{e} \\ \hat{d} \\ \hat{\omega}_s \\ \hat{v}_{th} \end{bmatrix} \tag{95}$$

$$\left[\widehat{v_o}\right] = \begin{bmatrix} \frac{K_{is}r_{oc}}{r_d} & \frac{K_{ic}r_{oc}}{r_d} & 0 & 0 & \frac{1}{r_s r_d} \end{bmatrix} \begin{bmatrix} \widehat{i_c} \\ \widehat{i_s} \\ \widehat{v_c} \\ \widehat{v_s} \\ \widehat{v_o} \end{bmatrix} + \begin{bmatrix} 0 & 0 & 0 & \frac{-1}{r_s r_d} \end{bmatrix} \begin{bmatrix} \hat{e} \\ \hat{d} \\ \widehat{\omega_s} \\ \widehat{v_{th}} \end{bmatrix} \quad (96)$$

In a system represented by state-space equations, where the circuit is essentially a model based on differential equations, the matrix A describes the relationship between the state variables and their derivatives. The input matrix B, relates the derivative of the state variables to the inputs and control variables, such as e and ω_S, respectively. The matrix C connects the states to the output of the converter, while the direct transmission matrix, D, represents elements that transmit input directly to the system's output. The two loops in the model of Figure 41 correspond to the sinusoidal and co-sinusoidal components of the small-signal state equations, where the upper loop is driven by the current i_s and represents the sinusoidal component of state equations, while the bottom loop represents the co-sinusoidal component i_c. It is important to note that the eigenvalues of matrix A correspond to the poles of the linearized state-space matrix for an LC resonant converter operating around a specific steady-state condition. Their position in the complex plane can be analyzed to investigate the dynamic behavior of the system. Compressed parameters for ease of representation are shown in (97) through (109).

Figure 41 - Small-signal model of the LC series Resonant Converter

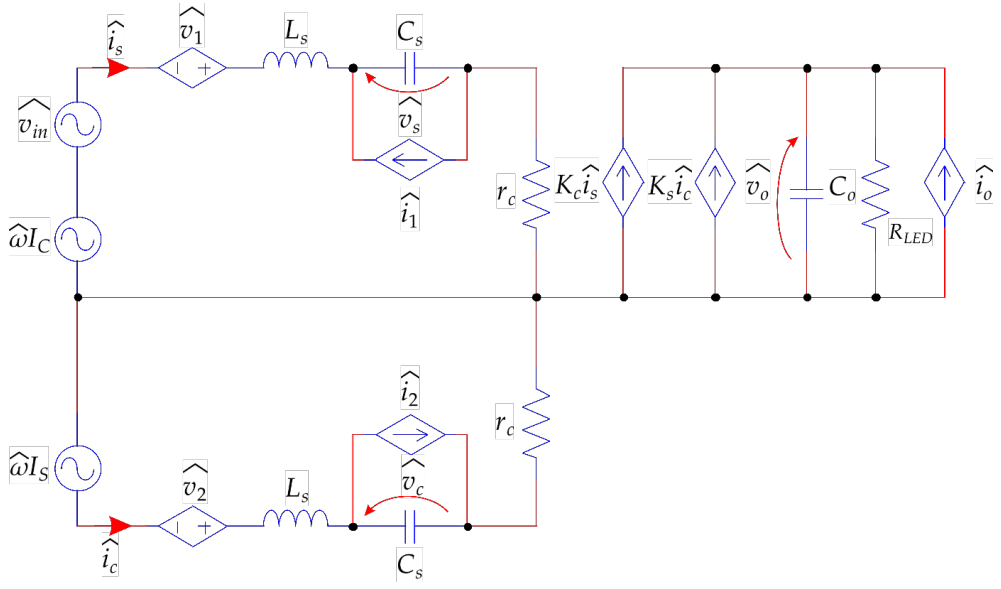

Source: Author

$$Z_L = \omega_s L_s \tag{97}$$

$$Z_C = \frac{1}{\omega_s C_s} \tag{98}$$

$$K_c = \frac{I_P}{\pi I_S} \tag{99}$$

$$K_s = \frac{I_P}{\pi I_C} \tag{100}$$

$$G_{cos} = L_s I_C \tag{101}$$

$$G_{sin} = L_s I_S \tag{102}$$

$$J_{cos} = C_s V_C \tag{103}$$

$$J_{sin} = C_s V_S \tag{104}$$

$$\widehat{v_{in}} = \frac{4}{\pi} sin\left(\frac{\pi}{2}d\right)\hat{e} + Ecos\left(\frac{\pi}{2}d\right)\hat{d} \tag{105}$$

$$\widehat{v_1} = -Z_L\widehat{i_s} - \frac{4I_C}{\pi I_P}\widehat{v_{C_o}} \tag{106}$$

$$\widehat{v_2} = Z_L\widehat{i_s} - \frac{4I_S}{\pi I_P}\widehat{v_{C_o}} \tag{107}$$

$$\widehat{i_1} = -Z_C\widehat{v_c} - J_{sin}\widehat{\omega_s} \tag{108}$$

$$\widehat{i_2} = Z_C\widehat{v_s} + J_{cos}\widehat{\omega_s} \tag{109}$$

As a secondary remark, but nonetheless still important is the interaction between the switching frequency and the natural resonant frequency of resonant states results in a phenomenon known as beat frequency dynamics (VORPERIAN; CUK, 1983). This interaction

cannot be studied using the averaging concept, as it eliminates information about the switching frequency. In (YANG; LEE; JOVANOVIC, 1992) proposed an equivalent circuit model for SRC based on small-signal modeling results obtained through the extended describing function concept which is precisely the methodology used in this research to construct an accurate model to obtain one of several parts that compose the LC-SORC. This model accurately captures beat frequency dynamics and is as precise as the describing function result. However, its major drawback is its higher order: it is a fifth-order circuit due to the presence of five energy storage elements. Nevertheless, it has been shown that a third-order circuit is sufficient to describe small-signal behavior (SUN; GROTSTOLLEN, 1993). Therefore, in (TIAN *et al.*, 2015) the author aims to leverage the accurate results of the equivalent circuit model presented in (YANG; LEE; JOVANOVIC, 1992) while addressing its shortcomings. Two main objectives are achieved: the first is simplifying the small-signal equivalent circuit model of SRC to a third-order circuit that is both simpler and accurate enough to predict beat frequency dynamics, and the second is providing analytical expressions for all transfer functions to aid engineers in designing feedback loops. The equivalent small-signal model is shown in Figure 42. This model is relevant when beat frequency dynamics are observed as present in the system and a the transfer functions that relate the output to control parameters are of orders higher than the required for the design.

Figure 42 - Small-signal equivalent LC series resonant converter as seen in (TIAN *et al.*, 2015).

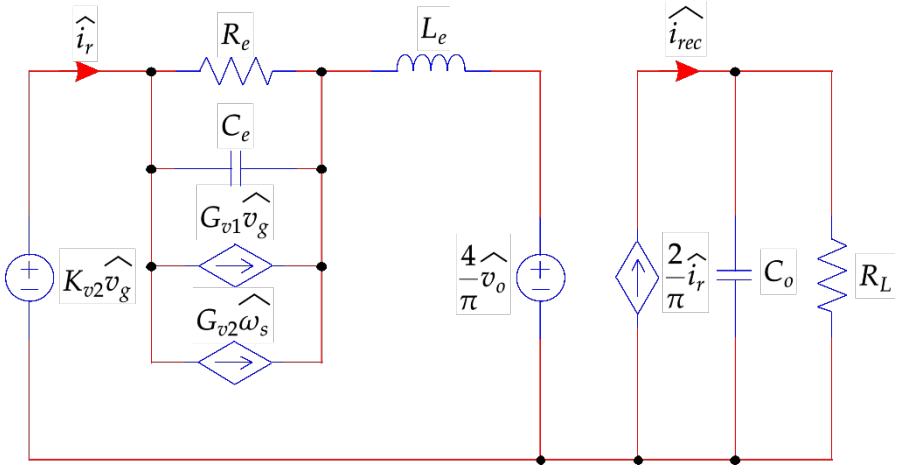

Source: (TIAN *et al.*, 2015)

The expressions to calculate the model are represented from (110) to (121). The control to output TF resulted from the analysis are shown in (122) and (123).

$$L_e = L\left(1 + \frac{\Omega_o^2}{\Omega_s^2}\right) \tag{110}$$

$$C_e = \frac{1}{L_e(\Omega_s - \Omega_o)^2} \tag{111}$$

$$R_e = \frac{L_e|X_{eq}||\Omega_s - \Omega_o|}{R_{eq}} \tag{112}$$

$$Q_{beat} = \frac{2}{\pi}\frac{1}{\sqrt{\frac{L_s}{C_o}}} \tag{113}$$

$$X_{eq} = \Omega_s L_s - \frac{1}{\Omega_s C_s} \tag{114}$$

$$R_{eq} = R_L\frac{8}{\pi^2} \tag{115}$$

$$G_d = -\frac{4}{\pi}\frac{V_g}{\Omega_s\sqrt{X_{eq}^2 + R_{eq}^2}}\frac{\Omega_s^2 + \Omega_o^2}{\Omega_s^2 - \Omega_o^2} \tag{116}$$

$$G_{v1} = \frac{2}{\pi}\frac{X_{eq}}{\Omega_s\sqrt{X_{eq}^2 + R_{eq}^2}} \tag{117}$$

$$K_{v2} = \frac{4}{\pi}\frac{R_{eq}}{\Omega_s\sqrt{X_{eq}^2 + R_{eq}^2}} \tag{118}$$

$$\omega_{beat} = \frac{2}{\pi}\frac{1}{\sqrt{L_s C_o}} \tag{119}$$

$$K_d = -\frac{E}{\Omega_s}\frac{R_{eq}}{\sqrt{X_{eq}^2 + R_{eq}^2}}\frac{\Omega_s^2 + \Omega_o^2}{\Omega_s^2 - \Omega_o^2}X_{eq}^2 \tag{120}$$

$$K_v = \frac{R_{eq}}{\sqrt{X_{eq}^2 + R_{eq}^2}} \tag{121}$$

$$\frac{\widehat{v_{LED}}}{\widehat{\omega_S}} = \frac{K_d}{\left(s^2 L_e^2 + sL_e R_{eq} + X_{eq}^2\right)(1 + R_L C_o s) + R_{eq}(sL_e + R_{eq})} \tag{122}$$

$$\frac{\widehat{v_{LED}}}{\hat{e}} = \frac{K_v(R_{eq^2} + X_{eq^2} + L_e R_{eq} s)}{\left(s^2 L_e^2 + sL_e R_{eq} + X_{eq}^2\right)(1 + R_L C_o s) + R_{eq}(sL_e + R_{eq})} \tag{123}$$

From the previous analysis that resulted in the matrixes A, B, C and D that compose the classical state space representation, the TF of interest can be extracted using (124) for further analysis with softwares like Matlab and PSIM. The TF shown has the information about the dynamic behavior of I_{LED} related to every input parameter (E, D, f_s and V_{th}). Hence, in order to generate the TF that relates small variations on I_{LED} due to f_s from the state space parameters, the Matlab command would be `ss2tf(Ap,Bp,Cp,Ep,3)`.

$$G_P(s) = C(sI - A)^{-1}B + D \tag{124}$$

3.6 SIMULATION RESULTS

Figure 43 shows the schematic diagram on PSIM used for the AC Sweep simulation of the LC series RC. This simulation is used to provide a comparison between magnitude and phase of the bode diagrams of both simulated and modeled systems.

Figure 43 - Schematic diagram of the LC RC on PSIM for AC Sweep simulation.

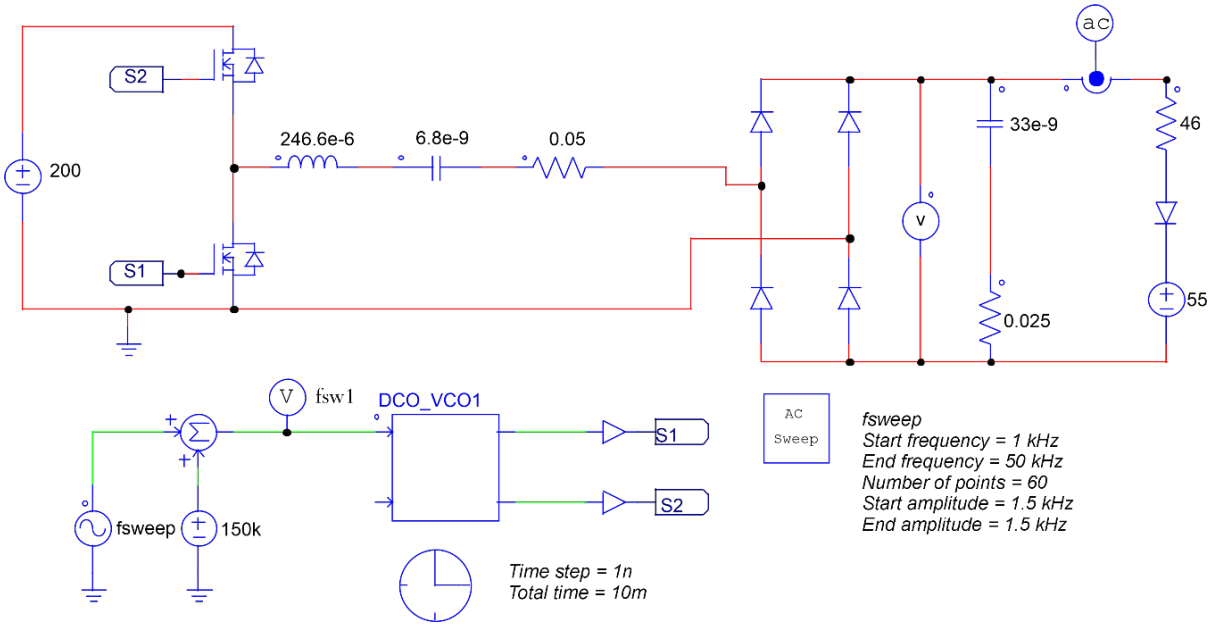

Source: Author

Using the `ss2tf(Ap,Bp,Cp,Ep,3)` command from Matlab yields (125).

$$G_P(s) = \frac{-2.215e8s^3 - 2.687e17s^2 - 3.57e23s - 2.298e29}{1s^5 + 1.144e6s^4 + 3.512e12.s^3 + 2.835e18.s^2 + 7.716e23.s + 1.27e29} \quad (125)$$

On PSIM, the comparison of the AC sweep from both the converter and the resulting TF G_P(s) are shown in Figure 44.

Figure 44 - Bode diagram of the LC series resonant converter comparing simulated and modeled Transfer Functions.

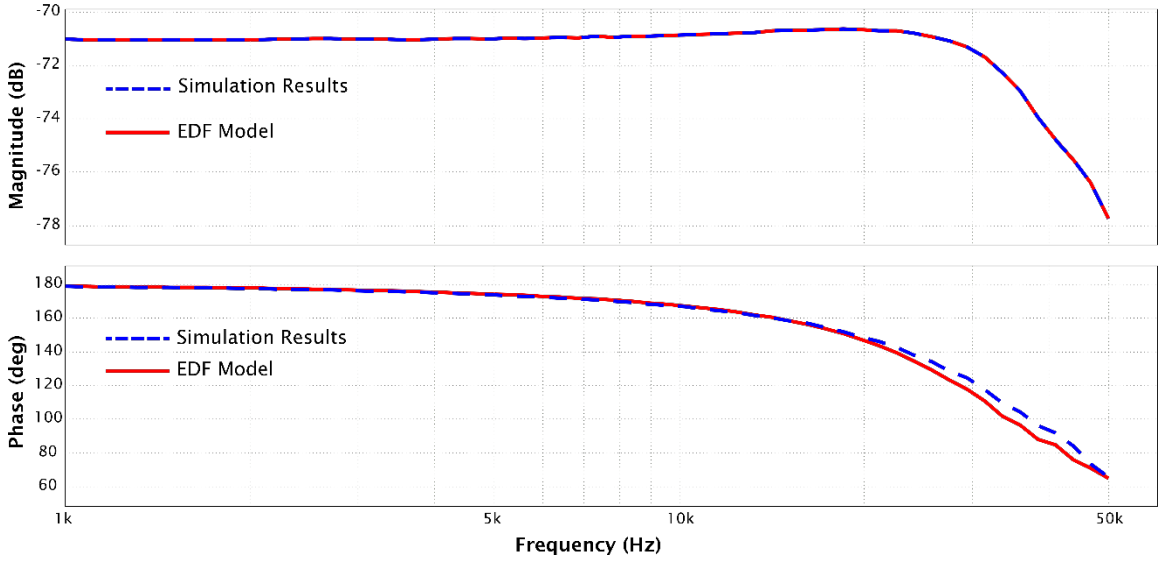

Source: Author

Applying a perturbation of 5 and -5 kHz on the PSIM simulation on both the converter and the resulting model as a comparison is shown in Figure 45.

Figure 45 - LC Series resonant converter output current dynamic response comparing simulated converter and modeled transfer function (C_o = 33 nF).

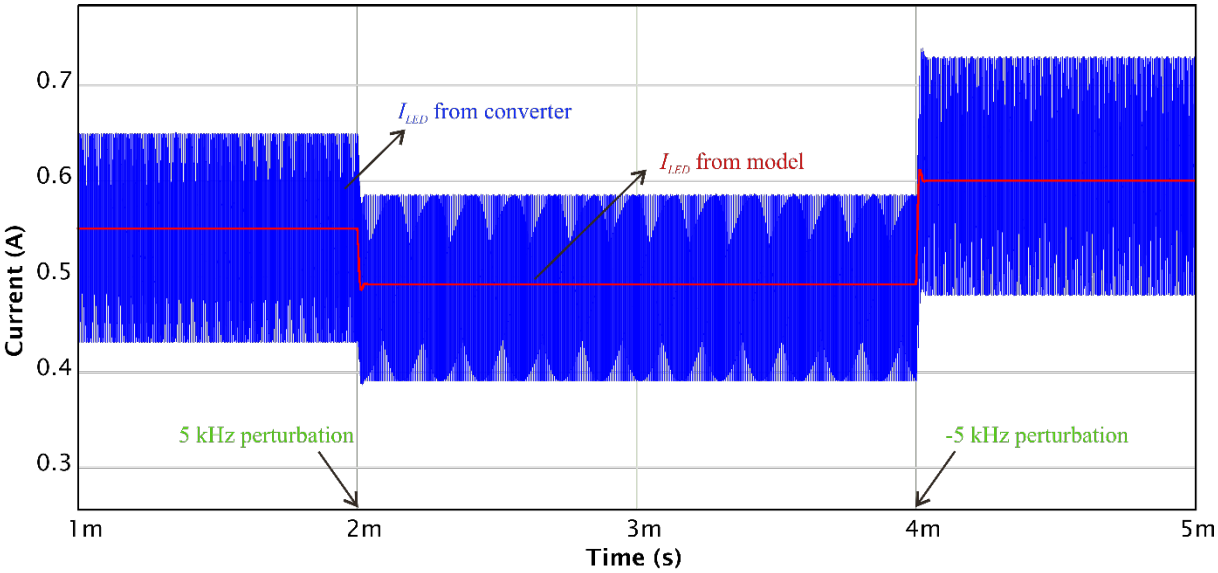

Source: Author

Increasing the output filtering capacitance C_o from 33 nF to 400 nF results in the dynamic of Figure 46, maintaining good accuracy between mathematical model and converter simulation despite seemingly introducing a small error on the representation of the new overshoot of a larger output filtering capacitor. In the presented analysis, it is interesting to note how accurate the model calculated through EDF is to the PSIM simulation, even on switching points higher than the resonant frequency. In (MENKE *et al.*, 2020), despite using a considerably more complex filter represented by the LLC resonant converter, interesting remarks that contemplate any filter topology are made regarding the effect of increasing r_d values for the LED string. The author analyses the frequency response of the system with a parametric sweep on r_d and concludes that, the higher the difference between r_d and the equivalent R_L, the higher the error between both approaches.

Figure 46 - LC Series resonant converter output current dynamic response comparing simulated converter and modeled transfer function (C_o = 400 nF).

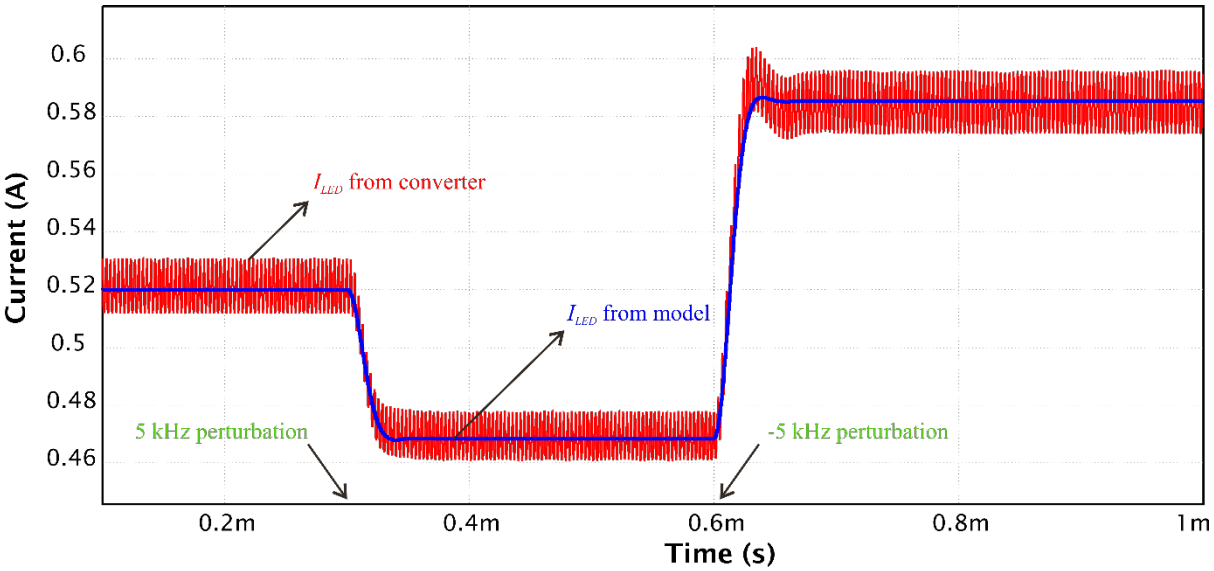

Source: Author

3.7 THE SELF-OSCILLATING L_M TO F_S DYNAMIC

The self-oscillating L_m to f_s dynamic is the final model required to obtain the complete i_{LED} to u_c TF. Recalling Chapter II, considering a standard SORC with only its intrinsic positive feedback, then the magnetizing inductance L_m is an important parameter that translates into the designed switching frequency, and results from the analysis of the SORC using the DFM and the ENC. For an LC-SORC that has an extra control loop for reference following, however, L_m is variable, and may assume a wide range of values depending on the required magnetizing inductance to achieve a certain frequency. The control of i_{LED} through u_c involves varying f_s through L_m, which means that in order to operate as a reference follower and disturb rejection over a given frequency range, all the L_m values need to be known within that range[27]. Adding to that, and assuming that the MOSFETs input capacitance starts affecting the values of L_m on frequency ranges higher than 100 kHz (MENKE *et al.*, 2015), a '*for*' loop using Python and the previously presented EDF and ENC equations provides an interesting graphical overview of the behavior of f_s versus L_m.

[27] In order to keep the output controlled within a certain bus voltage range, the switching frequency also needs to operate within a certain range. This frequency variation is achieved by the VCT that provides values for L_m based on the controlling signal u_c.

Figure 47 - Graphical representation of L_m versus f_s for cases considering and neglecting the effect of C_{gs}.

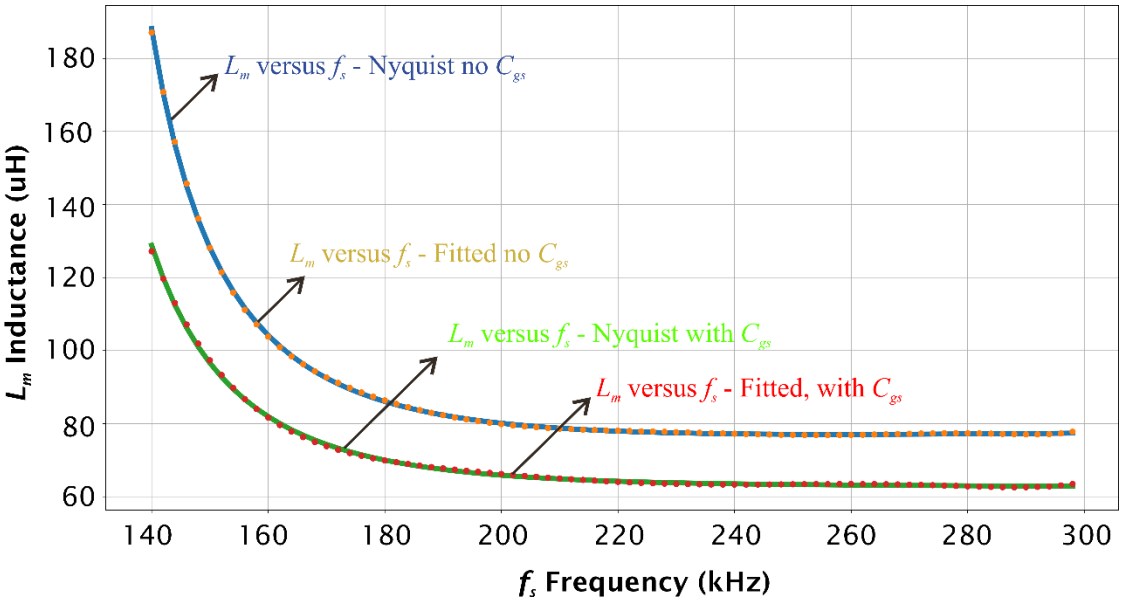

Source: Author

The dynamic of f_s versus L_m can be analyzed through this graphic under the assumption that f_s responds to L_m[28] significantly faster than the other dynamics present in the system, such as i_{LED}/f_s. Thus, the TF is a gain calculated by the slope of the characteristic f_s versus L_m. On the discussed graphic are also presented the fitted polynomial equations[29] that represent the relationship between L_m and f_s parameters for both cases, with and without C_{gs}, making it straightforward to calculate the slope by deriving the resulting polynomial and replacing f_s around the steady state operating point. Recalling the complete TF that describes the system's dynamic around the steady state point shown in (126).

$$\frac{I_{LED}(s)}{u_c(s)} = \frac{I_{Ctrl}(s)^{I}}{u_c(s)} \frac{L_m(s)^{II}}{I_{Ctrl}(s)} \frac{f(s)^{III}}{L_m(s)} \frac{I_{LED}(s)^{IV}}{f(s)} \tag{126}$$

Transfer Function I was described as gain acquired through the input impedance, forward current gain of the BJT h_{ie}, and h_{fe} respectively, as well as the resistance in series with the base of the device, R_b. To obtain TF II, the change on inductance due to B_b was considered

[28] Due to the intrinsic feedback characteristic of the SORC, varying L_m causes the frequency to change just as fast as being already increased or decreased within the next switching period.

[29] Using python and the *numpy* library, through commands `numpy.polyfit(`f_s`,` L_m`, order)` and `numpy.poly1d`, using a 6th order polynomial.

to be much faster than the dynamic pre-imposed on the auxiliary windings by I_{Ctrl} flowing through L_{auxT} and R_{auxT}, allowing for the calculation of the respective TF. Transfer Function III has also been considered as a gain calculated through the slope of the characteristic f_s versus L_m around the steady state operating point given the slower dynamic of the remaining TFs. And finally, TF IV has been obtained through the EDF, where the model has been compared to simulation in both AC Sweep and transient scenarios. It should be noted that the equivalent resistance of a singular LED operating point was used to construct the L_m and f_s behavior, and different regions of a PWL graphic should result in an offset in the graphic of Figure 47. That is, if a complete PWL model is to be considered, a more complex set of equations that model the L_m and f_s behavior should be used, where instead of a line on the previous graphic, a 'region' should instead be presented with a large number of matches between L_m, f_s and the corresponding equivalent resistance at the output of the resonant filter.

Using the complete system's schematic diagram from Figure 48 and comparing its simulation to the newly generated mathematical model of the full system yields Figure 49.

Figure 48 - Complete LC-SORC schematic diagram simulated on PSIM comparing i_{LED} from the system and from the modeled transfer functions.

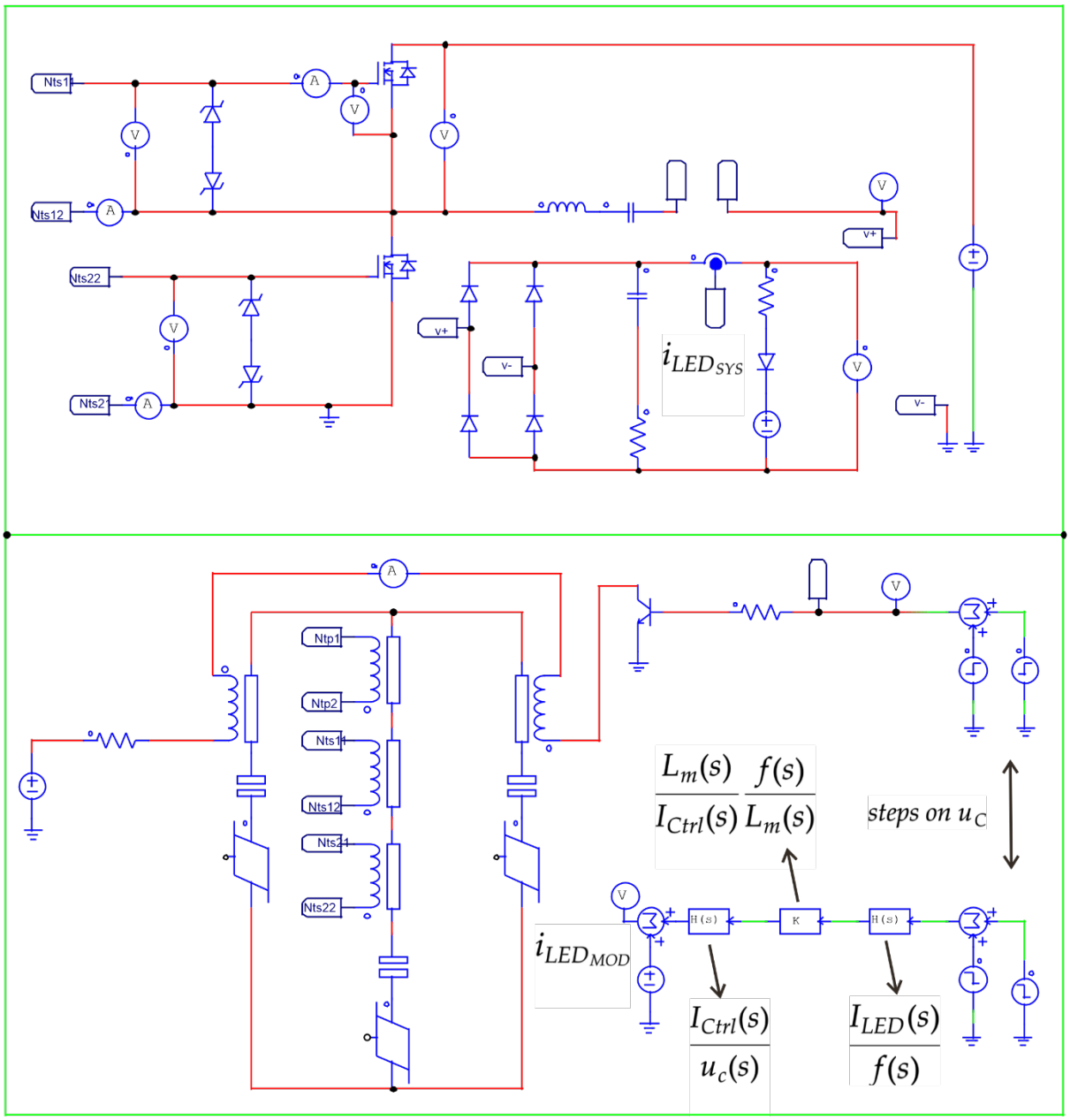

Source: Author

Figure 49 - Complete LC-SORC system output current i_{LED} dynamic response to the control signal u_c. Simulated and modeled system.

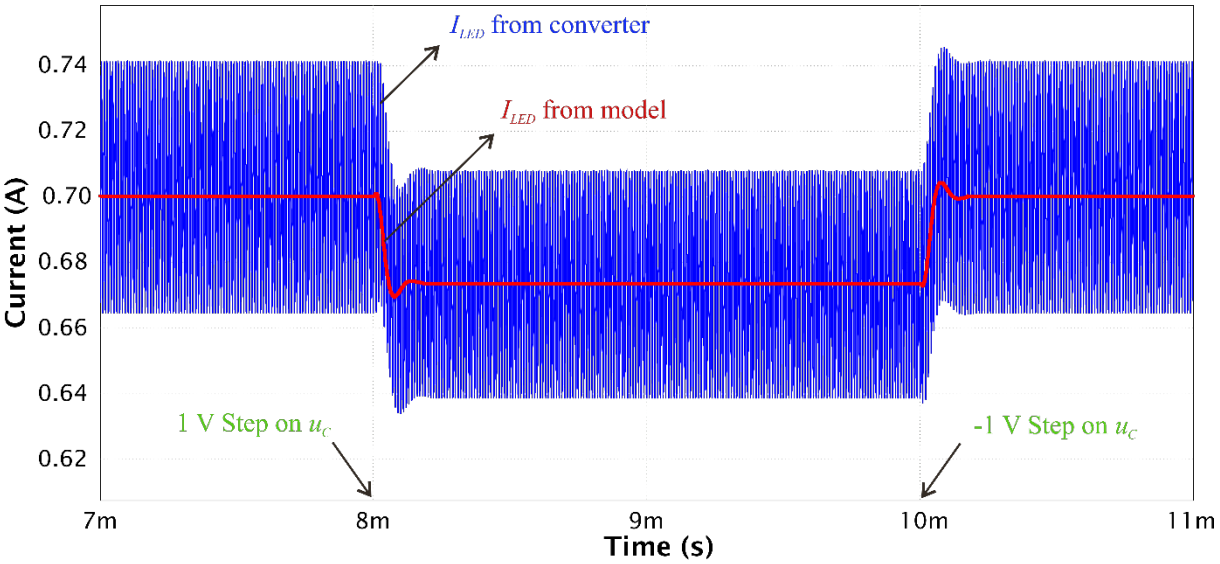

Source: Author

In summary, the complete system modeling has been performed using a number of techniques, but especially the EDF for inverter portion of the system. Figure 50 shows the comparison between the frequency response of the complete model obtained and the PSIM AC Sweep simulation, showing good accuracy between each other.

Figure 50 - Frequency response comparison between the complete model for the LC-SORC and the schematic diagram simulation

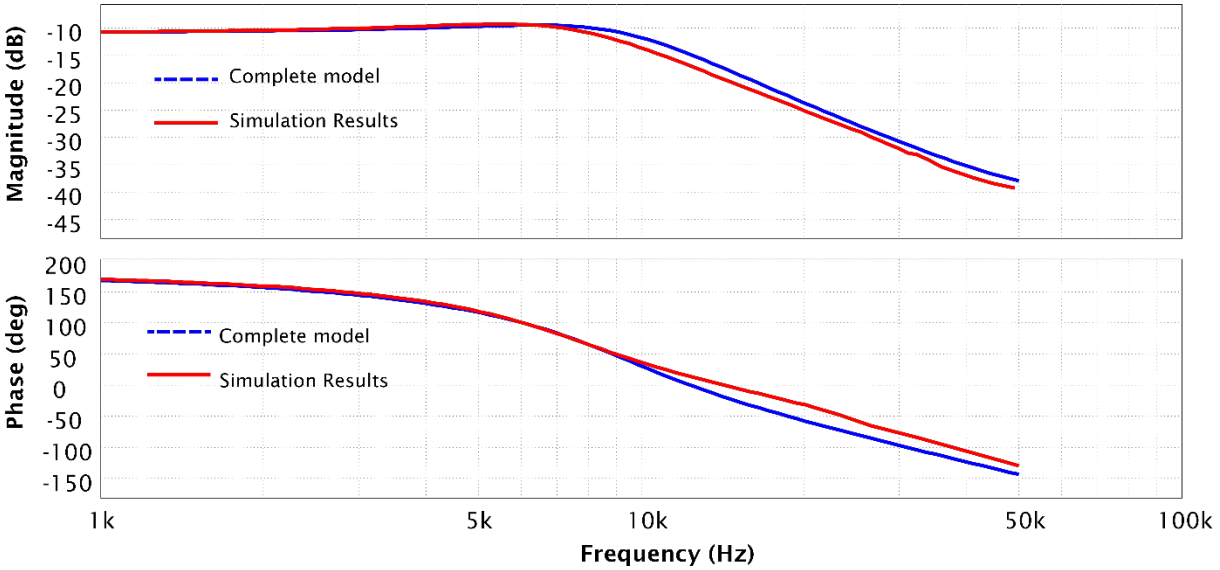

Source: Author

The last honorable mention in the LC-SORC modeling endeavor is the LSM of parametric estimation. Already shown in previous chapters, this is an interesting tool for modeling the complete system considering that no other techniques are analyzed as potential solutions at the time. Furthermore, it is a good solution for when the intermediate dynamics of the system are of no importance, such as the effect self-oscillating f_s related to u_c or i_{Ctrl}, as it treats the system with only the input and output of the system as variables of interest.

3.8 THE LEAST SQUARES METHOD FOR FULL OR PARTIAL MODELING

The LSM is a mathematical technique used to approximate or estimate a function from a set of observed data points. It is commonly used in various fields, including statistics, economics, engineering, and machine learning. The goal of LSM is to find the best-fitting function that represents the relationship between input variables (independent variables) and the corresponding output variables (dependent variables) in the data.

To understand the LSM, a simple example should suffice. Assuming a set of data points $\{(x_1, y_1), (x_2, y_2), ..., (x_n, y_n)\}$, where each data point consists of an input value x and its corresponding output value y. The methods main goal is to find a function $f(x)$ that provides the best estimate for y, given any input x.

The LSM begins by assuming a functional form for the estimated function, such as a polynomial, exponential, or logarithmic function. In the case of resonant converters, for example, a good estimate for the order of the polynomial function can be acquired from the order of the output filter. In the simple case where a linear function of the form $f(x) = \beta_0 + \beta_1 x$ is assumed, where β_0 and β_1 are coefficients to be determined, the next step is to define an error function that quantifies the discrepancy between the estimated function and the observed data points. In the case of LSM, the error function can typically be defined as the sum of squared differences between the observed values of y and the corresponding estimated values $f(x)$.

The LSM aims to minimize this error function by adjusting the coefficients β_0 and β_1. This is achieved by solving a system of equations derived from the error function. The system of equations is obtained by differentiating the error function with respect to the coefficients and setting the derivatives to zero. Solving the system of equations yields the values of β_0 and β_1 that minimize the error function, providing the best-fitting linear function. These coefficients represent the estimated parameters of the linear function, and the function itself provides an estimate for y given any input x.

Some interesting applications of the LSM are in Regression Analysis, where the LSM is widely used and the goal is to estimate the parameters of a linear or nonlinear regression model. This is applicable in fields such as economics, finance, social sciences, and engineering to analyze relationships between variables and make predictions. The authors in (MAULUD; ABDULAZEEZ, 2020) discuss various works by different researchers on linear regression and polynomial regression and compares their performance using the best approach to optimize prediction and precision.

On Curve Fitting applications, LSM is used for fitting curves to data points, aiming to find the best-fitting function that represents the relationship between variables. This is utilized in various scientific and engineering disciplines to analyze experimental data, calibration, and interpolation. One interesting application of in this field is its use in Multi-Term LSM for applying multiple a priori constraints in problems of Atmospheric Remote Sensing. The approach is used as a base for the first unified algorithm GRASP (Generalized Retrieval of Aerosol and Surface Properties) that is applicable to diverse remote sensing observations and retrieving a variety of atmospheric properties as seen in (DUBOVIK *et al.*, 2021).

On Time Series Analysis, LSM can be applied to data to estimate the parameters of autoregressive models, moving average models, or other time series models. This is valuable in financial forecasting, stock market analysis, weather prediction, and many other fields dealing with sequential data. One interesting application of LSM in Time Series Analysis is its use in forecasting wind speed when data are in the interval. A new least square method (LSM) for time series analysis under indeterminacy is proposed in (ASLAM; ALBASSAM, 2022). The proposed LSM under indeterminacy is known as the neutrosophic least square method (NLSM).

On Machine Learning, LSM can be employed in certain algorithms, such as linear regression and logistic regression. It plays a crucial role in estimating the coefficients or weights of the models, enabling prediction and classification tasks. One interesting application of LSM in Machine Learning is its use in a bioinspired digital liquid-state machine (LStM) for low-power very-large-scale-integration (VLSI)-based machine learning applications. An interesting bioinspired spike-based learning algorithm for the LSM is presented in (ZHANG *et al.*, 2015)

For Financial Modeling, LSM is commonly used for estimating parameters in asset pricing models, option pricing models, and portfolio optimization. It aids in understanding market behavior, risk management, and investment decision-making. One interesting application of LSM in Financial Modeling is its use in valuing American options by simulation, as seen in (LONGSTAFF; SCHWARTZ, 2001).

On the System Identification field, the LSM helps estimating the parameters of a mathematical model that represents the behavior of a dynamic system. It finds applications in control systems, signal processing, robotics, and aerospace engineering. A very interesting application of LSM here is its use in Structural Health Monitoring (SHM) systems.

In the field of Power Electronics, the Least Squares Method (LSM) can also be used for harmonic detection in power systems. One interesting application of LSM in Power Electronics is its use in a method based on improved FastICA-LSM for harmonic detection in power systems. This method is based on traditional FastICA and redefines the initial value when calculating the de-mixing matrix. LSM is then used to analyze the amplitude and phase of the separated signal (LI; HUANG; ZHAO, 2021). Furthermore, aligning both System Identification and Power Electronics fields, a very interesting work in the literature has used the LSM to estimate the mathematical parameters that model the dynamic behavior of an LLC resonant converter. This work is shown in (PANOV, 2014) and compares the LSM technique of modelling the converter with other techniques, such as the EDF method. The author concludes that both the ASS model and the approach based on the EDF have proven inadequate to model the behavior of the proposed LLC resonant converter, under the assumption that the resulting time domain models fail to provide sufficient information about the system's dynamics. Thus, the LSM is proposed as a solution to model the system, and according to the author, a comparison of the bode from the method's resulting transfer functions and the PSIM simulation provide a far better similarity as if compared to the modeling using EDF and ASS.

Applying the LSM to the LC-SORC is considerably straightforward. On a PSIM simulation, or even on the experimental setup as its going to show further in the developments of this doctoral dissertation, the technique requires a list of values of inputs and the respective outputs, like i_{LED} and u_C, for example. Then, after applying the already discussed methodology depicted on Chapter II, a TF is generated. This TF is shown in Figure 51 as a comparison with the AC Sweep simulation on PSIM, and also the system's full model. The frequency response from the LSM has an average accuracy when compared to the other two responses. However, usually this accuracy can be increased with the addition of a low-pass filter with an adequate cutoff frequency to the values of the output, due to i_{LED} having a ripple on the switching frequency of the converter, f_s, that may interfere with the methods precision. The LSM can also be used only for the LC series inverter portion of the LC-SORC, where the dynamics of the self-oscillating, as well as the VCT part are individually analyzed.

The data placed into the arrays to calculate the values of the polynomial parameters b_0, b_1, b_2, a_0, a_1, and a_2, result in the system's open-loop transfer function. The LSM input and

output arrays, the transfer function, and the matrix identities can be respectively expressed as (127), (128), (129) , and (130).

$$\vec{u} = [u(0),\ u(T_{sa}),\ u(2T_{sa}),\ \ldots,\ u(nT_{sa})] \tag{127}$$

$$\vec{y} = [y(0),\ y(T_{sa}),\ y(2T_{sa}),\ \ldots,\ y(nT_{sa})] \tag{128}$$

$$\frac{Y(z)}{U(z)} = \frac{b_2 z^2 + b_1 z + b_0}{z^3 + a_2 z^2 + a_1 z + a_0} \tag{129}$$

$$u = \left(A^T A\right)^{-1} A^T y \tag{130}$$

Figure 51 - Frequency response comparison between the complete model for the LC-SORC and the schematic diagram simulation, with the LSM model.

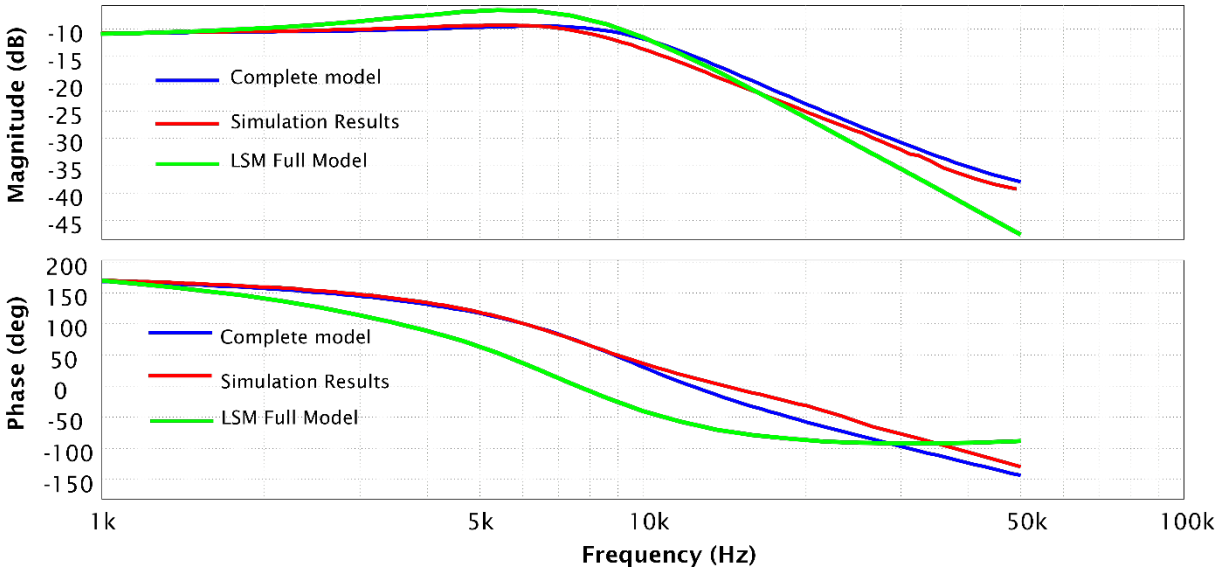

Source: Author

4

CLOSED LOOP LC-SORC DESIGN

In this chapter, the design of a closed-loop LC-SORC is carried out. The process involves designing the filter in conjunction with the definition of the electrical characteristics of the load. Additionally, the Self-Oscillating Command Circuit's (SOCC) magnetizing inductance L_m is determined by considering the effect of the MOSFET's parasitic capacitances and using the Extended Nyquist Criteria and the Describing Function Method. The feedback consists of using the Variable Current Transformer (VCT) as an actuator to add an external layer of control on top of the already existent intrinsic feedback of the SORC, and the usage of the Extended Nyquist Criteria to model a portion of the system and find its transfer functions.

This final chapter shows the feasibility of a practical application for the VCT closed-loop SORC. In order to demonstrate the SORC capability to self-oscillate with constant current control using the VCT actuation mechanism, a closed-loop LC-SORC is proposed. Through the addition of an external control layer apart from the intrinsic positive-type network already present in the system due to the SOCC, the output current is kept within a pre-established reference value. Table 2 shows the specifications for the proposed system, which is designed around the minimum input voltage, 170 V, where f_s is at its lowest value of 130 kHz, slightly higher than the filter's f_0, maintaining ZVS, and the control current flowing through the auxiliary windings of the SOCC is zero. The VCT increases the self-oscillating frequency to approximately 300 kHz at the highest input voltage, keeping the controlled variable within the reference value range through the injection of I_{Ctrl}.

Table 2 - Specifications and parameters of the closed-loop SORC.

Parameter	Symbol	Value
Minimum Bus Voltage	E	170 V
Resonant Frequency	f_0	100 kHz
Minimum Switching Frequency	f_s	120 kHz
Zener Voltage	V_Z	15 V
MOSFETs	S_1, S_2	NTP190N65S3
LED String Current	I_{LED}	50-300 mA
LED String Voltage	V_{LED}	65-70 V
LED String Dynamic Resistance	r_D	35 Ω
LED String Nominal Power	P_o	20 W
LED String Threshold Voltage	V_{TH}	61 V
Full-wave Rectifier Diodes	D_2 - D_5	MUR260
Rectifier Diodes voltage drop	V_F	0.7 V
Microcontroller	M_1	ATmega328
Filter capacitor SR	r_f	0.025 Ω
Output capacitor SR	r_{Co}	0.025 Ω

4.1 OVERVIEW OF THE OPERATING PRINCIPLE FOR THE PROPOSED CLOSED-LOOP SORC

The operating principle of the proposed closed-loop SORC is shown in Figure 52. The proposed VCT device operates in a double toroid configuration, where the three windings of the SOCC couple both toroids, while each one of the auxiliary windings, responsible for the inductance variation, are coupled with each toroid. The auxiliary windings are connected in series and to a voltage source whose current effectively varies the equivalent magnetizing inductance L_m.

Figure 52 – Principle of operation for the proposed closed-loop SORC.

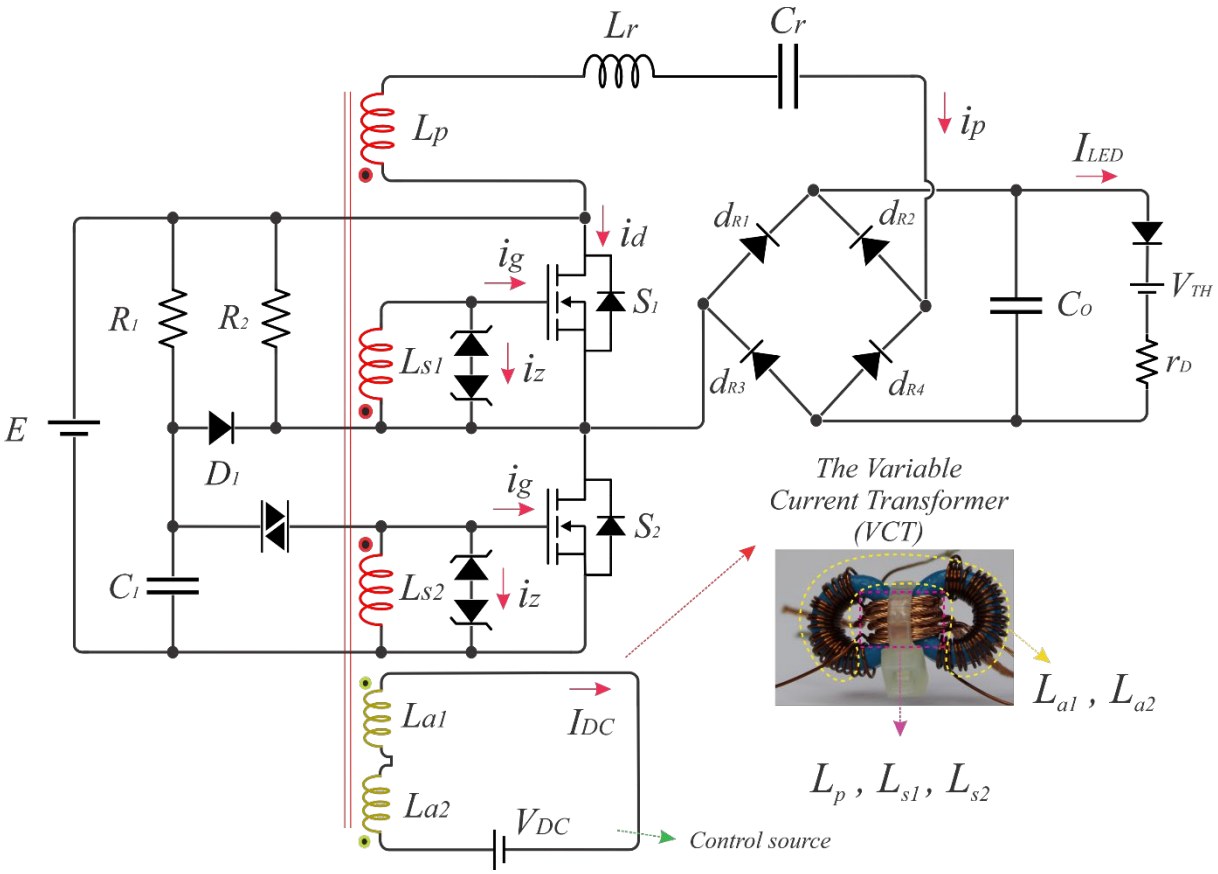

Source: Author

Despite its intrinsic positive feedback represented by the windings of the SOCC, the depicted SORC still operates in open-loop in regards to reference following. However, as it is, it can be considered a straightforward and cost-effective way of modulating the SORC's frequency through the insertion of a small DC current through L_{a1} and L_{a2}. This simplicity may

be helpful in many applications, significantly dimming for discharge lamps and LEDs. The feedback that connects the output of the SORC to the auxiliary windings of the VCT will be explored further in this section.

4.2 LC SERIES FILTER DESIGN

The LC series filter design starts with the definition of an LED model. Figure 53 shows, on its left, the experimental points for voltage and current for the tubular 20 W LED lamp employed. As it can be observed, the portion of the curve that extends from approximately 62 V until the end of the curve appears to be reasonably linear. Thus, seen in (LIN; CHEN, 2009), a single PWL model can emulate the LED behavior on the *v-i* curve through a simple equivalent circuit composed by a dinamic resistance r_D, an ideal diode d_i and its forward diode voltage drop V_{TH}. The model can be represented through (131), and the LED resistance can be found using (132).

Figure 53 – LED Voltage *vs* Current curve. Experimental (*v*, *i*) points on the left; and the PWL equivalent circuit and curve on the right.

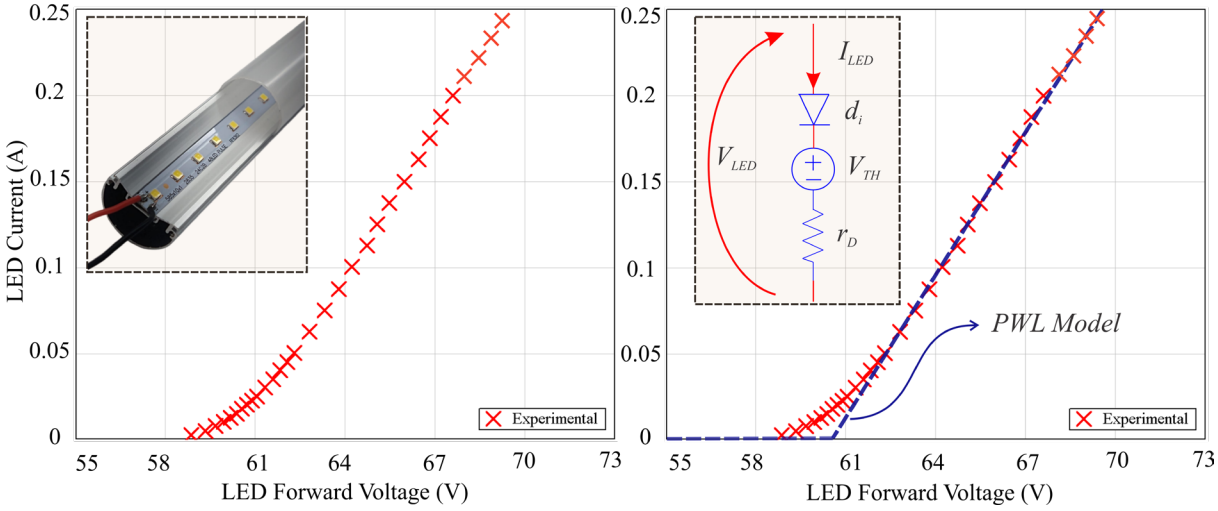

Source: Author

When wider ranges of modulation are required, in the sense that a single PWL model is not sufficient to accurately represent the behavior of the LED, (LIN; CHEN, 2009) also proposes the superposition concept of the multi-branch PWL, that splits the *v-i* curve into several parts. For the present case, however, for the current range that varies from 0.05 to 0.3 A, a single PWL branch is sufficient to provide acceptable accuracy. Furthermore, employing

least square fitting on the data depicted on the graphic, the obtained equivalent PWL model parameters are V_{TH} = 61 V and r_D = 35 Ω.

Figure 54 – LED equivalent model used in the SORC design.

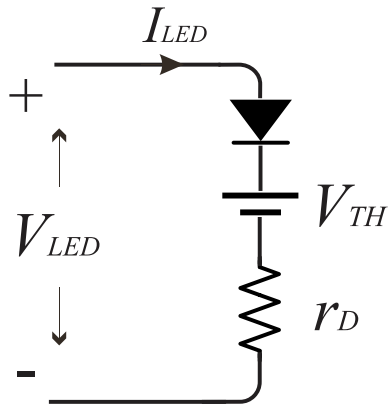

Source: Author

$$V_{LED} = V_{TH} + I_{LED} r_D \tag{131}$$

$$R_{LED} = \frac{V_{LED}}{I_{LED}} = 325\ \Omega \tag{132}$$

Figure 55 shows a widespread equivalent circuit for the SORC used for the filter design through the FHA. A simplification of the rectifying stage is necessary to obtain the LED string AC resistance seen by the resonant filter. This resistance is called R_{LEDac} and replaces the rectifying, filtering, and LED devices for an equivalent resistance (ALMEIDA, 2014; SÁ JR., 2010; STEIGERWALD, 2015), calculated through (133)[30]. Recalling the filter analysis from Chapter, R_{LEDac} is one of the most important parameters in the analysis of the feasibility of SORC modulation, along with Q.

[30] This equation is valid when certain conditions are met for quality factor and normalized frequency characteristics. For high quality factors and relationships between the switching and resonant frequency are close to unity, the filter current should have a low reactive characteristic and appear more sinusoidal, validating the usage of (133) with a higher accuracy.

Figure 55 – The (a) SORC equivalent circuit for the filter design and (b) the equivalent circuit with output stage replaced by AC resistance.

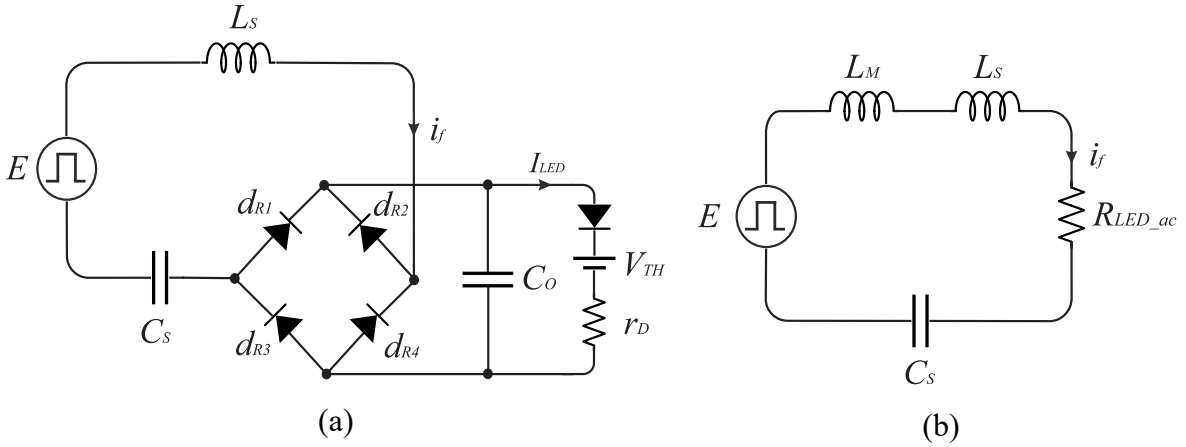

Source: Author

$$R_{LED_{ac}} = \frac{8R_{LED}}{\pi^2} = 263.43\ \Omega \tag{133}$$

Considering that the feasibility of modulation of the LC-SORC is higher for certain values of output resistance, this tubular LED achieves high values of R_{LEDac} and hence should present no instability problems over wide ranges of modulation. According to (KAZIMIERCZUK; CZARKOWSKI, 2011) the efficiency of the bridge rectifier can be calculated through (134).

$$\eta_R = \frac{1}{\left[1 + \frac{2V_F}{V_{LED}} + \frac{\pi^2 r_f}{4R_{LED}} + \frac{r_{C_O}}{R_{LED}}\left(\frac{\pi^2}{8} - 1\right)\right]} = 98.2\% \tag{134}$$

The voltage gain M_{RG} of the full-wave bridge rectifier can be found through (141).

$$M_{R_G} = \frac{\pi\eta_R}{2\sqrt{2}} \tag{135}$$

$$= \frac{\pi \times 0.982}{2\sqrt{2}} = 1.091$$

The voltage transfer function of the LC-SORC resonant converter can then be found through (143), with M_V being (137) and M_{Vs} being (138).

$$M_{V_r} = \frac{M_V}{M_{V_S} M_{R_G}} \tag{136}$$

$$= \frac{74\ V \times \pi}{200\ V \times 1.091 \times \sqrt{2}} = 0.753$$

$$M_V = \frac{V_{LED}}{E} \tag{137}$$

$$M_{V_S} = \frac{\sqrt{2}}{\pi} \tag{138}$$

Different methodologies are acceptable to carry out the filter series inductance and capacitance design, such as (LOPES, 2014) and (DE MELO *et al.*, 2015), each with its own characteristics. In (KAZIMIERCZUK; CZARKOWSKI, 2011), the author suggests calculating Q first, where the angular switching frequency ω_s is normalized with respect to the resonant frequency ω_0, and using the voltage transfer function from (136) and the overall inverter efficiency n_{inv}, Q is given by (139).

$$Q = \frac{\sqrt{\frac{n_{inv}}{M_{V_r}^2} - 1}}{\left(\frac{\omega}{\omega_o} - \frac{\omega_o}{\omega}\right)} \tag{139}$$

Furthermore, from Figure 56, it can be observed that Q values obtained from ω/ω_0 at around 1 to 1.1 are considerably high and can affect the modulated stability of the system. Normalized ω/ω_0 values that range from 1.1 to 1.4 and even further beyond are adequate from a modulation stability perspective.

Figure 56 – Plot of the quality factor Q versus normalized switching frequency ω/ω_0 of the converter.

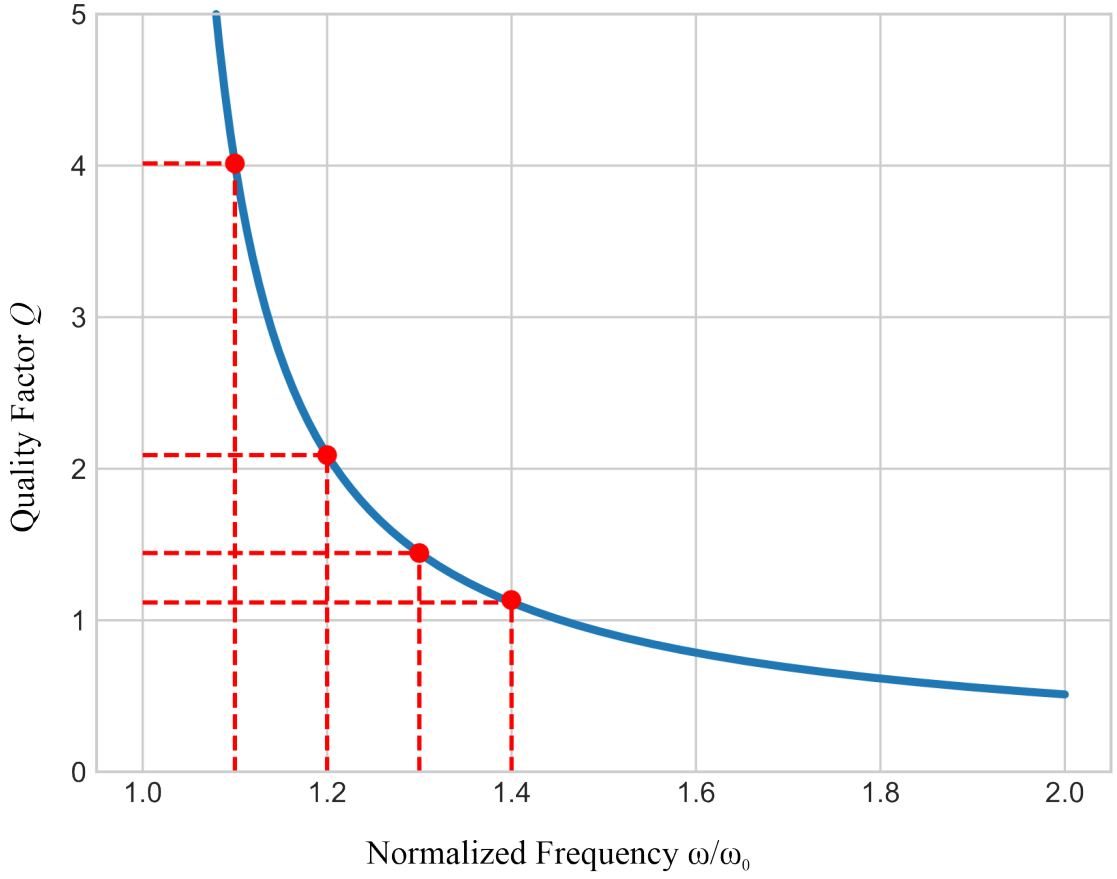

Source: Author

In this doctoral dissertation, the feasibility of SORC modulation is of paramount importance and is heavily affected by two parameters, R_{LEDac} and Q. Thus, it is interesting to work with an initial definition of a Q that is low enough to guarantee both feasibility of modulation with the given R_{LEDac} and still maintain an acceptable precision when using the FHA to design the filter. According to the graphic, value of ω/ω_0 around 1.3 should be sufficient to maintain the Q value aligned with the feasibility of modulation, which results in a Q of 1.5 using (139). Then, using (140), the series inductor is calculated. The series capacitor can be calculated through (141).

$$L_s = \frac{QR_{LED_{ac}}}{\omega_o} \tag{140}$$

$$= \frac{1.5 \times 103.48\ \Omega}{2 \times \pi \times 100\ kHz} = 246.2\ \mu H$$

$$C_s = \frac{1}{Q\omega_o R_{ac}} \tag{141}$$

$$= \frac{1}{1.5 \times 2 \times \pi \times 100\ kHz \times 103.48\ \Omega} = 10.2\ nF$$

The output impedance of the filter can be calculated through (142).

$$Z_o = \sqrt{\frac{L_s}{C_s}} \tag{142}$$

$$= \sqrt{\frac{246.2\ \mu H}{10.2\ nF}} = 155.23\ \Omega$$

The next step is to find the bus voltage value required to maintain the aforementioned electrical characteristics on the LED string using the calculated C_r and L_r, usually through the relationship between the fundamental voltage applied to the filter and the operating frequency. Due to the low-pass characteristic of the LC series filter, it can be represented as a Fourier Series of the type (143).

$$v_{ab} = \frac{E}{2} + \frac{2E}{\pi} \sum_{n=1}^{\infty} \frac{1 - (-1)^n}{2n} sin(n\omega t) \tag{143}$$

On lower frequencies in the order of dozens of kHz, when we consider that the filter input voltage has a square-wave characteristic, it suffices to consider the effect of fundamental harmonic. Then, the fundamental component's RMS value can be found through (144) and (145).

$$V_{ab_{pk}} = \frac{2E}{\pi} \tag{144}$$

$$V_{ab_{rms}} = \frac{2E}{\pi\sqrt{2}} \tag{145}$$

However, as the switching frequency for the proposed LC series closed-loop SORC varies from 100 to 300 kHz, the effect of the MOSFET output capacitance has to be taken into account and inserted into the design. This effect shifts the square-wave voltage into a more "trapezoidal" wave, caused by the charge and discharge times of C_{ds} (FLORES-GARCÍA *et al.*, 2011) from Figure 57. This change means that the peak value of the fundamental voltage applied to the filter is no longer ruled by (144). Instead, the higher the frequency, the more the bus voltage has to be compensated due to the loss in the value of the peak of the fundamental voltage. This compensation depends on the slope times of $v_{ds,}$ and the new bus voltage is given by (146).

Figure 57 – The (a) MOSFET C_{ds} capacitance's effect on the (b) SORC equivalent circuit for the filter design.

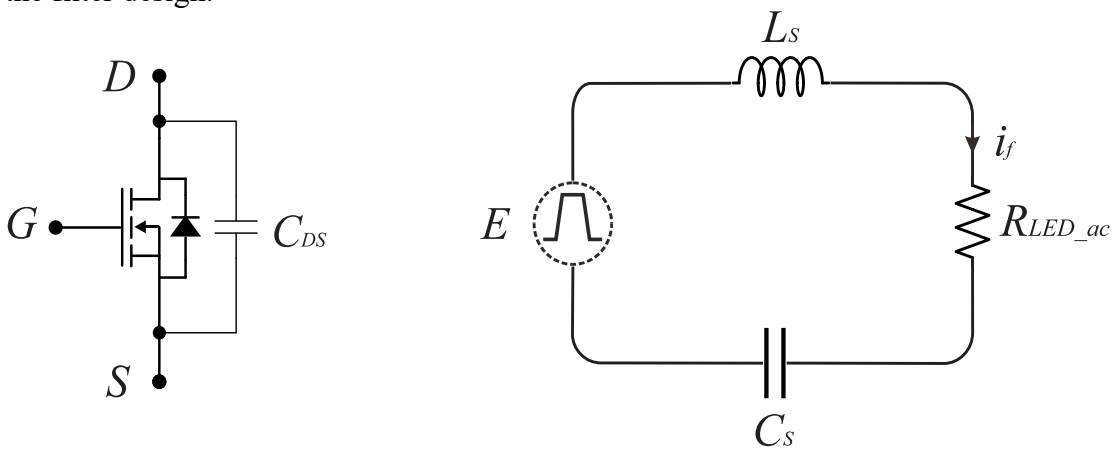

Source: Author

$$V_{ab_{pk\_t}} = E\frac{sin\left(\pi/2\right)}{\pi/2}\frac{sin\left(\omega t_s/2\right)}{\omega t_s/2} \tag{146}$$

Given the values of the series inductance, capacitance, and load characteristics, the value of the filter current can now be calculated, taking into account the slope of the voltage applied to it. The filter current can be represented as a sinusoid through (147).

$$i_R = I_{R_{pk}} sin(n\omega t) \tag{147}$$

The filter peak value can then be calculated (148) as the relationship between the peak voltage applied to the filter and its impedance. The peak voltage is now compensated through

the slope times of the C_{ds}, resulting in an equation for the filter current that provides information considering the frequency, the load, and the filter characteristics. As this equation relates to the peak value, a simple multiplication factor of 2/π is enough to finally provide an equation for the LED current as a function of the parameters mentioned above.

$$I_{R_{pk}} = \frac{V_{ab_{pk\_t}}}{|Z|} \tag{148}$$

$$I_{R_{pk}} = \frac{E\frac{sin\left(\pi/2\right)}{\pi/2}\frac{sin\left(\omega t_s/2\right)}{\omega t_s/2}}{\sqrt{L_R/C_R}} \tag{149}$$

The LED current, at this point, is a design parameter defined on the previous load analysis, which leads (149) to having only E as a parameter that needs calculation. Thus, for the trapezoidal waveform applied to a high-frequency LC series filter that feeds a string of LEDs, the final bus voltage equation is (150). It is interesting to note that, if this were the case of a low-frequency LC series filter design, equation (150) would not need compensation due to C_{ds}, becoming equation (151). For the 130 kHz frequency, a compensation of approximately 2.5 % on the bus voltage is required due to the effect of C_{ds}.

$$E_{trp} = \frac{\pi^2 I_{LED}\omega t_s}{8sin\left(\omega t_s/2\right)}\sqrt{R_{LED_{ac}}^2 + \left(\omega L_R - \frac{1}{\omega C_R}\right)^2} = 200\ V \tag{150}$$

$$E_{sqr} = \frac{\pi^2 I_{LED}}{4}\sqrt{R_{LED_{ac}}^2 + \left(\omega L_R - \frac{1}{\omega C_R}\right)^2} = 195\ V \tag{151}$$

The output filtering capacitor is designed around the point of minimum frequency, 130 kHz. The maximum ripple voltage across the output filtering capacitor is (152) and the voltage across the ESR is expressed as (153).

$$V_{rip} = 0.05V_{LED} = 0.05 \times 73 = 3.65\ V \tag{152}$$

$$V_{rip_{ESR}} = \frac{\pi}{2} r_{C_o} I_{LED} = \frac{\pi}{2} \times 0.025\ \Omega \times 0.3\ A = 0.012\ V \tag{153}$$

The voltage across the output filter is (154)

$$V_{C_o} = V_{rip} - V_{rip_{ESR}} = 3.65\ V - 0.012\ V = 3.638\ V \tag{154}$$

Thus, the minimum value of the output filtering capacitance is expressed as (164), in accordance to (KAZIMIERCZUK; CZARKOWSKI, 2011).

$$C_o = \frac{0.105 I_{LED}}{f V_{C_o}} = \frac{0.105 \times 0.3}{130\ kHz \times 3.638} = 66\ nF \tag{155}$$

The maximum voltage stress across the switches is (156). It depends directly on the maximum bus voltage, that coincides with the greater modulation value from the VCT's I_{Ctrl}.

$$V_{S_{S1,S2}} = E = 300\ V \tag{156}$$

The peak voltage stress across the resonant inductor and capacitor is (157). The higher the quality factor, the higher the voltage stress across both resonant inductor, and especially the capacitor.

$$V_{C_R} = V_{L_R} = \frac{Q2E}{\pi} = \frac{1.5 \times 2 \times 300}{\pi} = 286.48\ V \tag{157}$$

The peak value for both voltage and current across the output diodes is (158) and (159).

$$V_{D_{pk}} = V_{LED} = 73\ V \tag{158}$$

$$I_{D_{pk}} = \frac{\pi I_{LED}}{2} = 0.471 \tag{159}$$

The peak value of the switch current depends on the efficiency of both the inverter and the converter, as well as the output power and the LED equivalent ac resistance, as seen in (160).

$$I_{S_{S1.S2}} = \sqrt{\frac{2P_{LED}}{n_R R_{LED_{ac}}}} = \sqrt{\frac{2 \times 20}{0.982 \times 263}} = 0.4\ A \tag{160}$$

4.3 INPUT CAPACITANCE CALCULATION

Despite all the attractive characteristics of the MOSFETs, their input intrinsic capacitances, which in essence promote the device's switching, can cause design issues on specific topologies. The switching process is based on the charging and discharging of said

capacitances. In the case of the SORC, for example, that intrinsic feedback is responsible for the switching, the gate-to-source capacitance C_{gs} and the gate-to-drain capacitance C_{gd} can directly affect the analysis and design. On a construction level, the C_{gs} occurs due to the superposition of the source and its channels by the poly-Si gate. The C_{gd} capacitance presents a considerable non-linear characteristic and is associated with the gate superposition with the *Si* below it, known as the JFET region (BARKHORDARIAN, 1996).

Most efforts made in the literature to address the effect of these capacitances focused on the linear effect of C_{gs}, as it is easily accessible through the device's datasheet. However, the C_{gd} capacitance also considerably affects the switching process and is equally essential due to its non-linear characteristic. Also known as the Miller capacitance, this last one has an interesting effect, making the total capacitance of the MOSFET's input higher than the static capacitances, causing a feedback effect between the input and output of the switching device.

Calculating the exact value of each capacitance is not an easy task. A simplified method usually given by the manufacturers is the gate charge information. The gate charge or Q_g informs the amount of charge, in Coulombs, required to turn the device on and off, which translates to the charging and discharging of its capacitances. However, Q_g information is usually given for a single bus voltage and gate voltage value and can vary significantly for parameters different from those informed.

Hence, in (DA ROSA *et al.*, 2018), a method is shown to calculate the equivalent input capacitance of a MOSFET for a given range of parameters. This equivalent capacitance translates into the effect of both C_{gs} and C_{gd} capacitances, and despite requiring experimental measurements of each MOSFET, provides considerably precise information regarding the value of the capacitances for the SORC design. The methodology is based on the measurement of the gate current i_g on a single MOSFET, where this data is then converter into a CSV and manipulated in mathematical software. Figure 58 shows a set of gate waveforms for two MOSFETs, one is a Cascode GaN FET TPH3202 with a considerably small gate capacitance, and the blue gate current i_g waveform is observed to be minor, reflecting on a lower Q_g. However, the second MOSFET, an IRF640, has a much higher input capacitance, thus having a higher i_g current due to the need for a higher Q_g.

Figure 58 – The MOSFET gate waveforms for an (a) TPH3202 and a (b) IRF640.

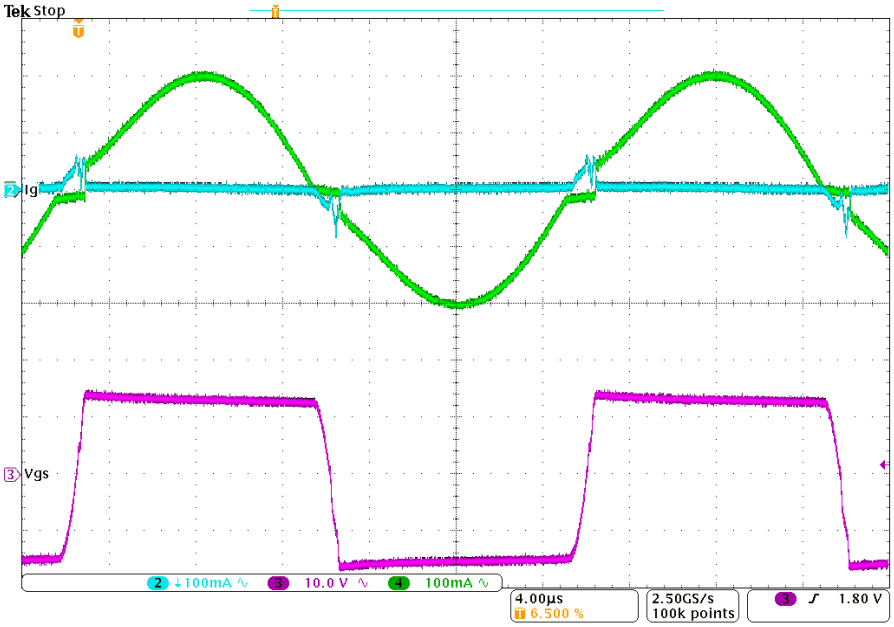

(a)

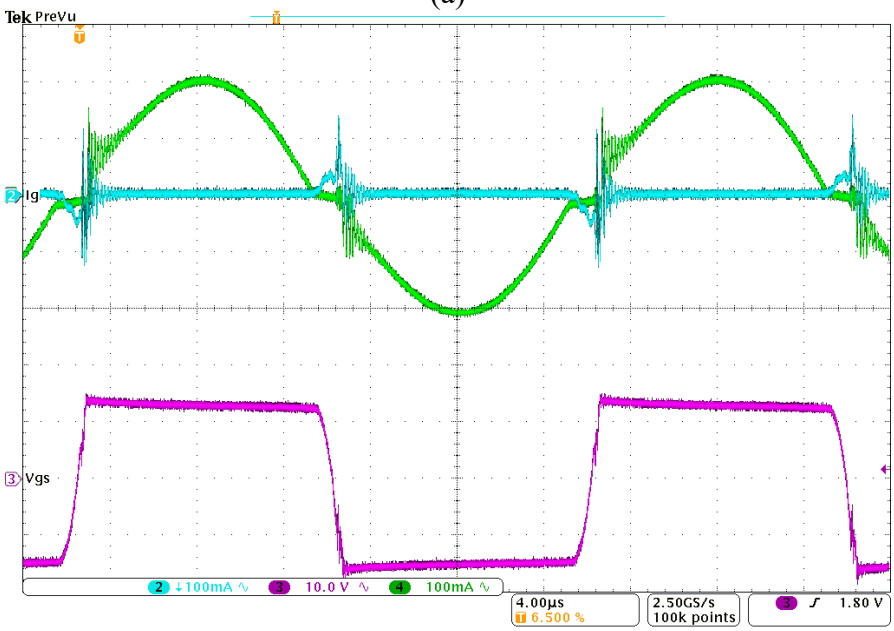

(b)

Source: Author

The gate current is integrated within the v_{gs} rise and fall times, which are the periods of charge and discharge of the capacitances, resulting in the amplitude of gate charge required for a switching cycle. Then, this gate charge amplitude is divided by the amplitude of the gate voltage within the same rise and fall times. The equivalent capacitance C_{eq} is then calculated according to (161).

$$C_{eq} = \frac{\Delta Q_g}{\Delta V_{gs}} = \frac{\int_{t_o}^{t_1} i_g(t)dt}{v_{gs}(t_1) - v_{gs}(t_0)} \tag{161}$$

Table 3 shows the equivalent capacitances calculated through (161) for a set of MOSFETs with different gate charge characteristics. Figure 59 shows a comparison between the equivalent simulated gate capacitance of several *Si* MOSFET models and how they vary with the bus (C_{gd} effect) and zener (C_{gs} and C_{gd} effects) voltages.

Figure 59 – Comparison between several *Si* MOSFET models and their equivalent gate capacitances C_{eq} for different Bus and Zener voltages.

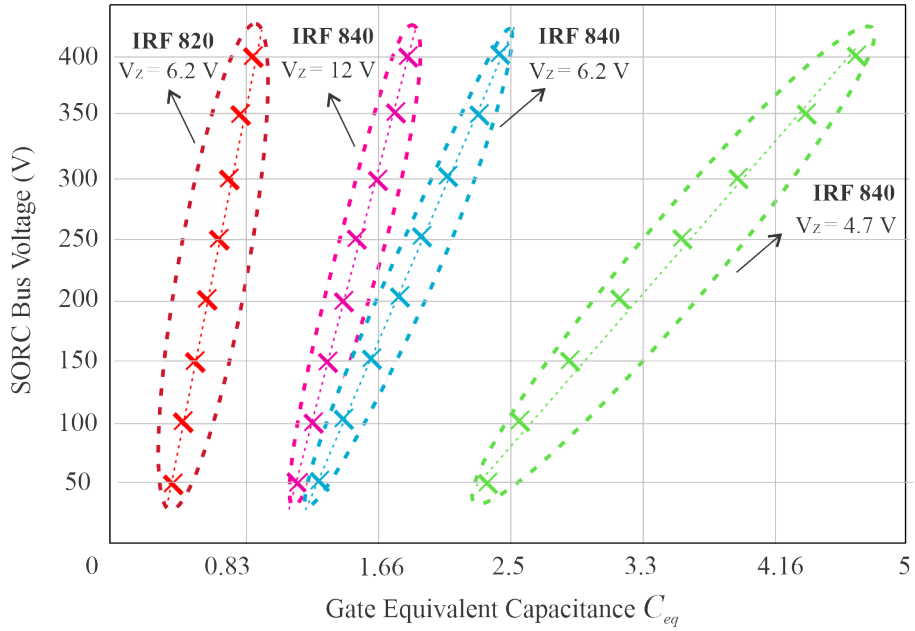

Source: Author

Table 3 - Equivalent capacitance C_{eq} for a set of MOSFETs with different gate charges.

Equivalent C_{eq} of several MOSFETs (Experimental)	
Si IRF640	2413 pF
Si IRF630	2000 pF
Si IRF620	1620 pF
NTP190N65S3	1482 pF
Cascode GaN TPH3202	1350 pF

Source: Author

4.4 HIGH FREQUENCY DESCRIBING FUNCTION DESIGN OF THE SORC

With the definition of a high-frequency LC series filter design and a methodology to calculate the equivalent input capacitance of the MOSFET connected to the equivalent model of the SOCC seen in A 61, using the methodology developed in (DA ROSA *et al.*, 2018), the DFM can be used to design the maximum value of the L_m for the closed-loop SORC. The waveforms in Figure 60 summarize the relationship between the different voltages and currents that are effectively responsible for the self-oscillation when the effect of C_{eq} is included.

Figure 60 – SOCC waveforms with the effects of the input capacitance C_{eq}.

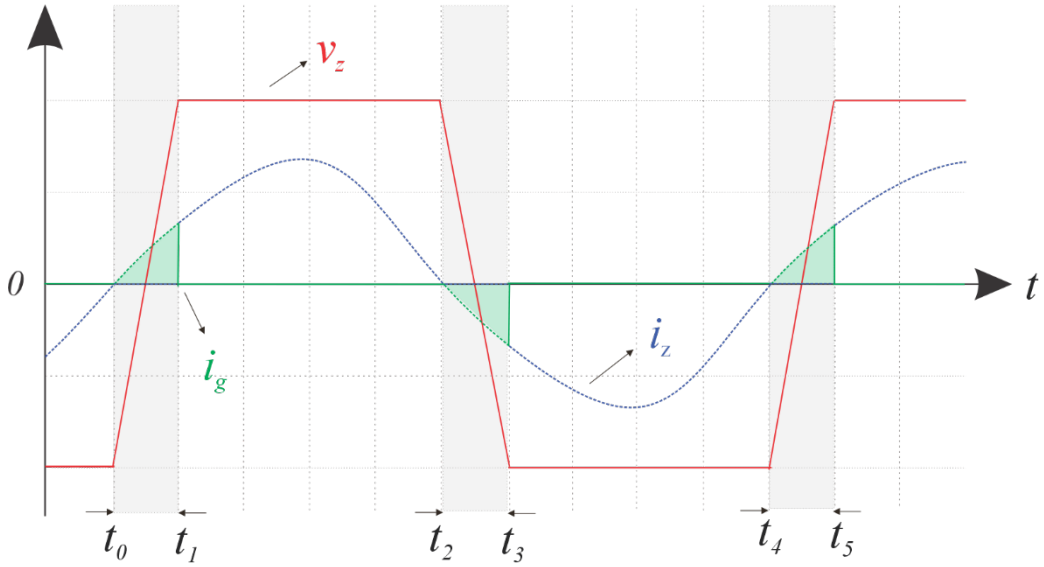

Source: Author

Initially, there needs to be a definition for the voltage applied to the MOSFET gate, i.e., to the equivalent input capacitance C_{eq}. Equation (162) defines the v_{gs} voltage.

Figure 61 – Equivalent model of the SOCC using the VCT actuation mechanism.

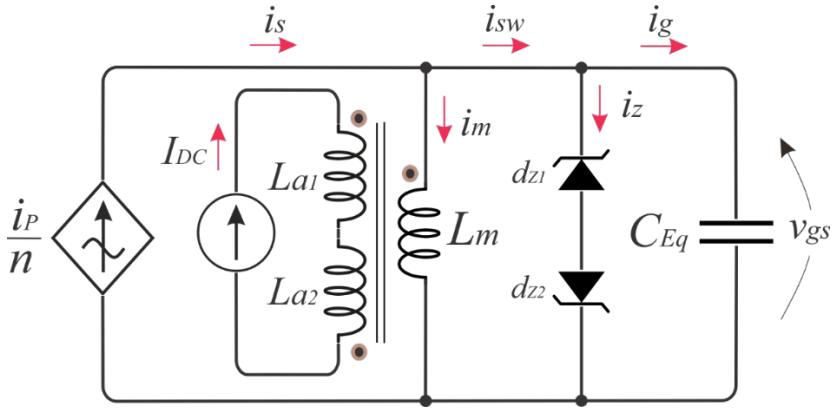

Source: Author

$$v_{gs}(t) = \begin{cases} v_{c_{eq}}(t), & if\ t_o < t < t_1 \\ V_Z + V_F, & if\ t_1 < t < t_2 \\ -v_{c_{eq}}(t), & if\ t_2 < t < t_3 \\ -(V_Z + V_F), & if\ t_3 < t < t_4 \end{cases} \quad (162)$$

The capacitor voltage can be found by integrating the i_{sw} current, given by (163). The i_{sw} current is the portion that flows from the secondary winding i_s, minus the magnetizing current i_m.

$$v_{C_{eq}}(t) = \frac{1}{C_{eq}} \int_0^t i_{sw}(t)dt \; - \; (V_Z + V_F)\,, \quad for\ t < t_1 \quad (163)$$

The maximum Zener voltage, including the forward voltage drop V_F, can be calculated using (164). The switching current i_{sw}, as being a portion of the TC's secondary current, has a sinusoidal characteristic similar to that of i_p, i.e., it can be considered to reach its amplitude I_{sw} during the Zener clamping stages.

$$V_Z + V_F = \frac{I_{sw}}{C_{eq}} \int_0^t sin(\omega t)dt \; - \; (V_Z + V_F) \quad (164)$$

From equations (163) and (164), the charging time for C_{eq} can be calculated in the form of t_r (165). Furthermore, this slope of the v_{gs} voltage works as a phase angle between this voltage and the switching current, i_{sw}. This phase angle, defined as ϕ, is calculated through (166).

$$t_r(\omega,\ C_{eq}) = \frac{1}{\omega} cos^{-1}\left(\frac{I_{sw} - 4(V_Z + V_F)C_{eq}\omega}{I_{sw}}\right) \quad (165)$$

$$\phi(\omega,\ C_{eq}) = \frac{180}{\pi} cos^{-1}\left(\frac{I_{sw} - 4(V_Z + V_F)C_{eq}\omega}{I_{sw}}\right) \quad (166)$$

From this point forward, the analysis returns to the block diagram of the SORC from Figure 28. The output filter elements linear block, $G_F(s)$, is the admittance of the LC series filter, given by (167).

$$G_F(j\omega) = \frac{1}{j\omega L_R + \frac{1}{j\omega C_S} + R_{LED_{ac}}} \tag{167}$$

Another linear block is the magnetizing inductance liner block, given by (168).

$$G_M(j\omega) = \frac{1}{L_m(j\omega)} \tag{168}$$

The gains K and α_i are proportionality gains between the output of the non-linear part of the system and the bus voltage, and the primary and secondary sides of the TWCT, respectively, given by (169) and (170).

$$K = \frac{E}{2V_Z} \tag{169}$$

$$\alpha_i = \frac{n_P}{n_S} \tag{170}$$

Recalling the simplified block diagram from Figure 29, the liner simplified block of the system is given by (171).

$$G(j\omega) = G_M(j\omega) - K\alpha_i G_F(j\omega) \tag{171}$$

Finally, as for the nonlinear part of the system, the DFM is employed as a linearization method. However, the nonlinear N block, which was previously a tangible gain that depicted the relationship between the fundamental harmonic of the output and the input of the nonlinear block shown in (172), now has a phase angle that originated from the rise and fall times of C_{eq}. Furthermore, as can be observed from the waveforms of the SOCC, when the effect of C_{eq} is accounted for, the v_{gs} voltage no longer has a square waveform but a trapezoidal one. Thus, the final block N of the DFM, with the fundamental value of its output, has to be compensated with regards to C_{eq}, which is given by (173).

$$N = \frac{4(V_Z + V_F)}{\pi I_Z} \rightarrow \frac{4(V_Z + V_F)}{\pi I_Z} \angle\phi(j\omega) \tag{172}$$

$$N(j,\omega,I_{sw}) = \frac{8sin\left(\frac{\omega t_R}{2}\right)}{\omega t_R I_{sw}} \angle -cos^{-1}\left(\frac{I_{sw} - 4(V_Z + V_F)C_{eq}\omega}{I_{sw}}\right)\frac{180}{\pi} \quad (173)$$

The final part of the DFM analysis can now be carried out. The values of the linear part were defined, as well as the linearization of the nonlinear block. Due to the characterization of this system as an SRCS with null input, as previously defined, the block G(s) needs to be equal to the -1/N(s) block. As the N block now has an imaginary part, a simple approach is to separate both real and imaginary parts of both blocks, as done in (174) and (175), to calculate the intersection point in the Nyquist plane.

$$Re\left(\frac{-1}{N(j,\omega,I_{sw})}\right) = Re(G_M(j\omega) - K\alpha_i G_F(j\omega)) \quad (174)$$

$$Im\left(\frac{-1}{N(j,\omega,I_{sw})}\right) = Im(G_M(j\omega) - K\alpha_i G_F(j\omega)) \quad (175)$$

Thus, in Figure 62, a comparison between the intersection points of -1/*N* and *G*. For the traditional methodologies that use the DFM and neglect the high-frequency effect of the switches capacitances, the intersection occurs in the real axis. On the other hand, for the improved design methodology that calculates the effect of C_{eq} and redesigns *N* with its new added angle, the intersection can be seen in the negative imaginary quadrant. MOSFETs with higher gate charges will have higher values for C_{eq}, which results in an intersection point that occurs even lower in the negative imaginary quadrant.

Figure 62 – Comparison between the traditional intersection of G(s) and -1/N and the high-frequency approach.

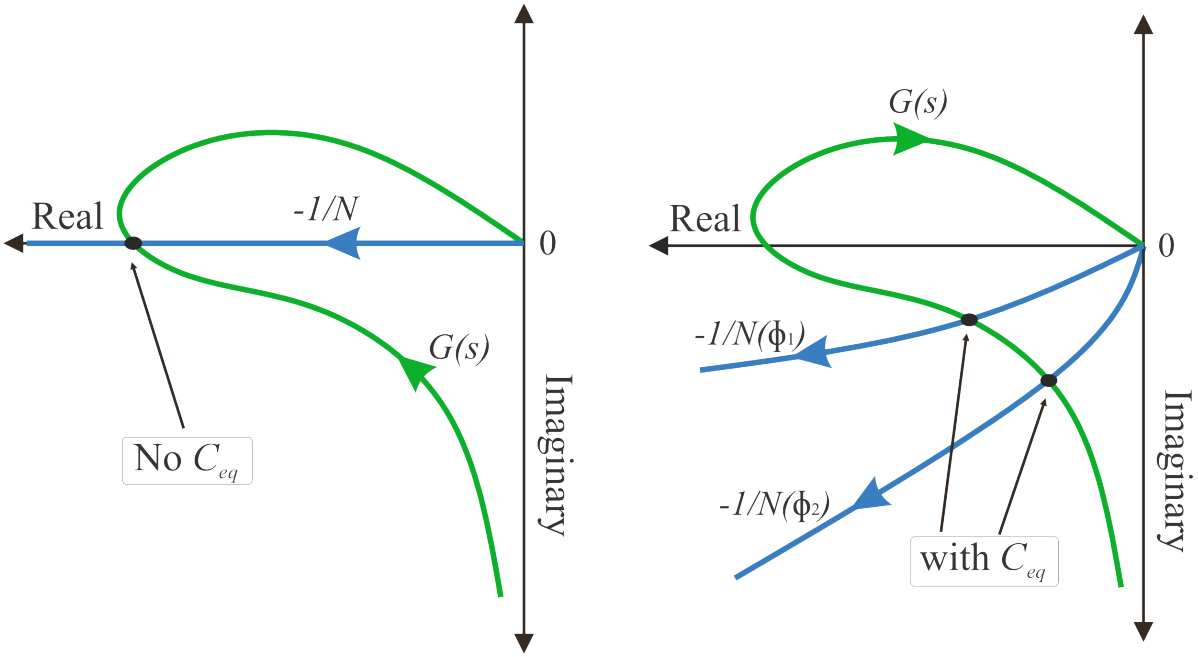

Source: Author

Figure 63 – The DFM as a utility to calculate the evolution of the SORC's frequency caused by variations of L_m.

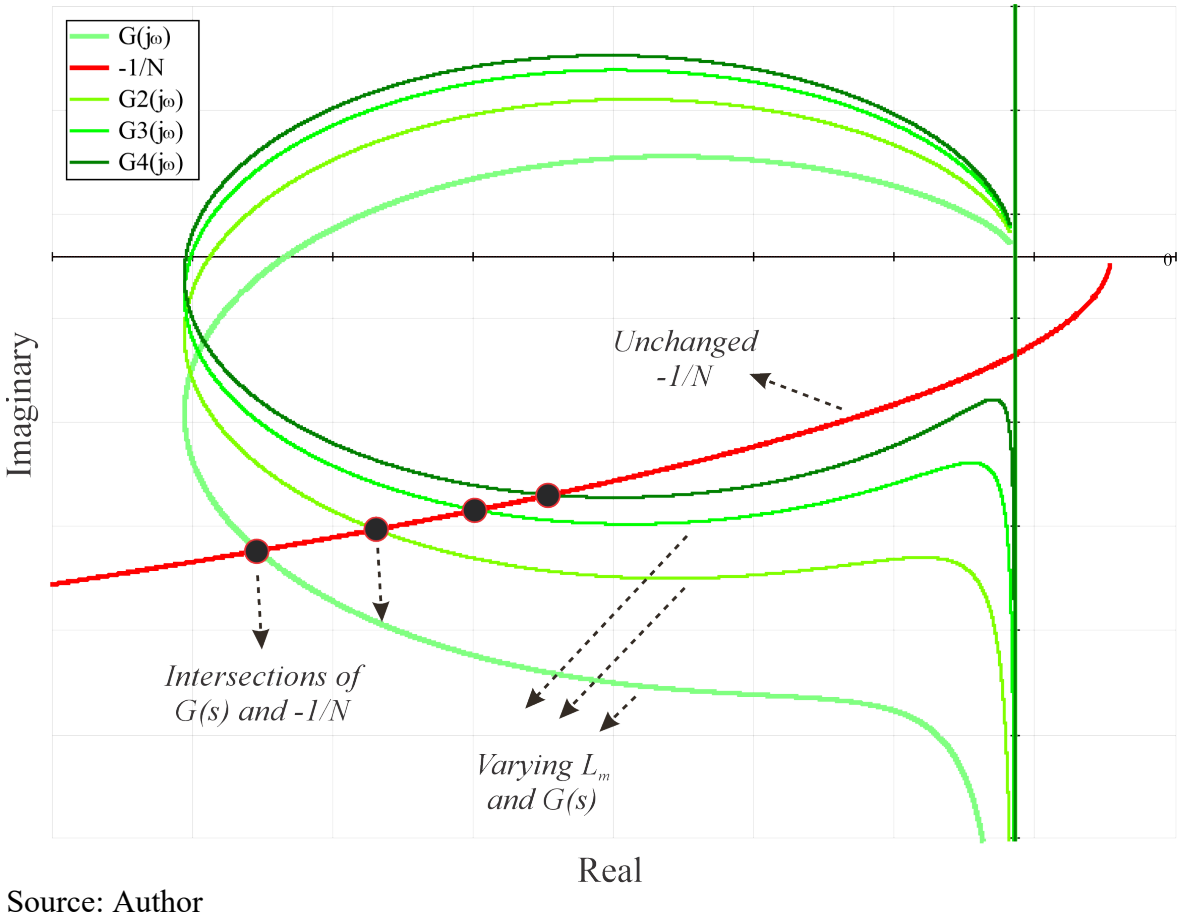

Source: Author

In Figure 63, the DFM is shown as an alternative tool to calculate the parameters of the intersection point between G(s) and -1/N. G, $G2$, $G3$, and $G4$, are various system linear blocks, each with its different value of L_m, which causes a shift upwards in the plane the higher the value of this inductance. Due to -1/N having no dependence on the magnetizing inductance, its evolution in the complex plane should not change regarding L_m, hence giving a graphic notion of how the system changes with the proposed VCT. This contrats to the Tsypkin hodograph of Figure 35.

4.5 SORC MODELING

Equation (176) shows the TF obtained for the LC series resonant converter using the EDF methodology from Chapter 3. Equation (177) shows the TF that describes the dynamic of the LR circuit defined by the auxiliary windings of the VCT, and equation (178) integrates the gain of the last two transfer functions that are only defined as gains.

$$\frac{\widehat{i_{LED}}(s)}{\widehat{f_s}(s)} = \frac{-9.686e7s^3 - 1.771e16s^2 - 1.86e22s - 1.542e28}{1s^5 + 6.497e05s^4 + 1.944e12s^3 + 7.735e17s^2 + 1.069e23s + 6.313e27} \tag{176}$$

$$\frac{\widehat{iCtrl(s)}}{\widehat{u_c}(s)} = \frac{0.08846}{3e-5s+1} \tag{177}$$

$$\frac{\widehat{L_m}(s)}{\widehat{i_{Ctrl}}(s)} \frac{\widehat{f_s}(s)}{\widehat{L_m}(s)} = 0.3 \tag{178}$$

Figure 66 shows the complete schematic for the closed-loop SORC. The current I_{LED} is measured through the current sensor module (CSM) used in (MENKE *et al.*, 2020) and shown in Figure 64 and its schematic shown in Figure 65. The CSM measures the DC output current for the power converter by measuring the voltage drop in a shunt resistor. The voltage drop in the shunt resistor is amplified, isolated, and converted to a current signal (4-20 mA). This singnal is then captured by an analogic input of the ATmega328 and compared with the current reference I_{REF}. Then, the PI controller acts accordingly, maintaining the desired current level through control of the u_c signal that determines the amount of current flowing through the auxiliary windings of the VCT.

Figure 64 - Photograph of the implemented current sensor module.

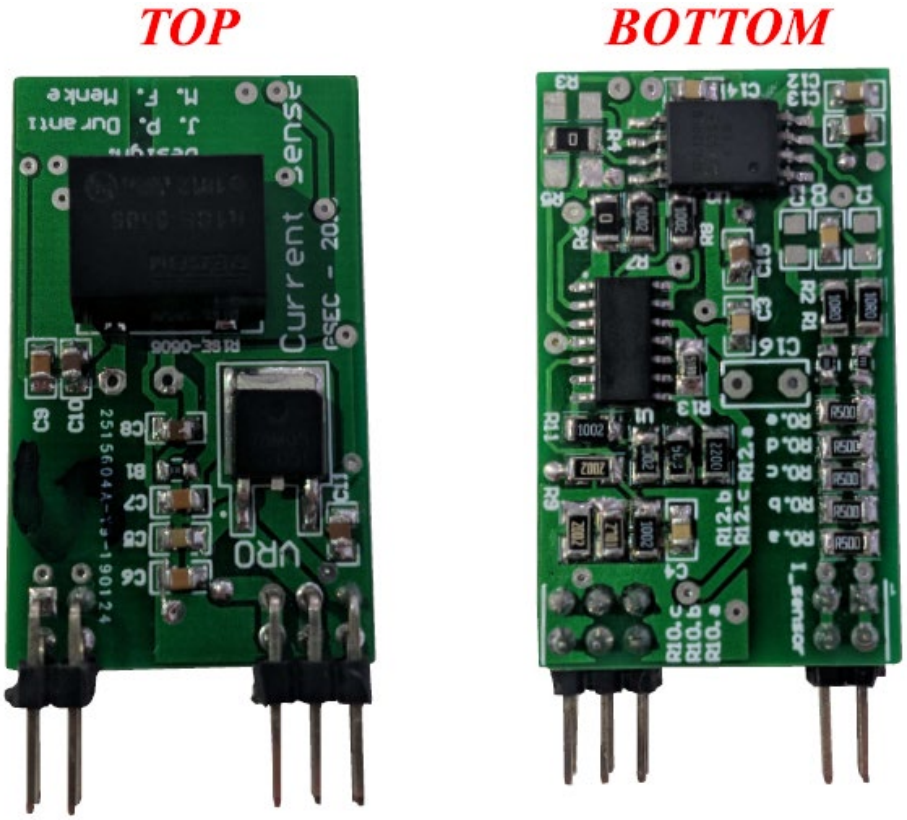

Source: (MENKE *et al.*, 2020)

Figure 65 - Circuit diagram of the Current sensor module (CSM).

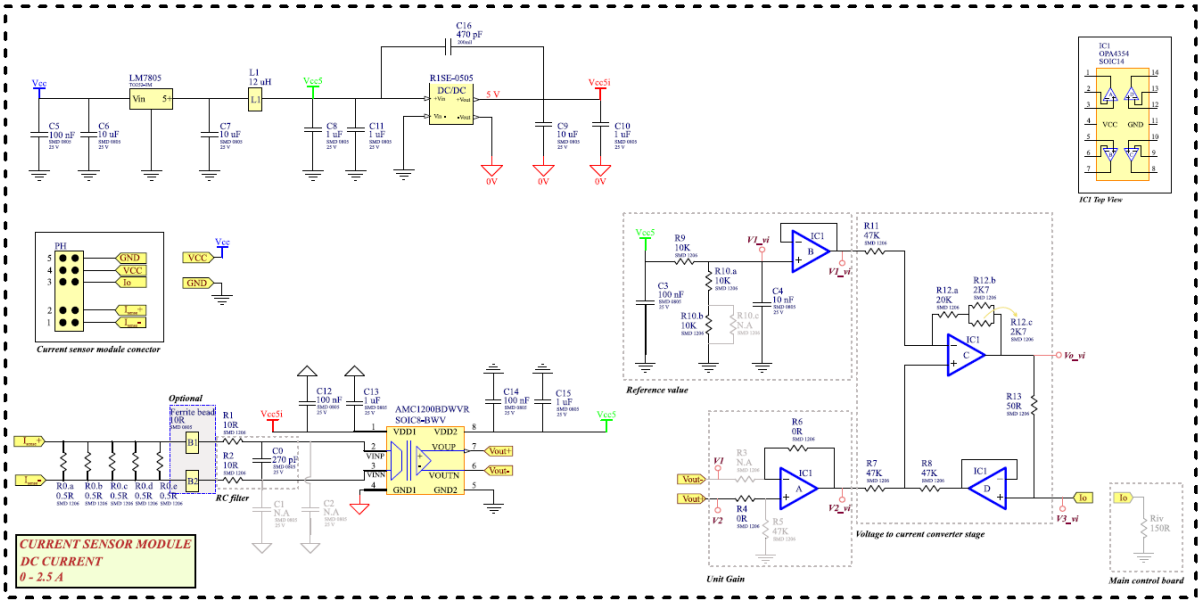

Source: (MENKE *et al.*, 2020)

Figure 66 - Full schematic of the closed-loop SORC.

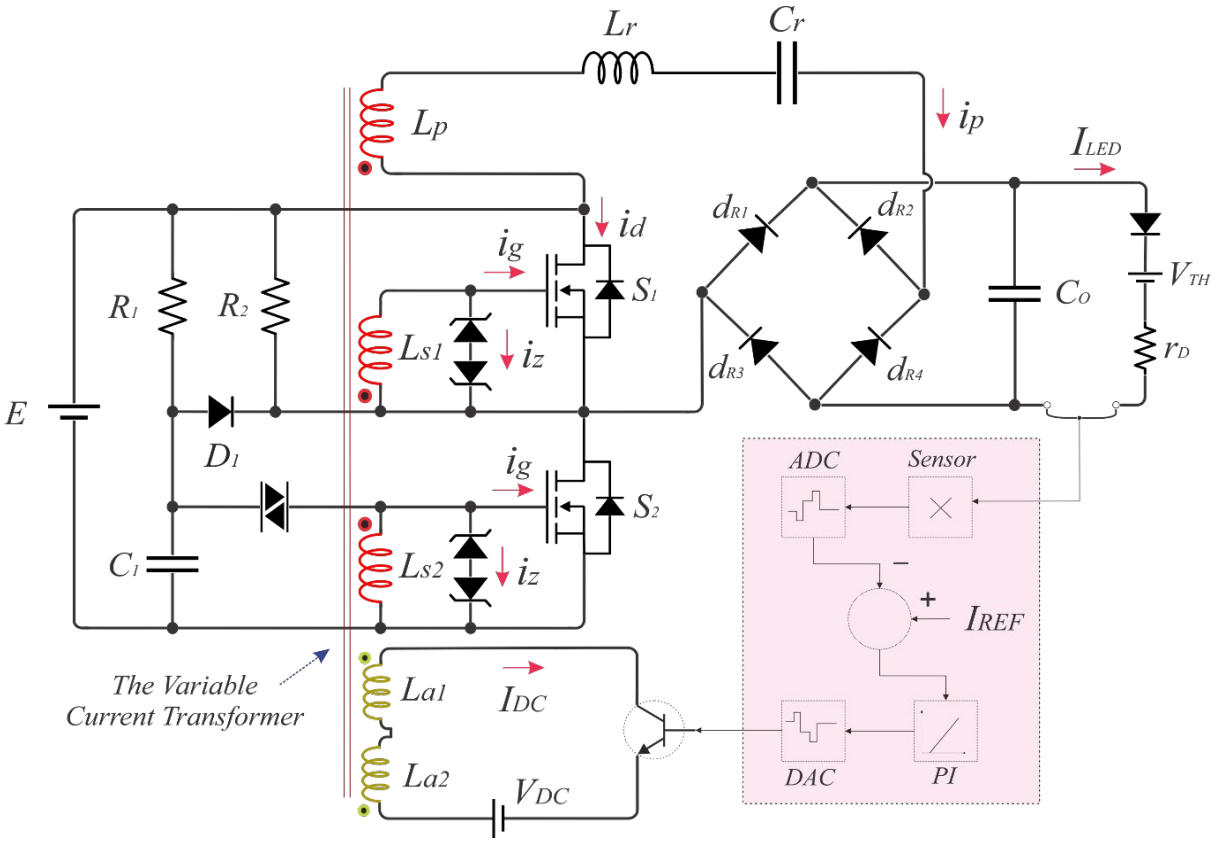

Source: Author

Figure 67 shows the open-loop dynamic behavior of I_{LED} when gradual steps are performed on the controlling signal u_c. The first interesting aspect shown is the nonlinearity imposed by the base-to-emitter saturation voltage V_{be}(sat) of the BJT, which for the emplyoed 2N2222A model is around 0.6 V. This effect can be seen as a non-existant response from I_{LED} when steps are performed on u_c, except when $V_{be}>V_{be}$(sat). This phenomenon can be easily avoided by implement a proper controller with a minimum value for u_c where $u_c>V_{be}$(sat) as shown in the implemented code for the digital controller in Appendix A. The second interesting point that is readily illustrated in the step dynamics relates to the points of maximum and minimum gains. Even though each step in u_c has exactly the same incremented value, I_{LED} responds differently to each step due to the non-linear characteristic of the VCT. Figure 26 shows the graphic of the equivalent variable L_m inductance as a function of the controling current I_{Ctrl}, and the point of maximum gain is close to the middle of I_{Ctrl} range, which translates to a middle-point for u_c as well.

Figure 67 - Gradual steps on the control signal u_c showing the dynamic of the LED current I_{LED} (Experimental).

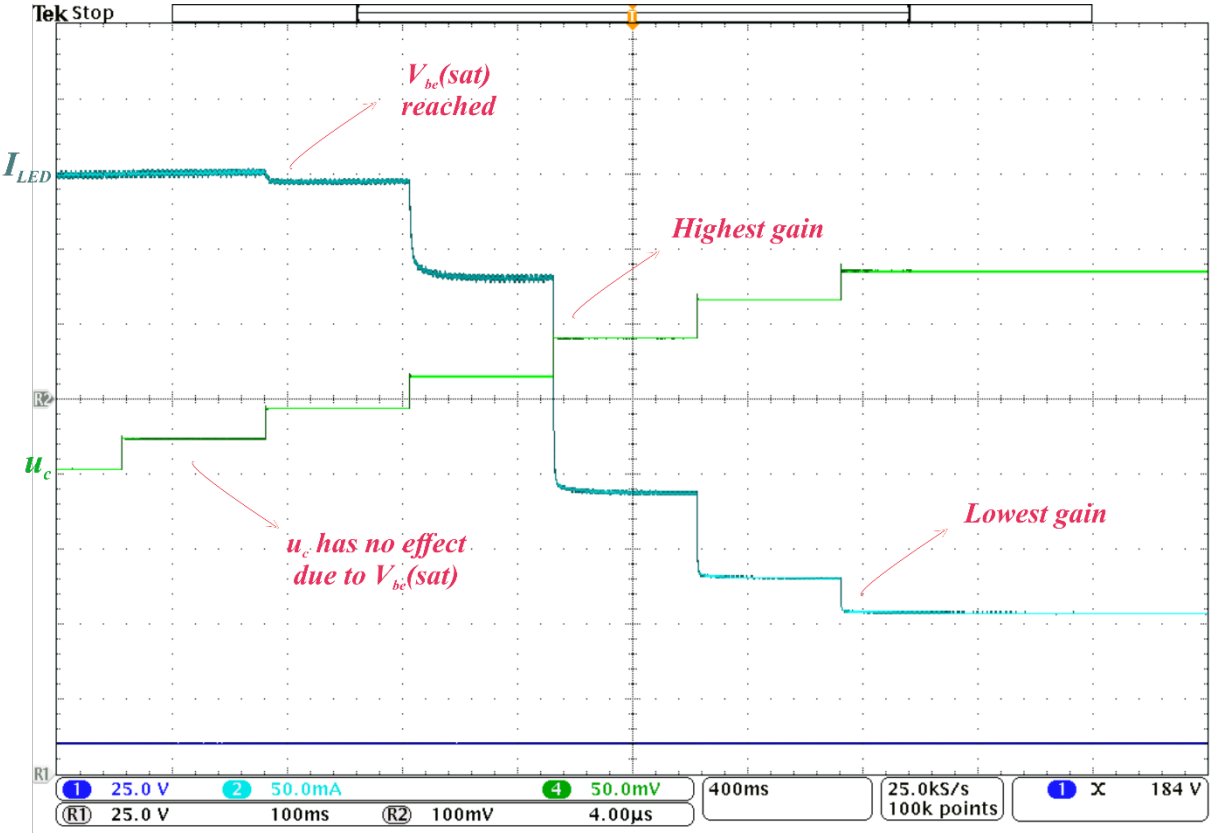

Source: Author

The aforementioned characteristics explain why the middle step on u_c in Figure 67 causes the largest step response seen from I_{LED}. In terms of control, when designing the feedback for a system such as the current one, that is capable of wide ranges of I_{LED} variation, there is usually going to be a compromise between characteristics such as overshoot (or undershoot) and settling times given that the most critical point is the one presenting the highest gains. This point will probably present the highest overshoot and designing the controller around itself should stretch the characteristic response of other gain points.

The lowest gain occurs due to the effect of the VCT's core saturation. Higher values of u_c result in even higher values of DC bias flux flowing through the external paths of the VCT, up to a point where the magnetizing inductance L_m suffers almost no change due to u_c. Furthermore, this point can be generally considered as the point with the systems' smallest overall efficiency due to the highest values of I_{Ctrl} flowing through the auxiliary windings in conjunction with the resulting switching frequency lying on the upper point of the range.

Figure 68 shows the piece of hardware used to implement a closed-loop SORC using an ACS722[31] as current sensor, which is positioned on the bottom side of the PCB on the right of the image. Due to the low sensitivity of the ACS722 and the low values of I_{LED}, a better approach ended up being to use the current sensor shown in Figure 64, resulting in more accurate results in terms of sensitivity for the measured current.

Figure 68 - Photograph of the implemented hardware.

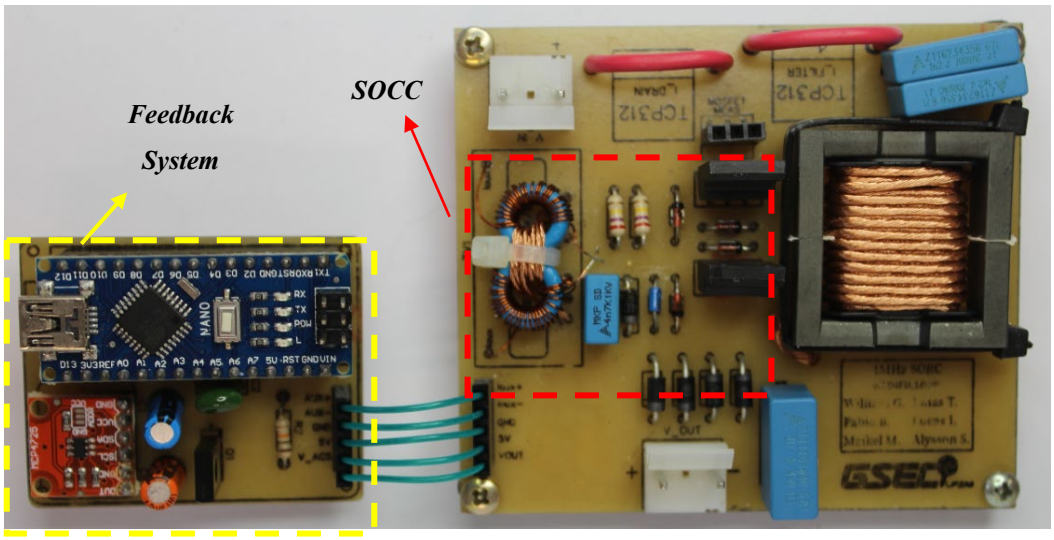

Source: Author

Figure 69 showcases the open-loop responses from I_{LED}, V_{LED} and P_{LED} as a function of u_c while the non-linear characteristic of the BJT is present. There is a visible delay in the response for two main reasons. The first one being the effect of V_{be}(sat), which withdstands any changes on I_{LED} when $u_c < V_{be}$(sat), considerably delaying the response. The second reason is related to the type of VCT configuration. Small values for I_{Ctrl} (next to zero, up to a dozen mA) usually dont effectively perform any changes on L_m on E cores, and despite performing these changes when a Toroid core is used due to its magnetic characteristics, these changes are still considerably small. Even though this delay caused by the initial I_{Ctrl} can be considered very small compared to the delay caused by V_{be}(sat), it can also be avoided by a further increasing,

[31] The ACS722 is a current sensor IC produced by Allegro Microsystems. It is an economical and precise solution for measuring AC or DC current in industrial, commercial, and communications systems. The small package is ideal for space-constrained applications while also saving costs due to reduced board area. The device consists of a precise, low-offset, linear Hall sensor circuit with a copper conduction path located near the surface of the die. Applied current flowing through this copper conduction path generates a magnetic field which is sensed by the integrated Hall IC and converted into a proportional voltage. The output of the device has a positive slope when an increasing current flows through the primary copper conduction path. For this research, and more specifically for the low current tubular LED employed, the CSM was preferred over the ACS722.

by a small amount, the value of the minimum u_c. Hence, the dynamic expressed by I_{LED} on this figure cannot be compared to the mathematical model and simulation results.

Figure 70 also shows the open-loop responses from I_{LED}, V_{LED} and P_{LED} as a function of u_c. However, these results have an u_c minimum value that is above V_{be}(sat) and also compensate the initial I_{Ctrl} problem, therefore the dynamic is absent of a delay as the non-linear characteristic is avoided, making the results of this experiment qualitatively comparable with the mathematical model and simulation results. It can be seen that at soon as the u_c signal starts changing, this change is immediately reflected into Lm changes and thus I_{LED} starts changing. Figure 72 begins the series of images of the closed-loop response of I_{LED} as steps are performed in the bus voltage E. It begins with a step from 175 to 185 V, and then 185 to 195 on Figure 73, 195 to 205 in Figure 74, and 205 to 215 in Figure 75. A negative offset was applied on u_c, I_{LED} and E in order to better visualize the closed-loop response and the bus voltage step instants. The PI controller was able to maintain closed-loop operation with reference following on the SORC by introducing an additional output current feedback into the control loop. This allowed for rapid and precise regulation of the output current. By changing the reference value of the current feedback loop, it was possible to adjust the LED current over a wide range of values while still maintaining the closed-loop reference following characteristic.

Figure 69 – Step on u_c showing the dynamics behind I_{LED} on (a) $u_c = 0$ to $u_c = 1$ and (b) $u_c = 1$ to $u_c = 0$ with the effect of BJT V_{be}(sat) present.

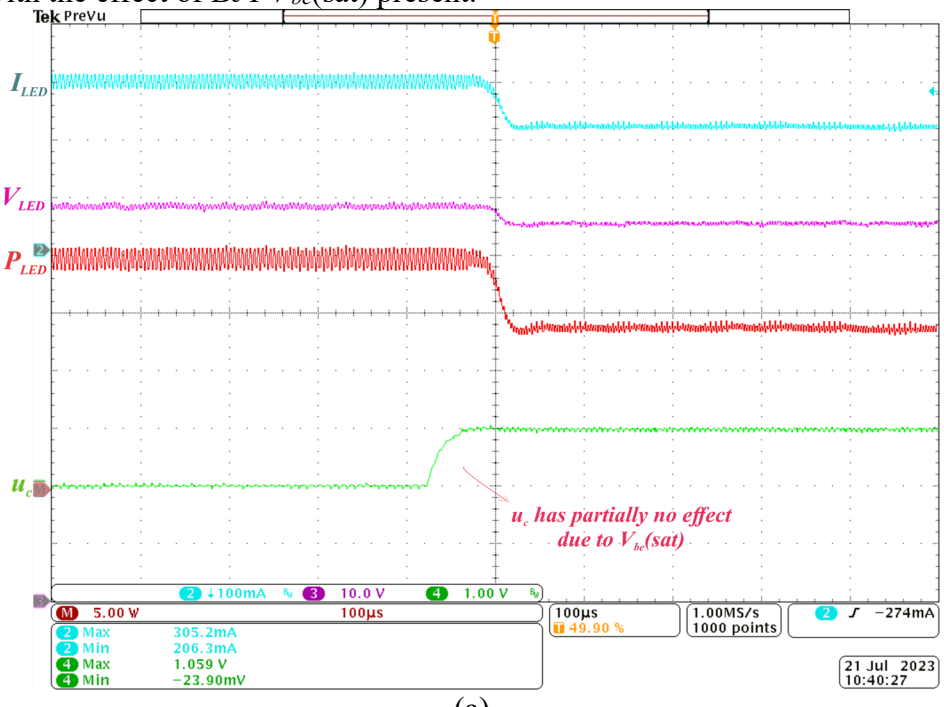

(a)

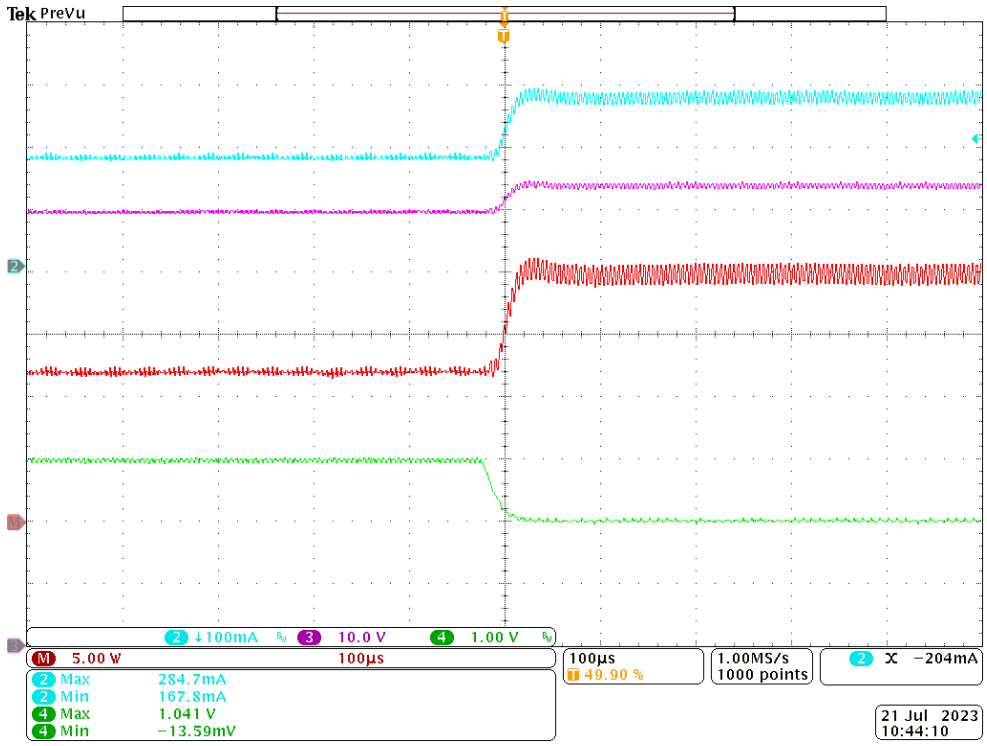

(b)

Source: Author

Figure 70 – Step on u_c showing the dynamics behind I_{LED} on (a) u_c = 1 to u_c = 1.5 and (b) u_c = 1.5 to u_c = 1 where the effect of the BJT V_{be}(sat) is not present .

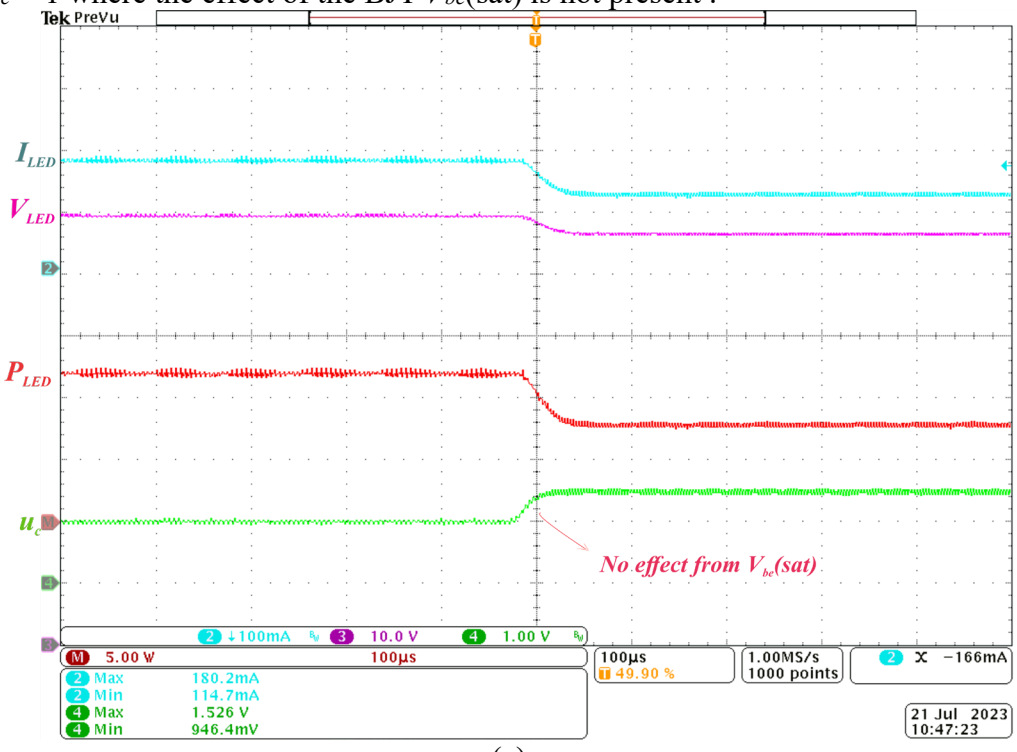

(a)

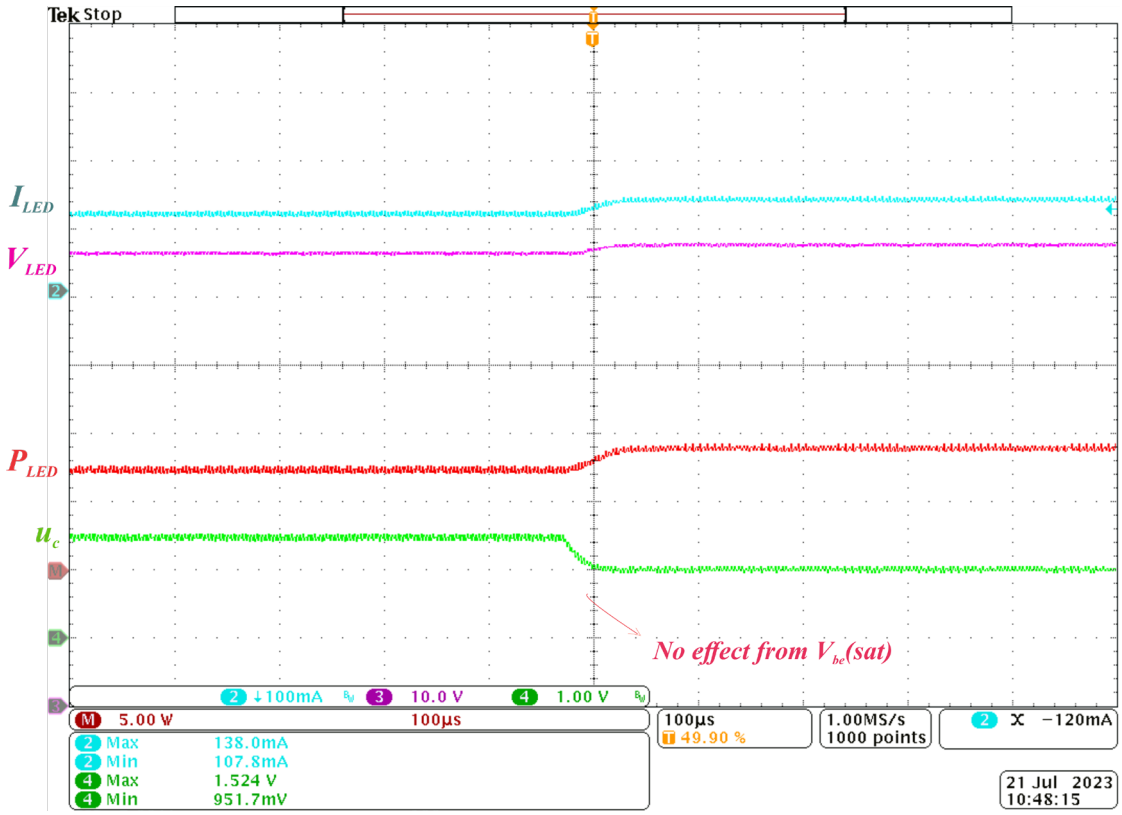

(b)

Source: Author

Figure 71 shows the comparison between the mathematical model and the PSIM simulation of the complete open-loop system composed by the BJT, VCT and LC SORC. The model was obtained around the 0.3 A nominal point, which means that the derivative of the curve L_m versus I_{Ctrl} for this point should be different than for 0.2 A, for example. In terms of quantities, this derivative – or gain, when translated into the TF – is considerably smaller for 0.3 A as compared to 0.2. This explains why the step on u_c from 0.7 (minimum V_{be}(sat) plus initial I_{Ctrl} compensation) to 0.9 translates into a good accuracy both in terms of dynamic and offset error on the mathematical model compared to the PSIM simulation. However, from 0.9 to 0.95 V, the system is still using the same derivative – or gain – of the TF designed around 0.3 A, which still gives accurate results regarding the dynamic of the system, but fails to predict the offset at around 0.26 A. When returning to values around the desgined point, the mathematical model rettains its full accuracy.

Figure 71 – Open-loop comparison between the full converter PSIM simulation and the calculated mathematical model of the complete transfer function.

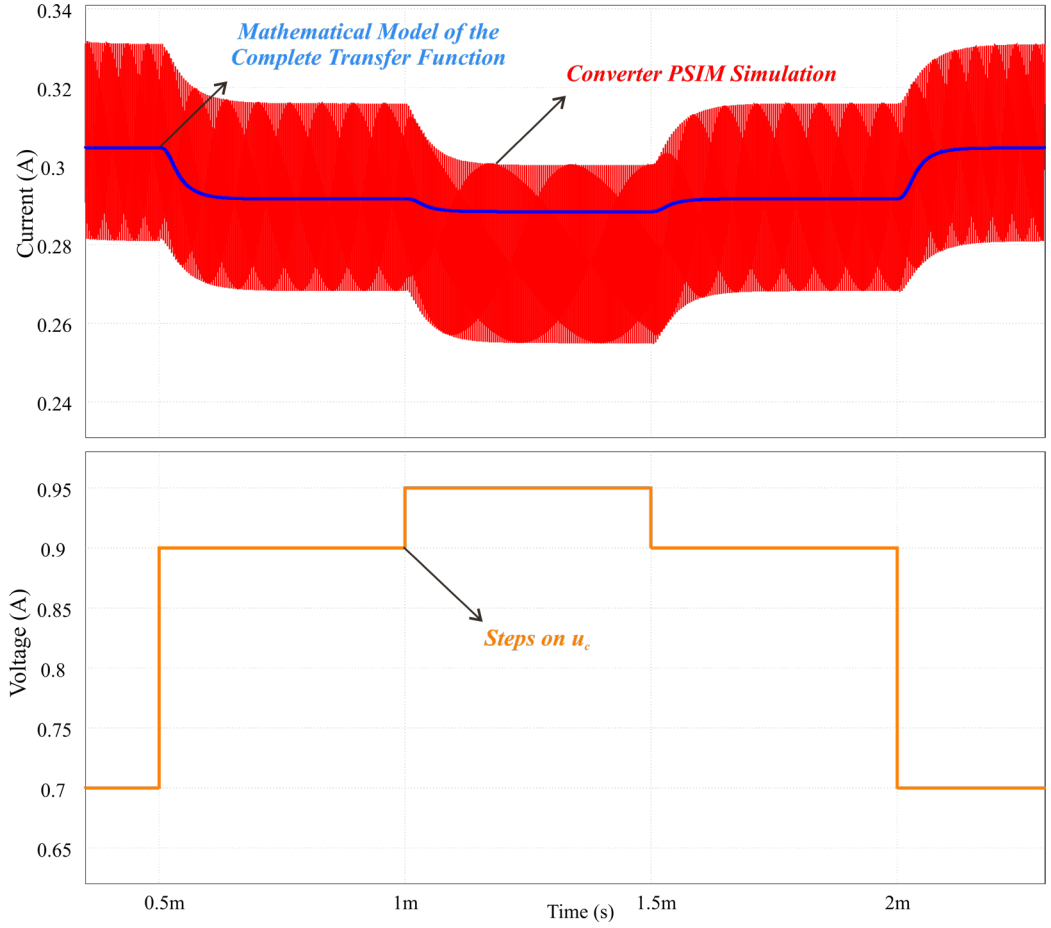

Source: Author

Figure 72 – Closed-loop response of I_{LED} as a step is performed in the bus voltage from 175 to 185 V and from 185 to 175 V.

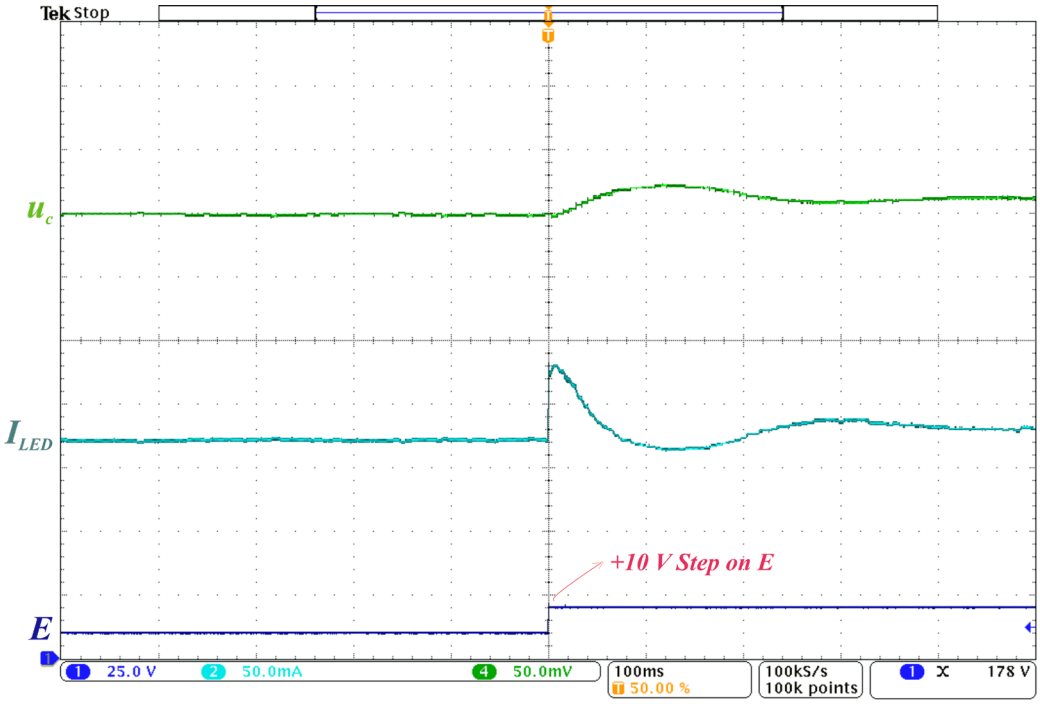

(a)

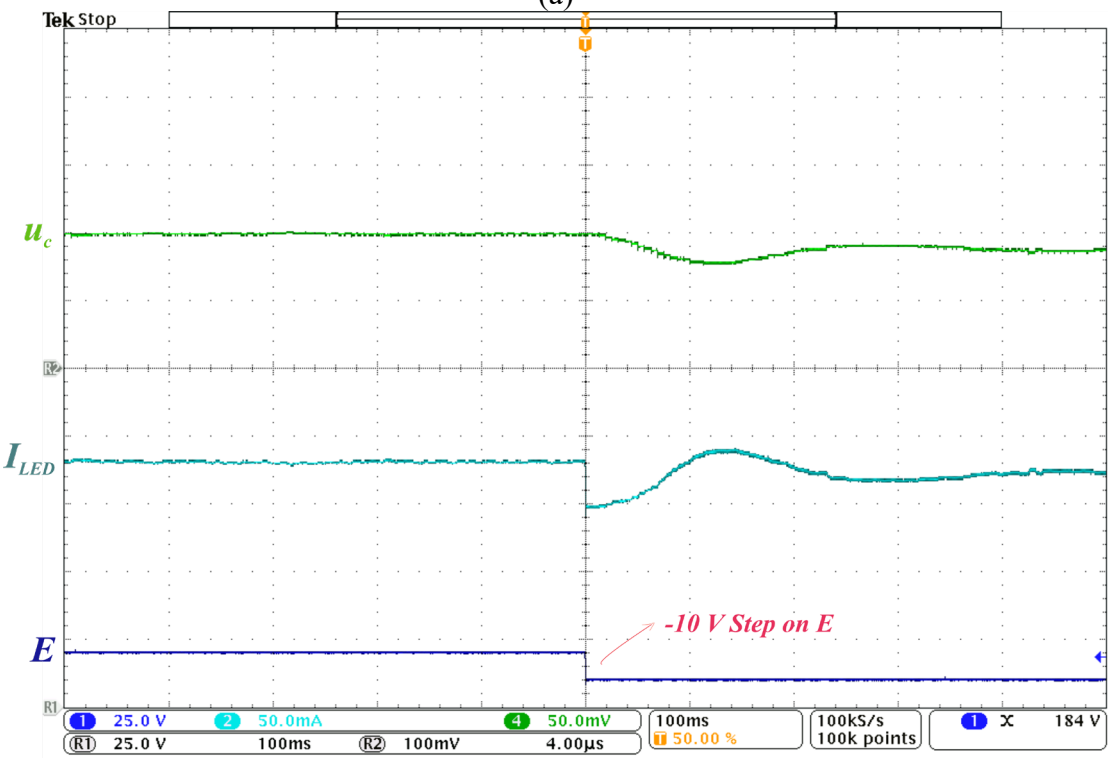

(b)

Source: Author

Figure 73 – Closed-loop response of I_{LED} as a step is performed in the bus voltage from 185 to 195 V and from 195 to 185 V.

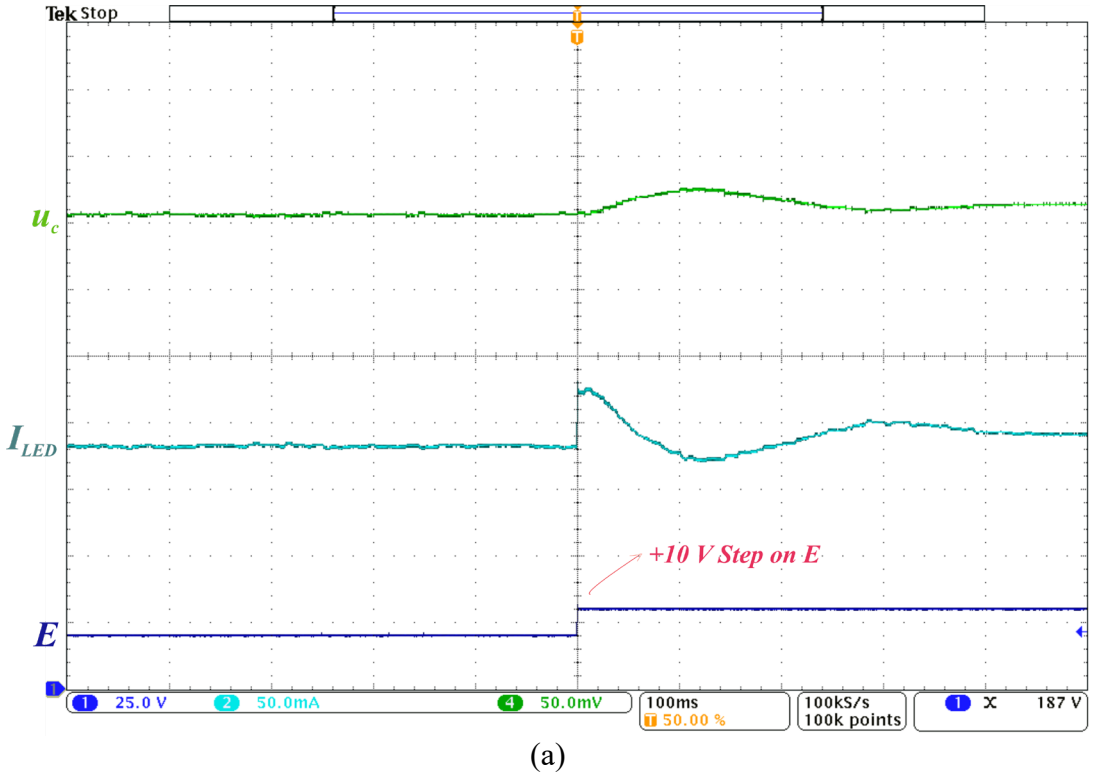

(a)

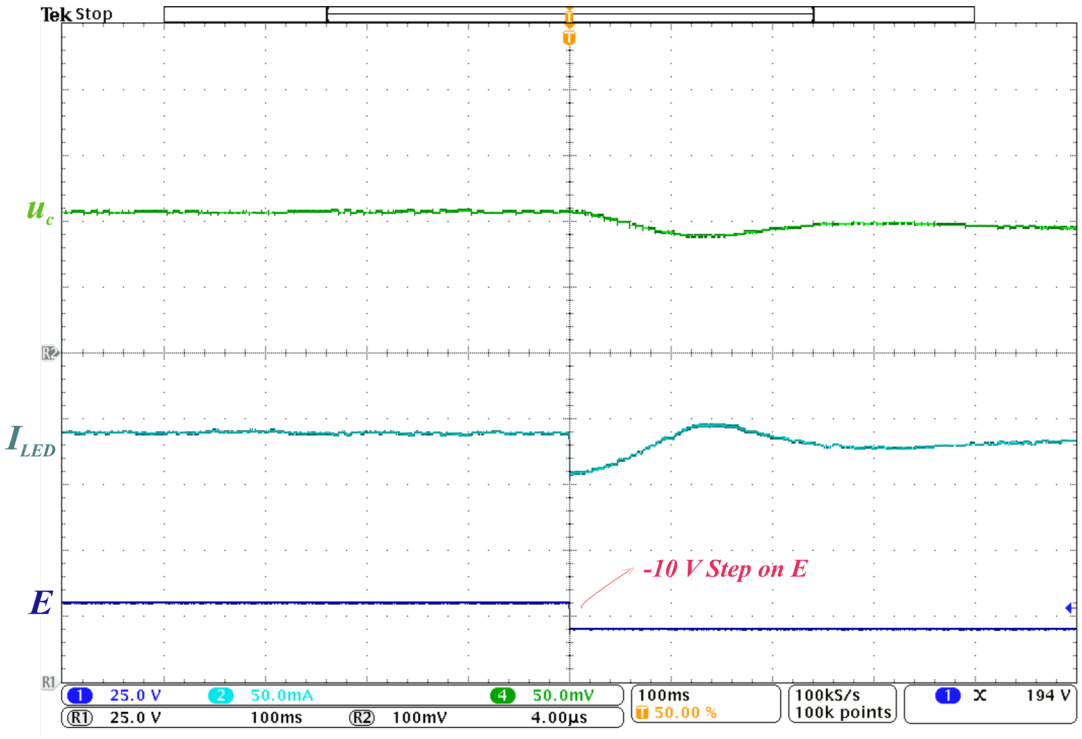

(b)

Source: Author

Figure 74 – Closed-loop response of I_{LED} as a step is performed in the bus voltage from 195 to 205 V and from 205 to 195 V.

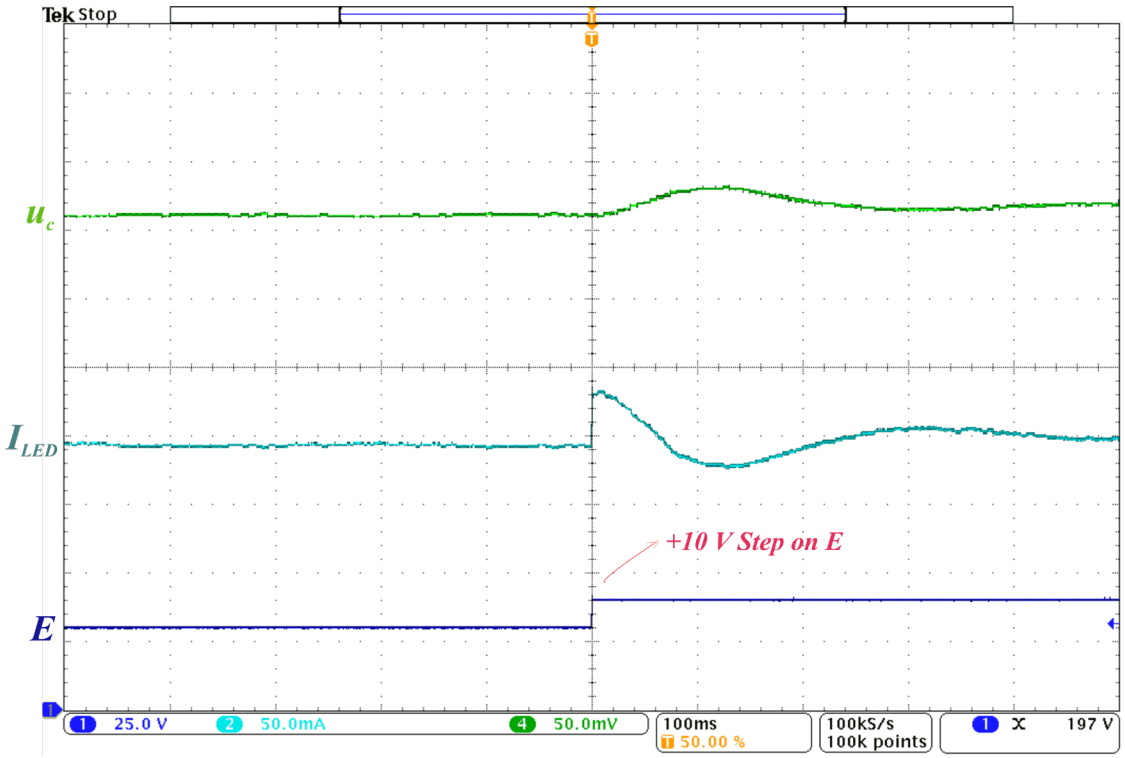

(a)

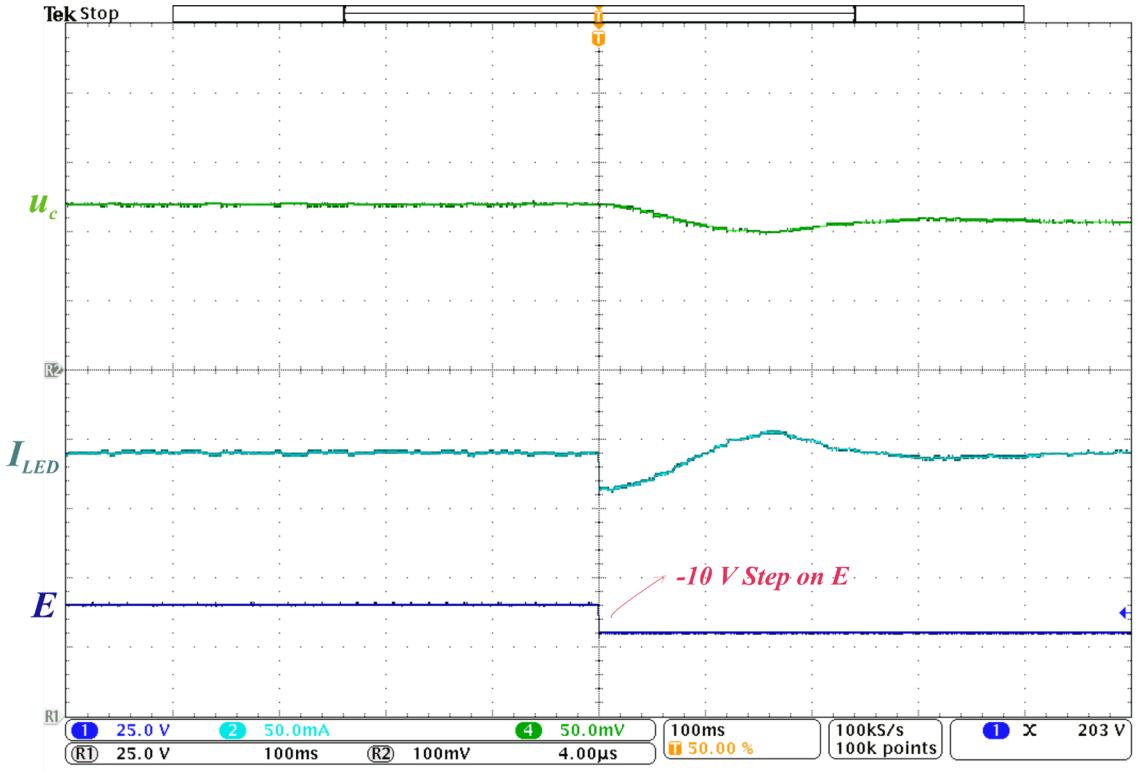

(b)

Source: Author

Figure 75 – Closed-loop response of I_{LED} as a step is performed in the bus voltage from 205 to 215 V and from 215 to 205 V.

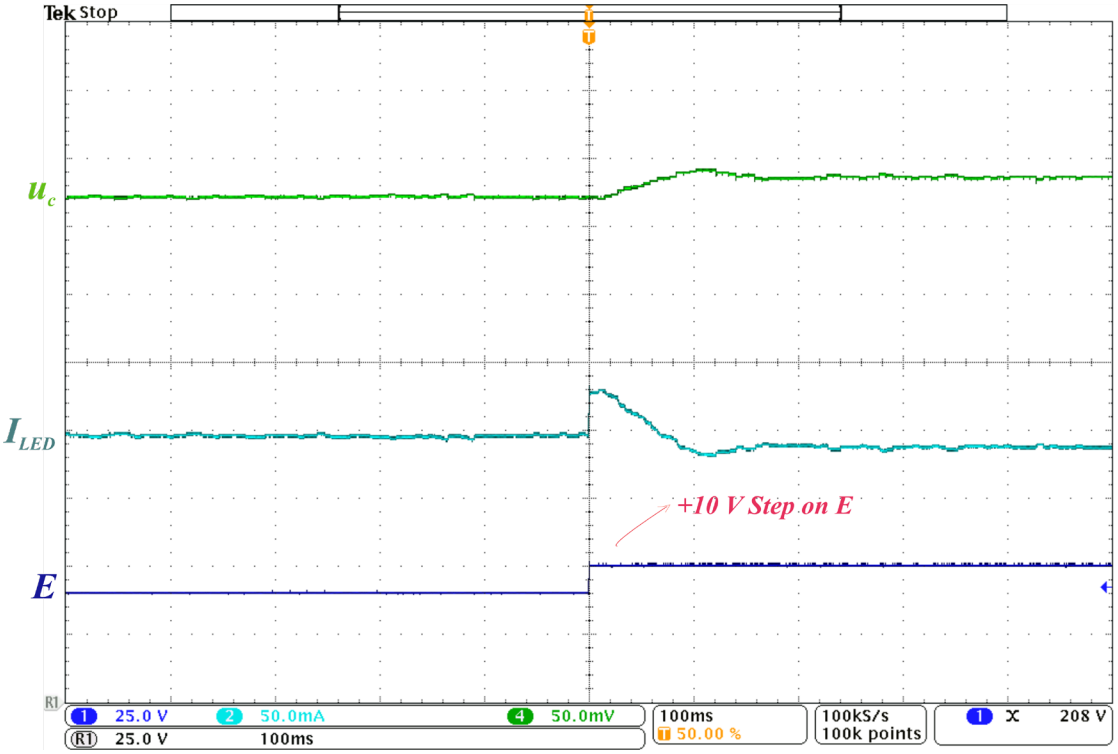

(a)

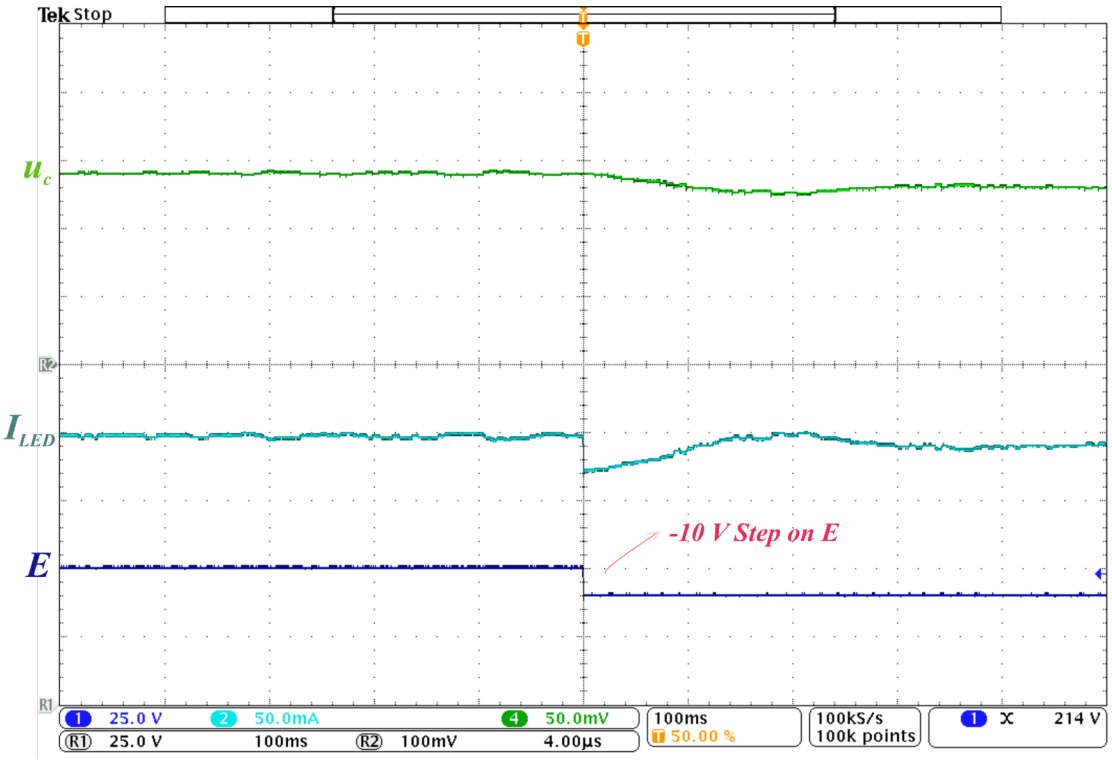

(b)

Source: Author

5

CONCLUSION AND FUTURE WORKS

5.1 CONCLUSION

This doctoral dissertation presents the development of a closed-loop SORC, beginning with an exploration of the fundamental knowledge surrounding self-oscillating systems, including their principles of operation and design techniques. The analysis then progresses to an examination of potential actuation concepts, culminating in the proposal of an actuation mechanism for the frequency variation of the SORC that stands in contrast to the methods currently available in the literature. This synergy between the device and the SORC enables closed-loop operation with an additional feedback layer on top of its intrinsic positive feedback network. The concept involves the utilization of a device called a Variable Current Transformer (VCT), where the injection of a DC current creates a DC bias flux that flows through the device's magnetic paths, effectively changing the SOCC magnetizing inductance L_m. Remarks were also made regarding the usage of the LED model in the calculation of the the LC series small signal model, where the literature review aided in showing that the LED electrical behavior should be considered during the modeling procedure, and not its equivalent resistance. However, when compared to the LED equivalent resistance, some ranges of the LED dynamic resistance can present a valid and accurate model when only the equivalent resistance is used, and this fact can be seen by the similarity between the bode plots.

The actuation method does not interfere with the filter characteristics and works similarly to traditional pulse frequency modulation, as it changes the output filter gain only through the variation of f_s and not by interfering with the duty cycle or tampering with the filter's reactive elements C_r and L_r. However, should the need arise for a change in the reactive elements of the filter, such as the series inductance working as a Variable Inductor, for example, multiple layers of control can potentially be achieved on a system where the core converter, i.e. the SORC, is usually overlooked as a solution for closed-loop applications due to its intrinsic feedback. In this case, an iterative method using the ENC and the DFM is encouraged due to the amount of varying parameters every new iteration of changes to L_r, which due to the intrinsic

positive feedback characteristic should also change f_s, along with the filter current, and output power.

Experimental and simulation results have shown the feasibility of the closed-loop SORC operating with LEDs as load, where the LED current was kept within range of the reference value. Due to the flexibility of this topology, it can operate with different types of loads, both AC and DC, under the proposed actuator mechanism. As the focus of this doctoral dissertation lies in such a mechanism, an offline data-based technique called Least Square Method was used to obtain the transfer functions related to the controlling current I_{DC} and the magnetizing inductance L_m and afterwards compared with a more complete modeling methodology using the EDF method. Even though the LSM presented satisfactory results, the complete EDF method seemed to better capture the dyanamics of the system as per the comparison of the magnitude and phase plots between the model and the simulation. The dynamic of the VCT is greatly dependent on the LR characteristic presented by its auxiliary windings. For higher number of turns on these auxiliary windings, the required u_c value to accomplish changes in I_{LED} is considerably smaller. However, the complete system dynamic shifts to a more slowly varying first order characteristic. For smaller number of turns, higher values of u_c are required to accomplish considerable changes on I_{LED}, while the complete system dynamic shifts to a second order underdamped characteristic.

The system's efficiency varied according to the necessity of modulation, based on the applied input voltage and the reference value for the LED current. Given the optimal design of the VCT with a safe turns ratio margin of 1:9 that granted a considerably low current level on its secondary, for the nominal case of 170 V, an efficiency of over 90 % was reached for the presented controled range. For wider ranges of modulation levels, the efficiency was not fully analyzed, but will certainly be smaller due to higher levels on . A more expanded analysis is due in the sense of experimentally testing the operation of the topology in terms of bus voltage and reference current over both their total ranges.

The scientific contribution of a work that analyses the intricacies of SORCs for lighting applications is significant. This is particularly true when the literature has no previous efforts that performed small signal model analysis or proposed a standard feedback control system by designing controllers such as a PI controller from the control-to-output transfer functions of SORCs. These converters are simple, robust, and cost-effective while performing their own gate drive with self-sustained frequency. However, the design and control of SORCs can be challenging due to their inherent inability to operate under pulse frequency modulation without extra circuitry. This is where the novelty of the work lies. By proposing a robust, efficient, and

simple way of controlling the SORC through frequency modulation, the work addresses a significant gap in the literature. The proposed method involves varying the self-oscillating frequency through the equivalent magnetizing inductance of the SOCC, using a mechanism called variable current transformer. Through the injection of a small controllable DC current, it becomes possible to modulate the frequency of resonant converters. This allows the self-oscillating system to follow a reference current signal, operating in closed-loop over a wide range of input voltage and load variation. In terms of small signal model analysis, accurate small-signal modeling for resonant converters has been a challenge due to the underlying assumptions and the presence of non-linearities. However, the work proposes the utilization of different small-signal analysis techniques such as the extended describing function modeling for the resonant converter stage, while proposing solutions for the characteristics of the small-signal transfer functions related to the self-oscillating portion of the system.

In conclusion, the work provides a significant contribution to the field by proposing a novel method for controlling SORCs and performing small signal model analysis. This not only enhances our understanding of SORCs but also opens up new possibilities for their application in lighting systems.

5.2 PROPOSAL FOR FUTURE WORKS

The following future works are proposed:

1. The temperature variability of an LED string can significantly affect its electrical characteristics. As the temperature increases, the forward voltage decreases. This can lead to performance issues in the SORC that drives these LEDs. One of the most important future works regarding the utilization of SORCs to operate LEDs relates to the prevention or compensation for the variances caused by the effect of the temperature. For that, some key aspects must be considered.
    a. Modeling Temperature Effects: The first step is to understand and model the temperature effects on the LED and the SORC. This involves creating a thermal model that captures the relationship between temperature and the electrical characteristics of the LED. For the SORC, an electro-thermal model can possibly be constructed, by coupling a temperature-dependent equivalent circuit model with the thermal model such as the one shown by (CAI *et al.*, 2021).

b. Temperature Compensation: Once the models are in place, the next step is to design a temperature compensation mechanism. This could involve using a high-precision temperature sensor and a high-performance digital circuit (GUO *et al.*, 2017), or a thermistor-based temperature compensation circuit. These systems can detect ambient temperature variations and adjust the operation of the SORC accordingly.
c. Feedback Control System: A feedback control system can be implemented to continuously monitor the temperature and adjust the operation of the SORC in real-time. This could involve using a phase-locked loop (PLL) configuration with thermal feedback (GORJI ZADEH *et al.*, 2022), which can significantly improve the temperature stability of the system.
d. Controller Design: The design of controllers such as a PI controller is crucial for the effective operation of the feedback control system. The controller parameters should be tuned to ensure optimal performance under varying temperature conditions.
e. Potential for Adaptive Control: Adaptive control is a method used by a controller which must adapt to a controlled system with parameters that vary or are initially uncertain. This is particularly relevant in the context of SORCs where the parameters of the system can change due to factors such as temperature variations, component aging, and load changes. In the context of SORCs, this could involve estimating parameters such as the resonant frequency, the quality factor of the resonant tank, and the load resistance. These parameters can be estimated using methods such as recursive least squares and gradient descent (ANNASWAMY; FRADKOV, 2021). Once these parameters are estimated, they can be used to adapt the control law of the SORC in real-time. For example, if the estimated resonant frequency deviates from its desired value, the control law can be adjusted to bring it back to the desired value through the injection of a small DC current on the auxiliary windings of the VCT. This can help to maintain the performance of the SORC under varying operating conditions.

By implementing these strategies, the SORC can effectively compensate for the electrical characteristic variance caused by the LED temperature, ensuring stable and efficient operation of the lighting system.

2. Study of an iterative method using the ENC and the DFM for when extra feedback loops are used in conjunction with the presented method, such as the variable L_r.
3. A similar study and modeling of the closed-loop SORC developed on the time-domain.

4. A more detailed analysis of the bus voltage limits and the efficiencies presented over the whole range of modulation.
5. Comparison between the different equivalent small signal models for the inverter stage and their effects on the complete final transfer function through an extensive analysis of information such as their bode plots.
6. A more detailed analysis on the weights of each transfer function represented by the generated EDF from the filter compared to the LR dynamic from the VCT. Analyze and discuss which presents a more dominant effect on the final transfer function and which number of turns on the auxiliary windings is capable of completely modeling the system as a first order equivalent.
7. Further understand the effects and characteristics of the instability zones detected during the filter analysis, the effect of both the filter Q and R and the implications of working within and without the stability limits.
8. The use of a microcontroller to implement a PI controller for a SORC opens up the possibility of having multiple PI controller designs, each tailored for a specific range of operating frequencies. This approach can be particularly beneficial in applications where the operating frequency of the SORC varies significantly. For instance, one could design a PI controller for the frequency range of 100 to 200 kHz, another for the range of 200 to 400 kHz, and yet another for the range of 400 to 600 kHz, and so on. Each of these PI controllers would be optimized for its specific frequency range, ensuring optimal performance across the entire operating frequency range of the SORC. The microcontroller could be programmed to automatically switch between these different PI controllers based on the current operating frequency of the SORC. This could be achieved by continuously monitoring the operating frequency and implementing a decision-making algorithm that selects the appropriate PI controller based on the current frequency. This approach would ensure that the SORC always operates with a PI controller that is optimized for its current operating frequency, thereby improving the overall performance and efficiency of the system. It would also make the system more robust to variations in operating conditions, as the control system would automatically adapt to changes in the operating frequency. Moreover, the use of a microcontroller allows for easy updates and modifications to the control system. If the performance of a particular PI controller is found to be suboptimal, its parameters can be easily adjusted. Similarly, if a new operating frequency range needs to be accommodated, a new PI controller can be designed and added to the system with relative ease.

9. The work presented in this doctoral dissertation has demonstrated the feasibility of using a PI controller for the feedback of a SORC, using a VCT to vary the magnetizing inductance of the SOCC in order to modify the frequency. The results have shown that this approach can effectively control the operation of the SORC, thereby validating the main objective of the doctoral dissertation. However, the design of the PI controller was not detailed in this work. This was primarily because the main objective of the doctoral dissertation was to show that a SORC can have an actuation mechanism, which can be used to close a loop on the SORC, and also to demonstrate that the SORC can be modeled. The in-depth details of the PI controller design were beyond the scope of this doctoral dissertation. As a future work, it would be valuable to delve into the specifics of the PI controller design. This would involve a detailed analysis of how the controller parameters are chosen and tuned for optimal performance. It would also involve a thorough investigation of the stability and robustness of the controller under varying operating conditions. Furthermore, the impact of the controller design on the overall performance and efficiency of the SORC could be explored. In addition, future work could also investigate the use of more advanced control strategies, such as adaptive control or model predictive control, for the SORC. These control strategies could potentially offer improved performance and robustness compared to a PI controller. In conclusion, while this doctoral dissertation has made significant strides in demonstrating the feasibility of using a controller for the feedback of a SORC, there is still much work to be done in terms of detailing the design of the PI controller and exploring more advanced control strategies. These are exciting avenues for future research in this field.
10. An interesting addition would be to extend the stability analysis of SORCs presented in the second chapter by varying the parameters of the self-oscillating command circuit, such as the Zener voltage. The Zener voltage plays a crucial role in determining the operating point of the SORC, and different Zener voltages could potentially lead to different stability characteristics. Additionally, the effect of using different MOSFETs should also be investigated. MOSFETs with different gate charges and capacitances can have a significant impact on the switching characteristics of the SORC, which in turn can affect its stability. By testing a variety of MOSFETs, a more comprehensive understanding of the stability of SORCs could be achieved. Thos proposal would not only contribute to a more in-depth stability analysis of SORCs but also provide valuable insights for the design and optimization of these converters. This could potentially lead to the development of more robust and efficient SORCs for a wide range of applications.

RESULTING SCIENTIFIC PRODUCTION

W. G. Rosa, L. M. Ilha, J. R. Tibola, M. F. Menke, F. E. Bisogno and Á. R. Seidel, "**A Control Actuation Concept for Self-Oscillating Resonant Converters**," in IEEE Journal of Emerging and Selected Topics in Power Electronics, doi: 10.1109/JESTPE.2021.3122838.

Abstract:

This paper presents a concept of controller actuation mechanism for Self-Oscillating Resonant Converters. Simplicity, robustness, and cost-effectiveness are amongst the main features of this type of converter. Described as a self-oscillating system with an intrinsic positive-type feedback switching network, also known as the Self-Oscillating Command Circuit, it performs its own gate-drive with self-sustained frequency, designed around an equilibrium point. Designers often disregard this converter as an explicit solution for closed-loop applications, especially those that require extra layers of control, due to its inherent inability to operate under pulse frequency modulation without extra circuitry. Thus, in this paper, a robust, efficient, and simple way of controlling the self-oscillating resonant converter through frequency modulation is proposed. The idea consists of varying the self-oscillating frequency through the equivalent magnetizing inductance of the self-oscillating command circuit, employing a mechanism called Variable Current Transformer. Thus, through the injection of a small controllable DC current, it is possible to modulate the frequency of resonant converters. This allows the self-oscillating system to follow a reference current signal, operating in closed-loop over a wide range of input voltage and load variation.

BIBLIOGRAPHY

ALMARDY, M.; BHAT, A. K. S. Three-phase fixed-frequency interleaved (LC)(L)-type series-resonant converter with a capacitive output filter. **The Journal of Engineering**, [*s. l.*], v. 2019, n. 17, p. 4178–4184, 2019.

ALMEIDA, P. S. *et al.* Matching LED and Driver Life Spans: A Review of Different Techniques. **IEEE Industrial Electronics Magazine**, [*s. l.*], v. 9, n. 2, p. 36–47, 2015.

ALMEIDA, P. S. **Síntese de conversores ressonantes com alto fator de potência e alta eficiência para o acionamento de diodos emissores de luz**. 2014. 218 f. - Universidade Federal de Juiz de Fora, [*s. l.*], 2014.

ALONSO, J. M. *et al.* A Systematic Approach to Modeling Complex Magnetic Devices Using SPICE: Application to Variable Inductors. **IEEE Transactions on Power Electronics**, [*s. l.*], v. 31, n. 11, p. 7735–7746, 2016a.

ALONSO, J. M. *et al.* A Systematic Approach to Modeling Complex Magnetic Devices Using SPICE: Application to Variable Inductors. **IEEE Transactions on Power Electronics**, [*s. l.*], v. 31, n. 11, p. 7735–7746, 2016b.

ALONSO, J. M. *et al.* SPICE Modeling of Variable Inductors and Its Application to Single Inductor LED Driver Design. **IEEE Transactions on Industrial Electronics**, [*s. l.*], v. 64, n. 7, p. 5894–5903, 2017.

ANNASWAMY, A. M.; FRADKOV, A. L. A historical perspective of adaptive control and learning. **Annual Reviews in Control**, [*s. l.*], v. 52, p. 18–41, 2021.

ASLAM, M.; ALBASSAM, M. Forecasting of Wind Speed Using an Interval-Based Least Square Method. **Frontiers in Energy Research**, [*s. l.*], v. 10, 2022.

ATHERTON, D. P. Relay Control Systems (Ya. Z. Tsypkin). **SIAM Review**, [*s. l.*], v. 29, n. 4, p. 643–647, 1987. Disponível em: http://www.worldscientific.com/doi/abs/10.1142/9789812564436_0003.

BARKHORDARIAN, V. Power MOSFET basics. **Powerconversion and Intelligent Motion**, [*s. l.*], v. 22, n. 6, p. 28–39, 1996. Disponível em: www.irf.com. Acesso em: 29 jan. 2018.

BISOGNO, F. E. *et al.* Resonant filter applications in electronic ballast. *In*: , 2002. **Conference Record - IAS Annual Meeting (IEEE Industry Applications Society)**. [*S. l.*]: IEEE, 2002. p. 348–354. Disponível em: http://ieeexplore.ieee.org/document/1044111/. Acesso em: 10 dez. 2018.

BONACHE-SAMANIEGO, R. *et al.* Analysis and Design of Self-Oscillating Resonant Converters with Loss-Free Resistor Characteristics. **Energies**, [*s. l.*], v. 13, n. 14, p. 3743, 2020. Disponível em: https://www.mdpi.com/1996-1073/13/14/3743.

CAI, Y. *et al.* Electro-thermal model for lithium-ion battery simulations. **Journal of Power Electronics**, [*s. l.*], v. 21, n. 10, p. 1530–1541, 2021.

CHANG, C. Self-oscillating electronic ballast analysis using the relay systems approach. **IEEE Transactions on Industry Applications**, [*s. l.*], v. 37, n. 1, p. 255–261, 2001.

CHANG, C. H. *et al.* Small signal modeling of LLC resonant converters based on extended describing function. **Proceedings - 2012 International Symposium on Computer, Consumer and Control, IS3C 2012**, [*s. l.*], p. 365–368, 2012.

CHANG, C.; CHANG, J.; BRUNING, G. W. Analysis of the self-oscillating series resonant inverter for electronic ballasts. **IEEE Transactions on Power Electronics**, [*s. l.*], v. 14, n. 3, p. 533–540, 1999.

CYR, J. M. *et al.* Etude comparative de differentes topologies de convertisseurs a resonance. **Canadian Journal of Electrical and Computer Engineering**, [*s. l.*], v. 20, n. 4, p. 193–201, 1995.

DA ROSA, W. G. *et al.* Design Approach for a Self-Oscillating Resonant Converter Operating in High Frequency for LED Applications. **IEEE Journal of Emerging and Selected Topics in Power Electronics**, [*s. l.*], v. 6, n. 3, p. 1154–1165, 2018.

DE, J. *et al.* Automatic lamp detection technique for fluorescent lamps electronic ballasts. *In*: , 2012. **Conference Record - IAS Annual Meeting (IEEE Industry Applications Society)**. [*S. l.*]: IEEE, 2012. p. 1–8. Disponível em: http://ieeexplore.ieee.org/document/6374058/.

DE MELO, M. F. *et al.* Self-oscillating series-resonant led driver applied to reduce low-frequency current ripple transmission. *In*: , 2015. **IEEE Industry Application Society - 51st Annual Meeting, IAS 2015, Conference Record**. [*S. l.*]: IEEE, 2015.

DO PRADO, R. N. *et al.* A design method for electronic ballast for fluorescent lamps. *In*: , 2000. **IECON Proceedings (Industrial Electronics Conference)**. [*S. l.*]: IEEE, 2000. p. 2279–2284. Disponível em: http://ieeexplore.ieee.org/document/972352/. Acesso em: 12 dez. 2018.

DUBOVIK, O. *et al.* A Comprehensive Description of Multi-Term LSM for Applying Multiple a Priori Constraints in Problems of Atmospheric Remote Sensing: GRASP Algorithm, Concept, and Applications. **Frontiers in Remote Sensing**, [*s. l.*], v. 2, 2021.

FLORES-GARCÍA, E. *et al.* Analysis and design method for high-frequency self-oscillating electronic ballasts. **IEEE Transactions on Industry Applications**, [*s. l.*], v. 47, n. 6, p. 2430–2436, 2011. Disponível em: http://ieeexplore.ieee.org/document/6022779/. Acesso em: 16 dez. 2018.

FLORES-GARCÍA, E. *et al.* Analysis and design method for high frequency self-oscillating electronic ballasts. **2010 IEEE Energy Conversion Congress and Exposition, ECCE 2010 - Proceedings**, [*s. l.*], v. 47, n. 6, p. 1343–1346, 2010.

GANZ, A. G. A Simple, Exact Equivalent Circuit for the Three-Winding Transformer. **IRE Transactions on Component Parts**, [*s. l.*], v. 9, n. 4, p. 212–213, 1962.

GAO, J. *et al.* The research on avoiding flux imbalance in sinusoidal wave inverter. *In*: , 2000. **Proceedings - IPEMC 2000: 3rd International Power Electronics and Motion Control Conference**. [*S. l.*]: Int. Acad. Publishers, 2000. p. 1122–1126.

GORJI ZADEH, S. A. *et al.* CMOS die area temperature compensation using a phase-locked loop with thermal-feedback. **Analog Integrated Circuits and Signal Processing**, [*s. l.*], v. 113, n. 3, p. 315–329, 2022.

GUO, Z. *et al.* Design and Experimental Research of a Temperature Compensation System for Silicon-on-Sapphire Pressure Sensors. **IEEE Sensors Journal**, [*s. l.*], v. 17, n. 3, p. 709–715, 2017.

HU, C. C. **Modern Semiconductor devices for Integrated Circuits**. [*S. l.*]: Prentice Hall, 2010.

HUANG, H. Designing an LLC resonant half-bridge power converter. **TI Power Supply Design Seminar SEM1900**, [*s. l.*], 2010.

INFINEON. **Calculate and minimize the dead time for IGBTs**. [*S. l.*], 2021. Disponível em: https://www.infineon.com/dgdl/Infineon-Deadtime_calculation_for_IGBT_modules-ApplicationNotes-v01_00-EN.pdf?fileId=db3a30431a5c32f2011a5daefc41005b. .

INSTRUMENTS, T. **LM5106 100-V Half-Bridge Gate Driver With Programmable Dead-Time**. [*S. l.*], 2006. Disponível em: https://www.ti.com/lit/pdf/snvs424. .

INTERNATIONAL RECTIFIER. **Use Gate Charge to Design the Gate Drive Circuit for Power MOSFETs and IGBTs - Application Note AN-944**. [*S. l.: s. n.*], [*s. d.*]. Disponível em: http://web.mit.edu/6.131/www/document/gate_drive.pdf. Acesso em: 29 jan. 2018.

J. S. GLASER, R. A. Z. **Dimmable self-oscillating electronic ballast for fluorescent lamp**. Concessão: 2002.

JAIN, A.; MASSIMIANI, I. C. LCC Resonant Converter Design and Transfer Function Computation Using FHA Analysis. **2021 International Conference on Nascent Technologies in Engineering, ICNET 2021 - Proceedings**, [*s. l.*], 2021.

JIN, K.; RUAN, X. Hybrid full-bridge three-level LLC resonant converter - A novel DC-DC converter suitable for fuel cell power system. *In*: , 2005. **PESC Record - IEEE Annual Power Electronics Specialists Conference**. [*S. l.: s. n.*], 2005. p. 361–367. Disponível em: http://ieeexplore.ieee.org/document/1705640/. Acesso em: 10 dez. 2018.

JUDD, F. F. Relationships between tsypkin, hamel and approximate limit cycle analyses. **International Journal of Control**, [*s. l.*], v. 21, n. 4, p. 641–653, 1975. Disponível em: http://www.tandfonline.com/doi/abs/10.1080/00207177508922018. Acesso em: 13 dez. 2018.

JUDD, F. F.; CHIRLIAN, P. M. Graphical analysis and design of limit cycles in autonomous relay control systems. **International Journal of Control**, [*s. l.*], v. 20, n. 2, p. 321–334, 1974. Disponível em: http://www.tandfonline.com/doi/abs/10.1080/00207177408932740. Acesso em: 13 dez. 2018.

KAZIMIERCZUK, M. K.; CZARKOWSKI, D. **Resonant Power Converters**. 2nd. ed. [*S. l.*]: New York: John Wiley & Sons, 2011.

KOHLER, S. V. *et al.* Self-oscillating LED driver with bus voltage regulation. **2018 13th IEEE**

International Conference on Industry Applications, INDUSCON 2018 - Proceedings, [*s. l.*], p. 495–501, 2019.

LAI, C. M.; SHYU, K. K. A single-stage AC/DC converter based on zero voltage switching LLC resonant topology. **IET Electric Power Applications**, [*s. l.*], v. 1, n. 5, p. 743–752, 2007. Disponível em: https://digital-library.theiet.org/content/journals/10.1049/iet-epa_20060322. Acesso em: 11 dez. 2018.

LI, L.; HUANG, W.; ZHAO, Y. Method Based on Improved FastICA-LSM for Harmonic Detection in Power System. **ACM International Conference Proceeding Series**, [*s. l.*], p. 6–10, 2021.

LIN, R. L.; CHEN, Y. F. Equivalent circuit model of light-emitting-diode for system analyses of lighting drivers. **Conference Record - IAS Annual Meeting (IEEE Industry Applications Society)**, [*s. l.*], 2009.

LIN, R. L.; CHEN, Y. F.; CHEN, Y. Y. Analysis and design of self-oscillating full-bridge electronic ballast for metal halide lamp at 2.65-MHz operating frequency. **IEEE Transactions on Power Electronics**, [*s. l.*], v. 27, n. 3, p. 1589–1597, 2012.

LIN, R. L.; WANG, Z. Q. 2.65 MHz self-oscillating electronic ballast with constant lamp-current control for metal halide lamp. *In*: , 2006. **PESC Record - IEEE Annual Power Electronics Specialists Conference**. [*S. l.*]: IEEE, 2006. p. 1–6.

LONG, X.; CHEN, D. Small Signal Modeling of LLC Converter with LED Load and Quasi-Resonant Controller Based Active Ripple Rejection. **Energies**, [*s. l.*], v. 16, n. 9, p. 3773, 2023. Disponível em: https://www.mdpi.com/1996-1073/16/9/3773/htm. Acesso em: 2 jul. 2023.

LONGSTAFF, F. A.; SCHWARTZ, E. S. Valuing American options by simulation: A simple least-squares approach. **Review of Financial Studies**, [*s. l.*], v. 14, n. 1, p. 113–147, 2001.

LOPES, J. D. P. Análise E Projeto Do Reator Eletrônico Auto-Oscilante Para Reconhecimento De Lâmpadas Fluorescentes. [*s. l.*], p. 172, 2014.

LUO, J. *et al.* Optimal design of a high efficiency LLC resonant converter with a narrow frequency range for voltage regulation. **Energies**, [*s. l.*], v. 11, n. 5, 2018.

MA, W.; XIE, X.; JIANG, S. LLC resonant converter with variable resonant inductor for wide LED dimming range. **Conference Proceedings - IEEE Applied Power Electronics Conference and Exposition - APEC**, [*s. l.*], p. 2950–2957, 2017.

MARCOS ALONSO, J. *et al.* Analysis and design of a novel variable-inductor-based LED driver for DC lighting grids. **IEEE Industry Application Society, 52nd Annual Meeting: IAS 2016**, [*s. l.*], 2016a.

MARCOS ALONSO, J. *et al.* Analysis and design of a novel variable-inductor-based LED driver for DC lighting grids. **IEEE Industry Application Society, 52nd Annual Meeting: IAS 2016**, [*s. l.*], 2016b.

MARCOS ALONSO, J. *et al.* SPICE-aided design of a variable inductor in LED driver

applications. *In*: , 2016c. **IEEE Industry Application Society, 52nd Annual Meeting: IAS 2016**. [*S. l.*]: IEEE, 2016.

MARCOS ALONSO, J. *et al.* Variable inductor modeling revisited: The analytical approach. **2017 IEEE Energy Conversion Congress and Exposition, ECCE 2017**, [*s. l.*], v. 2017-January, p. 895–902, 2017.

MATHEW, A. **FREQUENCY DOMAIN MODELLING OF SERIES LC-PARALLEL LC RESONANT CONVERTER WITH A CAPACITIVE OUTPUT FILTER**. 2021. 81 f. - Queen's University, [*s. l.*], 2021. Disponível em: https://qspace.library.queensu.ca/bitstream/handle/1974/28796/Mathew_Aiswarya_202104_MASc.pdf?sequence=6.

MAULUD, D.; ABDULAZEEZ, A. M. A Review on Linear Regression Comprehensive in Machine Learning. **Journal of Applied Science and Technology Trends**, [*s. l.*], v. 1, n. 4, p. 140–147, 2020.

MCVEY, E. S.; NURRE, G. S. The Application of Z-Transform Theory to the Analysis of Switched-Type Nonlinear Systems. **IEEE Transactions on Applications and Industry**, [*s. l.*], v. 83, n. 75, p. 353–360, 1964. Disponível em: http://ieeexplore.ieee.org/document/5407702/. Acesso em: 15 dez. 2018.

MENDES, A. P. *et al.* Experimental analysis of a dc current-controlled variable inductor in a DC-DC converter. *In*: , 2019. **Proceedings of the IEEE International Conference on Industrial Technology**. [*S. l.*]: IEEE, 2019. p. 440–445.

MENKE, M. F. *et al.* Analysis and Design of the LLC LED Driver Based on State-Space Representation Direct Time-Domain Solution. **IEEE Transactions on Power Electronics**, [*s. l.*], v. 35, n. 12, p. 12686–12701, 2020.

MENKE, M. F. *et al.* Comparison of self-oscillating electronic ballasts dimming methods with power factor correction for fluorescent lamps. *In*: , 2013. **Conference Record - IAS Annual Meeting (IEEE Industry Applications Society)**. [*S. l.*]: IEEE, 2013. p. 1–8. Disponível em: http://ieeexplore.ieee.org/document/6682547/. Acesso em: 31 maio 2019.

MENKE, M. F. *et al.* Improved design considerations for a self-oscillating resonant converter. *In*: , 2015. **2015 IEEE 13th Brazilian Power Electronics Conference and 1st Southern Power Electronics Conference, COBEP/SPEC 2016**. [*S. l.*]: IEEE, 2015. p. 1–6.

MENKE, M. F.; SEIDEL, A. R.; TAMBARA, R. V. LLC LED Driver Small-Signal Modeling and Digital Control Design for Active Ripple Compensation. **IEEE Transactions on Industrial Electronics**, [*s. l.*], v. 66, n. 1, p. 387–396, 2019.

MICHEL, A. L. *et al.* Electronic ballast with automatic luminous variation and presence detection using microcontroller and self-oscillating command. **Conference Record - IAS Annual Meeting (IEEE Industry Applications Society)**, [*s. l.*], v. 2, p. 1071–1077, 2002.

MIN, L. U. O.; HUI, L. Characteristic Analysis of LC Series Resonant Bidirectional DC-DC Converter. **Proceedings - 2019 6th International Conference on Information Science and Control Engineering, ICISCE 2019**, [*s. l.*], p. 690–695, 2019.

NI, B.; CHUNG, C. Y.; CHAN, H. L. Design and comparison of parallel and series resonant topology in wireless power transfer. **Proceedings of the 2013 IEEE 8th Conference on Industrial Electronics and Applications, ICIEA 2013**, [*s. l.*], p. 1832–1837, 2013.

NIWA, A. *et al.* A Dead-Time-Controlled Gate Driver Using Current-Sense FET Integrated in SiC MOSFET. **IEEE Transactions on Power Electronics**, [*s. l.*], v. 33, n. 4, p. 3258–3267, 2018.

OUTEIRO, M. T.; BUJA, G. Comparison of resonant power converters with two, three, and four energy storage elements. **IECON 2015 - 41st Annual Conference of the IEEE Industrial Electronics Society**, [*s. l.*], p. 1406–1411, 2015.

PANOV, V. **LLC resonant converter modelling**. 2014. - University of British Columbia, [*s. l.*], 2014. Disponível em: https://open.library.ubc.ca/soa/cIRcle/collections/ubctheses/24/items/1.0167311.

PAPPIS, D.; MACHADO, M. L.; PRADO, R. N. Self-oscillating electronic ballast with universal input voltage range. **PESC Record - IEEE Annual Power Electronics Specialists Conference**, [*s. l.*], v. 1, p. 659–664, 2004.

PAVÃO, R. K. *et al.* Self-oscillating electronic ballast design based on the point of view of control system. **Conference Record - IAS Annual Meeting (IEEE Industry Applications Society)**, [*s. l.*], v. 1, n. C, p. 211–217, 2001. Disponível em: http://ieeexplore.ieee.org/document/955413/. Acesso em: 11 dez. 2018.

PERDIGAO, M. S. *et al.* A review on variable inductors and variable transformers: Applications to lighting drivers. **IEEE Transactions on Industry Applications**, [*s. l.*], v. 52, n. 1, p. 531–547, 2016. Disponível em: http://ieeexplore.ieee.org/document/7283587/. Acesso em: 26 ago. 2019.

ROSA, W. G. *et al.* Self-oscillating resonant converter for led applications at 500 Khz. *In*: , 2017. **14th Brazilian Power Electronics Conference, COBEP 2017**. [*S. l.*]: IEEE, 2017. p. 1–7. Disponível em: http://ieeexplore.ieee.org/document/8257283/. Acesso em: 29 dez. 2018.

SÁ JR., E. M. **Estudo de Estruturas de Reatores Eletrônicos para LEDs de Iluminação**. 2010. 185 f. [*s. l.*], 2010.

SALEM, M. *et al.* Resonant power converters with respect to passive storage (LC) elements and control techniques – An overview. **Renewable and Sustainable Energy Reviews**, [*s. l.*], v. 91, p. 504–520, 2018.

SEIDEL, A. R. *et al.* Automatic Luminous Control for Self-Oscillating Electronic Ballast. **Conference Record - IAS Annual Meeting (IEEE Industry Applications Society)**, [*s. l.*], v. 2, p. 773–778, 2003.

SEIDEL, Á. R. *et al.* Self-Oscillating Dimmable Electronic Ballast. **IEEE Transactions on Industrial Electronics**, [*s. l.*], v. 50, n. 6, p. 1267–1274, 2003.

SEIDEL, Á. R.; BISOGNO, F. E.; DO PRADO, R. N. A design methodology for a self-oscillating electronic ballast. **IEEE Transactions on Industry Applications**, [*s. l.*], v. 43, n.

6, p. 1524–1533, 2007.

SHAIK, M.; KANKANALA, R. **AN1477, Digital compensator design for LLC resonant converter**. [*S. l.: s. n.*], 2012.

SHRIVASTAVA, A.; SINGH, B. LLC series resonant converter based LED lamp driver with ZVS. *In*: , 2012. **2012 IEEE 5th Power India Conference, PICONF 2012**. [*S. l.*]: IEEE, 2012. p. 1–5.

STEIGERWALD, R. L. A comparison of half-bridge resonant converter topologies. *In*: , 2015. **APEC 1987 - 2nd Annual IEEE Applied Power Electronics Conference and Exposition, Conference Proceedings**. [*S. l.: s. n.*], 2015. p. 135–144.

STMICROELECTRONICS. **AN3400 - Analysis and simulation of a BJT complementary pair in a self-oscillating CFL solution**. [*S. l.*], 2011. Disponível em: https://www.st.com/resource/en/application_note/dm00029455-analysis-and-simulation-of-a-bjt-complementary-pair-in-a-selfoscillating-cfl-solution-stmicroelectronics.pdf. .

SUN, J.; GROTSTOLLEN, H. Averaged modeling and analysis of resonant converters. **PESC Record - IEEE Annual Power Electronics Specialists Conference**, [*s. l.*], p. 707–713, 1993.

TAO, F. *et al.* Self-oscillating electronic ballast with dimming control. *In*: , 2001. **PESC Record - IEEE Annual Power Electronics Specialists Conference**. [*S. l.*]: IEEE, 2001. p. 1818–1823. Disponível em: http://ieeexplore.ieee.org/document/954386/. Acesso em: 26 ago. 2019.

TIAN, S. *et al.* Small-signal equivalent circuit model of series resonant converter. **2015 IEEE Energy Conversion Congress and Exposition, ECCE 2015**, [*s. l.*], p. 172–179, 2015.

VENTURINI, W. A. *et al.* Analysis and design methodology of a self-oscillating system based on integrated sepic half-bridge for LED lightning applications. *In*: , 2013. **2013 Brazilian Power Electronics Conference, COBEP 2013 - Proceedings**. [*S. l.*]: IEEE, 2013. p. 1120–1127. Disponível em: http://ieeexplore.ieee.org/document/6785255/. Acesso em: 11 dez. 2018.

VORPERIAN, V.; CUK, S. Small Signal Analysis of Resonant Converters. **PESC Record - IEEE Annual Power Electronics Specialists Conference**, [*s. l.*], p. 269–282, 1983.

WILSON, B. **2.6: Small Signal Model for Bipolar Transistor - Engineering LibreTexts**. [*S. l.*], [*s. d.*]. Disponível em: https://eng.libretexts.org/Bookshelves/Electrical_Engineering/Electronics/Introduction_to_Physical_Electronics_%28Wilson%29/02%3A_Bipolar_Transistors/2.06%3A_Small_Signal_Model_for_Bipolar_Transistor. Acesso em: 2 jul. 2023.

WONG, C. S. *et al.* Independent control of multicolor-multistring LED lighting systems with fully switched-capacitor-controlled LCC resonant network. **IEEE Transactions on Power Electronics**, [*s. l.*], v. 33, n. 5, p. 4293–4305, 2018.

YAGNIK, U. P.; SOLANKI, M. D. Comparison of L, LC & LCL filter for grid connected converter. **Proceedings - International Conference on Trends in Electronics and Informatics, ICEI 2017**, [*s. l.*], v. 2018-Janua, p. 455–458, 2018.

YANG, E. X.; LEE, F. C.; JOVANOVIC, M. M. Small-signal modeling of series and parallel resonant converters. **Conference Proceedings - IEEE Applied Power Electronics Conference and Exposition - APEC**, [*s. l.*], p. 785–792, 1992.

YOU, J. *et al.* Half-bridge LLC resonant converter design with GaN HEMT. *In*: , 2016. **2016 IEEE 8th International Power Electronics and Motion Control Conference, IPEMC-ECCE Asia 2016**. [*S. l.*]: IEEE, 2016. p. 2145–2149.

ZAUPA, N. *et al.* Hybrid Control of Self-Oscillating Resonant Converters. **IEEE Transactions on Control Systems Technology**, [*s. l.*], v. 31, n. 2, p. 881–888, 2023.

ZHANG, Y. *et al.* A Digital Liquid State Machine with Biologically Inspired Learning and Its Application to Speech Recognition. **IEEE Transactions on Neural Networks and Learning Systems**, [*s. l.*], v. 26, n. 11, p. 2635–2649, 2015.

ZHENG, J.; LU, S.; LI, J. LLC and LCC analysis and comparison of resonant converters. **Proceedings - 2020 35th Youth Academic Annual Conference of Chinese Association of Automation, YAC 2020**, [*s. l.*], p. 226–231, 2020.

APPENDIX A – CODE FOR THE CONTROLLER

```
#define ledPin 13
#include <Wire.h>
#include <Adafruit_MCP4725.h>
Adafruit_MCP4725 dac;
#define CH1 (B01000000)
#define ADC_START      (B01000000)
#define ADC_NOT_START  (B10111111)
volatile int measurementCounter = 0;
volatile int measurements[NUM_MEASUREMENTS];
volatile int ADC1 = 0;
volatile float xint = 0.0, erro = 0.0;
volatile float KP = 0.5, KI = 0.1, KW= 0.99, KD = 0.0;
volatile float UMAX=800.0, UMIN=500.0;
volatile float u=0.0, u_sat=0.0, ref=500.0, medida=0.0, prevErro=0.0;
volatile char XX = '0';
volatile unsigned char flag_controle = 0;
volatile unsigned char conversaoAD = 0;
volatile int aux=0;
float val=0;

void Inicializa_ADC()
        cli();          //disable interrupts
        pinMode(A0, INPUT);
        //CLEAR
        PRR =  0;
        ADCSRA = 0;
        ADCSRB = 1;
        ADMUX  = 0;
        DIDR0  = B00111111;
        ADCSRA |= (1 << ADPS2) | (1 << ADPS1); // | (1 << ADPS0); //set ADC clock with
128 prescaler- 16mHz/128=125kHz
        //ADCSRA |= (1 << ADATE); //enabble auto trigger
```

```
  ADCSRA |= (1 << ADIE);  //enable interrupts when measurement complete
  ADCSRA |= (1 << ADEN);  //enable ADC
  ADCSRA |= (1 << ADSC);  //start ADC measurements
  sei();         //enable interrupts

}

ISR(ADC_vect) {

  cli();         //disable interrupts
  ADC1 = ADCL + (ADCH << 8);
  ADMUX=CH1;
  conversaoAD = 1;
  sei();         //enable interrupts
}

void Inicializa_Timer() {

  pinMode(ledPin, OUTPUT);
  pinMode(A0, INPUT);
  TCCR1A = 0;
  TCCR1B = 0;
  TCCR1B |= (1<<CS10)|(0 << CS12)|(1 << CS11);
  TCNT1 = 0xF9E6;
  ICR1  = 16000000/freq_amostragem;
  TIMSK1 |= (1 << TOIE1);          // habilita a interrupção do TIMER1

}

ISR(TIMER1_OVF_vect)                        //interrupção do TIMER1
{

  TCNT1 = 0xF9E6;                           // Renicia TIMER
  ADCSRA |= (1 << ADSC); // dispara a conversao ad
```

```
  while(conversaoAD==0){}
  conversaoAD = 0;

  medida = ADC1;
  erro = medida - ref;
  u = KP*erro + xint;

   u_sat = u;
  if(u > UMAX) u_sat=UMAX;
  if(u < UMIN) u_sat=UMIN;

  xint = xint + KI*erro + KW * (u_sat - u) ;      /// 0 < KW  < 1

  flag_controle = 1;
}

void setup()
{
  Wire.begin();                  //Begins the I2C communication
  dac.begin(0x60);
  Serial.begin(115200);
  Inicializa_ADC();
  Inicializa_Timer();
}

void loop()
{

   if(flag_controle == 1){
    flag_controle = 0;
    dac.setVoltage(u_sat, false);
  }
}
```